Heavy Quark Production and Hadronisation at LEP

Dissertation
zur Erlangung des Doktorgrades
des Fachbereichs Physik
der Universität Hamburg

vorgelegt von
Frank Fiedler
geboren in Hamburg

Hamburg
1999

Gutachter der Dissertation:	Prof. Dr. A. Wagner Prof. Dr. B. Naroska
Gutachter der Disputation:	Prof. Dr. A. Wagner Prof. Dr. F.-W. Büßer
Datum der Disputation:	10. 12. 1999
Dekan des Fachbereichs Physik und Vorsitzender des Promotionsausschusses:	Prof. Dr. F.-W. Büßer

Für Grit und Lukas

Wer links und rechts nicht unterscheiden kann,
das ist ein armer Mann, das ist ein armer Mann.
Wer links und rechts nicht unterscheiden kann,
für den fang' ich nochmal von vorne an.

(Rolf Zuckowski)

Abstract

The bottom and charm forward-backward asymmetries $A_{\rm FB}^{\rm b}$ and $A_{\rm FB}^{\rm c}$ are measured with the OPAL detector at LEP in $\rm e^+e^-$ collisions at effective centre-of-mass energies of 74 GeV and between 130 GeV and 189 GeV. For the measurement at 74 GeV, events with significant initial state radiation recorded at LEP1 are boosted into the effective rest frame of the hadronic system, while for the LEP2 measurements events without significant initial state radiation are analysed. The forward-backward asymmetries are measured using leptons from semileptonic decays of bottom and charm hadrons as well as pions from $\rm D^{*+} \to D^0\pi^+$ decays. The bottom asymmetry measurements at LEP2 energies are combined with OPAL measurements obtained with a hemisphere charge technique in secondary vertex tagged events. All results are in agreement with the Standard Model predictions.

The measured asymmetries are interpreted together with OPAL measurements of the cross-section ratio $R_{\rm b} = \sigma(\rm e^+e^- \to b\bar{b})/\sigma(e^+e^- \to q\bar{q})$ at LEP2 energies and previous measurements in $\rm e^+e^-$ collisions around and below the Z resonance. The bottom and charm quark couplings to the Z boson are studied. With the measurements above and below the Z resonance, an unambiguous determination of the couplings is obtained, which is not possible from measurements in Z decays alone.

For the first time, the measurements are also interpreted using the S-Matrix parametrisation of the $\rm e^+e^- \to b\bar{b}$ and $\rm e^+e^- \to c\bar{c}$ processes. The contributions of interference between s-channel photon and Z exchange to the cross-sections and asymmetries are thus extracted in a model independent way. Future improvements of this analysis are assessed.

In a second analysis, $\rm D^{*0}$ mesons are reconstructed using data collected with the OPAL detector in $\rm e^+e^-$ collisions around the Z resonance. The hadronisation fraction of $\rm D^{*0}$ mesons in $\rm Z \to c\bar{c}$ decays is measured to be

$$f(\rm c \to D^{*0}) = 0.218 \pm 0.054 \pm 0.045 \pm 0.007\,,$$

where the errors correspond to the statistical and systematic errors specific to this analysis, and to systematic uncertainties from externally measured branching ratios, respectively. This value is consistent with the hadronisation fraction for $\rm D^{*+}$ mesons. The first measurement of the inclusive $\rm D_s^{*+}$ production rate in hadronic Z decays is also presented.

Together with previous OPAL measurements of the hadronisation fractions of other charmed mesons, the measurement of $f(\rm c \to D^{*0})$ is used to investigate the relative production of vector (V) and pseudoscalar (P) charmed mesons in $\rm Z \to c\bar{c}$ decays. The production ratio is determined to be

$$P_V^{\rm eff} = V/(V+P) = 0.57 \pm 0.05\ .$$

The relative primary production of vector and pseudoscalar mesons, $P_V^{\rm prim}$, is studied in the context of the production and decay of orbitally excited charmed resonances. A model independent formula for the $P_V^{\rm prim}$ ratio in charm hadronisation is derived. The results show a clear deviation from the prediction of HQET in the heavy quark limit, whereas measurements of bottom hadronisation are in agreement with these expectations.

Inhalt

Die Vorwärts-Rückwärts-Asymmetrien $A_{\mathrm{FB}}^{\mathrm{b}}$ und $A_{\mathrm{FB}}^{\mathrm{c}}$ für bottom- und charm-Quarks werden mit dem OPAL-Detektor bei LEP in $\mathrm{e^+e^-}$-Kollisionen bei effektiven Schwerpunktsenergien von 74 GeV und zwischen 130 GeV und 189 GeV gemessen. Für die Messung bei 74 GeV werden bei LEP1 aufgenommene Ereignisse mit signifikanter Photonabstrahlung im Anfangszustand in das effektive Schwerpunktssystem des hadronischen Systems transformiert, während für die LEP2-Messungen Ereignisse ohne signifikante Photonabstrahlung analysiert werden. Die Vorwärts-Rückwärts-Asymmetrien werden mittels Leptonen aus semileptonischen Zerfällen von bottom- und charm-Hadronen sowie Pionen aus $\mathrm{D}^{*+} \to \mathrm{D}^0\pi^+$-Zerfällen gemessen. Die Meßwerte der Vorwärts-Rückwärts-Asymmetrie für bottom-Quarks bei LEP2-Energien werden mit OPAL-Messungen kombiniert, die mit einer Hemisphärenladung in Ereignissen mit einem identifizierten Sekundärvertex erhalten wurden. Alle Resultate sind in Übereinstimmung mit den Vorhersagen des Standardmodells.

Die gemessenen Asymmetrien werden zusammen mit OPAL-Messungen des partiellen hadronischen Wirkungsquerschnitts $R_{\mathrm{b}} = \sigma(\mathrm{e^+e^-} \to \mathrm{b\bar{b}})/\sigma(\mathrm{e^+e^-} \to \mathrm{q\bar{q}})$ bei LEP2-Energien sowie früheren Messungen in $\mathrm{e^+e^-}$-Kollisionen um und unterhalb der Z-Resonanz interpretiert. Die Kopplungen von bottom- und charm-Quarks an das Z-Boson werden studiert. Durch die Messungen ober- und unterhalb der Z-Resonanz sind die Kopplungen eindeutig bestimmt, was durch Messungen in Z-Zerfällen allein nicht möglich ist.

Zum ersten Mal werden die Messungen auch im Rahmen des S-Matrix-Ansatzes für die Prozesse $\mathrm{e^+e^-} \to \mathrm{b\bar{b}}$ und $\mathrm{e^+e^-} \to \mathrm{c\bar{c}}$ interpretiert. Die Beiträge der Interferenz zwischen s-Kanal Photon- und Z-Austausch zu den Wirkungsquerschnitten und Asymmetrien werden so auf modellunabhängige Weise bestimmt. Zukünftige Verbesserungen dieser Analyse werden abgeschätzt.

In einer zweiten Analyse werden in Daten, die mit dem OPAL-Detektor in $\mathrm{e^+e^-}$-Kollisionen nahe der Z-Resonanz aufgezeichnet wurden, D^{*0}-Mesonen rekonstruiert. Der Hadronisations-Anteil von D^{*0}-Mesonen in $\mathrm{Z} \to \mathrm{c\bar{c}}$-Zerfällen wird zu

$$f(\mathrm{c} \to \mathrm{D}^{*0}) = 0.218 \pm 0.054 \pm 0.045 \pm 0.007$$

bestimmt, wobei die Fehler den statistischen und systematischen Fehlern aus dieser Analyse sowie systematischen Unsicherheiten aufgrund von externen Messungen von Verzweigungsverhältnissen entsprechen. Dieser Wert ist konsistent mit dem Hadronisations-Anteil von D^{*+}-Mesonen. Außerdem wird die erste Messung der inklusiven Produktionsrate von $\mathrm{D}_{\mathrm{s}}^{*+}$-Mesonen in hadronischen Z-Zerfällen vorgestellt.

Zusammen mit früheren OPAL-Messungen der Hadronisations-Anteile anderer charm-Mesonen wird die Messung von $f(\mathrm{c} \to \mathrm{D}^{*0})$ zur Bestimmung der relativen Produktion von Vektor- (V) und Pseudoskalarmesonen (P) in $\mathrm{Z} \to \mathrm{c\bar{c}}$-Zerfällen herangezogen. Das Produktionsverhältnis wird zu

$$P_V^{\mathrm{eff}} = V/(V+P) = 0.57 \pm 0.05$$

bestimmt. Das primäre Produktionsverhältnis von Vektor- und Pseudoskalarmesonen, P_V^{prim}, und sein Zusammenhang mit Produktion und Zerfall orbital angeregter charm-Resonanzen werden studiert. Eine modellunabhängige Formel für das P_V^{prim}-Verhältnis in charm-Hadronisation wird hergeleitet. Die Resultate zeigen eine klare Abweichung von der HQET-Vorhersage im Grenzfall schwerer Quarks, während Messungen der bottom-Hadronisation in Übereinstimmung mit diesen Erwartungen sind.

Contents

1 Physics Processes in Heavy Quark Production and Hadronisation 8

1.1 Cross-Sections and Asymmetries in e^+e^- Collisions . . . 9

1.1.1 Concepts and Born Level Formulae . . . 9

1.1.2 Higher-Order Corrections . . . 12

1.1.3 Measurements of Heavy Quark Production and Asymmetries . . . 13

1.2 Hadronisation of Heavy Quarks . . . 14

1.2.1 Heavy-Light Hadron Formation . . . 15

1.2.2 Properties and Decays of Bottom and Charm Mesons . . . 16

1.2.3 Analysis of Charmed Vector Meson Production . . . 17

2 The OPAL Detector 21

2.1 The Central Tracking System . . . 23

2.2 The Calorimeter System and the Muon Chambers . . . 24

2.3 The Forward Detectors . . . 26

3 Heavy Quark Production above the Z Resonance 27

3.1 Methods Used in Heavy Flavour Electroweak Measurements . . . 27

3.2 Event Selection . . . 30

3.3 Measurement of R_b . . . 33

3.3.1 Secondary Vertex Tag . . . 33

3.3.2 Determination of R_b from the Vertex Tagged Events . . . 35

3.4 Measurement of Forward-Backward Asymmetries . . . 38

3.4.1 Measurement of A_{FB}^b with a Hemisphere Charge Technique . . . 39

3.4.2 Identification of Prompt Leptons and Slow Pions . . . 42

3.4.2.1 Electron Identification . . . 42

3.4.2.2 Muon Identification . . . 43

3.4.2.3 Preselection of Slow Pion Candidates . . . 46

3.4.3 Flavour Separation of the Lepton and Slow Pion Samples 47
3.4.4 Measurement of A_{FB}^{b} and A_{FB}^{c} with Leptons and Slow Pions 53
3.4.5 Combination of the A_{FB}^{b} Measurements 58
3.5 Systematic Errors 60
3.5.1 Systematic Errors on R_b and A_{FB}^{b} with the Secondary Vertex Tag 61
3.5.1.1 Event Selection 61
3.5.1.2 Bottom and Charm Physics Modelling 62
3.5.1.3 Four-Fermion Background 63
3.5.1.4 Monte Carlo Statistics 63
3.5.1.5 Track Reconstruction 63
3.5.2 Systematic Errors on A_{FB}^{b} and A_{FB}^{c} with the Lepton and Slow Pion Tag . 63
3.5.2.1 Detector Systematics 64
3.5.2.2 Physics Systematics 66
3.5.2.3 Monte Carlo Statistics 68
3.5.2.4 Checks of the Fitting Method 68
3.6 Results 69

4 Heavy Quark Production below the Z Resonance 73
4.1 Region of Interest 73
4.2 Simulation of Events 75
4.3 Identification of Events with Hard Initial State Radiation 76
4.3.1 Event Selection 76
4.3.2 Calibration of the Event Selection Efficiency 78
4.4 Asymmetry Analysis 80
4.5 Cross-Check of the Analysis 85
4.6 Systematic Errors 86
4.6.1 Event Selection and Determination of the Effective Centre-of-Mass Frame 87
4.6.2 Interference between Initial and Final State Radiation 88
4.6.3 Asymmetry Analysis 88
4.7 Summary 89

5 Interpretation of the Measurements of Heavy Quark Production 90
5.1 Heavy Flavour Measurements used in the Fits 90
5.2 Determination of the Effective Heavy Quark Couplings 95
5.3 An S-Matrix Parametrisation of the $e^+e^- \to b\bar{b}$ and $e^+e^- \to c\bar{c}$ Processes 97
5.4 Conclusion 101

6 Measurements of D^{*0} and D_s^{*+} Production in Z Decays **103**

6.1 Reconstruction and Selection of D^{*0} Candidates . . . 103

6.1.1 Reconstruction of D^0 Mesons, Photons, and π^0 Mesons . . . 104

6.1.2 Background Determination . . . 107

6.1.3 Reconstruction Efficiency . . . 110

6.2 Measurement of $f(c \to D^{*0})$ . . . 111

6.2.1 Subtraction of the Component from b Hadron Decays . . . 111

6.2.2 The Fit to the Mass Difference Distributions . . . 112

6.2.3 Consistency Checks . . . 113

6.2.4 Systematic Uncertainties . . . 114

6.2.4.1 Uncertainties from the Modelling of Selection Variables . . . 114

6.2.4.2 Uncertainties in the Detector Resolution . . . 116

6.2.4.3 Uncertainties in the Fit Procedure . . . 116

6.2.4.4 Uncertainties from the b Subtraction and the Extrapolation . . . 117

6.3 Measurement of D_s^{*+} Production . . . 117

6.4 Results of the D^{*0} and ${D_s}^{*+}$ Measurements . . . 120

7 Analysis of Charmed Vector Meson Production **121**

7.1 Tests of Isospin Invariance . . . 121

7.2 The Relative Production Rate of Charmed Vector Mesons in $Z \to c\bar{c}$ Decays . . . 123

7.2.1 Effective Charmed Meson Production . . . 123

7.2.2 Primary Charmed Meson Production . . . 124

7.3 Comparison of Charm and Bottom Meson Production . . . 126

7.4 Summary . . . 128

8 Summary **129**

A An Artificial Neural Network For Muon Identification **132**

A.1 Muon Identification at OPAL . . . 133

A.2 The Selection Variables . . . 134

A.3 Implementation and Performance of the Neural Net . . . 136

A.4 Systematic Errors . . . 136

A.4.1 Systematic Errors at LEP1 . . . 138

A.4.2 Systematic Errors at LEP2 . . . 139

A.5 Conclusion . . . 139

B Systematic Errors Related to the Slow Pion Reconstruction **143**

B.1 The Technique 143

B.2 Determination of the Slow Pion Reconstruction Efficiency 144

C Model Independent Calculation of P_V^{prim} **148**

Chapter 1

Physics Processes in Heavy Quark Production and Hadronisation

In recent years, important progress has been made in elementary particle physics through the analysis of e^+e^- annihilation. To lowest order, this process can be described by the s-channel exchange of a photon or a Z boson, and depicted by the diagrams in figure 1.1. At centre-of-mass energies around the Z mass[1], the Z exchange in the s-channel dominates, and the cross-section is enhanced. The experiments at LEP and SLC have taken large event samples of e^+e^- collisions close to the Z resonance. Among the major goals of these experiments are precision tests of the electroweak theory and measurements of hadron production and properties.

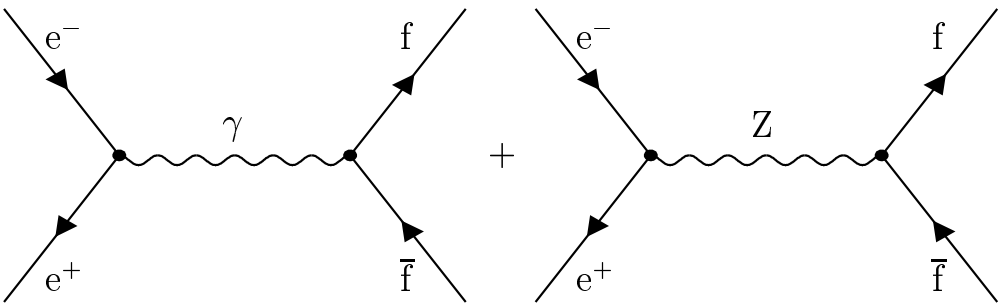

Figure 1.1: The Feynman graphs of the two leading-order processes in e^+e^- annihilation. Photon exchange does not contribute if the final state fermion f is a neutrino.

Above and below the Z resonance, the size of the s-channel Z exchange amplitude is reduced, and the contribution from the s-channel photon exchange amplitude becomes important. Although the cross-section is reduced, e^+e^- collisions at these centre-of-mass energies allow a study of $\gamma - Z$ interference, which vanishes in collisions at the Z mass. The region of centre-of-mass energies between around 30 GeV and 60 GeV has been explored by the experiments at the PEP, PETRA, and TRISTAN accelerators, while since 1995, the LEP2 programme allows e^+e^- collisions at centre-of-mass energies above the Z resonance up to around 200 GeV to be studied.

[1]The convention $\hbar = c = 1$ is used throughout this thesis.

Any fermion-antifermion pair can be created in the processes shown in figure 1.1 if the centre-of-mass energy is large enough. In quark-antiquark pair production, colourless hadrons are formed in the hadronisation process[2], and the information on the primary quark and antiquark is diluted. Nevertheless, because of the precise knowledge of the initial state, the clean experimental environment in e^+e^- collisions, and the particular properties of heavy hadrons, it is possible to recuperate information on the primary quarks for the heavy quark species bottom and charm, and to measure their coupling parameters to the Z boson[3].

In this thesis, measurements of the forward-backward asymmetries in heavy quark production are presented for effective centre-of-mass energies above and below the Z resonance, using the OPAL detector at LEP. These measurements are based on heavy hadron identification via semileptonic and $D^{*+} \to D^0\pi^+$ decays[4]. They are then combined with OPAL measurements of the bottom production rate and forward-backward asymmetry based on secondary vertex reconstruction. The combined measurements are used to constrain the bottom and charm couplings to the Z boson and to investigate the effects of interference between s-channel photon and Z exchange on bottom and charm production. This analysis is outlined in section 1.1.

In addition, e^+e^- collisions offer the possibility to study the formation and decay of hadrons under clean experimental conditions. Except for the possible radiation of energetic gluons, the hadronisation process is governed by non-perturbative QCD. Due to the lack of a comprehensive theoretical calculation of this process, measurements are needed to tune model descriptions. In the second part of this thesis, the hadronisation of heavy quarks is studied, with particular emphasis on the production of vector and pseudoscalar charmed mesons. This analysis is briefly described in section 1.2.

1.1 Cross-Sections and Asymmetries in e^+e^- Collisions

1.1.1 Concepts and Born Level Formulae

To first order ("Born approximation") and in the approximation of massless fermions, the differential cross-section for the process $e^+e^- \to f\bar{f}$ ($f \neq e, \nu_e$)[5] for unpolarized electron and positron beams at a centre-of-mass energy $\sqrt{s}$ is [1]

$$\frac{\mathrm{d}\,\sigma^{\mathrm{f}}}{\mathrm{d}\,(\cos\theta)}(s) = \frac{G_F^2 m_{\mathrm{Z}}^4 \sin^4\theta_W \cos^4\theta_W}{\pi} N_C^{\mathrm{f}} \frac{1}{s} \left[\sigma_{\mathrm{tot}}^{\mathrm{f}}(s)\left(1+\cos^2\theta\right) + 2\,\sigma_{\mathrm{FB}}^{\mathrm{f}}(s)\cos\theta\right] , \qquad (1.1)$$

where

$$\begin{aligned} \sigma_{\mathrm{tot}}^{\mathrm{f}}(s) &= \underbrace{q_{\mathrm{f}}^2}_{\gamma\text{ exchange}} - \underbrace{2\,\tilde{v}_{\mathrm{e}}\tilde{v}_{\mathrm{f}}\,q_{\mathrm{f}}\,\mathrm{Re}\chi_0(s)}_{\gamma-\mathrm{Z}\text{ interference}} + \underbrace{(\tilde{v}_{\mathrm{e}}^2+\tilde{a}_{\mathrm{e}}^2)(\tilde{v}_{\mathrm{f}}^2+\tilde{a}_{\mathrm{f}}^2)\,|\chi_0(s)|^2}_{\mathrm{Z}\text{ exchange}} \quad \text{and} \\ \sigma_{\mathrm{FB}}^{\mathrm{f}}(s) &= \underbrace{\phantom{q_{\mathrm{f}}^2}}_{\gamma\text{ exchange}} - \underbrace{2\,\tilde{a}_{\mathrm{e}}\tilde{a}_{\mathrm{f}}\,q_{\mathrm{f}}\,\mathrm{Re}\chi_0(s)}_{\gamma-\mathrm{Z}\text{ interference}} + \underbrace{4\,\tilde{v}_{\mathrm{e}}\tilde{a}_{\mathrm{e}}\tilde{v}_{\mathrm{f}}\tilde{a}_{\mathrm{f}}\,|\chi_0(s)|^2}_{\mathrm{Z}\text{ exchange}} \quad . \end{aligned} \qquad (1.2)$$

[2] The production of $t\bar{t}$ pairs is not considered here.

[3] The coupling to the photon is assumed to be known in the context of these measurements.

[4] Charge conjugate modes are included implicitly here and throughout this thesis.

[5] For electrons and electron-neutrinos, there are also first-order t-channel contributions which are not discussed here.

Here, G_F is the Fermi constant, m_{Z} is the mass of the Z boson, and θ_W stands for the weak mixing angle. The colour factor N_C^{f} equals 1 for leptons and 3 for quarks in the final state. The angle θ is measured between the directions of the incoming electron and the outgoing fermion. The vector and axial vector couplings v_{f} and a_{f} of fermion f to the Z boson enter equation 1.2 via the abbreviations

$$\tilde{v}_{\mathrm{f}} = \frac{v_{\mathrm{f}}}{2\sin\theta_W\cos\theta_W} \quad \text{and} \quad \tilde{a}_{\mathrm{f}} = \frac{a_{\mathrm{f}}}{2\sin\theta_W\cos\theta_W}\,, \tag{1.3}$$

and q_{f} denotes the fermion charge. Apart from the factor $1/s$ in equation 1.1, the energy dependence of the cross-section is given by the propagator function $\chi_0(s) = s/\left(s - m_{\mathrm{Z}}^2 + im_{\mathrm{Z}}\Gamma_{\mathrm{Z}}\right)$, which yields

$$\begin{aligned} \mathrm{Re}\chi_0(s) &= \frac{s}{\left(s-m_{\mathrm{Z}}^2\right)^2 + m_{\mathrm{Z}}^2\Gamma_{\mathrm{Z}}^2}\left(s - m_{\mathrm{Z}}^2\right) \quad \text{and} \\ \left|\chi_0(s)\right|^2 &= \frac{s^2}{\left(s-m_{\mathrm{Z}}^2\right)^2 + m_{\mathrm{Z}}^2\Gamma_{\mathrm{Z}}^2}\,. \end{aligned} \tag{1.4}$$

Here, Γ_{Z} stands for the total width of the Z boson.

In the Standard Model, the Born level cross-sections for any final state fermion are completely determined by three parameters. Commonly, the following measurements[6] are taken as inputs [2]:

- the fine structure constant $\alpha = 1/(137.0359895 \pm 0.0000061)$,
- the Fermi constant $G_F = (1.16639 \pm 0.00001)\cdot 10^{-5}\,\mathrm{GeV}^{-2}$, and
- the mass of the Z boson, $m_{\mathrm{Z}} = 91.1867 \pm 0.0021$ GeV [3], or equivalently [2], the weak mixing angle θ_W with $\sin^2\theta_W = 0.23157 \pm 0.00018$ [3].

The vector and axial vector coupling constants of a fermion f to the Z boson are then given by

$$\begin{aligned} v_{\mathrm{f}} &= I_3^{\mathrm{f}} - 2q_{\mathrm{f}}\sin^2\theta_W \text{ and} \\ a_{\mathrm{f}} &= I_3^{\mathrm{f}}\,, \end{aligned} \tag{1.5}$$

where I_3^{f} stands for the third component of the weak isospin.

In unpolarized $\mathrm{e^+e^-}$ annihilation, one generally measures the total cross-section and the forward-backward asymmetry for a given final state fermion to determine its couplings to the Z boson[7]. This thesis focuses on a study of heavy quarks, for which one measures the partial hadronic cross-section R_{q} and forward-backward asymmetry $A_{\mathrm{FB}}^{\mathrm{q}}$, defined as

$$R_{\mathrm{q}} = \frac{\sigma^{\mathrm{q}}}{\sum\limits_{\mathrm{q}'}\sigma^{\mathrm{q}'}} = \frac{\sigma_{\mathrm{tot}}^{\mathrm{q}}}{\sum\limits_{\mathrm{q}'}\sigma_{\mathrm{tot}}^{\mathrm{q}'}} \quad \text{and} \tag{1.6}$$

$$A_{\mathrm{FB}}^{\mathrm{q}} = \frac{\sigma^{\mathrm{q}}(\cos\theta > 0) - \sigma^{\mathrm{q}}(\cos\theta < 0)}{\sigma^{\mathrm{q}}(\cos\theta > 0) + \sigma^{\mathrm{q}}(\cos\theta < 0)} = \frac{3}{4}\frac{\sigma_{\mathrm{FB}}^{\mathrm{q}}(s)}{\sigma_{\mathrm{tot}}^{\mathrm{q}}(s)}\,. \tag{1.7}$$

From equation 1.2, one can conclude that at the Z resonance, a measurement of the partial hadronic cross-section yields information on $\left(v_{\mathrm{e}}^2 + a_{\mathrm{e}}^2\right)\left(v_{\mathrm{q}}^2 + a_{\mathrm{q}}^2\right)$, while the forward-backward

[6] All of these values include higher-order corrections. For $\mathrm{e^+e^-}$ collisions, these are outlined in section 1.1.2.

[7] Additional information from final state polarisation can in practice only be obtained in the case of the $\mathrm{e^+e^-} \to \tau^+\tau^-$ process.

asymmetry is determined by the product $v_e a_e v_q a_q$. From measurements above and below the Z resonance, additional information can be obtained from the $\gamma - Z$ interference term. Since $|v_e|$ is small ($c_V^e = -0.03781 \pm 0.00052$ [3]), the additional constraints on v_q from measurements of R_q at centre-of-mass energies above and below m_Z are expected to be weak. The information on a_q from asymmetry measurements is in principle larger, but compromised for quarks due to the larger experimental errors of the asymmetry measurement.

If the electron beam is polarized, as is the case at the SLD experiment, the cross-section asymmetry A_{LR} and the left-right forward-backward asymmetry $A_{LR,FB}^q$ can also be measured, which are defined as

$$\begin{aligned} A_{LR} &= \frac{1}{\mathcal{P}} \frac{\sigma_L - \sigma_R}{\sigma_{tot}} \quad \text{and} \\ A_{LR,FB}^q &= \frac{1}{\mathcal{P}} \frac{\left(\sigma_L^q(\cos\theta > 0) - \sigma_L^q(\cos\theta < 0)\right) - \left(\sigma_R^q(\cos\theta > 0) - \sigma_R^q(\cos\theta < 0)\right)}{\sigma_{tot}^q} . \end{aligned} \tag{1.8}$$

Here, $\mathcal{P}$ denotes the polarisation of the electron beam, and σ_L and σ_R denote the cross-sections for left-handed and right-handed electrons, respectively. For pure Z exchange, the left-right asymmetry is sensitive only to the electron couplings:

$$A_{LR} = \frac{2 v_e a_e}{v_e^2 + a_e^2} \equiv \mathcal{A}_e , \tag{1.9}$$

independent of the final state fermion, and the left-right forward-backward asymmetry yields additional information on the couplings of the final state fermions:

$$A_{LR,FB}^q = \frac{3}{4} \frac{2 v_q a_q}{v_q^2 + a_q^2} \equiv \frac{3}{4} \mathcal{A}_q . \tag{1.10}$$

For pure s-channel Z exchange, the predictions for all heavy flavour observables depend only on the parameters $\mathcal{A}_e$ and $\mathcal{A}_q$. Thus, they are invariant either under a sign change of both the vector and axial vector couplings or under an exchange of the two couplings. These ambiguities can be resolved with measurements at energies above and below m_Z, where the vector and axial vector couplings are accessible separately, as discussed above.

In the above description of e^+e^- annihilation, the $\gamma - Z$ interference term is assumed to be fully determined from the couplings to the photon and the Z boson. A less model dependent description of experimental observables is obtained in the S-Matrix approach [4], where the total and forward-backward cross-sections are parameterised as

$$\sigma_a^f(s) \sim \left[g_f^a + \frac{r_f^a \, s^2 + j_f^a \, s \, (s - \overline{m}_Z^2)}{(s - \overline{m}_Z^2)^2 + \overline{m}_Z^2 \overline{\Gamma}_Z^2} \right] , \; a = \text{tot}, \; \text{FB}. \tag{1.11}$$

Here, g and r denote the contributions from γ and Z exchange, while the interference term is parametrized by j. Similar formulae with independent parameters exist for the left-right and left-right forward-backward asymmetric cross-sections; these are not used in this thesis. The formula is valid for any fermion species in the final state and for both the total ($a = \text{tot}$) and forward-backward ($a = \text{FB}$) cross-sections. The photon exchange term g is assumed to be known from QED, and it does not contribute to the asymmetry: $g_f^{FB} = 0$. The Z mass and

width are usually defined using a Breit-Wigner shape with s-dependent width; the parameters $\overline{m}_{\mathrm{Z}}$ and $\overline{\Gamma}_{\mathrm{Z}}$ are related to these definitions via

$$\overline{m}_{\mathrm{Z}} = \frac{m_{\mathrm{Z}}}{\sqrt{1+\Gamma_{\mathrm{Z}}^2/m_{\mathrm{Z}}^2}} \qquad \text{and} \qquad \overline{\Gamma}_{\mathrm{Z}} = \frac{\Gamma_{\mathrm{Z}}}{\sqrt{1+\Gamma_{\mathrm{Z}}^2/m_{\mathrm{Z}}^2}}\,. \tag{1.12}$$

When only vector (V) and axial vector (A) couplings of the Z are allowed, as in the Standard Model, the S-Matrix parameters r and j are approximately given by [4]

$$\begin{array}{lcl} r_{\mathrm{f}}^{\mathrm{tot}} & \sim & (a_{\mathrm{e}}^2+v_{\mathrm{e}}^2)\,(a_{\mathrm{f}}^2+v_{\mathrm{f}}^2)\ , \\ j_{\mathrm{f}}^{\mathrm{tot}} & \sim & v_{\mathrm{e}}\,v_{\mathrm{f}}\ , \\ r_{\mathrm{f}}^{\mathrm{FB}} & \sim & a_{\mathrm{e}}\,v_{\mathrm{e}}\ +a_{\mathrm{f}}\,v_{\mathrm{f}}\ , \text{ and} \\ j_{\mathrm{f}}^{\mathrm{FB}} & \sim & a_{\mathrm{e}}\,a_{\mathrm{f}}\ . \end{array} \tag{1.13}$$

1.1.2 Higher-Order Corrections

For precision electroweak measurements, the above Born-level description is not adequate. The fermion masses and higher-order corrections have to be taken into account. The latter can be grouped into three categories:

- **Electroweak corrections:**
  These corrections are due to contributions from loop diagrams, which lead to corrections both to the Z or photon propagator and to the Zff̄ vertex. They are in general parametrised by effective coupling constants $c_{\mathrm{V}}^{\mathrm{f}}$ and $c_{\mathrm{A}}^{\mathrm{f}}$. When these effective couplings replace v_{f} and a_{f}, the Born-level formulae 1.1 and 1.2 remain valid ("improved Born approximation"). Due to the loop contributions, the predicted couplings become sensitive to the masses of the top quark and the Higgs boson. Thus, measurements of the fermion couplings to the Z boson provide a check of the Standard Model and, within the Standard Model, constrain the top and Higgs masses [3]. The analytical programs ZFITTER [5] and SMATASY [6] allow a calculation of experimental observables from a given set of effective couplings, or S-Matrix parameters.
- **Final state QCD corrections:**
  Hard gluon radiation from final state quarks may distort the kinematics of hadronic events. For instance, the definition of the scattering angle θ (which is needed in measurements of forward-backward asymmetries) becomes ambiguous when both quarks are emitted into the same event hemisphere. The actual effects on measurements of partial hadronic widths and forward-backward asymmetries depend on the details of the experimental analyses.
- **QED corrections:**
  In contrast to gluons, photons can be radiated from both the incoming and outgoing fermions if the latter are charged. Final state photon radiation ("fsr") has similar effects as described above, but for quarks, it is suppressed with respect to gluon radiation. Photon radiation off the initial state fermions ("isr") influences the physics of the $\mathrm{e^+e^-}$ collision in their rest frame much more drastically:

  In general, the differential cross-section for the process $\mathrm{e^+e^-} \to \mathrm{f\bar{f}}(n\gamma)$, where f denotes a quark or a charged lepton and radiation of an unspecified number of photons is allowed

for, can be written as

$$\frac{\mathrm{d}^2\sigma^{\mathrm{f}}}{\mathrm{d}x\,\mathrm{d}\,(\cos\theta^*)}(s) = \frac{1}{\sigma^{\mathrm{f}}(s)} H(s,x)\left[\frac{3}{8}\sigma^{\mathrm{f}}_{\mathrm{tot}}(s')\left(1+\cos^2\theta^*\right) + \frac{3}{4}\sigma^{\mathrm{f}}_{\mathrm{FB}}(s')\cos\theta^*\right], \qquad (1.14)$$

where $\sigma^{\mathrm{f}}_{\mathrm{tot}}$ and $\sigma^{\mathrm{f}}_{\mathrm{FB}}$ are defined in equation 1.2, with electroweak corrections included as described above. In this equation, s denotes the total available centre-of-mass energy squared, while $s' \equiv s(1-x)$ is the invariant mass squared of the $\mathrm{f\bar{f}}$ system after photon radiation. In the case of only one photon, its energy is given by $E^{\mathrm{isr}} = \sqrt{sx}$. The angle θ^* is defined in the $\mathrm{f\bar{f}}$ rest frame, where it denotes the angle of the outgoing fermion with respect to the direction of the incoming electron. The photon bremsstrahlung is taken into account via the radiator function $H(s,x)$, which is the probability density at a given centre-of-mass energy $\sqrt{s}$ that photons are emitted in the initial state such that the mass of the $\mathrm{f\bar{f}}$ pair is lowered to $\sqrt{s'}$. The predicted hadronic cross-section as a function of the effective centre-of-mass energy $\sqrt{s'}$ is shown in figure 4.1 for $\mathrm{e^+e^-}$ collisions at the Z mass.

Photons from initial state and final state radiation are in principle indistinguishable in the observed final state $\mathrm{f\bar{f}}\gamma$, and the two processes interfere. This leads to a complication in the interpretation of equation 1.14 for charged fermions in the final state, since $\sqrt{s'}$ can only be interpreted as the effective centre-of-mass energy of the $\mathrm{e^+e^-}$ collision after photon radiation if one neglects this interference. The resulting uncertainties are in general small when an integration over the parameter x in equation 1.14 is performed and the integrated region in $\sqrt{s'}$ is large compared to the width of the Z resonance [7], and they do not limit the measurements presented in this thesis.

1.1.3 Measurements of Heavy Quark Production and Asymmetries

The heavy quark partial hadronic widths and forward-backward asymmetries in Z decays have been measured very accurately at LEP1 and SLD [3], and measurements at $\mathrm{e^+e^-}$ centre-of-mass energies between $\sim 30\,\mathrm{GeV}$ and $\sim 60\,\mathrm{GeV}$ have been performed at PEP [8], PETRA [9], and TRISTAN [10]. In the first part of this thesis, heavy quark asymmetry measurements are performed with the OPAL detector[8] over a broad range of (effective) centre-of-mass energies, extending the energy range far beyond the Z resonance peak and closing the gap between the TRISTAN and LEP1 energies. An analysis of events at these energies can only be performed by the LEP experiments (the SLD data sample being too small for an analysis of radiative events). Furthermore, the measurement profits from the excellent understanding of the detector from the LEP1 running. The LEP2 measurements are cross-checked using detector calibration data taken on the Z resonance in the same years as the high energy data; and the analysis of radiative events at LEP1 is calibrated with radiative events at LEP2, where a clean identification of events with "radiative return to the Z peak" is possible. The event samples used for the measurements and the cross-checks are shown schematically in table 1.1.

For the measurements of heavy quark forward-backward asymmetries, hadronic events with heavy quarks have to be identified, and in these events, the quark and antiquark event hemispheres have to be distinguished. The measurements in this thesis are based on the identification of leptons from semileptonic decays of bottom and charm hadrons as well as on pions from

[8] The OPAL results at centre-of-mass energies above the Z resonance can be found in [11, 12, 13]. Similar measurements have also been presented by ALEPH [14] and DELPHI [15].

	radiative events	non-radiative events
$\sqrt{s} \approx m_{\mathrm{Z}}$ (LEP1)	**measurement:** bottom and charm asymmetries below the Z resonance ($\sqrt{s'} < m_{\mathrm{Z}}$)	*cross-check:* for the measurement of bottom and charm asymmetries above the Z resonance (using calibration data at $\sqrt{s'} \approx m_{\mathrm{Z}}$)
$\sqrt{s} > m_{\mathrm{Z}}$ (LEP2)	*cross-check:* for the measurement of bottom and charm asymmetries below the Z resonance (using "radiative return" events with $\sqrt{s'} \approx m_{\mathrm{Z}}$)	**measurement:** bottom and charm asymmetries above the Z resonance ($\sqrt{s'} > m_{\mathrm{Z}}$)

Table 1.1: An overview over the four different event samples used in the asymmetry measurements presented in this thesis.

$\mathrm{D}^{*+} \to \mathrm{D}^0\pi^+$ decays. These particles provide a tag of bottom and charm events, and also allow the quark and antiquark hemispheres to be distinguished based on the lepton or pion charge. The LEP2 results are combined with OPAL measurements of R_{b} and $A_{\mathrm{FB}}^{\mathrm{b}}$ based on secondary vertex reconstruction. The combined values are then interpreted as follows:

- The measurements provide a test of the Standard Model that is independent from the measurements at the Z resonance. Any deviation of the quark couplings from the Z resonance values would indicate new physics effects at the corresponding centre-of-mass energy.
- In the absence of significant deviations, the measurements place additional constraints on the quark couplings, and help resolve the ambiguities in the vector and axial vector couplings to the Z that are present for pure Z exchange.
- A model independent determination of the $\gamma - \mathrm{Z}$ interference terms for the processes $\mathrm{e^+e^-} \to \mathrm{b\bar{b}}$ and $\mathrm{e^+e^-} \to \mathrm{c\bar{c}}$ is performed in the framework of an S-Matrix parametrisation of the Z resonance.

1.2 Hadronisation of Heavy Quarks

The large samples of hadronic Z decays recorded at the LEP and SLD experiments offer a unique opportunity to study the process of hadron formation. Analyses of hadron production in $\mathrm{e^+e^-}$ collisions benefit from the detailed knowledge of the electroweak processes of quark-antiquark pair production. In particular, the production of the heavy quarks charm and bottom (collectively referred to by the symbol Q in the following) has been measured so accurately that the associated errors are in general negligible in the context of analyses of the hadronisation process. Another advantage of $\mathrm{e^+e^-}$ with respect to hadron colliders is the fact that the resulting hadronic final states are relatively clean due to the absence of hadronic interactions of the colliding particles.

The second part of this thesis concentrates on the production of mesons containing a heavy quark and a light antiquark ("heavy-light" mesons). In section 1.2.1, the process of hadron formation is described, with an emphasis on heavy-light meson production. Section 1.2.2 gives an overview of the spectra and decays of excited bottom and charm mesons, and section 1.2.3 outlines the analysis of charmed meson production that is described in this thesis.

1.2.1 Heavy-Light Hadron Formation

The strong interaction between the two primary quarks in $Z \to q\bar{q}$ decays leads to the formation of colourless hadrons. Because of the high centre-of-mass energy, the hadrons are observed in jets. For practical purposes, the process of hadron formation is often divided into two phases:

1. In the first phase the relevant energies are large enough for the processes to be calculated in perturbative QCD. For example, the third jet in hadronic three-jet events from e^+e^- collisions can be attributed to an energetic gluon that is radiated from one of the primary quarks and subsequently fragments as well.
2. In the fragmentation process, the available energy in each interaction is distributed among more and more partons. With the decrease in available energy at a given interaction vertex, the value of the strong coupling constant α_s increases so that perturbation theory eventually fails. In the following non-perturbative phase, the observable colourless hadrons are formed.

The non-perturbative phase is described with phenomenological models, which are tuned to reproduce measured quantities. In this thesis, the production of mesons that contain a primary heavy quark is investigated further, in order to provide input for refinements of such models.

The analysis of heavy-light hadron formation benefits from the fact that the production of a heavy quark-antiquark pair in the non-perturbative phase of the fragmentation process is severely suppressed. Thus, for practical purposes, only the following sources of heavy-light hadrons need to be considered:

- Heavy-light hadrons containing the primary quark Q or antiquark $\overline{\mathrm{Q}}$ from the process $e^+e^- \to Q\bar{Q}$, $Q = b,\ c$ ("direct production"),
- heavy-light hadrons that contain the primary quark or antiquark, but are formed in the strong or electromagnetic decay of a resonance ("indirect production"),
- charm hadrons formed in the weak decay of bottom hadrons ("weak cascade decays"), and
- heavy-light hadrons containing a heavy quark from a $g \to Q\bar{Q}$ process, where an energetic gluon is radiated from the primary quark or antiquark and subsequently splits into a heavy quark-antiquark pair ("gluon splitting").

The first two processes are analysed in this thesis. The splitting of a hard gluon into a $b\bar{b}$ or $c\bar{c}$ pair is suppressed due to the large b and c quark masses. The $g \to c\bar{c}$ process is the more important one: The fractions $g_{Q\bar{Q}}$ of hadronic Z decays with a $g \to Q\bar{Q}$ process have been measured at LEP to be $g_{b\bar{b}} = (2.77 \pm 0.42 \pm 0.57) \times 10^{-3}$ [16], $g_{b\bar{b}} = (2.1 \pm 1.1 \pm 0.9) \times 10^{-3}$ [17], and $g_{c\bar{c}} = (3.20 \pm 0.21 \pm 0.38) \times 10^{-2}$ [18]. However, the gluon splitting contributions generally do not affect charm hadronisation analyses since they yield low-energy charm hadrons to which the measurements are not very sensitive. The contribution of charm hadrons from weak bottom hadron decays remains an important background that has to be taken into account.

The distinction between the first two processes is arbitrary, because there is no clear boundary between the non-perturbative phase of hadron production on the one hand and the strong decay of resonances on the other. For example, it cannot be decided in principle whether an observed system with a mass above $\sim$ 2.6 GeV, consisting of a D^0 and a π^+ meson, should be viewed as hadrons from the non-perturbative hadronisation phase or as decay products of a high mesonic $c\bar{c}$ resonance. Such resonances are expected to have very short lifetimes and consequently large widths, which means that their decay products cannot be distinguished from non-resonant particle production. However, as shown in the following two sections, it is essential for many observables to correctly account for $L = 1$ meson production and decay, since these may have a sizeable impact on the measured values. In this thesis, the production of heavy-light L=1 mesons is taken into account, while production and decay of higher states are considered a part of the fragmentation process.

1.2.2 Properties and Decays of Bottom and Charm Mesons

Apart from the flavour content of a meson, its properties are determined by the spin, where the relative orientation of the two quark spins and their relative orbital angular momentum L have to be considered. A meson with no orbital angular momentum can be a vector (V) state with spin-parity $J^P = 1^-$ or a pseudoscalar (P) state with $J^P = 0^-$. For a given flavour content, four orbitally excited mesons with $L = 1$ are predicted: A triplet of states from the vector addition of the orbital angular momentum with the spin 1 system formed by the constituent quark and antiquark, and a singlet state from the spin 0 quark-antiquark system.

Properties of $L = 1$ mesons:
Heavy Quark Effective Theory (HQET) provides a description of heavy-light hadron properties in an expansion in powers of $1/m_Q$, where m_Q is the heavy quark mass. In the limit of infinite heavy quark mass, the heavy quark spin decouples from the light quark spin and orbital angular momentum. For a heavy-light meson, the four $L = 1$ states can thus be grouped into two doublets according to the total angular momentum $j = s_q + L$ of the light quark ($j = \frac{1}{2}$ or $j = \frac{3}{2}$). The naming convention for the $L = 1$ charmed mesons is $D_J^{(*)}$, where J denotes the total spin of the meson, and an asterisk indicates that the meson has parity $(-1)^J$. Corresponding names apply for the excited bottom mesons. The charm and bottom $L = 1$ mesons are collectively referred to by the symbols D^{**} and B^{**}, respectively. As an example, the properties of the neutral D^{**} mesons are listed in table 1.2. In addition, the measured spectra of the lowest charm mesons are shown in figure 1.2.

The decays of the $L = 1$ resonances are restricted because of spin-parity conservation in the strong interaction. The two $j = \frac{1}{2}$ states can decay via an S-wave and are thus expected to be broad. The $j = \frac{3}{2}$ states can only decay via a D-wave and are consequently narrower[9]. The $J^P = 0^+$ and 2^+ charm states decay to $D\pi$ final states (DK for D_s^{**} decays), while the 1^+ and 2^+ charm states decay to $D^*\pi$ (D^*K) final states.

Decays of D_s^{**} mesons via π^0 emission are suppressed since they violate isospin conservation, while γ emission is disfavoured because of the smaller couplings. There is however enough phase-space for decays via kaon emission, and thus, indirect D_s^* production via $L = 1$ meson decays can be neglected for practical purposes.

[9]For finite heavy quark masses, the two 1^+ states can mix, and there is a possible S-wave contribution in the decay of the narrow resonance [19]. It is because of the proximity to threshold that the narrow D_1 resonance is still narrower than the D_2^*.

particle name	D_0^{*0}	$D_1'^0$	D_1^0	D_2^{*0}
$j = s_q + L$	$(1/2)^+$		$(3/2)^+$	
decay	S-wave		D-wave	
spin-parity J^P	0^+	1^+	1^+	2^+
decay channels	$D\pi$	$D^*\pi$	$D^*\pi$	$D\pi$, $D^*\pi$
width (MeV) [2]	~ 100	~ 100	$18.9 \pm^{4.6}_{3.5}$	23 ± 5
mass (MeV) [2]	(not observed)		2422.2 ± 1.8	2458.9 ± 2.0

Table 1.2: Properties of the neutral excited D mesons with orbital angular momentum $L = 1$. These states are collectively referred to as D^{**0} mesons. The two states with $J^P = 1^+$, $D_1'^0$ and D_1^0, correspond to two possible combinations of the quark spins and orbital angular momentum. The same restrictions as shown here apply to the decay channels of D^{**+} and D_s^{**+} mesons, where in the case of D_s^{**+} decays, pions have to be replaced by kaons. Qualitatively, this table also applies to orbitally excited bottom mesons, although measurements so far have not been able to distinguish the different light-quark flavours nor the two narrow states for a given flavour.

Similar predictions apply to the decays of $L = 1$ bottom mesons: Non-strange B^{**} mesons can be reconstructed as $B^{(*)}\pi$ final states, and B_s^{**0} mesons as $B^{(*)}K$ states. In contrast to the charm case, inclusive techniques yield the most precise results for bottom $L = 1$ mesons, but do not distinguish between B^{**0} and B^{**+} mesons. Exclusive measurements are severely limited by the small product branching ratios. So far, the measurements do not distinguish between the different B^{**} spin states[10].

Properties of $L = 0$ mesons:
The properties of vector and pseudoscalar bottom and charm mesons are well established [2]. The mass difference between D^* and D mesons is very close to the pion mass, so that small mass splittings between $c\bar{u}$ and $c\bar{d}$ mesons have the effect that $D^{*+} \to D^0\pi^+$ decays occur (and provide a unique kinematical signature for the reconstruction of D^{*+} mesons) while the corresponding decay $D^{*0} \to D^+\pi^-$ is forbidden kinematically. Because of the higher mass of the bottom quark, the mass difference between B^* and B mesons is smaller than in the charm case, and B^* mesons can only decay via photon emission. Measurements of B^* mesons [20] so far sum over the different light quark flavours.

1.2.3 Analysis of Charmed Vector Meson Production

The relative production rate

$$P_V = \frac{V}{V + P} \tag{1.15}$$

of ($L = 0$) vector and pseudoscalar mesons containing a primary heavy quark from Z decay is investigated. This ratio is sensitive to non-perturbative effects in the hadronisation process and cannot be calculated exactly. Several models [21] have been proposed which predict the P_V ratio. A simple spin counting picture predicts a value of P_V=0.75 when only vector and pseudoscalar meson production are considered. "Spin counting" in this thesis refers to a model

[10] A measurement of the $B^{**} \to B^* \to B$ decay chain is in preparation at OPAL.

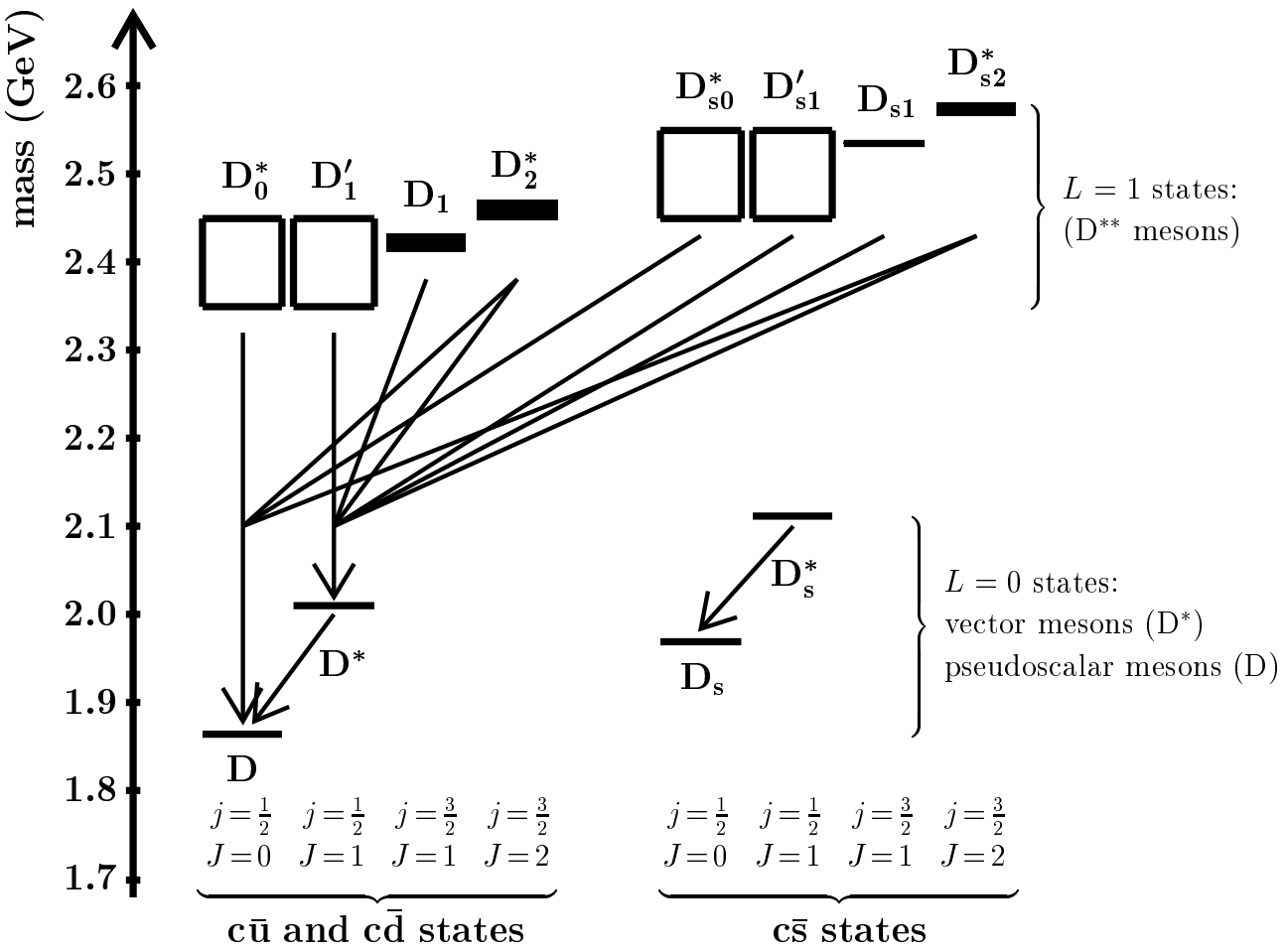

Figure 1.2: The spectrum [2] of the lowest charm mesons is shown. Mesons containing strange quarks are shown separately, while the mass splittings between corresponding $c\bar{u}$ and $c\bar{d}$ meson states are small due to isospin invariance and would not be visible on this scale. The broad orbitally excited $L = 1$ states have not yet been measured. They are indicated by the open boxes. The angular momentum of the light quark j and the total spin J are listed. Those decays which are allowed by spin and parity conservation are indicated by the arrows.

where the relative direct production of mesons with the same quark content and the same orbital angular momentum is given according to the corresponding numbers of spin degrees of freedom. For the production of heavy-light vector and pseudoscalar mesons, the spin counting model corresponds to the HQET prediction in the limit of infinite heavy quark mass, where the masses of the pseudoscalar and vector states become degenerate. More sophisticated models take into account the non-zero mass difference between vector and pseudoscalar mesons, as well as the masses of the constituent quarks. In general, they predict P_V to be less than 0.75.

The situation is complicated by the presence of the orbitally excited mesons, and there are two possible definitions of P_V: The observed ratio $P_V^{\rm eff}$, which includes those ground state mesons which are produced indirectly in decays of the excited states, and the quantity $P_V^{\rm prim}$, which is defined when considering direct production only. Experimentally, the effective ratio $P_V^{\rm eff}$ is easily accessible. In Z decays, values around $P_V^{\rm eff} \approx 0.75$ have been measured for B^* and

B meson production [20], while $P_V^{\rm eff}\approx 0.55$ has been found for the charm sector [22, 23]. For light mesons, $P_V^{\rm eff}$ has been estimated to be between 0.4 and 0.5 [24].

As can be seen from figure 1.2, the contributions from resonance decays may affect the $P_V^{\rm eff}$ ratio because of the restrictions from spin and parity conservation as discussed in section 1.2.2 and because of the difference in available phase space for decays to vector and pseudoscalar $L = 0$ mesons. To measure the primary ratio $P_V^{\rm prim}$, corrections have to be applied to account for effects from excited states, depending on the probability to hadronize to an $L = 1$ state and on the relative production of those states that decay to vector mesons.

The P_V ratio is related to the *spin alignment* of vector mesons: While P_V denotes the relative production of vector and pseudoscalar mesons, spin alignment measurements provide information on the relative production of longitudinal and transverse vector meson spin states. Thus, the combination of these two measurements provides further insight into the production of mesons in the fragmentation process [22]. Experimentally, the spin alignment is accessible via the angular distribution of the vector meson decay products. Spin alignment measurements for the heavy vector mesons D^{*+} and B^* have been performed at LEP [25, 26], but no distinction is made between direct and indirect production. In contrast, information on the *polarisation* of vector mesons is lost due to parity conservation in their strong or electromagnetic decay.

This thesis focuses on a study of both $P_V^{\rm eff}$ and $P_V^{\rm prim}$ for charmed meson production. Charm hadronisation is particularly interesting since the charm quark is heavy enough so that the production of $\mathrm{c\bar{c}}$ pairs during the non-perturbative phase of hadron formation can be neglected. On the other hand, the charm quark is less heavy than the bottom quark, and thus, the corrections to the limit of infinite heavy quark mass are larger. It can therefore be expected that the charm system is particularly sensitive to any processes that go beyond the description in HQET.

For an analysis of the hadronisation of charm quarks from Z decays, charm hadrons from bottom hadron decays have to be treated as background. Experimentally, the P_V ratio in charm hadronisation is measured most easily from the production of non-strange charmed mesons in $\mathrm{Z} \to \mathrm{c\bar{c}}$ decays. The $\mathrm{c\overline{u}}$ and $\mathrm{c\overline{d}}$ meson systems cannot be viewed independently because $\mathrm{D}^{*+} \to \mathrm{D}^0\pi^+$ decays occur, while D^{*0} mesons do not decay to final states containing a D^+ meson (the $\mathrm{D}^{*0} - \mathrm{D}^+$ mass difference being below the charged pion threshold). Thus, measurements of D^0, D^+, and D^{*+} production in $\mathrm{Z} \to \mathrm{c\bar{c}}$ decays have been used in the previous determinations of $P_V^{\rm eff}$ [22, 23] for charm hadronisation according to the formula

$$P_V^{\rm eff} = \frac{2f(\mathrm{c}\to\mathrm{D}^{*+})}{f(\mathrm{c}\to\mathrm{D}^0) + f(\mathrm{c}\to\mathrm{D}^+)} \ , \tag{1.16}$$

where the symbol $f(\mathrm{q} \to \mathrm{X})$ denotes the hadronisation fraction, defined as the total production rate of hadron X per hadronisation of a primary quark q. The D^{*0} meson has so far not been observed in Z decays, since it only decays via the emission of a photon or a π^0 meson, which are difficult to reconstruct experimentally. Therefore, the determinations of $P_V^{\rm eff}$ values have relied on the assumption of isospin invariance, which suggests equal D^{*0} and D^{*+} production rates. However, isospin symmetry is not exact, and for example, $\mathrm{D}_{\mathrm{s}}^{**+} \to \mathrm{D}^{(*)}\mathrm{K}$ decays occur close to threshold. So there may be differences between indirect production of D^{*0} and D^{*+} mesons, similar to those between indirect D^0 and D^+ production due to $\mathrm{D}^{*+} \to \mathrm{D}^0\pi^+$ decays.

In this thesis, the first measurement of the hadronisation fraction $f(\mathrm{c}\to\mathrm{D}^{*0})$ in $\mathrm{Z}\to\mathrm{c\bar{c}}$ decays is presented. This measurement is used to test the assumption of isospin invariance made in

equation 1.16 and thereby confirm the validity of the previous approaches for measuring P_V values in the charm sector. A value of P_V^{eff} is derived, which is interpreted in conjunction with a measurement of the spin alignment of D^{*+} mesons in $\mathrm{Z} \to \mathrm{c\bar{c}}$ decays.

The production ratio P_V^{prim} is investigated for the first time. Here, the contributions from decays of both non-strange and strange D^{**} mesons are taken into account according to the formula

$$\begin{aligned} P_V^{\text{prim}} &= \frac{V^{\text{direct}}}{V^{\text{direct}} + P^{\text{direct}}} \\ &= \frac{V^{\text{eff}} - \left(T_{(\mathrm{s})} \to V\right)}{(V+P)^{\text{eff}} - \left(T_{(\mathrm{s})} \to V \text{ or } P\right)} , \end{aligned} \tag{1.17}$$

where V and P stand for non-strange charmed vector and pseudoscalar mesons, respectively, whereas $T_{(\mathrm{s})}$ denotes the sum of non-strange and strange charmed tensor mesons (D^{**} and $\mathrm{D}_{\mathrm{s}}^{**}$). The dependence of P_V^{prim} on the production of the unmeasured broad D^{**} states is studied. In addition, this analysis allows a check of hadronisation models, which is illustrated with a simple spin counting picture as an example.

In principle, a comparison of the hadronisation fractions of $\mathrm{D}_{\mathrm{s}}^{*+}$ and $\mathrm{D}_{\mathrm{s}}^{+}$ mesons provides an independent determination of P_V^{prim}, since the branching ratio for processes $\mathrm{D}_{\mathrm{s}}^{**+} \to \mathrm{D}_{\mathrm{s}}^{(*)+}\mathrm{X}$ is expected to be small [2] such that indirect $\mathrm{D}_{\mathrm{s}}^{*+}$ production is suppressed. This method has been used in [27], but yields large experimental errors. Since the experimental signatures of D^{*0} and $\mathrm{D}_{\mathrm{s}}^{*+}$ decays are similar, the D^{*0} reconstruction techniques are applied also for the reconstruction of $\mathrm{D}_{\mathrm{s}}^{*+}$ mesons. The measurement of $\mathrm{D}_{\mathrm{s}}^{*+}$ production provides a cross-check of the D^{*0} measurement. However, only the total production rate of $\mathrm{D}_{\mathrm{s}}^{*+}$ mesons in hadronic Z decays is measured in this thesis. Thus, in the absence of a precise measurement of the $\mathrm{B} \to \mathrm{D}_{\mathrm{s}}^{*+}\mathrm{X}$ branching ratio from B factories, no information exists on the separation of the $\mathrm{c} \to \mathrm{D}_{\mathrm{s}}^{*+}$ and $\mathrm{b} \to [\mathrm{c}, \bar{\mathrm{c}}] \to \mathrm{D}_{\mathrm{s}}^{*\pm}$ processes as it is used in the D^{*0} measurement, and the $\mathrm{D}_{\mathrm{s}}^{*+}$ measurement cannot be used to determine P_V^{prim}.

The P_V analysis is also applied to previous measurements of bottom production. In this case, the corrections to the heavy quark limit are expected to be much smaller. In conclusion, a comparison is made between bottom and charm quark hadronisation.

Chapter 2

The OPAL Detector

The OPAL detector is one of the four large experiments at the e^+e^- collider LEP at CERN. It is described in full detail elsewhere [28]. In this chapter, the design requirements, the detector components, and their performance are summarized in the light of the measurements that are presented in this thesis.

The OPAL detector has been designed as a general purpose experiment to study all physics processes in e^+e^- collisions at centre-of-mass energies around the Z resonance and beyond. This leads to the following main requirements:

- precision measurement of charge particle tracks; determination of their momentum and identification of the particle species;
- reconstruction of both the primary event vertex and possible secondary vertices from the tracks;
- measurement of the energy and direction of neutral particles, both photons and hadrons;
- coverage over as much of the solid angle as possible to identify events with missing energy due to non-interacting particles; and
- precision luminosity measurement via low-angle Bhabha scattering.

The general layout of the OPAL detector is described in the following, and is also shown in figure 2.1. Charged particle tracks are reconstructed in a central tracking system, which consists of a silicon microvertex detector around the beam pipe and a set of three drift chambers, all of which are embedded in a homogeneous magnetic field oriented parallel to the z axis[1]. This system provides precise momentum measurements of charged particles and a determination of the charge sign via the curvature of the track, an identification of the particle species by a measurement of the specific energy loss $\mathrm{d}E/\mathrm{d}x$, and the possibility to reconstruct secondary vertices. The central tracking system and charged track reconstruction are described in section 2.1.

Outside the magnet coil follows the electromagnetic calorimeter system, which is described in section 2.2. It consists of a time-of-flight counter, a presampler detector, and a lead-glass

[1]The OPAL coordinate system is defined as a right-handed Cartesian coordinate system, with the x axis pointing in the plane of the LEP collider towards the centre of the ring, the z axis in the direction of the outgoing electrons, and θ, and ϕ defined as the usual spherical polar coordinates. This definition of the polar angle θ is identical to that used in chapter 1.

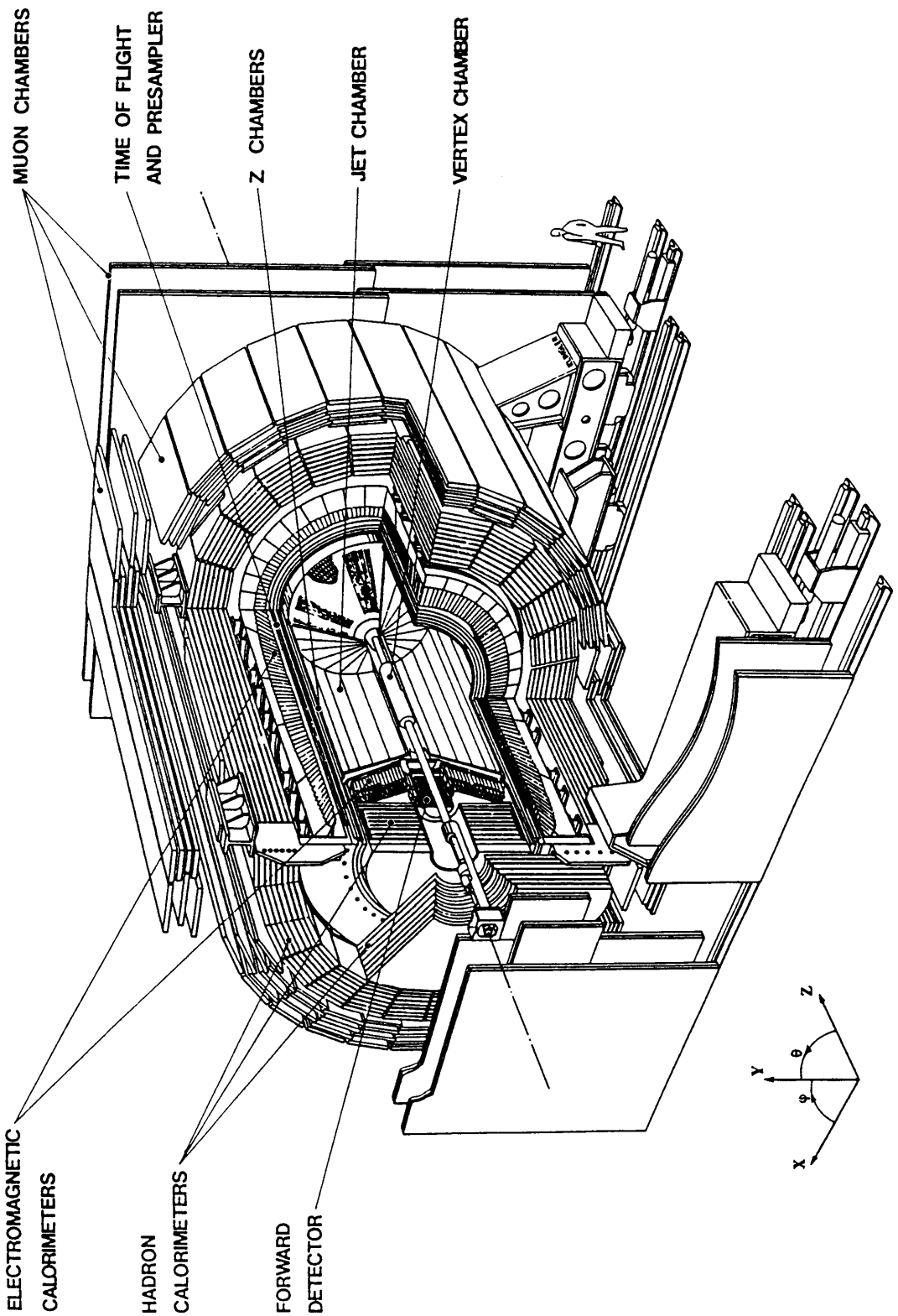

Figure 2.1: The OPAL detector.

electromagnetic calorimeter for the measurement of the energy of electromagnetic showers initiated by photons or electrons. The magnet return yoke is instrumented as a hadronic sampling calorimeter for the measurement of hadronic energy. It is surrounded by four layers of muon chambers for the identification of muons, which predominantly pass through the inner layers of the detector. The endcaps are equipped with similar detector layers. Additional detectors are installed close to the beam pipe in the very forward regions of the detector for a measurement of the luminosity via Bhabha scattering, as described in section 2.3.

2.1 The Central Tracking System

The central part of the OPAL detector is equipped for the reconstruction of charged particle tracks. It consists of a silicon microvertex detector and three drift chambers, embedded in a homogeneous magnetic field of 0.435 T parallel to the beam pipe.

The silicon microvertex detector was installed in 1991 in order to improve the tracking resolution in the vicinity of the interaction region and thus enhance the precision in the reconstruction of secondary vertices from decays of long-lived particles such as bottom hadrons. It consists of two layers of silicon detectors at radii of 6.1 cm and 7.4 cm, respectively. After upgrades in 1993 and 1995, the inner and outer layers consist of 12 and 15 ladders, respectively, where each ladder is equipped with two silicon strip detectors for $r\phi$ and rz coordinate readout, glued back-to-back. The ladders extend in the polar angle range given by $|\cos\theta| < 0.93$ for the inner and $|\cos\theta| < 0.89$ for the outer layer. A measure of the precision is the impact parameter resolution as determined from lepton pairs produced in Z decays. A resolution of $\sigma(d_0) = 18$ μm in the xy plane and of $\sigma(z_0) = 24$ μm in z direction is obtained.

Surrounding the microvertex detector are three drift chambers, called vertex chamber, jet chamber, and z chamber. They are operated at a gas pressure of 4 bar, which is a compromise between momentum resolution (which degrades for higher pressure due to multiple scattering) and particle identification capability via the $\mathrm{d}E/\mathrm{d}x$ measurement (which improves for higher pressure).

The vertex chamber consists of two drift chambers which together cover the radial region between 8.8 cm and 23.5 cm from the interaction point. The vertex chamber covers the polar angle range of $|\cos\theta| < 0.98$. The wires of the inner chamber are parallel to the beam axis, while those of the outer chamber are tilted by 4° to improve the measurement of the z coordinate. The hit resolution in the $r\phi$ plane is ~ 55 μm, and a z resolution of ~ 700 μm is obtained with the tilted wires of the outer chamber.

The jet chamber surrounds the vertex chamber and has an outer radius of 1.85 m and a length of 4 m. It consists of 24 azimuthal sectors, which are each equipped with 159 anode wires along the beam direction. The maximum drift length is 3 cm to the innermost and 25 cm to the outermost wire. Tracks within a polar angle range of $|\cos\theta| < 0.73$ pass all 159 wires; for a particle to pass at least eight wires, the requirement is $|\cos\theta| < 0.98$. At each wire, the $r\phi$ coordinate of a charged track is determined from the wire position and a measurement of the drift time to within 135 μm. The z coordinate is obtained with a resolution of 6 cm from the difference of integrated charges as measured at the two ends of each wire. The sum of the integrated charges is used to measure the specific energy loss $\mathrm{d}E/\mathrm{d}x$ of the charged particle.

For charged particles, the momentum component p_t perpendicular to the beam axis is measured from the curvature of the track in the magnetic field. The resolution has been found

to be

$$\frac{\sigma(p_t)}{p_t} = \sqrt{0.020^2 + \left(0.0015 \frac{p_t}{\mathrm{GeV}}\right)^2} \; . \tag{2.1}$$

The first component of the error is due to multiple scattering, and the second describes the uncertainty in the track curvature due to the single hit resolution.

The z chamber is needed for a second precise measurement of the z coordinate in addition to that in the microvertex detector, in order to obtain an acurate measurement of the momentum component along the beam. The z chamber surrounds the full 4 m length of the jet chamber. It consists of 24 drift chambers of 50 cm width and 0.59 cm thickness, each of which is divided in z into 8 cells of 50 cm length. The z coordinate is determined with an accuracy between 100 μm and 300 μm, while the ϕ measurement relies on the charge division method (as used for the z coordinate in the jet chamber) and reaches a resolution of 1.5 cm. For tracks outside the geometrical acceptance of the z chamber of $|\cos\theta| < 0.73$, the second precise measurement of the z coordinate along a track is obtained from the radius of the outermost measurement wire in the jet chamber. The total track momentum is obtained from the transverse momentum and the polar angle of the track.

The mean specific energy loss $\mathrm{d}E/\mathrm{d}x$ of a charged particle due to ionisation as given by the Bethe-Bloch formula [29] is a function of the particle velocity. Thus, the measurement of the specific energy loss in the gas of the chamber, when combined with the momentum measurement, allows a determination of the mass of the charged particle and therefore an identification of the particle type. A relative error of 3.3% on the energy loss is achieved for tracks where $\mathrm{d}E/\mathrm{d}x$ samplings from all wires in the jet chamber can be used. Given the track momentum, the predictions for different particle hypotheses are compared with the measured value $\mathrm{d}E/\mathrm{d}x(meas.)$ and the measurement uncertainty $\sigma(\mathrm{d}E/\mathrm{d}x)$. Either the normalised deviation from the expected value,

$$\frac{\mathrm{d}E/\mathrm{d}x(meas.) - \mathrm{d}E/\mathrm{d}x(exp.)}{\sigma(\mathrm{d}E/\mathrm{d}x)} \tag{2.2}$$

is taken to select a given charged particle type, or this quantity is transformed into a χ^2 probability. The $\mathrm{d}E/\mathrm{d}x$ weight W is then defined as the χ^2 probability, signed according to the sign of the normalised deviation.

2.2 The Calorimeter System and the Muon Chambers

The central tracking chambers and the magnet coil are surrounded by the electromagnetic calorimeter system, which is used to determine the energy and position of electromagnetic showers initiated by photons and electrons. It consists of a time-of-flight counter, a socalled presampler, and a lead-glass calorimeter. The magnet return yoke outside the electromagnetic calorimeter is equipped as a hadronic sampling calorimeter for the measurement of the energy and position of hadronic showers. On the outside, the detector is surrounded with chambers for muon identification.

Time-of-flight counters both surround the barrel part of the detector and have also been installed in the endcap regions at the beginning of the LEP2 programme. The barrel system consists of 160 scintillator counters, each 6.84 m long, 9.1 cm wide and 4.5 cm thick. It is read out with photomultipliers and covers an acceptance region of $|\cos\theta| < 0.82$. In the endcaps,

120 scintillating tiles with fibre readout are installed in front of the electromagnetic calorimeter blocks. The time-of-flight counters are used for triggering purposes and to reject events from cosmic rays.

The material in the central detector and the magnet corresponds to roughly two electromagnetic radiation lengths, and thus, most electromagnetic showers are initiated before the electromagnetic calorimeter. Unless tracks from a converted photon can be reconstructed, this effect degrades the energy and angular resolution of the electromagnetic calorimeter. This loss is partly recuperated with the presampler, which is installed on the inside of the calorimeter to measure the multiplicity of electromagnetic showers. In the barrel region, it consists of 16 streamer chambers of 6.6 m length, 94 cm width, and 3 cm thickness. The endcap part is made of 32 drift chambers. The lateral spread of electromagnetic showers in the presampler varies between 2 mm and 6 mm. An angular resolution of ~ 2 mrad is achieved.

The electromagnetic calorimeter is divided into a barrel, covering the region $|\cos\theta| < 0.82$, and two endcaps for polar angles within $0.82 < |\cos\theta| < 0.98$. The barrel part consists of 9440 lead glass blocks with a cross-section of 10×10 cm^2, corresponding to roughly 40×40 mrad^2, and a length of 37 cm, equivalent to 24.6 electromagnetic radiation lengths. The blocks are arranged in a pointing geometry; they are oriented towards a point on the z axis close to the interaction region. This arrangement helps in the reconstruction of electromagnetic showers, while preventing particles from escaping through the small gaps between the calorimeter blocks. In the endcaps, 1132 lead glass blocks with a cross-section of 9.2×9.2 cm^2 and roughly 22 radiation lengths thickness are aligned parallel to the beam. The intrinsic energy resolution is $\sigma_E/E = 0.2\% + 6.3\%/\sqrt{E/\mathrm{GeV}}$ in the barrel and $\sigma_E/E = 5\%/\sqrt{E/\mathrm{GeV}}$ in the endcap regions, respectively. For isolated electromagnetic showers, an intrinsic spatial resolution of around 11 mm is achieved when using an energy-weighted mean from several adjacent lead glass blocks ("cluster").

In the hadronic calorimeter, the energy of hadronic showers is determined. In addition, the information from the hadronic calorimeter can be used in the identification of muons. The magnet return yoke is segmented into 10 layers of iron of 10 cm thickness each. In between, streamer tubes are mounted as a sandwich calorimeter to measure the development of hadronic showers. Three systems are used in different polar angular regions, which together cover 97% of the full solid angle. The material in the electromagnetic calorimeter corresponds to two roughly hadronic absorption lengths, so that most hadronic showers are initiated before reaching the hadronic calorimeter. When the signals from both the electromagnetic and the hadronic calorimeters are combined, an energy resolution of $\sigma_E/E = 120\%/\sqrt{E/\mathrm{GeV}}$ is obtained.

The hadronic calorimeter is surrounded by the muon chambers. Of the full solid angle, 93% are covered with at least one detector layer, while the coverage for most of the detector is three or more layers of muon chambers. The detector can be divided into a barrel, which consists of four layers of drift chambers, and two endcaps, where four layers of streamer chambers are used. Over most of the full solid angle, a pion traverses more than seven absorption lengths to reach the outside of the hadronic calorimeter, corresponding to a probability not to interact of less than 0.001. The identification of muons is based on the extrapolation of charged particle tracks from the central detector through the calorimeter, and the identification of a matching track segment in the muon chambers. The required positional and angular accuracy is determined by multiple scattering in the material in front of the muon chambers to about 2 mm and 3 mrad, respectively. Isolated muons with momentum greater than 3 GeV are identified within the 93% of the solid angle with an efficiency of close to 100%, while the mis-identification probability

for isolated pions of 5 GeV is less than 1%.

2.3 The Forward Detectors

In the forward regions, i.e. in the regions $|\cos\theta| \gtrsim 0.95$, a system of drift chambers, calorimeters, and scintillating tiles is installed to measure small angle Bhabha scattering ($e^+e^- \to e^+e^-$), and to detect the scattered electron or positron in deep inelastic two-photon events. The cross-section of Bhabha scattering can be calculated very precisely and is inversely proportional to the square of the scattering angle θ, such that Bhabha scattering under small angles θ can be used for a precision luminosity measurement. The forward detectors are mounted around the beam pipe, 2.4 m away from the interaction point. Until 1992, a system of drift chambers and lead-scintillator sandwich detectors allowed a luminosity measurement in the angular range $58\,\text{mrad} < \theta < 120\,\text{mrad}$ with an accuracy of 1%. In 1993, a silicon-tungsten sandwich calorimeter was installed in the region $62\,\text{mrad} < \theta < 142\,\text{mrad}$, which improves the luminosity measurement to a relative precision of better than 0.1%.

Chapter 3

Heavy Quark Production above the Z Resonance

In this chapter, measurements of R_{b}, $A_{\mathrm{FB}}^{\mathrm{b}}$, and $A_{\mathrm{FB}}^{\mathrm{c}}$ with the OPAL detector at centre-of-mass energies between 130 GeV and 189 GeV are described[1]. Section 3.1 gives an overview of the methods used in the measurements, followed by a description of the event selection in section 3.2. The measurement of R_{b} is summarized in section 3.3, and the measurements of forward-backward asymmetries are discussed in section 3.4. Details of the evaluation of systematic uncertainties are given in section 3.5, and section 3.6 summarizes the results. The measurement at effective centre-of-mass energies below the Z resonance is described in chapter 4. The results are interpreted in chapter 5.

3.1 Methods Used in Heavy Flavour Electroweak Measurements

In this section, the different methods used in heavy flavour electroweak measurements in $\mathrm{e^+e^-}$ collisions are qualitatively described and compared. In heavy flavour measurements, the following tasks have to be performed in general:

- event selection;
- identification of the primary quark flavour;
- determination of $|\cos\theta|$, where θ is the angle between the incoming electron and outgoing fermion momenta as in equation 1.1; and
- determination of the sign of $\cos\theta$.

In the event selection, hadronic events of the desired effective centre-of-mass energy are selected. While the reconstruction of the effective centre-of-mass energy is not an issue on the Z resonance, where radiative events give rise only to small corrections when an inclusive event

[1] The analyses in this chapter have been performed in collaboration with Silvia Arcelli, Alessandra Fanfani, and Stefano Marcellini at INFN Bologna, who have worked on the determination of R_{b} and $A_{\mathrm{FB}}^{\mathrm{b}}$ using secondary vertex tagged events, while I have concentrated on the asymmetry measurements with leptons and pions from $\mathrm{D}^{*+} \to \mathrm{D}^0\pi^+$ decays, as well as the combination of $A_{\mathrm{FB}}^{\mathrm{b}}$ values.

sample is considered, it becomes important for the measurements both above and below the Z resonance which are performed in this thesis:

- For centre-of-mass energies above the Z resonance, "radiative return" events, with effective centre-of-mass energy close to the Z mass, dilute the information on e^+e^- collisions at the full centre-of-mass energy. However, these radiative return events can be relatively easily separated from events without significant initial state radiation, as discussed in section 3.2.
- For a measurement at effective centre-of-mass energies below the Z mass, events with hard initial state radiation have to be identified within the data taken on the Z resonance. In this case, initial state radiation is suppressed because of the large cross-section peak at $\sqrt{s} \sim m_Z$. In addition to the reconstruction of the effective centre-of-mass energy, care must be taken to suppress background from hadronic Z decays with missing energy along the beam direction. The identification of events with hard initial state radiation at $\sqrt{s} \sim m_Z$ is described in section 4.3.

The determination of the primary quark flavour is essential for measurements of both the total heavy quark production and the forward-backward asymmetry, while the $\cos\theta$ determination is only needed in asymmetry measurements. The determination of $\cos\theta$ is split into the determination of the absolute value and its sign: The absolute value, although not directly accessible in hadronic events, can be well approximated by the event thrust axis. This technique has been used in many previous publications (see [30, 31, 32, 33] for the OPAL results) and will not be discussed further here. The decision into which thrust hemisphere of the event the primary quark is emitted is more difficult.

In table 3.1, an overview of different techniques is given together with a qualitative discussion of their advantages and disadvantages. Only small event samples are available for the measurements presented in this thesis, which introduces an additional difficulty.

method	flavour identification		sign($\cos\theta$)		statistics	application
	$b\bar{b}$	$c\bar{c}$	$b\bar{b}$	$c\bar{c}$		
secondary vertex tag / hemisphere charge	++	−	∘	∘	++	R_b, A_{FB}^b
semileptonic decays	+	+	++	++	+	A_{FB}^b, A_{FB}^c
$D^{(*)}$ meson decays (exclusive)	∘	+	++	++	−	(on the Z resonance)
charged pions from D^{*+} decays	−	∘	++	++	∘	(A_{FB}^b,) A_{FB}^c

Table 3.1: A qualitative overview of the different methods used in heavy flavour measurements. While an inclusive secondary vertex tag provides the best method to identify bottom events, the selection of semileptonic or $D^{(*)}$ decays is advantageous for charm tagging and asymmetry measurements.

- **Secondary vertex tag:**
  Due to the long lifetime and high boost of bottom hadrons produced in $e^+e^- \to b\bar{b}$ events, their decays lead to secondary vertices that are displaced from the primary interaction

point by decay lengths of the order of millimeters. With the silicon micro-vertex detectors installed at the LEP and SLD experiments, these secondary vertices can be reconstructed, and their presence used as an indication of a b hadron decay. Most bottom physics analyses rely heavily on this technique. Since the secondary vertex tag makes use of a common property of all weakly decaying bottom hadrons, it yields a comparatively large event sample. It follows that the secondary vertex tag is the principal method for a measurement of R_{b}.

For the identification of charm events, the secondary vertex tag is less suitable for two main reasons:

1. The lifetimes of weakly decaying charm hadrons are smaller than those of weakly decaying bottom hadrons, typically by a factor of 3 for mesons. Because of the smaller mass, the fragmentation of charm quarks is softer than that of bottom quarks. Together with the smaller lifetimes, this leads to typically much shorter decay lengths for secondary vertices in primary charm events.
2. At large decay lengths, the contribution from bottom events becomes dominant, which means that a pure charm sample is difficult to obtain (this is different, for instance, in the analysis of hadronic W decays, where bottom quark production is heavily suppressed due to the small CKM matrix element V_{cb}).

In order to use a vertex tagged sample of bottom events for an asymmetry measurement, the sign of $\cos\theta$ must still be determined for each event. An inclusive hemisphere charge technique is applied so that the total tagged sample can be used. It exploits the fact that statistically, some information on the primary quark charge is retained in the observed hadrons after the hadronisation process. Charged particles with high momenta are more likely to have the same charge sign as the primary quark than particles at low momenta. Thus, the momentum-weighted charge average is formed for each event hemisphere as

$$Q_{\mathrm{hem}} = \frac{\sum_{i=1}^{n} |p_i|^{\kappa} \cdot q_i}{\sum_{i=1}^{n} |p_i|^{\kappa}}\,, \tag{3.1}$$

where the sum runs over all n tracks in the hemisphere, p_i is the momentum component of track i along the thrust axis, q_i denotes its charge, and κ is a parameter tuned for an optimal charge identification of a primary b or $\overline{\mathrm{b}}$ quark in a hemisphere. The charge identification probability is defined as the fraction of hemispheres for which the sign of the hemisphere charge is equal to the charge sign of the primary (anti-)quark in the corresponding event hemisphere; it is typically below 70%. Nevertheless, the hemisphere charge method provides a means of using the inclusive sample of bottom tagged events for an asymmetry measurement without further loss of statistics.

- **Semileptonic decays of heavy hadrons:**
  A complementary approach towards the identification of heavy flavour events is to identify particular decays of heavy hadrons with distinct signatures. Since this involves per se a loss of statistics, no important gain is expected for the R_{b} measurement, where an efficient and pure tag exists with the secondary vertex tag. For the asymmetry measurements, however, a significant improvement can be expected when these decays allow a clean identification of the event hemisphere that contains the primary quark.

One possibility is the identification of leptons from the semileptonic decay of bottom and charm hadrons ("prompt" leptons). Once the origin of the lepton is determined, the charge of the lepton allows an unambiguous determination of the charge of the decaying heavy quark. Experimentally, electrons and muons can be distinguished relatively easily from hadrons. Leptons from other sources are generally found at lower momenta and lower transverse momenta with respect to the jet axis than leptons from heavy hadron semileptonic decays.

In the separation of prompt leptons from $b\bar{b}$ and $c\bar{c}$ events and the rejection of non-prompt leptons, the reconstruction of secondary vertices can still help. In addition to the separation of $b\bar{b}$ and $c\bar{c}$ events, leptons from $b\bar{b}$ events must be assigned to either $b \to \ell$ or $b \to c \to \ell$ decays, since a lepton of a given charge would yield different primary quark charges for the two processes. Furthermore, $B - \overline{B}$ mixing[2] and the contribution from $b \to \overline{c} \to \ell$ decays have to be taken into account.

- **Exclusive reconstruction of $D^{(*)}$ mesons:**
  The presence of a charged charmed hadron allows to infer the charge of the primary bottom or charm quark when $B - \overline{B}$ mixing and $b \to \overline{c}$ decays are accounted for. This is particularly useful in the case of D^{*+} mesons, where a very clean experimental reconstruction is possible in the decay chain $D^{*+} \to D^0\pi^+$, $D^0 \to K^-\pi^+$, but also for other exclusive and semi-exclusive D^0 decays. Furthermore, the charge of the kaon in $D^0 \to K^-X$ decays is indicative of the charge of the primary heavy quark, since $D^0 \to K^+X'$ decays are Cabibbo suppressed. In contrast, the exclusive reconstruction of bottom hadrons is not feasible due to the small branching ratios.

  While exclusive charm hadron reconstruction has been used in LEP1 analyses, this technique is not useful at LEP2 and in radiative events because of the small data samples.

- **Inclusive reconstruction of pions from $D^{*+} \to D^0\pi^+$ decays:**
  An alternative is the inclusive reconstruction of $D^{*+} \to D^0\pi^+$ decays, where it is possible to identify the socalled "slow" pion due to the distinct kinematic signature of the D^{*+} decay. As in the prompt lepton case, the primary quark charge can then be inferred from the slow pion charge. Roughly equal numbers of prompt leptons (electrons plus muons) and slow pions are expected for charm events. The number of prompt leptons in bottom events is roughly twice as large due to the contributions from both $b \to \ell$ and $b \to c \to \ell$ decays. However, the purity of inclusive slow pion samples is much lower than for prompt leptons.

In this thesis, a secondary vertex tag is used to measure R_b, which is complemented with a hemisphere charge technique for a determination of A_{FB}^b. Semileptonic decays of heavy hadrons and inclusively reconstructed slow pions from $D^{*+} \to D^0\pi^+$ decays are used for a simultaneous measurement of A_{FB}^b and A_{FB}^c.

3.2 Event Selection

Starting in 1995, the LEP experiments have collected data at increasing energies well above the Z resonance peak. In this thesis, the energy points are classified in five different sets, at

[2]In the Standard Model, $D^0 - \overline{D^0}$ mixing is suppressed and does not play a role for practical purposes.

centre-of-mass energies which will be generically called $\sqrt{s}$=133, 161, 172, 183, and 189 GeV. Table 3.2 shows the luminosity-weighted mean centre-of-mass energies at which data were taken and the corresponding integrated luminosities. Additionally, calibration data taken at the Z resonance during 1996, 1997, and 1998 are used to cross-check the analyses.

dataset	133 GeV	161 GeV	172 GeV	183 GeV	189 GeV
$\langle\sqrt{s}\rangle$ (GeV)	133.3	161.3	172.1	182.7	188.6
integrated luminosity (pb^{-1})	9.9	9.6	9.9	55.8	177

Table 3.2: The effective centre-of-mass energies and integrated luminosities of data collected with the OPAL detector above the Z resonance peak. The uncertainties on these quantities have a negligible effect on the analyses presented in this thesis.

Hadronic events, $\mathrm{e^+e^-} \to \mathrm{q\overline{q}}$, are selected based on the number of reconstructed charged tracks and the energy deposited in the calorimeters. The selection of the subsample of non-radiative hadronic events, defined by the requirement $\sqrt{s'/s} > 0.85$, and the identification and rejection of the $\mathrm{W^+W^-}$ background are described in detail in [34] and are summarized below. The remaining contamination from radiative hadronic events with true effective centre-of-mass energy below $0.85\sqrt{s}$ is $5-10\%$, depending on the centre-of-mass energy. The residual contamination from four-fermion events (mainly W and Z pairs) is largest at $\sqrt{s} = 189$ GeV, where it is about 8%. These backgrounds to non-radiative hadronic $\mathrm{q\bar{q}}$ events are accounted for in the measurements.

For all measurements presented in this thesis, hadronic events are selected based on the clusters in the electromagnetic calorimeter and the number of reconstructed charged particle tracks. Clusters in the barrel region of the detector are required to have an energy of at least 100 MeV, and clusters in the endcap detectors are accepted if they are formed out of at least two adjacent lead glass blocks and have an energy of at least 200 MeV. Tracks are required to have at least 20 measurement points. The point of closest approach to the nominal beam axis has to lie less than 2 cm in the $r\phi$ plane and less than 40 cm along the beam axis from the interaction point. Tracks are also required to have a minimum momentum component transverse to the beam direction of 50 MeV.

The following requirements are then used to select hadronic events:

- To reject leptonic final states, events are required to contain at least 7 electromagnetic clusters and at least 7 tracks, selected according to the above criteria.
- Background from two-photon events is reduced by requiring a total energy deposit measured in the electromagnetic calorimeter (calculated as the sum of the cluster energies) of at least 10% of the centre-of-mass energy.
- To reject remaining background from beam-gas and beam-wall interactions and further reduce the contribution from two-photon events, the energy imbalance along the beam direction is required to satisfy

$$R_{\mathrm{bal}} \equiv \left|\sum \left(E \cdot \cos\theta\right)_{\mathrm{clus}}\right| / \sum E_{\mathrm{clus}} < 0.75 \ , \tag{3.2}$$

  where the sum runs over all clusters in the event, E is the energy of a cluster, and θ denotes its polar angle.

In addition to these criteria, it is necessary to distinguish radiative from non-radiative events. For the measurements at centre-of-mass energies above the Z resonance, the effective centre-of-mass energy $\sqrt{s'}$ of the e^+e^- collision is estimated as follows. Isolated photons in the electromagnetic calorimeter are identified, and the remaining tracks, electromagnetic and hadron calorimeter clusters are formed into jets using the Durham (k_T) scheme [35] with a jet resolution parameter $y_{\rm cut} = 0.02$. If more than four jets are found, the number is forced to be four. The jet energies and angles are corrected for energy double counting using the algorithm described in reference [36]: For each charged track, the average energy (according to the simulation) deposited in the electromagnetic and hadronic calorimeters by a charged pion having the same momentum as that of the track is subtracted. The jets and observed photons are then subjected to a series of kinematic fits with the constraint of energy and momentum conservation, in which zero, one, or two additional photons emitted close to the beam direction are allowed. The fit with the lowest number of extra photons which gives an acceptable χ^2 is chosen. The value of $\sqrt{s'}$ is then computed from the fitted four-momenta of the jets, i.e. excluding photons identified in the detector or those close to the beam direction resulting from the fit. If none of the kinematic fits gives an acceptable χ^2, $\sqrt{s'}$ is estimated directly from the angles of the jets as in reference [37]. Non-radiative events are selected by demanding $\sqrt{s'/s} > 0.85$. The distribution of reconstructed $\sqrt{s'}$ is shown in figure 3.1 for hadronic events at $\sqrt{s} = 189$ GeV.

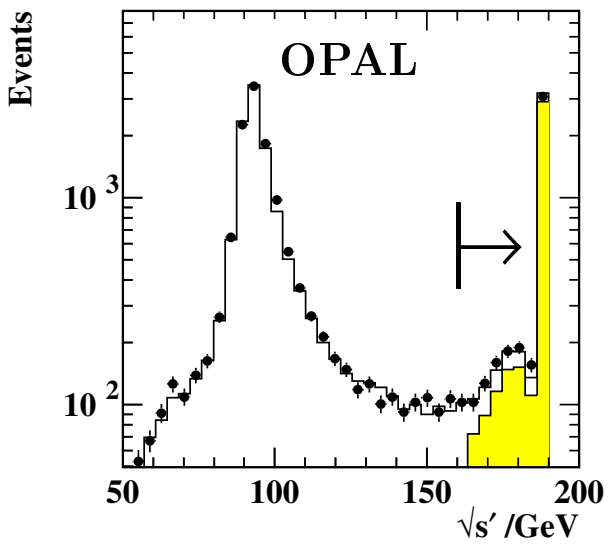

Figure 3.1: The distribution of reconstructed $\sqrt{s'}$ at 189 GeV centre-of-mass energy [38]. The points with error bars show the data, while the histogram corresponds to the expectation from the simulation. The contribution from simulated events with true $\sqrt{s'/s} > 0.85$ is shown shaded, and the arrow indicates the accepted region. Note that the algorithm results in s' equal to s for events which give a good kinematic fit with no photon either in the detector or along the beam direction.

In e^+e^- collisions at energies close to the Z resonance, $Z \to q\bar{q}$ decays dominate the hadronic cross-section. However, at LEP2 energies, the cross-section contribution from event types with four fermions in the final state ("four-fermion" events) becomes similar to that from non-

radiative $e^+e^- \to q\bar{q}$ events (hadronic "two-fermion" events). The cross-sections for several different processes at LEP2 energies are shown in figure 3.2. Above the threshold for the production of an on-shell W^+W^- pair, this background dominates: at 189 GeV centre-of-mass energy, the cross-sections for W^+W^- pairs and non-radiative hadronic two-fermion events are almost equal. In around 90% of the cases, at least one of the two W bosons decays hadronically. To reject W^+W^- pair events, three distinct selections are used to identify $\ell\nu_\ell\overline{\ell}'\overline{\nu}_{\ell'}$, $q\overline{q}'\ell\nu_\ell$, and $q\overline{q}'q''\overline{q}'''$ final states. In general, the events involving quarks in the final state are characterized by two jets, an energetic charged lepton, and missing energy, or four hadronic jets. Above the ZZ production threshold, background from ZZ events has to be taken into account. The W^+W^- cross-section is larger by an order of magnitude; however, bottom quark production in W decays is strongly suppressed since $|V_{cb}|$ is small, such that in the secondary vertex tagged event sample at 189 GeV centre-of-mass energy, the size of the contributions from ZZ and W^+W^- events is roughly equal. Only an insignificant fraction of the hadronic two-photon events passes the event selection criteria, since for such events, the $q\bar{q}$ system in the final state has mostly a very small invariant mass.

For the subsequent analysis, jets are reconstructed in the selected events using the JADE algorithm [40] with the E0 recombination scheme [41], keeping the invariant mass cut-off $x_{\min} = 49\,\mathrm{GeV}^2$ fixed at all centre-of-mass energies. This jet finding algorithm has been found to maximize the b tagging efficiency with the secondary vertex tag at a given purity [42]. The jet axis is computed from the sum of the momenta of the charged tracks within the jet and the energies of those clusters in the electromagnetic calorimeter which cannot be assigned to any track. The particles that cause clusters in the electromagnetic calorimeter are assumed to originate at the nominal e^+e^- interaction point.

Hadronic events are simulated using the PYTHIA 5.7 Monte Carlo generator [43]. Heavy quark fragmentation is modelled according to the scheme by Peterson et al. [44] with fragmentation parameters tuned according to the results in [45]. Four-fermion background events are simulated with the grc4f generator [46]. The events are passed through a detailed simulation of the OPAL detector [47] before being analysed using the same procedure as for the data.

3.3 Measurement of R_b

The tagging of $b\bar{b}$ events within the selected event sample is based on the long lifetime ($\sim$1.5 ps) and hard fragmentation of bottom hadrons, which result in detectable secondary vertices significantly displaced from the primary vertex. The secondary vertex tag as described in section 3.3.1 allows a clean and efficient reconstruction of bottom events. In section 3.3.2, the measurement of R_b with vertex tagged events is discussed.

3.3.1 Secondary Vertex Tag

The primary vertex in each event is reconstructed as described in [48], incorporating the average beam spot position determined from the measured tracks and the LEP beam-orbit measurements as a constraint. Although the beam spot is less precisely determined at energies above the Z resonance than at the Z peak, the resulting error on the primary vertex position is still

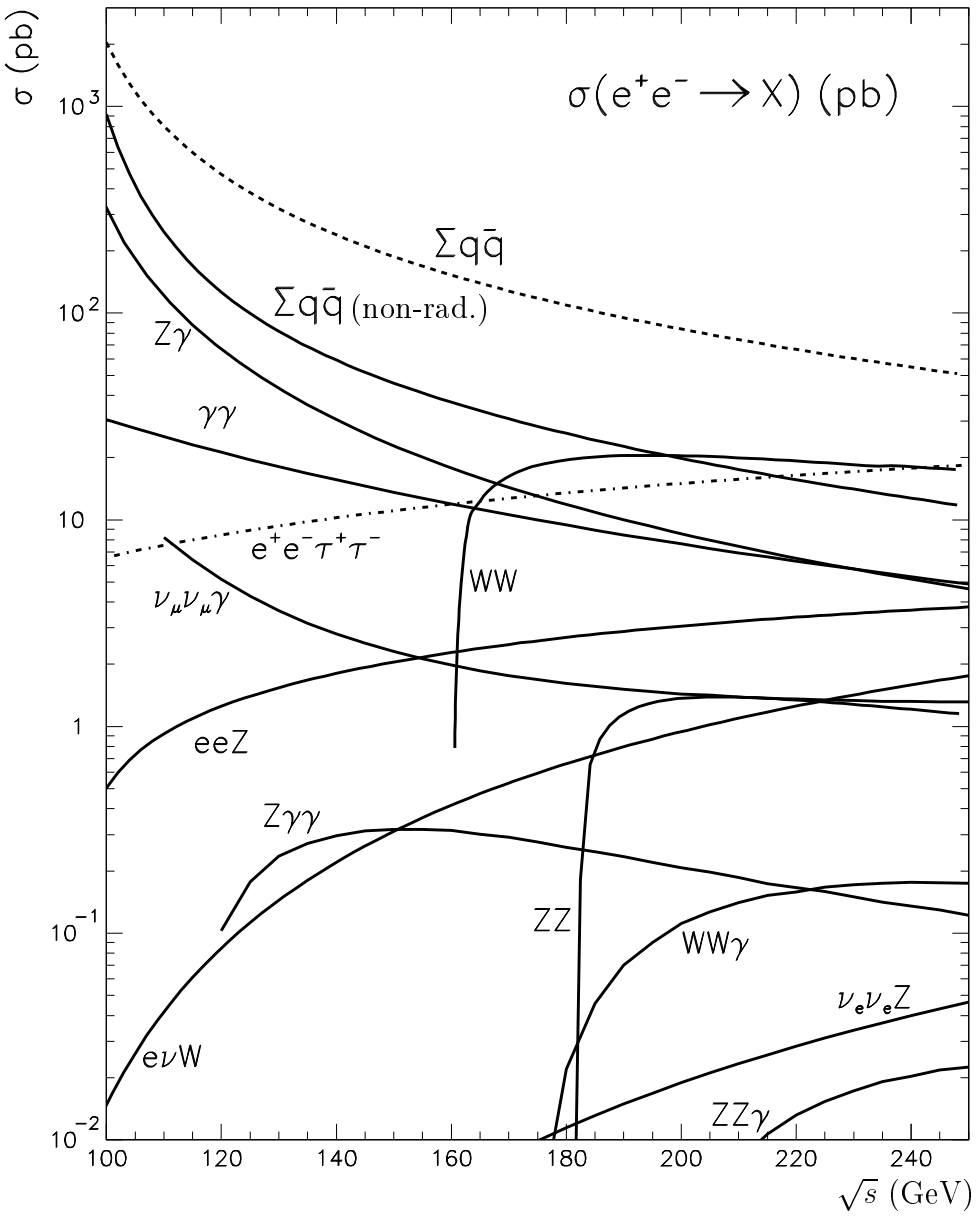

Figure 3.2: The cross-sections for various Standard Model processes in e^+e^- collisions at centre-of-mass energies within the LEP2 range. The figure has been taken from [39]. The hadronic two-fermion cross-section is shown both for inclusive events ($\sum q\bar{q}$) and for events without significant initial state radiation ($\sum q\bar{q}$ (non-rad.)). For some processes, only the dominant t-channel contribution is taken into account, and acceptance cuts have been applied.

small compared to the error on the reconstructed secondary vertex position. The angular acceptance is restricted to $|\cos\theta_T| < 0.9$, where θ_T denotes the polar angle of the thrust axis of the event.

Tracks used for secondary vertex reconstruction are required to have a momentum greater than 0.5 GeV. The impact parameter in the xy plane relative to the reconstructed primary vertex is required to satisfy $|d_0| < 0.3\,\mathrm{cm}$, and its error $\sigma_{d_0} < 0.1\,\mathrm{cm}$. This mainly removes badly measured tracks and tracks from K^0 or Λ decays. Secondary vertices are reconstructed

from these tracks as described in [49][3]: Within each jet the vertexing algorithm takes the three tracks with the most significant separation from the primary vertex as seed tracks and forms seed vertices from the crossing points of pairs of these tracks. Each seed vertex is considered in turn. A trial combination of each charged track in the jet with the seed vertex is made and the combination resulting in the vertex with the smallest χ^2 is retained, provided the χ^2 probability of the resulting vertex is at least 1%. The seed vertex parameters are updated and the process is iterated until there are no acceptable tracks to add. If several acceptable vertices are found in the same jet, the vertex with the largest number of assigned tracks is retained; if this choice is not unambiguous, the candidate vertex with the most significant separation from the primary vertex is chosen. Vertices that contain only two tracks are rejected.

Each hadronic event is divided into two hemispheres by the plane perpendicular to the thrust axis and containing the nominal interaction point. For each reconstructed secondary vertex, the signed decay length L is defined as the distance between the secondary and the primary vertex. L is taken to be positive if the secondary vertex is in the hemisphere pointed at by the momentum vector of the jet which contains the vertex, and negative otherwise. The decay length significance L/σ_L is defined as the ratio of the decay length and its error. Secondary vertices with $L/\sigma_L > 8$ are used to tag $\mathrm{b\bar{b}}$ events. This cut represents the best compromise between tagging efficiency and purity.

3.3.2 Determination of R_b from the Vertex Tagged Events

For the measurement of R_b, the number of events tagged by a secondary vertex is determined and corrected for tagging efficiency and background. Due to the limited statistics compared with the data collected at the Z resonance, a double tag technique as e.g. in [30] cannot be applied. In order to reduce the sensitivity of the analysis to the detector resolution, a *folded tag* technique [48] is used: a hemisphere is assigned a *forward tag* if it contains a secondary vertex with a decay length significance $L/\sigma_L > 8$, or a *backward tag* if it contains a vertex with a decay length significance $L/\sigma_L < -8$. The number of backward tagged hemispheres is then subtracted from the number of forward tagged hemispheres. After subtraction of the four-fermion background, the difference between the number of forward and backward tagged hemispheres, $N - \overline{N}$, in a sample of N_had hadronic events can be expressed as

$$N - \overline{N} = 2N_\mathrm{had}[(\epsilon_\mathrm{b} - \overline{\epsilon}_\mathrm{b})R_\mathrm{b} + (\epsilon_\mathrm{c} - \overline{\epsilon}_\mathrm{c})R_\mathrm{c} + (\epsilon_\mathrm{uds} - \overline{\epsilon}_\mathrm{uds})(1 - R_\mathrm{b} - R_\mathrm{c})] \ , \qquad (3.3)$$

where $(\epsilon_\mathrm{b} - \overline{\epsilon}_\mathrm{b})$, $(\epsilon_\mathrm{c} - \overline{\epsilon}_\mathrm{c})$, and $(\epsilon_\mathrm{uds} - \overline{\epsilon}_\mathrm{uds})$ are the differences between the forward and backward hemisphere tagging efficiencies for a given quark flavour. The tagging efficiencies for $\mathrm{u\bar{u}}$, $\mathrm{d\bar{d}}$, and $\mathrm{s\bar{s}}$ events (uds) are averaged, since they are very similar. For the relative production cross-section of $\mathrm{c\bar{c}}$ events, R_c, the prediction of ZFITTER is used. The four-fermion background is determined from the Standard Model production cross-sections and from the selection efficiencies as estimated from the Monte Carlo simulation. The b-purity for the sample with the folded tag is defined as the fraction of $\mathrm{b\bar{b}}$ event hemispheres contained in the sample $N - \overline{N}$, and is about 75%. The distribution of the decay length significance L/σ_L is shown in figure 3.3 for events at 189 GeV centre-of-mass energy, together with the expectation from the Monte Carlo simulation. The relative difference between data and Monte Carlo simulation is below 1% for

[3]For the results presented here, the algorithm has been extended to three dimensions to take advantage of the precise z information provided by the OPAL microvertex detector.

the folded-tag rate and $(8 \pm 4)\%$ for the backward-tag rate, which is more sensitive to modelling of the detector resolution. The agreement between data and simulation is similar at the other centre-of-mass energies.

The selected event sample contains a $5 - 10\%$ contamination of radiative hadronic events, with one or more energetic photons emitted in the initial state. In these events the effective centre-of-mass energy is reduced to values below $\sqrt{s'/s} = 0.85$, where the predicted value of R_b is up to 30% larger. In addition, the selection of non-radiative events is around 3% less efficient for $b\overline{b}$ final states than for other flavours, because of a larger missing energy due to neutrinos in semileptonic b hadron decays. The results are corrected for these effects, which are estimated from Monte Carlo simulation. The measured values of R_b are also corrected for interference between initial and final state radiation as described in [50]. This correction comes from the fact that the Monte Carlo simulation which is used to model the data does not account for interference between initial and final-state radiation.

The numbers of selected events and of forward and backward tagged hemispheres are given in table 3.3. The differences in hemisphere tagging efficiency, also listed in table 3.3, have been determined from Monte Carlo simulation. Their errors include all the systematic uncertainties that will be described in section 3.5.1. No systematic uncertainties other than those due to Monte Carlo statistics and detector resolution are assigned to the efficiencies in $u\overline{u}$, $d\overline{d}$, and $s\overline{s}$ events, as they represent a small fraction of the tagged samples. The systematic error is dominated by the uncertainties from the event selection, the modelling of b and c fragmentation and decay, and from the simulation of the detector resolution.

energy	events	N	$\overline{N}$	tagging efficiency differences	R_b	R_b^{SM}
133 GeV	745	153	11	$\epsilon'_b = 0.347 \pm 0.026$ $\epsilon'_c = 0.045 \pm 0.009$ $\epsilon'_{uds} = 0.0035 \pm 0.0014$	0.190±0.023±0.007	0.184
161 GeV	347	58	4	$\epsilon'_b = 0.331 \pm 0.013$ $\epsilon'_c = 0.045 \pm 0.002$ $\epsilon'_{uds} = 0.0090 \pm 0.0010$	0.195±0.035±0.007	0.171
172 GeV	228	23	3	$\epsilon'_b = 0.338 \pm 0.012$ $\epsilon'_c = 0.041 \pm 0.002$ $\epsilon'_{uds} = 0.0066 \pm 0.0010$	0.091±0.034±0.005	0.168
183 GeV	1186	232	25	$\epsilon'_b = 0.351 \pm 0.009$ $\epsilon'_c = 0.048 \pm 0.002$ $\epsilon'_{uds} = 0.0084 \pm 0.0008$	0.213±0.020±0.009	0.165
189 GeV	3209	551	87	$\epsilon'_b = 0.363 \pm 0.008$ $\epsilon'_c = 0.053 \pm 0.002$ $\epsilon'_{uds} = 0.0099 \pm 0.0008$	0.158±0.012±0.007	0.164

Table 3.3: The numbers of selected non-radiative events, forward (N) and backward ($\overline{N}$) tagged hemispheres, and tagging efficiency differences $\epsilon'_q = (\epsilon_q - \overline{\epsilon}_q)$ in the R_b analysis. The errors on the tagging efficiencies include systematic uncertainties. The R_b results with the statistical and systematic errors and their Standard Model expectations are given in columns 6 and 7.

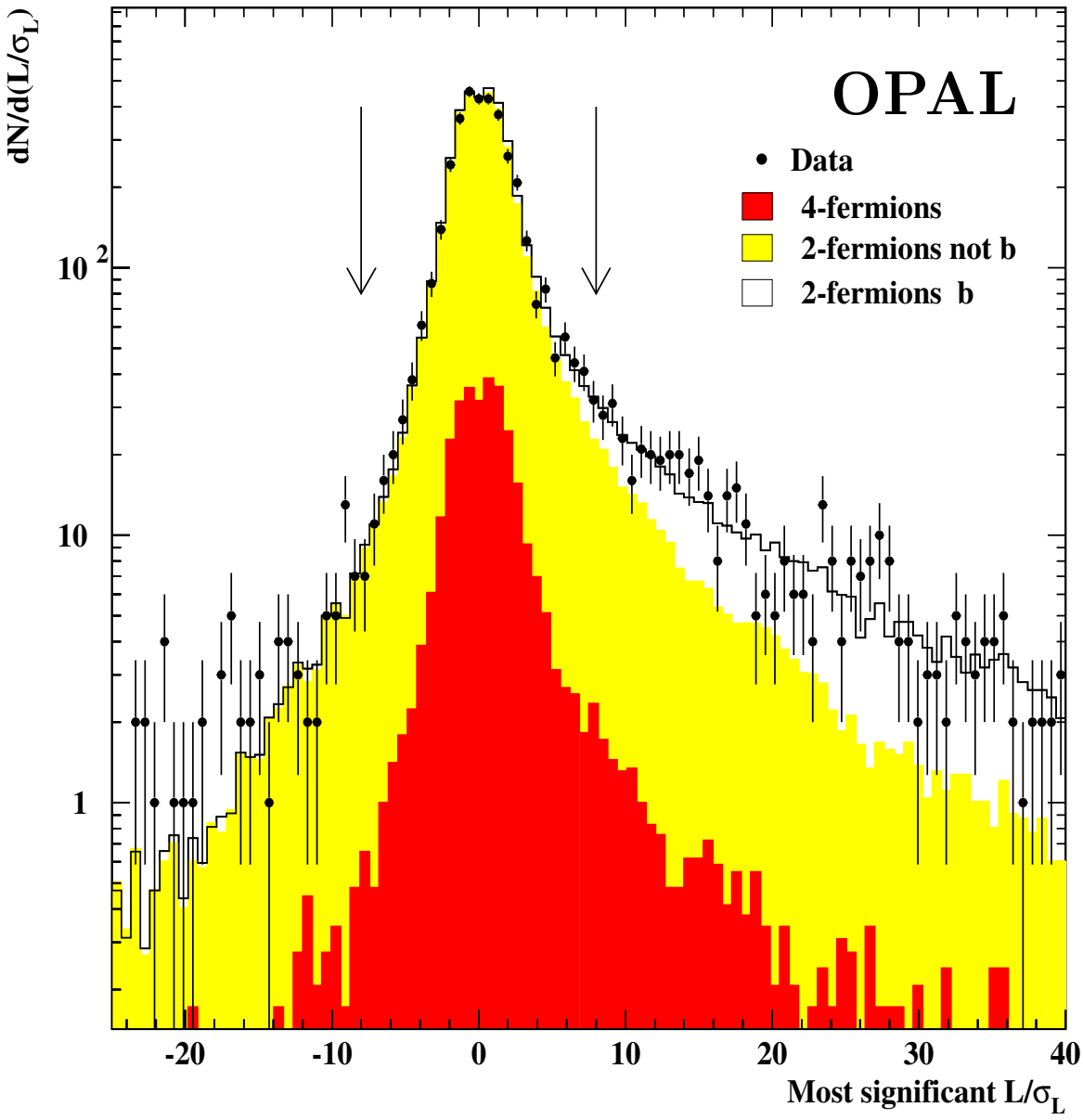

Figure 3.3: The decay length significance distribution for selected events at 189 GeV centre-of-mass energy. Only the most significant value is used for each event. The points with error bars represent the data. The dark-shaded histogram represents the expected contribution from four-fermion background, and the light-shaded area corresponds to the background from non-$b\bar{b}$ two-fermion events. The unshaded histogram indicates the $b\bar{b}$-content in the sample. The arrows show the position of the cut.

The dependence of the result on the assumed value of R_c can be parametrised as

$$\Delta R_b = b\, \Delta R_c\,, \tag{3.4}$$

where $\Delta R_c = R_c - R_c^{SM}$. The parameter b has been determined separately for each centre-of-mass energy. Its values are given in table 3.4.

dataset	133 GeV	161 GeV	172 GeV	183 GeV	189 GeV
$b \equiv (\Delta R_b)/(\Delta R_c)$	-0.12	-0.11	-0.11	-0.12	-0.13
R_c^{SM}	0.223	0.244	0.249	0.253	0.255

Table 3.4: The dependence of the measured R_b value on the assumed value of R_c for each centre-of-mass energy. The parameter b gives the change in R_b for an assumed deviation of R_c from its Standard Model prediction.

As a cross-check, the analysis is repeated on calibration data collected at the Z resonance. A value of $R_b(\sqrt{s} = m_Z) = 0.221 \pm 0.002(stat.) \pm 0.010(syst.)$ is obtained. The systematic error has been determined as for the high-energy data samples. This result agrees within the errors with the LEP1 combined value of $R_b^0 = 0.21664 \pm 0.00076$ [3] and can be regarded as a check of the evaluation of systematic errors for the measurements at energies above the Z resonance. Note that the 4% systematic error which is assigned to the R_b measurement at $\sqrt{s} = 189$ GeV is larger than the 2% difference with respect to the LEP1 average which is observed at $\sqrt{s} = m_Z$.

3.4 Measurement of Forward-Backward Asymmetries

For the measurement of heavy quark forward-backward asymmetries, it is necessary to distinguish the event hemispheres of the primary quark and antiquark in addition to the quark flavour tagging. Two complementary techniques are used. The first analysis provides a measurement of the bottom asymmetry for the events that have been tagged by the presence of a secondary vertex. A hemisphere charge method is used to distinguish between quark and anti-quark hemispheres.

The second technique is used for a simultaneous measurement of both the bottom and charm asymmetries. It is based on the identification of leptons from semileptonic decays of heavy hadrons ("prompt leptons") and pions from $D^{*+} \to D^0\pi^+$ decays ("slow pions"). The charge of these particles provides a clean distinction between the primary quark and anti-quark hemispheres in addition to the heavy flavour tagging.

In section 3.4.1, the measurement of the bottom asymmetry with the hemisphere charge technique is described. After a discussion of the lepton and slow pion identification in section 3.4.2 and the flavour separation of the tagged samples (section 3.4.3), the asymmetry measurement based on prompt leptons and slow pions is presented in section 3.4.4. Finally, the combination of the two measurements is discussed in section 3.4.5.

3.4.1 Measurement of $A_{\rm FB}^{\rm b}$ with a Hemisphere Charge Technique

To obtain a sample enriched in $\mathrm{b\overline{b}}$ events suitable for the $A_{\rm FB}^{\rm b}$ measurement, the secondary vertex algorithm used for the $R_{\rm b}$ analysis is employed. The analysis is limited to the range $|\cos\theta_T| < 0.9$. Only forward tags are used, since Monte Carlo studies show that with the current statistics, the folded tag would result in a larger error on the forward-backward asymmetry. Thus, an event is considered if it contains a secondary vertex with a decay length significance $L/\sigma_L > 8$ and no other secondary vertex with $L/\sigma_L < -8$. This cut is chosen to minimize the overall error.

Each non-radiative hadronic event is divided into two hemispheres by the plane perpendicular to the thrust axis that contains the nominal interaction point. Monte Carlo simulation shows that the direction of the thrust axis is a good approximation of the direction of emission of the initial $\mathrm{q\overline{q}}$ pair. For each hemisphere, the hemisphere charge $Q_{\rm hem}$ is computed according to equation 3.1 as $Q_{\rm hem} = \left(\sum_{i=1}^{n} |p_i|^{\kappa} \cdot q_i\right) / \left(\sum_{i=1}^{n} |p_i|^{\kappa}\right)$, where the sum runs over all n tracks in the hemisphere, p_i is the momentum component of track i along the thrust axis, and q_i denotes its charge. The parameter $\kappa = 0.4$ has been tuned according to the simulation to optimise the charge identification of a primary b or $\overline{\mathrm{b}}$ quark. To ensure a good hemisphere charge reconstruction, only events with more than three charged tracks per hemisphere are used. Events are classified according to the sign of the difference $Q_F - Q_B$ between the forward (Q_F) and backward (Q_B) hemisphere charges, where the forward hemisphere is defined as the one that contains the momentum vector of the incoming electron.

In order to ensure that each event is used at most once in this analysis and the measurement based on prompt leptons and slow pions described below, every event is assigned a figure of merit $\mathcal{P}_{\rm sig}^{\rm (vtx)}$ defined as

$$\mathcal{P}_{\rm sig}^{\rm (vtx)} = \tilde{F}_{\rm b} \cdot (2\tilde{P}_{\rm b} - 1)\,, \tag{3.5}$$

where $\tilde{F}_{\rm b}$ denotes the estimated $\mathrm{b\bar{b}}$ purity as a function of decay length significance and $\tilde{P}_{\rm b}$ stands for the estimated probability of correct charge identification[4] as a function of $|Q_F - Q_B|$, both determined from the simulation. Events are rejected from the vertex tagged sample if they are also tagged by the presence of a prompt lepton or slow pion with a corresponding figure of merit $\mathcal{P}_{\rm sig}^{(\ell/\pi_s)} > \mathcal{P}_{\rm sig}^{\rm (vtx)}$, where $\mathcal{P}_{\rm sig}^{(\ell/\pi_s)}$ is determined according to equation 3.13. At $\sqrt{s} = 189$ GeV, the events that contain both a tagged secondary vertex and a prompt lepton or slow pion correspond to 56% of the vertex tagged and 28% of the lepton or slow pion tagged samples, respectively. Of these common events, 58% are assigned to the secondary vertex tagged event sample by the procedure described above. It has been checked that systematic cross-dependences between the two asymmetry measurements, which may in principle be introduced by this method, are negligibly small. Note that the quantity $\mathcal{P}_{\rm sig}^{\rm (vtx)}$ is not used in the fit which determines $A_{\rm FB}^{\rm b}$, but only to define the selected sample of events.

For the final vertex tagged event sample, the tagging efficiencies for each flavour are determined from Monte Carlo and are shown in table 3.5. The uncertainties include the systematic errors, which will be discussed in detail in section 3.5.1. They are dominated by uncertainties in the bottom and charm physics modelling and detector resolution, as in the $R_{\rm b}$ analysis. The b purity is about 60%, with a fraction of four-fermion background up to 5%. The lower b purity with respect to the folded tag purity does not limit the precision of the asymmetry

[4]The charge identification probability $\tilde{P}_{\rm b}$ does not depend significantly on the decay length significance of the tagged vertex.

measurement with the present statistics. Because of the rejection of some of the events that are also lepton or slow pion tagged, the final $b\bar{b}$ efficiencies and purities are lower than those which could otherwise be obtained for a vertex-tagged event sample.

flavour q	event selection efficiency ϵ_q	charge identification probability P_q
d	0.032 ± 0.005	0.673 ± 0.021
u	0.036 ± 0.005	0.743 ± 0.015
s	0.035 ± 0.005	0.683 ± 0.020
c	0.097 ± 0.005	0.645 ± 0.011
b	0.383 ± 0.025	0.683 ± 0.012

Table 3.5: Event tagging efficiencies ϵ_q and charge identification probabilities P_q at 189 GeV centre of mass energy, as determined from Monte Carlo simulation. The errors include systematic uncertainties. The efficiencies and charge identification probabilities are computed for the final selected samples after rejection of events with $\mathcal{P}_{\rm sig}^{(\ell/\pi_s)} > \mathcal{P}_{\rm sig}^{(\rm vtx)}$. Similar values have been obtained for the other centre-of-mass energies.

The quantities P_q are the probabilities for the hemisphere charge method to correctly identify the event hemisphere into which the primary quark q is emitted. They are determined from Monte Carlo simulation and are given in table 3.5 for the different quark flavours at $\sqrt{s} = 189$ GeV. Similar values are obtained at the other centre-of-mass energies. Their errors include systematic uncertainties which will be discussed in detail in section 3.5.1. The largest contribution to the systematic error of the b and c quark charge identification probabilities arises from the modelling of heavy flavour fragmentation and decay. For light flavours the uncertainties on fragmentation are expected to have a small effect on the total systematic error, and only Monte Carlo statistics and detector resolution are considered. Possible detector biases in the charge identification probability for positive and negative quarks have been investigated using Z calibration data, and have been found to be negligible.

The quantity

$$x = -\text{sign}(Q_F - Q_B) \cdot |\cos\theta_T| \tag{3.6}$$

is computed for each event, where θ_T denotes the polar angle of the thrust axis. Its observed distribution at 189 GeV centre-of-mass energy is compared with the Monte Carlo prediction in figure 3.4. When only vector and axial vector couplings of the heavy quarks to a gauge boson exchanged in the s-channel are allowed, the observed angular distribution of the outgoing quark is determined by equation 1.1 and can be expressed as

$$\frac{\mathrm{d}\sigma^{obs}}{\mathrm{d}x} = \mathcal{C}\,\epsilon(x)\,(1 + x^2 + \frac{8}{3}A_{\rm FB}^{obs}x)\,, \tag{3.7}$$

where the quark masses have been neglected. The constant $\mathcal{C}$ is for normalization, and $\epsilon(x)$ is the tagging efficiency as a function of $\cos\theta_T$ for an event. It is assumed that the efficiencies are symmetric functions of x, and it has been checked in the simulation that their dependence on x is the same for all primary flavours. For other event types (e.g. four-fermion events), the predicted differential cross-section is not a second-order polynomial in x, but the resulting effects are negligible within the precision of the measurements presented here.

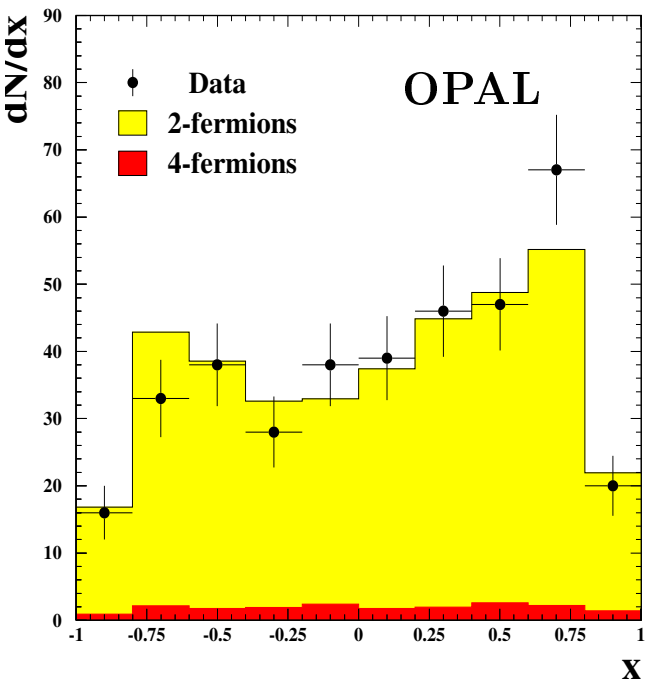

Figure 3.4: The distribution of the observed $x = -\text{sign}(Q_F - Q_B) \cdot |\cos\theta_T|$ at 189 GeV centre-of-mass energy. The points with error bars are the data, and the histogram is the Monte Carlo expectation. The dark shaded histogram represents the expected contribution from four-fermion background. The histogram showing the Monte Carlo expectation has been scaled to the same number of entries as found in the data.

Using equation 3.7, the observed asymmetry $A_{\rm FB}^{obs}$ is obtained by maximising the log likelihood

$$\ln\mathcal{L} = \sum_{j=1}^{N} \ln\left\{\mathcal{C}\epsilon(x_j)\right\} + \sum_{j=1}^{N} \ln\left\{1 + x_j^2 + \frac{8}{3}A_{\rm FB}^{obs}x_j\right\} , \tag{3.8}$$

where the sum is over all N selected events, and $A_{\rm FB}^{obs}$ is the only free parameter in the fit. The first term is a constant for a given set of events, so that the efficiency as a function of x does not need to be known.

After four-fermion background subtraction, $A_{\rm FB}^{\rm b}$ is determined from the relation

$$A_{\rm FB}^{obs} = \sum_{\rm q=u,d,s,c,b} s_{\rm q} \cdot F_{\rm q} \cdot (2P_{\rm q} - 1) \cdot A_{\rm FB}^{\rm q} \ . \tag{3.9}$$

Here, $s_{\rm q}$ is -1 $(+1)$ for up-type (down-type) quarks, and $A_{\rm FB}^{\rm q}$ is the forward-backward asymmetry for flavour q. The asymmetries for non-b events are fixed to their Standard Model values as calculated by ZFITTER. The fractions $F_{\rm q}$ of events of flavour q in the sample are determined as

$$F_{\rm q} = \frac{R_{\rm q}\epsilon_{\rm q}}{\sum_j R_j\epsilon_j} \ , \tag{3.10}$$

where $R_{\rm q}$ is the ratio of the cross-section of quark type q to the total hadronic cross-section, determined from ZFITTER, and $\epsilon_{\rm q}$ is the tagging efficiency, determined from Monte Carlo simulation. The factor $(2P_{\rm q} - 1)$ is to account for charge misassignment. The small contamination from four-fermion events is evaluated as for the $R_{\rm b}$ measurement and subtracted from

the sample. Its observed asymmetry is found to be consistent with zero within the available Monte Carlo statistics.

The numbers of tagged events, the observed asymmetries $A_{\rm FB}^{obs}$, and the corrected bottom asymmetries $A_{\rm FB}^{\rm b}$ with their statistical and systematic errors are given in table 3.6, together with the Standard Model expectations at the different centre-of-mass energies. Most of the systematic error sources are in common with the $R_{\rm b}$ analysis, as discussed in section 3.5.1. The largest systematic errors arise from uncertainties in the detector resolution and the event selection procedure. Uncertainties in the fragmentation of light quarks are assumed to be negligible and are not considered. For all centre-of-mass energies, the statistical error is dominant.

While the observed asymmetries are well within the physical range of $-0.75 < A_{\rm FB}^{obs} < 0.75$, values of $A_{\rm FB}^{\rm b}$ outside this range are possible because of the corrections due to sample composition and charge identification probability. All corrected $A_{\rm FB}^{\rm b}$ values are compatible with a value inside the physical range. No constraint is applied to force the corrected $A_{\rm FB}^{\rm b}$ values to lie within this range, in order to facilitate the combination with the values determined in the lepton and slow pion analysis and with measurements by other experiments.

energy	events	$A_{\rm FB}^{obs}$	$A_{\rm FB}^{\rm b}$	$A_{\rm FB}^{\rm b,SM}$
133 GeV	75	0.12 ± 0.12	$0.67 \pm 0.50 \pm 0.06$	0.48
161 GeV	35	$-0.17\ ^{+0.18}_{-0.16}$	$-0.59\ ^{+0.76}_{-0.68} \pm 0.04$	0.55
172 GeV	14	$0.32\ ^{+0.27}_{-0.25}$	$1.9 \pm 1.3 \pm 0.1$	0.56
183 GeV	157	$0.182\ ^{+0.082}_{-0.073}$	$1.15\ ^{+0.41}_{-0.37} \pm 0.08$	0.57
189 GeV	372	$0.194\ ^{+0.055}_{-0.047}$	$1.22\ ^{+0.28}_{-0.24} \pm 0.08$	0.58

Table 3.6: The numbers of tagged events with the vertex tag analysis, the observed asymmetries, the resulting $A_{\rm FB}^{\rm b}$ values, and their Standard Model predictions. The first error on $A_{\rm FB}^{\rm b}$ is statistical, the second systematic.

3.4.2 Identification of Prompt Leptons and Slow Pions

Prompt leptons from semileptonic decays of heavy hadrons provide a means of tagging both $\rm b\bar{b}$ and $\rm c\bar{c}$ events that is largely independent of the secondary vertex tag. In addition, slow pions from $\rm D^{*+} \to D^0 \pi^+$ decays are used for tagging heavy flavour events. Both prompt leptons and slow pions allow a clean identification of the event hemisphere that contains the primary quark.

3.4.2.1 Electron Identification

The selection of electrons relies mainly on the specific energy loss $\mathrm{d}E/\mathrm{d}x$ and the reconstructed energy in the electromagnetic calorimeter region the candidate track points to. The $\mathrm{d}E/\mathrm{d}x$

information gives the best separation for tracks with a momentum within $2\,\mathrm{GeV} \lesssim p \lesssim 10\,\mathrm{GeV}$, while the information from the calorimeter is important for larger momenta where the predicted $\mathrm{d}E/\mathrm{d}x$ values for electrons and heavier particles become similar. For an optimal identification, electron candidates are preselected and then classified according to the output of an artificial neural network which uses both tracking and calorimeter information.

Electron candidates are required to have a momentum of at least 2 GeV. Tracks with less than 20 $\mathrm{d}E/\mathrm{d}x$ samplings in the jet chamber are rejected to ensure a good measurement of the specific energy loss. The difference between the measured energy loss and that expected for an electron, divided by the measurement error, is required to be between -2 and 4.

In this sample of preselected tracks, electrons are identified with the help of an artificial neural network denoted $\mathcal{N}_{\mathrm{el}}$ in the following. The network is described in detail in [30]. In the barrel region of the detector, for $|\cos\theta| < 0.8$, it uses the following six input variables:

- p, the track momentum;
- $|\cos\theta|$, the absolute value of the cosine of the polar angle of the track;
- $(\mathrm{d}E/\mathrm{d}x)_{norm}$, the difference between the specific energy loss of the particle in the tracking chamber and that expected for an electron, divided by its error;
- $\sigma_{\mathrm{d}E/\mathrm{d}x}$, the error of the specific energy loss measurement;
- E_{cone}/p, the energy deposited in the electromagnetic calorimeter in a cone of 30 mrad half angle around the track, divided by the track momentum; and
- the number of lead glass blocks used to calculate E_{cone}.

In the endcap, for $|\cos\theta| > 0.8$, two additional variables are used:

- $\theta_{\mathrm{track}} - \theta_{\mathrm{cluster}}$, the difference in the polar angle between the track position extrapolated to the electromagmetic calorimeter and the centre of the associated cluster; and
- $\phi_{\mathrm{track}} - \phi_{\mathrm{cluster}}$, the corresponding difference in ϕ.

In addition to the electron preselection, a network output $\mathcal{N}_{\mathrm{el}} > 0.9$ is required. At 189 GeV, this selection has an efficiency for prompt electrons of approximately 25%, defined with respect to the total number of prompt electrons that are reconstructed as tracks in the detector. The resulting sample is 75% pure in electrons.

After this selection, electrons from photon conversions are an important background in the sample. A separate artificial neural network is used to identify pairs of conversion electrons, as described in detail in [31, 30]. The contribution of electrons from photon conversions is reduced by requiring a network output of $\mathcal{N}_{\mathrm{cv}} < 0.4$. In the Monte Carlo simulation at 189 GeV centre-of-mass energy, 89% of the electrons from photon conversions are rejected by this cut, while 90% of the prompt electrons are kept. In figure 3.5, the $\mathcal{N}_{\mathrm{el}}$ and $\mathcal{N}_{\mathrm{cv}}$ output distributions are shown for tracks at 189 GeV centre-of-mass energy.

3.4.2.2 Muon Identification

The identification of muons is based mainly on the matching of track segments in the muon chamber with extrapolated tracks from the central detector. In addition, information from the hadronic calorimeter, where muons are expected to leave hits in all layers, and from the specific

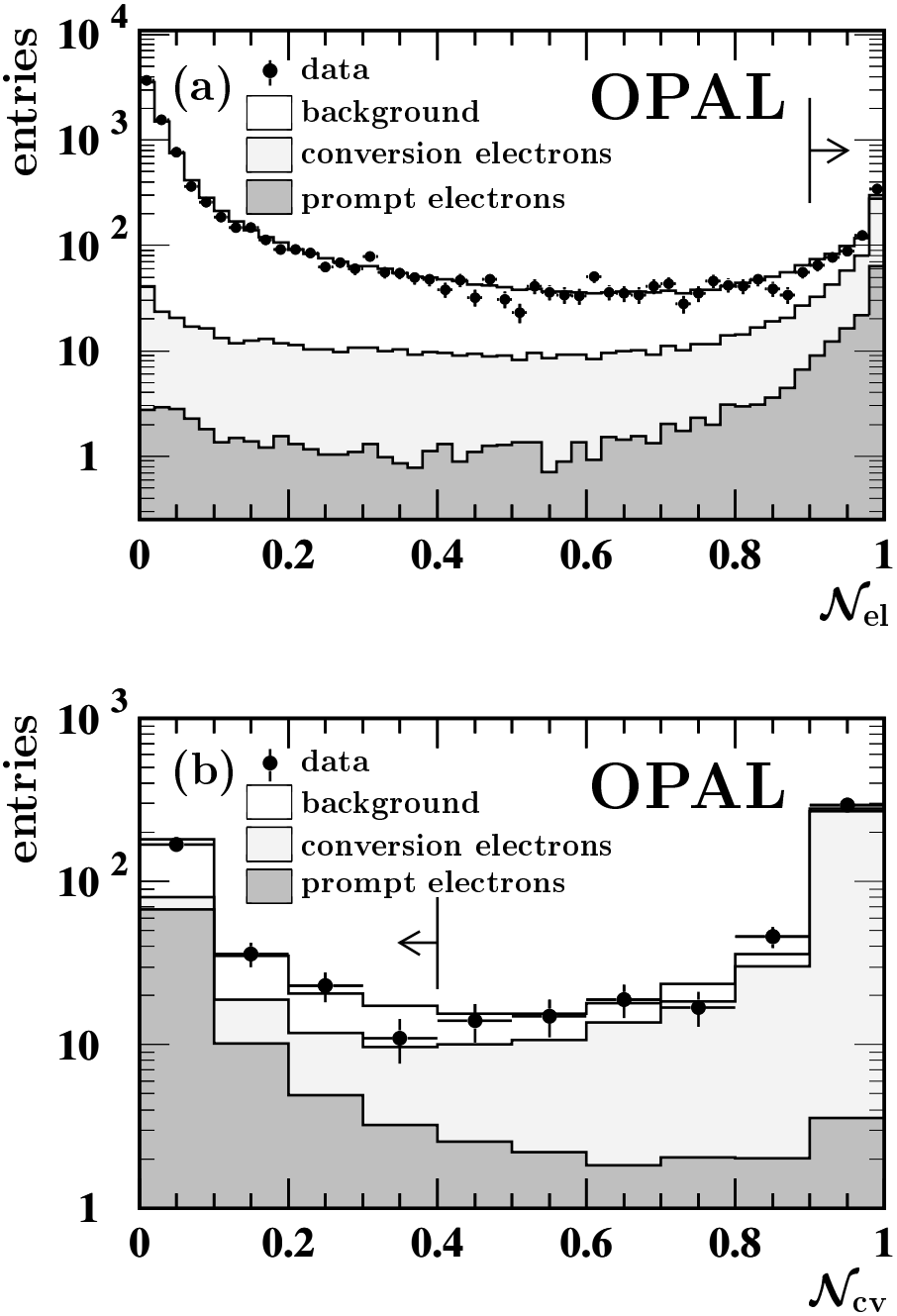

Figure 3.5: The $\mathcal{N}_{\mathrm{el}}$ distribution is shown in figure (a) for tracks at 189 GeV centre-of-mass energy that pass the electron momentum and $\mathrm{d}E/\mathrm{d}x$ cuts. In (b), the $\mathcal{N}_{\mathrm{cv}}$ distribution is given for those tracks that also pass the requirement of $\mathcal{N}_{\mathrm{el}} > 0.9$. In each case, the points with error bars represent the data distribution, and the histograms the Monte Carlo simulation, scaled to the same number of entries. The dark and light grey areas are the expected contributions from prompt electrons and conversion electrons, respectively, while the open area corresponds to hadrons. The arrows point into the accepted regions.

energy loss in the central tracking chamber is used. To use the available information in an optimal way, an artificial neural network has been developed.

The muon selection proceeds in two steps. First, muon track segments are formed from the hits in the muon chambers. Tracks from the central tracking chambers with a momentum greater than 2 GeV are extrapolated to the muon chambers. For each track segment in the muon chambers, only the "best matching track" is considered further, which is defined as the extrapolated track that has the smallest angular separation α to the muon track segment in question.

In a second step, an artificial neural network trained for muon identification is used to enhance the purity of the muon sample. The following eleven inputs are used in the network. Their distributions are shown in figure A.1.

- Information from the matching:
  - The square root of the χ^2 for the position match in θ and ϕ between the extrapolated track and the associated muon track segment in the muon chambers, as described in [51];
  - the ratio of distances $R_{\mu mis} = \alpha^{(1)}/\alpha^{(2)}$ of the best and second best matching track to the muon segment; this is a measure of how ambiguous the choice of the best matching track was in the preselection; and
  - the χ^2 probability for the matching which is computed using both position and direction information for the track in the central detector and the associated muon track segment [52].
- Information from the hadronic calorimeter:
  - The number of calorimeter layers in the cluster associated with the central track;
  - the number of the outermost such layer; and
  - the χ^2 probability for the match in θ and ϕ between the track (extrapolated to the hadron calorimeter) and the associated cluster.
- Specific energy loss:
  - The muon $\mathrm{d}E/\mathrm{d}x$ weight for the track, which is a measure of the probability that the track is compatible with a muon hypothesis, signed negative if the observed energy loss is smaller than that expected for a muon of the observed momentum;
  - $\sigma_{\mathrm{d}E/\mathrm{d}x}$, the error on the $\mathrm{d}E/\mathrm{d}x$ measurement; and
  - the momentum of the track.
- Geometrical information:
  - The position in $|\cos\theta|$ and ϕ where the extrapolated track enters the muon chambers.

The distribution of the neural network output $\mathcal{N}_\mu$ is shown in figure 3.6 for "best matching" tracks according to the definition above. Muon candidates are retained if $\mathcal{N}_\mu$ is larger than 0.65. In Monte Carlo simulated events at 189 GeV centre-of-mass energy, the muon selection results in an efficiency of 43% for prompt muons, defined with respect to all prompt muons that are reconstructed as tracks, and a muon purity of 73%.

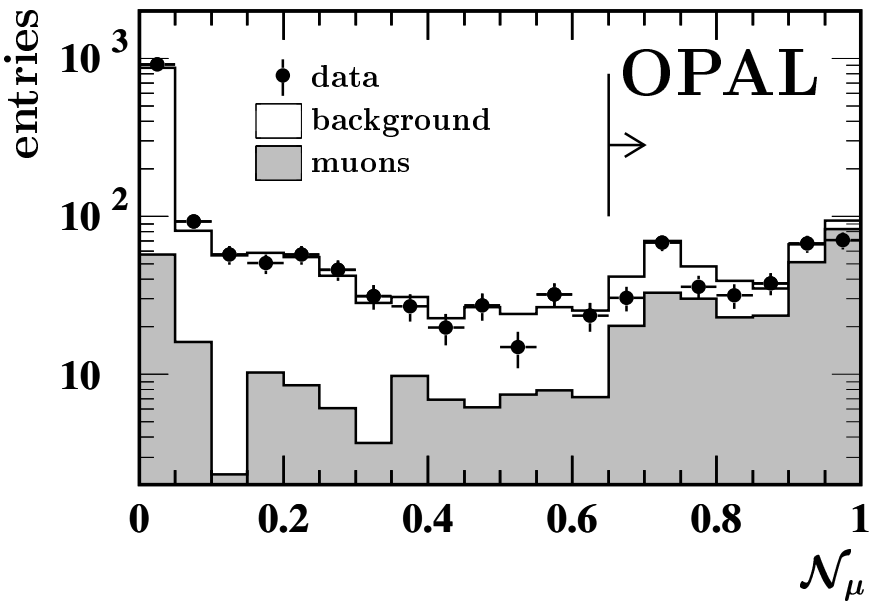

Figure 3.6: The $\mathcal{N}_\mu$ distribution for best matching tracks at 189 GeV centre-of-mass energy that pass the muon momentum cut. The points with error bars represent the data distribution, and the histogram the Monte Carlo simulation, scaled to the same number of entries. The shaded area is the expected contribution from true muons. The accepted region is indicated by the arrow. The structure at values $\mathcal{N}_\mu \approx 0.75$ is due to the sample of tracks for which the matching based on both position and direction information failed; for these tracks, the neural network does not obtain a subsample with a purity above $\sim 75\%$.

3.4.2.3 Preselection of Slow Pion Candidates

Pions from $\mathrm{D}^{*+} \to \mathrm{D}^0\pi^+$ decays, denoted π_s in the following, are selected based on the kinematic properties of this decay. Due to the low momentum $p^* = 39$ MeV [2] of the decay products in the D^{*+} rest frame, pions from this decay can be found only at momenta

$$p < p_{\pi_s}^{\max} = \frac{\sqrt{s}}{2m_{\mathrm{D}^{*+}}}\,(E^* + p^*) = 0.0458\,\sqrt{s} \tag{3.11}$$

in the laboratory frame, where $E^* = \sqrt{(p^*)^2 + m_{\pi^+}^2}$, and $m_{\mathrm{D}^{*+}}$ and m_{π^+} denote the D^{*+} and π^+ masses, respectively. In addition, slow pions have a transverse momentum with respect to the D^{*+} flight direction of at most p^*, and are thus dominantly found in the core of the jet containing the D^{*+} meson.

Slow pion candidates are required to have a momentum p between 1.0 GeV and $p_{\pi_s}^{\max}$ and, if at least 20 $\mathrm{d}E/\mathrm{d}x$ samplings are available, a specific energy loss $\mathrm{d}E/\mathrm{d}x$ whose probability for the pion hypothesis exceeds 2%. Tracks that form single charged particle jets are rejected. The D^{*+} flight direction is estimated by the jet direction, which is recalculated in an iterative procedure similar to the one described in [53], based on the rapidities of the tracks and clusters in the jet containing the slow pion candidate. If the jet mass exceeds 2.3 GeV, the track or

calorimeter cluster in the jet with the smallest rapidity with respect to the jet axis is removed from the calculation, and the direction is recomputed. The transverse momentum p_t of the slow pion candidate is calculated with respect to this jet direction. The p_t^2 distribution is shown in figure 3.7 for tracks at 189 GeV centre-of-mass energy. Slow pion candidates are accepted if $p_t^2 < 0.02$ GeV^2.

In Monte Carlo simulated events at 189 GeV, this preselection is 56% efficient and yields a sample that contains 5.7% of slow pions. This sample is further enriched with a cut that is described in section 3.4.3 below.

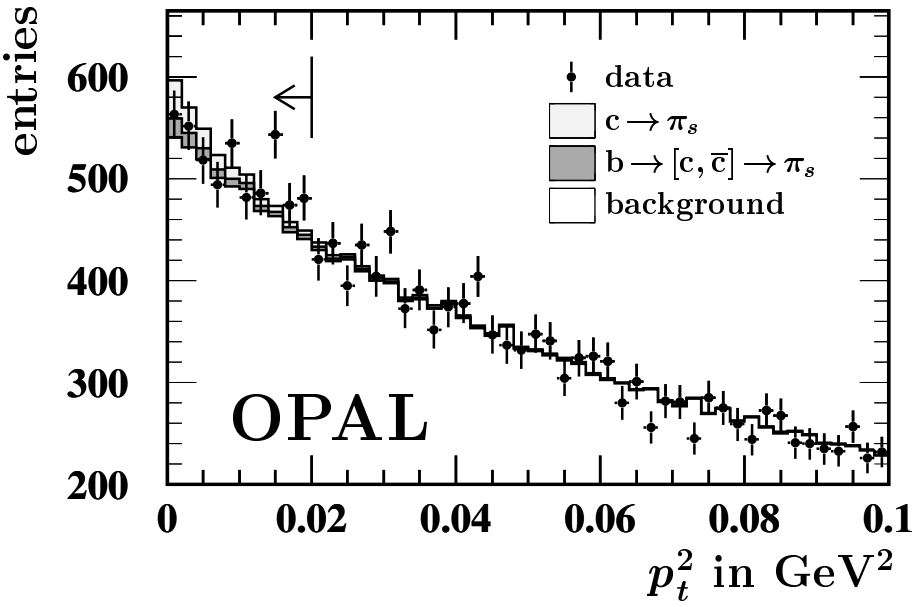

Figure 3.7: The p_t^2 distribution for tracks at 189 GeV centre-of-mass energy that pass the slow pion momentum and $\mathrm{d}E/\mathrm{d}x$ cuts. Tracks that form single charged particle jets have been excluded. The points with error bars represent the data distribution, and the topmost histogram the Monte Carlo simulation, scaled to the same number of entries. The dark grey area is the expected contribution from true slow pions from cascade $b \to [c, \overline{c}] \to \pi_s$ decays, and the light grey area represents $c \to \pi_s$ decays. The arrow indicates the accepted region.

3.4.3 Flavour Separation of the Lepton and Slow Pion Samples

Three different sources of prompt leptons are distinguished: $b \to \ell$, meaning leptons from semileptonic decays of bottom hadrons, regardless of $B-\overline{B}$ mixing which is accounted for in the asymmetry fit; cascade bottom decays, which include the contributions from $b \to c \to \ell$ and $b \to \overline{c} \to \ell$ processes; and $c \to \ell$, leptons from semileptonic decays of charm hadrons containing a primary charm quark. The background can be classified as "non-prompt" leptons, i.e. all other leptons that are not produced in the decay of bottom or charm hadrons, and particles that are mis-identified as electrons or muons.

For electrons and muons, separate artificial neural networks have been constructed with the aim of separating prompt $b \to \ell$ decays, cascade $b \to [c, \overline{c}] \to \ell$ decays, prompt $c \to \ell$ decays,

and all other contributions. The technique used is similar to the one described in [31], but the inputs and training have been re-optimized for centre-of-mass energies above the Z resonance; also an artificial neural network for the identification of cascade decays is included. Lepton candidates that form single charged particle jets are rejected since they are expected to be dominantly produced in leptonic W decays.

The first network, denoted $\mathcal{N}_{\mathrm{b}}$ in the following, is designed to separate $\mathrm{b} \to \ell$ decays from all other contributions. The two other networks, $\mathcal{N}_{\mathrm{bc}}$ and $\mathcal{N}_{\mathrm{c}}$, have been trained on a Monte Carlo simulation that does not contain $\mathrm{b} \to \ell$ decays in order to classify lepton candidates that are background to the $\mathcal{N}_{\mathrm{b}}$ net. All three networks use the following input variables, where jet variables are defined with the lepton candidate included in the jet. The input variable distributions are shown in figure 3.8 for lepton candidates at a centre-of-mass energy of 189 GeV. Simulated events at 183 GeV centre-of-mass energy have been used to train the neural networks. The same networks are applied for the flavour separation at all LEP2 energies; where appropriate, input variables are scaled by the ratio of centre-of-mass energies to obtain a similar behaviour at all energies.

- p, the lepton track momentum, scaled by $\sqrt{s}$;
- p_t, the transverse momentum of the lepton track calculated relative to the jet which contains the track;
- L/σ_L, the scaled decay length significance of the vertices[5] in the jet containing the lepton and the most energetic jet in the opposite hemisphere not containing the lepton, where secondary vertices are reconstructed with the same algorithm as described in section 3.3.1;
- $q_\ell \cdot Q_{\mathrm{jet}}^{\kappa=0.4}$, the jet charges of the jet containing the lepton and the most energetic jet in the hemisphere not containing the lepton, each multiplied by the lepton charge, where the jet charge is defined as in equation 3.1 with $\kappa = 0.4$, but only tracks in the jet are considered;
- N_{fwd}, the forward multiplicity in the lepton jet, defined as the number of tracks with an impact parameter significance with respect to the primary vertex larger than 2.0. For each track, the impact parameter is defined as the distance between the primary vertex and the track at its the point of closest approach; the impact parameter significance is defined as this distance divided by its error;
- the $|\cos\theta|$ of the jet momentum vector, where θ is the jet polar angle;
- the outputs $\mathcal{N}_{\mathrm{el}}$ and $\mathcal{N}_{\mathrm{cv}}$ of the electron identification network and the conversion finder network, respectively, in the case of electrons; and
- the output $\mathcal{N}_{\mu}$ of the muon identification network, in the case of muons.

From the $\mathcal{N}_{\mathrm{b}}$, $\mathcal{N}_{\mathrm{bc}}$, and $\mathcal{N}_{\mathrm{c}}$ network outputs, the following quantities are computed, which are related to the probabilities of a candidate to come from one of the three sources:

$$
\begin{aligned}
\mathcal{P}_{\mathrm{sig}}^{(\mathrm{b}\to\ell)} &= \mathcal{N}_{\mathrm{b}} \ , \\
\mathcal{P}_{\mathrm{sig}}^{(\mathrm{b}\to[\mathrm{c},\overline{\mathrm{c}}]\to\ell)} &= (1-\mathcal{N}_{\mathrm{b}})\,\frac{[\mathcal{N}_{\mathrm{bc}}\,(1-\mathcal{N}_{\mathrm{c}})]}{[\mathcal{N}_{\mathrm{bc}}\,(1-\mathcal{N}_{\mathrm{c}})]+[\mathcal{N}_{\mathrm{c}}\,(1-\mathcal{N}_{\mathrm{bc}})]+[(1-\mathcal{N}_{\mathrm{c}})\,(1-\mathcal{N}_{\mathrm{bc}})]} \ , \text{ and} \quad (3.12) \\
\mathcal{P}_{\mathrm{sig}}^{(\mathrm{c}\to\ell)} &= (1-\mathcal{N}_{\mathrm{b}})\,\frac{[\mathcal{N}_{\mathrm{c}}\,(1-\mathcal{N}_{\mathrm{bc}})]}{[\mathcal{N}_{\mathrm{bc}}\,(1-\mathcal{N}_{\mathrm{c}})]+[\mathcal{N}_{\mathrm{c}}\,(1-\mathcal{N}_{\mathrm{bc}})]+[(1-\mathcal{N}_{\mathrm{c}})\,(1-\mathcal{N}_{\mathrm{bc}})]} \ .
\end{aligned}
$$

The difference in the treatment of the $\mathcal{N}_{\mathrm{b}}$ output from $\mathcal{N}_{\mathrm{bc}}$ and $\mathcal{N}_{\mathrm{c}}$ is due to the fact that $\mathrm{b} \to \ell$ decays were omitted in the training of the latter two networks. Only candidates that satisfy

[5] The existence of a reconstructed secondary vertex is not required in this analysis. If no secondary vertex is reconstructed, the corresponding neural net input is set to a value that registers the lack of information.

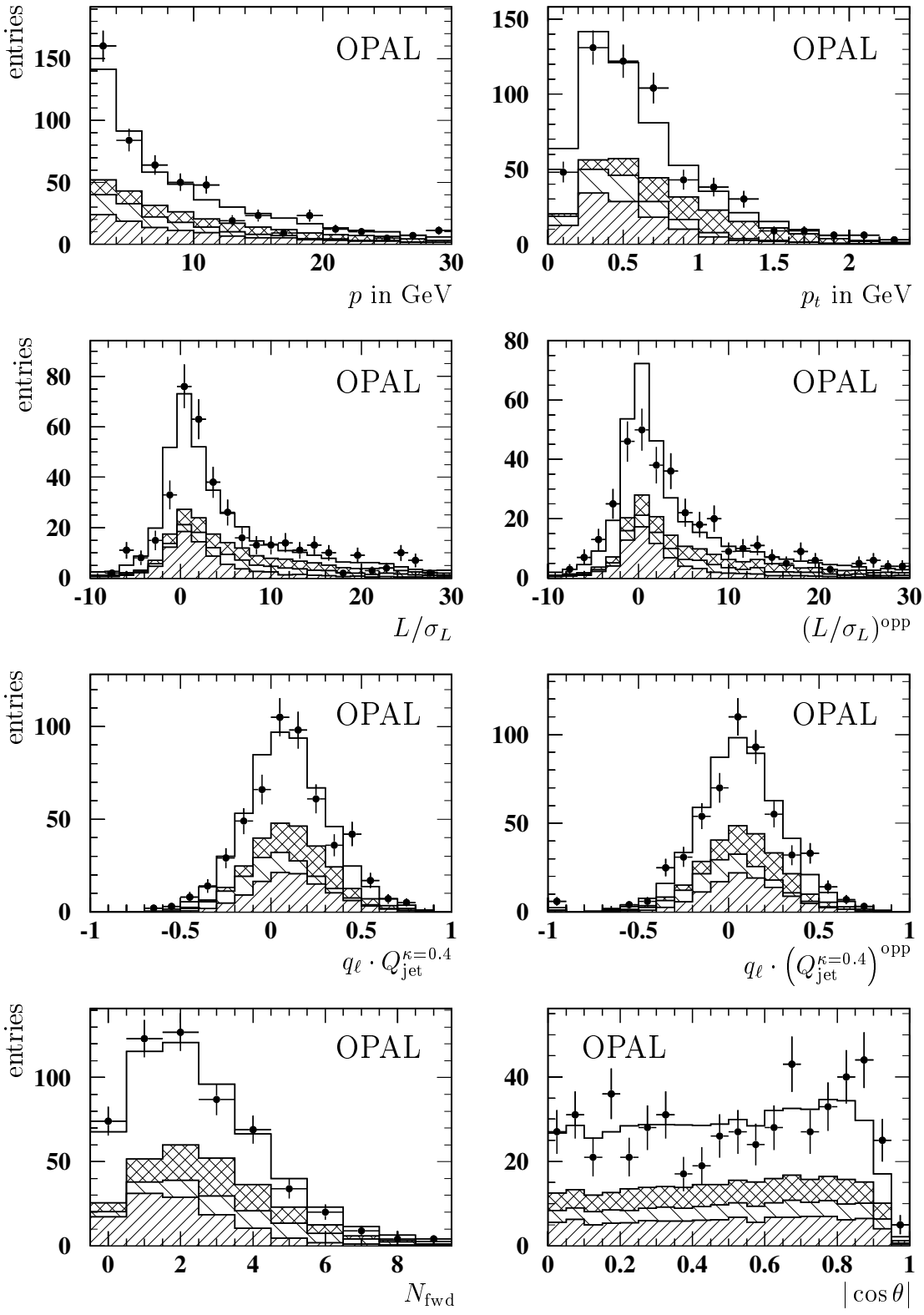

Figure 3.8: The distribution of the inputs for the flavour separation networks for leptons are shown, except for $\mathcal{N}_{\rm el}$, $\mathcal{N}_{\rm cv}$, and $\mathcal{N}_{\mu}$ which are given in figures 3.5 and 3.6. The notation for the variables is explained in the text. The points with error bars correspond to lepton candidates in the 189 GeV data that pass the lepton selection, and the solid histogram shows the corresponding Monte Carlo expectation. Also plotted are the individual signal contributions from $\mathrm{b} \to \ell$ (cross-hatch), $\mathrm{b} \to [\mathrm{c},\overline{\mathrm{c}}] \to \ell$ (wide diagonal hatch), and $\mathrm{c} \to \ell$ decays (narrow diagonal hatch) as expected from the Monte Carlo simulation. The white area corresponds to the expected background.

the condition

$$\mathcal{P}_{\rm sig}^{(\ell)} = \sqrt{\left(\mathcal{P}_{\rm sig}^{(\mathrm{b}\to\ell)}\right)^2 + \left(\mathcal{P}_{\rm sig}^{(\mathrm{b}\to[\mathrm{c},\overline{\mathrm{c}}]\to\ell)}\right)^2 + \left(\mathcal{P}_{\rm sig}^{(\mathrm{c}\to\ell)}\right)^2} > 0.1 \tag{3.13}$$

are used in the subsequent analysis. Candidates with lower values of $\mathcal{P}_{\rm sig}^{(\ell)}$ are expected to be dominantly background and to have a negligible contribution to the overall result. Note that the quantity $\mathcal{P}_{\rm sig}^{(\ell)}$, although used to define the selected sample of events, is not itself used in the fit that determines the bottom and charm asymmetries.

Similarly to the lepton case, slow pion candidates are classified as cascade $\mathrm{b} \to [\mathrm{c},\overline{\mathrm{c}}] \to \pi_s$ decays, $\mathrm{c} \to \pi_s$, and background. Another two artificial neural networks, $\mathcal{N}_{\rm bc}$ and $\mathcal{N}_{\rm c}$, have been trained for the separation of the three components in the preselected slow pion sample. The following inputs are used by both networks:

- p, the slow pion track momentum, scaled by $\sqrt{s}$;
- p_t^2, the transverse momentum squared of the slow pion track calculated relative to the jet direction obtained with the rapidity based algorithm that is described in section 3.4.2.3;
- $E_{\pi_s-\rm jet}$, the total energy of the slow pion jet, scaled by $\sqrt{s}$;
- $E_{\pi_s-\rm sub-jet}$, the scaled energy of the slow pion sub-jet [54]: Each jet containing a slow pion is split into two sub-jets, where the slow pion sub-jet is seeded by the slow pion track. In an iterative procedure, any particle that forms a smaller opening angle with the slow pion sub-jet than with the remainder of the jet is then assigned to the slow pion sub-jet;
- L/σ_L, the scaled decay length significance of the vertex in the slow pion jet, if a vertex is found;
- $q_{\pi_s} \cdot Q_{\rm jet}^{\kappa=0.4}$, the jet charge of the slow pion jet calculated with $\kappa = 0.4$, multiplied by the slow pion charge; and
- the $|\cos\theta|$ of the jet momentum vector.

In addition, the network for identification of $\mathrm{b} \to [\mathrm{c},\overline{\mathrm{c}}] \to \pi_s$ decays uses:

- L, the decay length of the vertex (if existing) in the jet containing the slow pion, scaled by $\sqrt{s}$;
- $q_{\pi_s} \cdot Q_{\rm jet}^{\kappa=2.0}$, the jet charge of the jet containing the slow pion, calculated with a different parameter $\kappa = 2.0$ and multiplied by the slow pion charge;
- $N_{\rm fwd}$, the forward multiplicity in the slow pion jet, defined as above;
- $(\sum p_t)_{\rm jet}$, the scalar sum of the transverse momenta relative to the jet axis of all tracks in the jet; and
- $\max(p_l)$, the maximum longitudinal momentum component of any track in the slow pion jet, measured relative to the jet direction and scaled by $\sqrt{s}$.

The quantities $\mathcal{P}_{\rm sig}^{(\mathrm{b}\to[\mathrm{c},\overline{\mathrm{c}}]\to\pi_s)}$ and $\mathcal{P}_{\rm sig}^{(\mathrm{c}\to\pi_s)}$ are computed in analogy to equation 3.12 for prompt lepton candidates, while $\mathcal{P}_{\rm sig}^{(\mathrm{b}\to\pi_s)}$ is set to zero. The same requirement on $\mathcal{P}_{\rm sig}^{(\pi_s)}$ (computed according to equation 3.13) is imposed as for prompt leptons. The distributions of all input variables are shown in figures 3.9 and 3.10 for tracks at 189 GeV that pass the slow pion selection.

If more than one lepton or slow pion candidate per event passes the selection, the one with the highest $\mathcal{P}_{\rm sig}^{(\ell/\pi_s)}$ value is taken. Furthermore, this $\mathcal{P}_{\rm sig}^{(\ell/\pi_s)}$ value is required to be larger than the value of $\mathcal{P}_{\rm sig}^{(\rm vtx)}$ as determined for the hemisphere charge measurement (see section 3.4.1) if the event is also tagged by the presence of a secondary vertex.

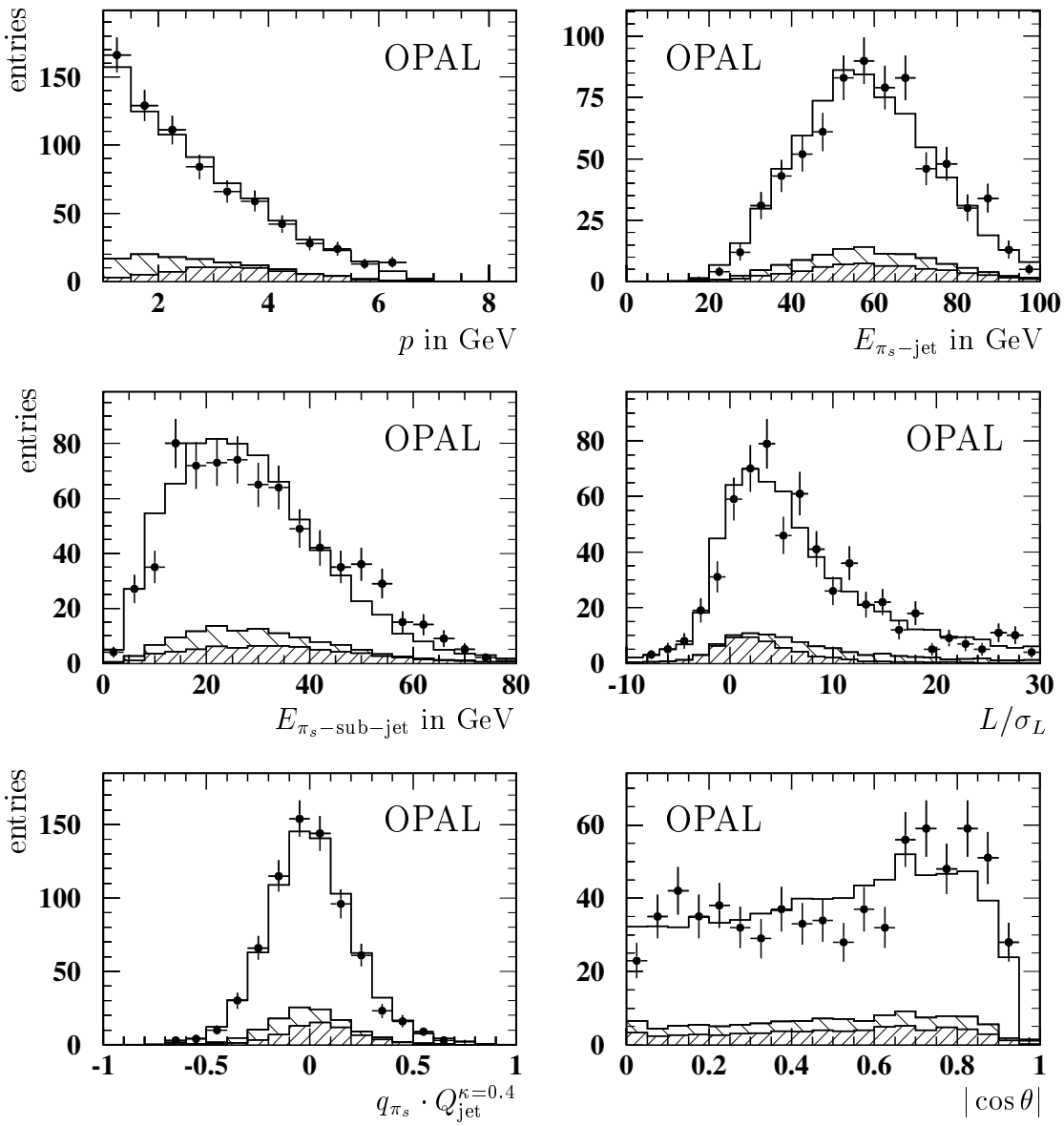

Figure 3.9: The distribution of the inputs for the neural nets for identifying $c \to \pi_s$ and $b \to [c, \overline{c}] \to \pi_s$ decays are shown, except for p_t^2, which is given in figure 3.7. The notation for the variables is explained in the text. The points with error bars correspond to slow pion candidates in the 189 GeV data that pass the slow pion selection, and the solid histogram shows the corresponding Monte Carlo expectation. Also plotted are the individual signal contributions from $b \to [c, \overline{c}] \to \pi_s$ (wide diagonal hatch) and $c \to \pi_s$ decays (narrow diagonal hatch) as expected from the Monte Carlo simulation.

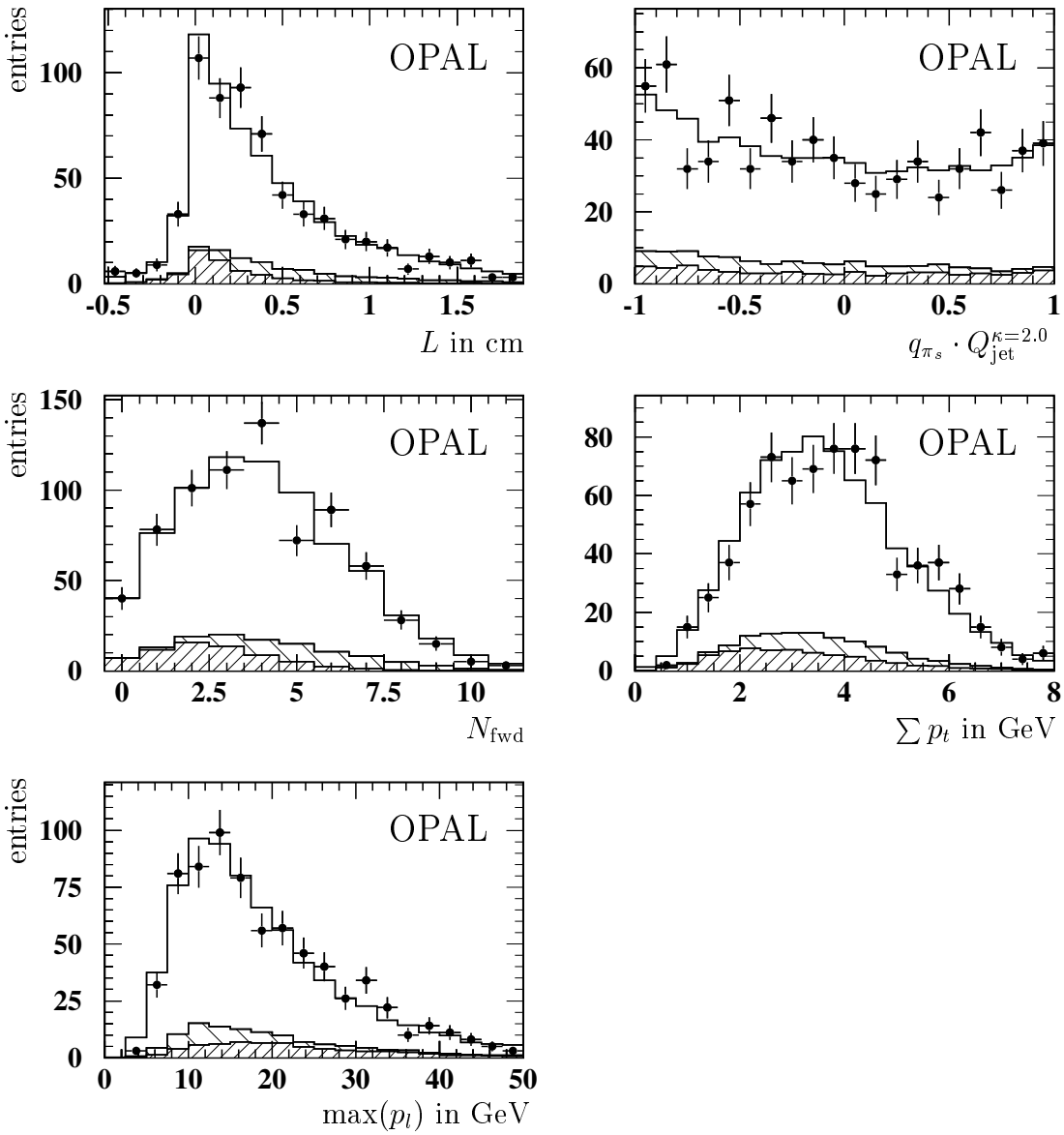

Figure 3.10: The distribution of the additional inputs used only in the neural net for identifying $b \to [c, \overline{c}] \to \pi_s$ decays are shown. The notation for the variables is explained in the text. The points with error bars correspond to slow pion candidates in the 189 GeV data that pass the slow pion selection, and the solid histogram shows the corresponding Monte Carlo expectation. Also plotted are the individual signal contributions from $b \to [c, \overline{c}] \to \pi_s$ (wide diagonal hatch) and $c \to \pi_s$ decays (narrow diagonal hatch) as expected from the Monte Carlo simulation.

A breakdown of the composition of the samples of electron, muon, and slow pion tagged events at 189 GeV centre-of-mass energy together with the efficiencies is given in table 3.7. In figure 3.11, the output distributions of the flavour separation networks are shown for the events that pass all cuts.

	sample composition			efficiencies		
source	electrons	muons	slow pions	electrons	muons	slow pions
$b \to \ell$	19 %	19 %	—	26 %	50 %	—
$b \to [c, \overline{c}] \to \ell/\pi_s$	9 %	11 %	3 %	16 %	31 %	6 %
$c \to \ell/\pi_s$	19 %	24 %	13 %	18 %	38 %	13 %
non-prompt leptons	15 %	20 %	—			
other background	37 %	25 %	85 %			

Table 3.7: The estimated composition of the lepton and slow pion tagged event samples at 189 GeV centre-of-mass energy after the selection. The efficiencies of the prompt lepton and slow pion selection are given for the final event sample with respect to all prompt leptons and slow pions that are reconstructed as tracks in the detector.

3.4.4 Measurement of A_{FB}^{b} and A_{FB}^{c} with Leptons and Slow Pions

The forward-backward asymmetries for bottom and charm, A_{FB}^{b} and A_{FB}^{c}, are extracted from the data using an unbinned maximum likelihood fit to the charge signed polar angle distribution of the thrust axis $\vec{T}$ in lepton and slow pion tagged events. It is assumed that $\vec{T}$ is the axis along which the primary quark-antiquark pair is emitted. The quantity $y = -q \cos\theta_T$ is computed event by event, where q is the charge of the lepton or slow pion, and the thrust direction $\vec{T}$ is defined such that $\vec{T}\cdot\vec{p} > 0$, with $\vec{p}$ being the momentum of the jet containing the lepton or slow pion. The inclusive y distributions for electron, muon, and slow pion tagged events at 189 GeV are presented in figure 3.12.

The fit is similar to that used in section 3.4.1 for the hemisphere charge measurement. However, both the bottom and charm asymmetries are to be determined in the fit. Therefore, the fit uses for each event its probabilities to be a correctly tagged $b\bar{b}$ or $c\bar{c}$ event or background, as determined from the simulation: The events are divided into several subsamples according to their $\mathcal{N}_b$, $\mathcal{N}_{bc}$, $\mathcal{N}_c$, and $|y|$ values. Three bins are used for each quantity, making a total of 81 subsamples separately for both electron and muon tagged events and 27 subsamples for the slow pion tagged events. These subsamples have different bottom and charm purities and are fitted simultaneously. The distributions of purities used in the fit to the 189 GeV data are shown in figure 3.13.

The cross-section for producing a $q\bar{q}$ pair is assumed to depend on y according to

$$\frac{d\sigma_{q\bar{q}}}{dy} \sim 1 + y^2 + \frac{8}{3} A_{FB}^{q}\, y \ . \tag{3.14}$$

The likelihood $\mathcal{L}_{sub}$ for one subsample is given by

$$\ln \mathcal{L}_{sub} = \sum_{candidates} \ln\left(1 + y^2 + \frac{8}{3} A_{FB}^{obs}\, y\right) \ , \tag{3.15}$$

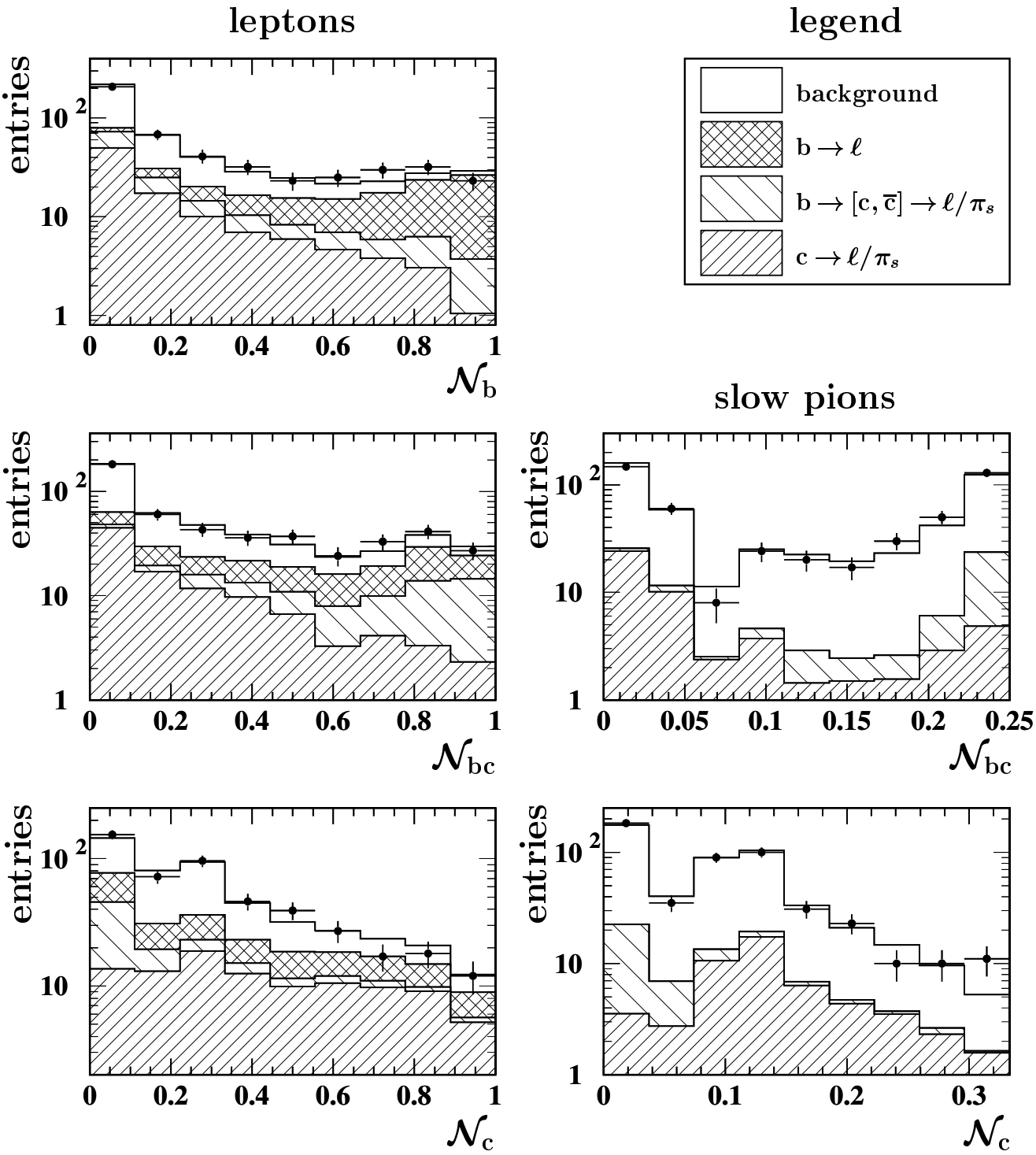

Figure 3.11: The $\mathcal{N}_{\mathrm{b}}$, $\mathcal{N}_{\mathrm{c}}$, and $\mathcal{N}_{\mathrm{bc}}$ distributions for lepton and slow pion tagged events at 189 GeV centre-of-mass energy. The points with error bars correspond to the data. The open histogram represents the Monte Carlo expectation, where the contributions from signal events are shown hatched as explained in the legend. The purity in the slow pion selection is limited, which is reflected in the fact that the range of $\mathcal{N}_{\mathrm{c}}$ and $\mathcal{N}_{\mathrm{bc}}$ values for slow pions does not extend up to 1. Note that better purities than shown in this figure are obtained for some of the subsamples used in the fit, where simultaneous requirements on $\mathcal{N}_{\mathrm{b}}$, $\mathcal{N}_{\mathrm{bc}}$, and $\mathcal{N}_{\mathrm{c}}$ are made.

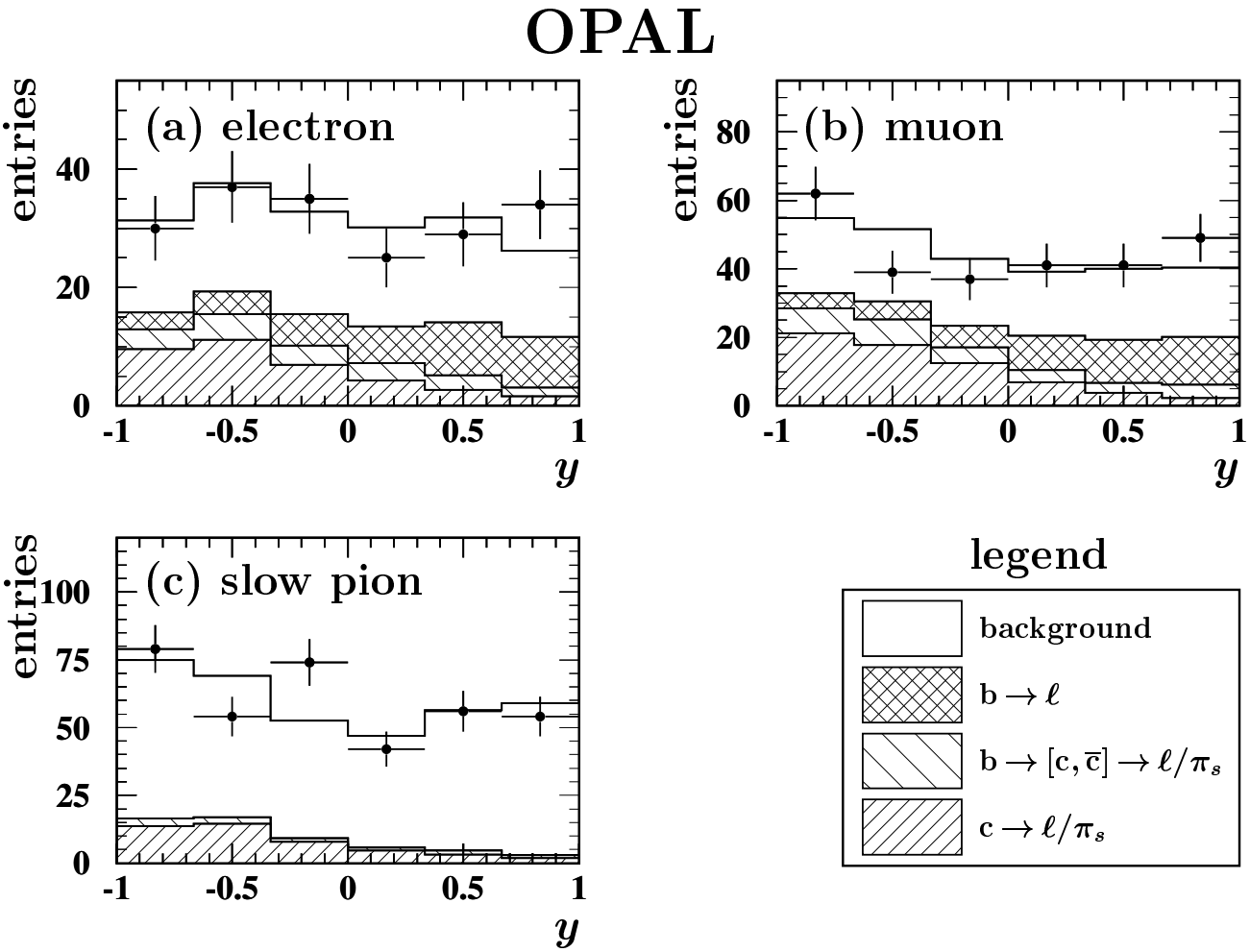

Figure 3.12: The y distributions of (a) electron, (b) muon, and (c) slow pion tagged events at a centre-of-mass energy of 189 GeV are given by the points with error bars. Also plotted is the expectation from the simulation together with the contributions from background (open histogram) and b $\to \ell$ (cross-hatch), b $\to [\mathrm{c},\overline{\mathrm{c}}] \to \ell/\pi_s$ (wide diagonal hatch), and c $\to \ell/\pi_s$ decays (narrow diagonal hatch). Note that in the fit, the tagged events are divided into subsamples of different bottom and charm purities to allow an extraction of both the bottom and charm asymmetries.

where the sum is taken over all candidates in the subsample. The total likelihood is then given by the product of the likelihoods of all the subsamples. The expected observed asymmetry A_{FB}^{obs} in each subsample is computed as

$$A_{\mathrm{FB}}^{obs}(\mathcal{N}_{\mathrm{b}},\mathcal{N}_{\mathrm{bc}},\mathcal{N}_{\mathrm{c}},|y|) = \sum_{i=1}^{5} f_i(\mathcal{N}_{\mathrm{b}},\mathcal{N}_{\mathrm{bc}},\mathcal{N}_{\mathrm{c}},|y|)\, A_{\mathrm{FB}}^{i} \ . \tag{3.16}$$

In this equation, f_i denotes the predicted fraction of leptons or slow pions from source i, and

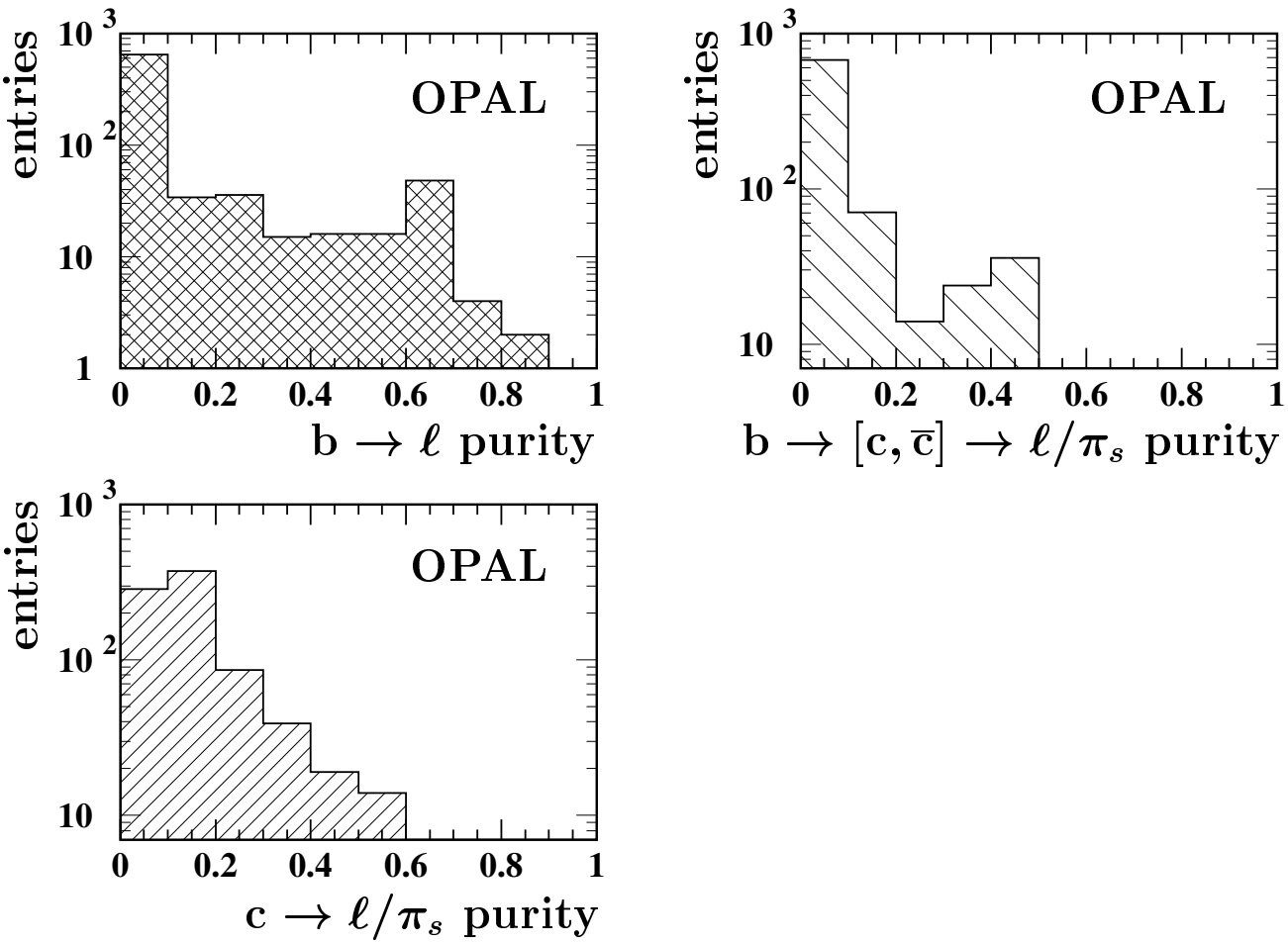

Figure 3.13: The distributions of the probabilities of the selected leptons and slow pions at 189 GeV centre-of-mass energy to come from the processes $\mathrm{b} \to \ell$, $\mathrm{b} \to [\mathrm{c}, \overline{\mathrm{c}}] \to \ell/\pi_s$, and $\mathrm{c} \to \ell/\pi_s$, respectively. In each plot, all data events are shown according to the sample composition determined from the simulation, and each bin contains the number of events in those subsamples whose purities are within the bin width.

A^i_{FB} is the corresponding asymmetry:

$$\begin{cases} A^1_{\mathrm{FB}} = \quad (1-2\overline{\chi_1}^{\mathrm{eff}})\, A^{\mathrm{b}}_{\mathrm{FB}} & \text{for } \mathrm{b} \to \ell\,, \\ A^2_{\mathrm{FB}} = -(1-2\overline{\chi_2}^{\mathrm{eff}})\, A^{\mathrm{b}}_{\mathrm{FB}} & \text{for } \mathrm{b} \to \mathrm{c} \to \ell/\pi_s\,, \\ A^3_{\mathrm{FB}} = \quad (1-2\overline{\chi_3}^{\mathrm{eff}})\, A^{\mathrm{b}}_{\mathrm{FB}} & \text{for } \mathrm{b} \to \overline{\mathrm{c}} \to \ell/\pi_s\,, \\ A^4_{\mathrm{FB}} = \quad -A^{\mathrm{c}}_{\mathrm{FB}} & \text{for } \mathrm{c} \to \ell/\pi_s\,, \text{ and} \\ A^5_{\mathrm{FB}} = \quad 0 & \text{for background,} \end{cases} \tag{3.17}$$

where $\overline{\chi_i}^{\mathrm{eff}}$ is the effective $\mathrm{B}-\overline{\mathrm{B}}$ mixing parameter. The fractions f_i have been calculated from the Monte Carlo simulation[6] and depend on the production rates of bottom and charm quarks, on the hadronisation fractions $f(\mathrm{b} \to [\mathrm{c}, \overline{\mathrm{c}}] \to \mathrm{D}^{*\pm})$ and $f(\mathrm{c} \to \mathrm{D}^{*+})$, on the semileptonic

[6]The fractions f_i are determined from samples of simulated events that are statistically independent from the sample used for the neural net training.

branching ratios of heavy hadrons, and on the mis-identification probability in each bin of $\mathcal{N}_{\rm b}$, $\mathcal{N}_{\rm bc}$, $\mathcal{N}_{\rm c}$, and $|y|$. Variations in the sample composition with $|\cos\theta_T|$ are taken into account since the f_i are binned in $|y|$. As described in section 3.4.1, this likelihood fit has the advantage that the $|\cos\theta_T|$ dependence of the efficiency for identifying leptons and slow pions is not needed explicitly. The effective mixing parameters $\overline{\chi}_1^{\rm eff}$, $\overline{\chi}_2^{\rm eff}$, and $\overline{\chi}_3^{\rm eff}$ are determined from the simulation for each subsample of events. The mixing parameter $\overline{\chi} = 0.118 \pm 0.006$ [2] used in the simulation for inclusive $\rm b\bar{b}$ events is taken as an external input. The small non-zero contributions to the observed asymmetry from prompt leptons and slow pions from radiative and four-fermion events are accounted for, but left out of the above list for simplicity. The assumption that the backgrounds from mis-identified leptons and slow pions do not contribute to the observed asymmetry has been checked and will be discussed in section 3.5.2.2.

The fit is done separately for the data taken at 133 GeV, 161 GeV, 172 GeV, 183 GeV, and 189 GeV. In table 3.8, the numbers of lepton and slow pion tagged events are given, and the results of the fit for the bottom and charm asymmetries are summarised for each energy point together with the errors and correlation. The systematic errors have been evaluated as described in section 3.5.2.

energy	electrons	muons	slow pions	measured asymmetries	correlation	predicted asymmetries
91 GeV	7770	12560	21721	$A_{\rm FB}^{\rm b} = 0.108 \pm 0.021 \pm 0.124$ $A_{\rm FB}^{\rm c} = 0.087 \pm 0.026 \pm 0.098$	+19%	$A_{\rm FB}^{\rm b,SM} = 0.095$ $A_{\rm FB}^{\rm c,SM} = 0.062$
133 GeV	48	69	82	$A_{\rm FB}^{\rm b} = -0.01\ ^{+0.37}_{-0.35} \pm 0.18$ $A_{\rm FB}^{\rm c} = 0.50\ ^{+0.31}_{-0.32} \pm 0.13$	+14%	$A_{\rm FB}^{\rm b,SM} = 0.48$ $A_{\rm FB}^{\rm c,SM} = 0.69$
161 GeV	16	37	42	$A_{\rm FB}^{\rm b} = 0.18\ ^{+0.56}_{-0.52} \pm 0.15$ $A_{\rm FB}^{\rm c} = 0.83\ ^{+0.59}_{-0.60} \pm 0.12$	+14%	$A_{\rm FB}^{\rm b,SM} = 0.55$ $A_{\rm FB}^{\rm c,SM} = 0.69$
172 GeV	14	29	20	$A_{\rm FB}^{\rm b} = 0.55\ ^{+0.85}_{-0.87} \pm 0.18$ $A_{\rm FB}^{\rm c} = 0.67\ ^{+0.49}_{-0.54} \pm 0.12$	+23%	$A_{\rm FB}^{\rm b,SM} = 0.56$ $A_{\rm FB}^{\rm c,SM} = 0.67$
183 GeV	77	104	126	$A_{\rm FB}^{\rm b} = 0.59\ ^{+0.29}_{-0.31} \pm 0.12$ $A_{\rm FB}^{\rm c} = 0.56\ ^{+0.27}_{-0.28} \pm 0.11$	+23%	$A_{\rm FB}^{\rm b,SM} = 0.57$ $A_{\rm FB}^{\rm c,SM} = 0.67$
189 GeV	190	269	359	$A_{\rm FB}^{\rm b} = 0.28\ \pm 0.21 \pm 0.12$ $A_{\rm FB}^{\rm c} = 0.52\ ^{+0.18}_{-0.19} \pm 0.11$	+19%	$A_{\rm FB}^{\rm b,SM} = 0.58$ $A_{\rm FB}^{\rm c,SM} = 0.66$

Table 3.8: For each centre-of-mass energy, the numbers of lepton and slow pion tagged events, the results for the bottom and charm asymmetries as measured with the lepton and slow pion tag, and their correlation are listed. The first error is statistical, and the second systematic. In the last column, the Standard Model predictions for the asymmetries are given. The values in the line entitled "91 GeV" have been determined from the Z calibration data.

As a cross-check, the fit is also performed on the calibration data taken at the Z resonance in the years 1996, 1997, and 1998. The results of this fit are also given in table 3.8. They are

consistent with the average of LEP1 and SLD measurements given in [3].

No systematic effect has been found which could cause the discrepancy between the $A_{\mathrm{FB}}^{\mathrm{b}}$ values at $\sqrt{s} = 189\,\mathrm{GeV}$ as measured with the analyses based on hemisphere charge and lepton or slow pion identification (see tables 3.6 and 3.8). For those events which are tagged both by a secondary vertex and a lepton or slow pion, the measured bottom asymmetries differ by 2.7 standard deviations, where the statistical correlation is taken into account. The simulated events have been divided into 32 samples to match the data sample size. The asymmetries have been measured for each of these samples using both techniques. In one case, a similar discrepancy has been found.

3.4.5 Combination of the $A_{\mathrm{FB}}^{\mathrm{b}}$ Measurements

By construction, the samples used in the hemisphere charge analysis do not have any events in common with the lepton or slow pion tagged samples. The bottom asymmetry as measured with the vertex tag depends on the assumed value of the charm asymmetry, while the fit to the lepton and slow pion tagged events yields results for the bottom and charm asymmetries with a non-zero correlation. This dependence on the charm asymmetry has to be taken into account when combining the two bottom asymmetry measurements. The vertex tag measurement is applied as a constraint in the fit to the lepton and slow pion tagged events that is described in section 3.4.4. Since the bottom and charm asymmetries are correlated in the fit to the lepton and slow pion tagged events, both the fitted bottom and charm asymmetries are expected to change in the constrained fit; but the error on the charm asymmetry is essentially unchanged.

The results for $A_{\mathrm{FB}}^{\mathrm{b}}$ and $A_{\mathrm{FB}}^{\mathrm{c}}$ are listed in table 3.9. In figure 3.14, they are compared to the Standard Model expectations as a function of the centre-of-mass energy, and they are shown in figure 5.1 together with the values obtained in chapter 4 and in context with previous measurements at other centre-of-mass energies. Good agreement is observed between the measurements and the predictions from ZFITTER.

In all asymmetry measurements, R_{c} and R_{b} are fixed to the Standard Model values as predicted by ZFITTER. The dependence of the measured values on the assumed values of R_{b} and R_{c} is parametrised as

$$\begin{aligned} \Delta A_{\mathrm{FB}}^{\mathrm{b}} &= a^{\mathrm{b}}(R_{\mathrm{b}})\,\frac{\Delta R_{\mathrm{b}}}{R_{\mathrm{b}}^{\mathrm{SM}}} + a^{\mathrm{b}}(R_{\mathrm{c}})\,\frac{\Delta R_{\mathrm{c}}}{R_{\mathrm{c}}^{\mathrm{SM}}} \\ \Delta A_{\mathrm{FB}}^{\mathrm{c}} &= a^{\mathrm{c}}(R_{\mathrm{b}})\,\frac{\Delta R_{\mathrm{b}}}{R_{\mathrm{b}}^{\mathrm{SM}}} + a^{\mathrm{c}}(R_{\mathrm{c}})\,\frac{\Delta R_{\mathrm{c}}}{R_{\mathrm{c}}^{\mathrm{SM}}}\ , \end{aligned} \tag{3.18}$$

where $\Delta R_{\mathrm{q}} = R_{\mathrm{q}} - R_{\mathrm{q}}^{\mathrm{SM}}$ for q=b, c. The Standard Model values for R_{b} and R_{c} are given in table 3.10 together with the values of the coefficients $a^{\mathrm{q}}(R_{\mathrm{q}'})$.

Any systematic error from a common source (see section 3.5 for the description of systematic uncertainties) is treated as fully correlated between the two measurements. However, there are large contributions to the systematic error that affect only one of the analyses, such that systematic errors are clearly no limitation to the combination of the two results.

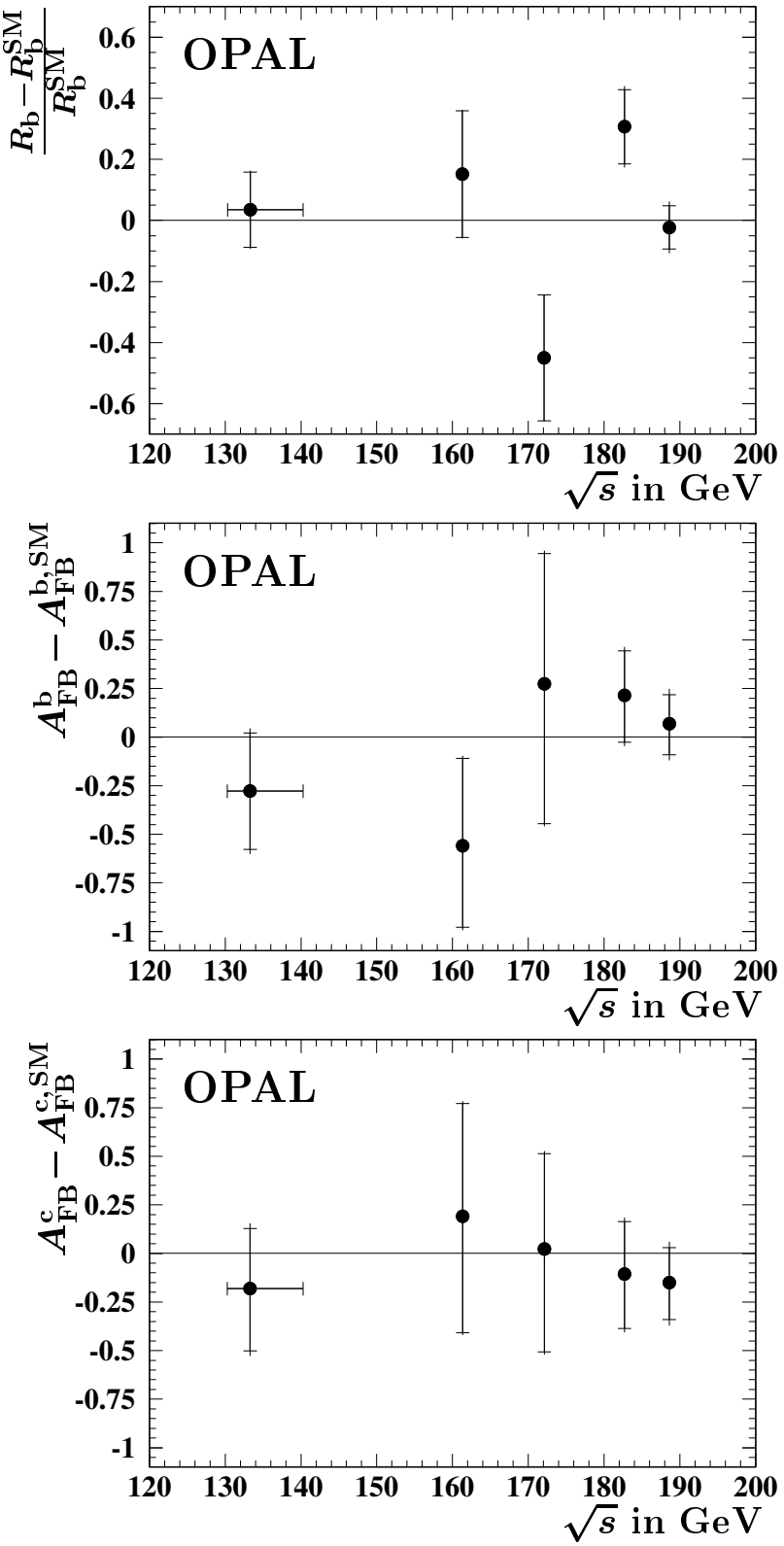

Figure 3.14: The R_b, A_{FB}^b, and A_{FB}^c measurements are compared to the Standard Model predictions. The relative deviations of the R_b measurements and the absolute deviations of the measured bottom and charm asymmetries from the Standard Model expectation are shown. The total measurement errors are given by the vertical error bars, with statistical components indicated by the small horizontal lines. The horizontal error bars show the range of centre-of-mass energies used in each measurement. The results of the measurements presented in this thesis are also shown in figure 5.1.

energy	measured asymmetries	correlation	predicted asymmetries
133 GeV	$A_{\rm FB}^{\rm b} = 0.19 \pm 0.30 \pm 0.12$ $A_{\rm FB}^{\rm c} = 0.50\ ^{+0.31}_{-0.32} \pm 0.13$	+20%	$A_{\rm FB}^{\rm b,\,SM} = 0.48$ $A_{\rm FB}^{\rm c,\,SM} = 0.69$
161 GeV	$A_{\rm FB}^{\rm b} = -0.03\ ^{+0.45}_{-0.42} \pm 0.11$ $A_{\rm FB}^{\rm c} = 0.87\ ^{+0.58}_{-0.60} \pm 0.12$	+23%	$A_{\rm FB}^{\rm b,\,SM} = 0.55$ $A_{\rm FB}^{\rm c,\,SM} = 0.69$
172 GeV	$A_{\rm FB}^{\rm b} = 0.82\ ^{+0.67}_{-0.72} \pm 0.14$ $A_{\rm FB}^{\rm c} = 0.69\ ^{+0.49}_{-0.53} \pm 0.12$	+27%	$A_{\rm FB}^{\rm b,\,SM} = 0.56$ $A_{\rm FB}^{\rm c,\,SM} = 0.67$
183 GeV	$A_{\rm FB}^{\rm b} = 0.77\ ^{+0.23}_{-0.24} \pm 0.10$ $A_{\rm FB}^{\rm c} = 0.55\ ^{+0.27}_{-0.28} \pm 0.11$	+34%	$A_{\rm FB}^{\rm b,\,SM} = 0.57$ $A_{\rm FB}^{\rm c,\,SM} = 0.67$
189 GeV	$A_{\rm FB}^{\rm b} = 0.63\ ^{+0.15}_{-0.16} \pm 0.10$ $A_{\rm FB}^{\rm c} = 0.50\ ^{+0.18}_{-0.19} \pm 0.11$	+29%	$A_{\rm FB}^{\rm b,\,SM} = 0.58$ $A_{\rm FB}^{\rm c,\,SM} = 0.66$

Table 3.9: The results of the combined $A_{\rm FB}^{\rm b}$ and $A_{\rm FB}^{\rm c}$ measurements together with the Standard Model predictions from ZFITTER. The first error is statistical, and the second systematic.

energy	$R_{\rm b}^{\rm SM}$	$R_{\rm c}^{\rm SM}$	$a^{\rm b}(R_{\rm b})$	$a^{\rm b}(R_{\rm c})$	$a^{\rm c}(R_{\rm b})$	$a^{\rm c}(R_{\rm c})$
133 GeV	0.184	0.223	−0.24	+0.12	+0.06	−0.28
161 GeV	0.171	0.244	−0.07	−0.06	+0.14	−0.86
172 GeV	0.168	0.249	−0.64	+2.48	+0.07	−0.11
183 GeV	0.165	0.253	−0.40	+0.21	+0.07	−0.36
189 GeV	0.164	0.255	−0.38	+0.23	+0.10	−0.30

Table 3.10: The Standard Model predictions for the partial hadronic decay widths $R_{\rm b}$ and $R_{\rm c}$ and the dependence of the results on their values are given. The coefficients apply to the combined measurements. The symbols are defined in the text.

3.5 Systematic Errors

In this section, the evaluation of the systematic errors for the analyses presented here is discussed. Both the secondary vertex and the lepton and slow pion tags depend crucially on the knowledge of the detector resolution for reconstructing charged particle tracks. Most of the other main systematic errors are independent for the two measurements.

3.5.1 Systematic Errors on R_b and A_{FB}^b with the Secondary Vertex Tag

In table 3.11, a breakdown of the systematic error is given for both the R_b and A_{FB}^b measurements with the vertex tag at 189 GeV centre-of-mass energy. The systematic errors considered for these measurements are described in the following paragraphs.

error source	ΔR_b	ΔA_{FB}^b
event selection	0.0038	0.037
b fragmentation	0.0003	0.004
b decay multiplicity	0.0027	0.018
b hadron composition	0.0017	0.011
b lifetime	<0.0001	<0.001
c fragmentation	<0.0001	0.001
c decay multiplicity	<0.0001	0.003
c hadron composition	0.0011	0.011
c lifetime	<0.0001	<0.001
four-fermion background	0.0009	<0.001
Monte Carlo statistics	0.0015	0.031
track reconstruction	0.0051	0.057
total systematic error	0.0074	0.078

Table 3.11: Systematic error breakdown for the R_b and the A_{FB}^b measurements with the vertex tag at $\sqrt{s} = 189$ GeV. Similar uncertainties have been determined for the other centre-of-mass energies.

3.5.1.1 Event Selection

The bias on the measurement of R_b from the selection of non-radiative events has already been discussed in section 3.3.2. A correction is applied, and an uncertainty of 100% is assigned to the correction. The uncertainty on the corrections for the interference between initial and final state radiation results in a systematic error of 0.5% on R_b. For the asymmetry measurements, the corresponding error is negligible. The contamination from radiative events has the effect of decreasing the measured asymmetry by 3%. The value is corrected accordingly, and a 3% systematic error is assigned. The asymmetry fit is based on the assumption that the shape of the tagging efficiency as a function of $|\cos\theta_T|$ is the same for all flavours, which might not be true at the edges of the acceptance. The effect is estimated by dividing the sample in bins of $|\cos\theta_T|$, over which the above assumption is valid, determing the asymmetry in each bin independently and comparing their average with the reference result. It is found to affect the asymmetry by less than 1%, and is thus neglected. It has been checked in the simulation that final state gluon radiation does not significantly affect the measured asymmetries at the current level of precision.

Final state QCD corrections are included in the calculation of the predictions with which the asymmetry measurements are compared. However, the experimental event selection is less efficient for events with hard gluon radiation due to the cuts on the decay length significance

(for the vertex tag) and the lepton or slow pion momentum (for the lepton and slow pion analysis). The fraction of the QCD correction that has to be applied to the measurements has been determined previously at LEP1 and is typically between 0.3 and 0.6 [55]. The overall QCD corrections at $\sqrt{s} = 189\,\mathrm{GeV}$ have been determined from ZFITTER to be 0.015 for $A_{\mathrm{FB}}^{\mathrm{b}}$ and 0.022 for $A_{\mathrm{FB}}^{\mathrm{c}}$, respectively. Half of this correction is assigned as a systematic error.

3.5.1.2 Bottom and Charm Physics Modelling

Uncertainties in bottom and charm fragmentation and decay properties may affect the efficiency and purity of the secondary vertex tag and can also influence the simulated charge identification probability. They are treated as follows:

- **b Fragmentation:** Although the mean scaled energy $2\langle E_{\mathrm{b}}\rangle/\sqrt{s}$ of weakly decaying b hadrons is expected to change from LEP1 to LEP2 energies, the Peterson fragmentation parameter ϵ_P^{b}, which describes one step in the fragmentation process, is assumed not to vary with energy. Simulated $\mathrm{b\bar{b}}$ events are reweighted within the range of $0.0030 < \epsilon_P^{\mathrm{b}} < 0.0048$, which corresponds to a variation of the mean scaled energy $2\langle E_{\mathrm{b}}\rangle/\sqrt{s}$ of weakly decaying b hadrons in Z decays in the range of $2\langle E_{\mathrm{b}}\rangle/\sqrt{s} = 0.702 \pm 0.008$ [45].
- **b Decay Multiplicity:** The charged decay multiplicity of hadrons containing a b quark is varied in the Monte Carlo simulation by ± 0.35, according to [45].
- **b Hadron Composition:** The tagging efficiency differs for the various b hadron species. The hadronisation fractions of b hadrons and their errors are taken from [2] to be

$$\begin{aligned} f(\overline{\mathrm{b}} \to \mathrm{B}^+) = f(\overline{\mathrm{b}} \to \mathrm{B}^0) &= \left(39.7^{+1.8}_{-2.2}\right)\%, \\ f(\overline{\mathrm{b}} \to \mathrm{B}_{\mathrm{s}}^0) &= \left(10.5^{+1.8}_{-1.7}\right)\%, \text{ and} \\ f(\mathrm{b} \to \Lambda_{\mathrm{b}}^0) &= \left(10.1^{+3.9}_{-3.1}\right)\%. \end{aligned}$$

  The fractions $f(\overline{\mathrm{b}} \to \mathrm{B}^0 \text{ or } \mathrm{B}^+)$ and $f(\overline{\mathrm{b}} \to \mathrm{B}_{\mathrm{s}}^0)$ are varied independently within their errors, and their variation is compensated by the b baryon fraction.
- **b Hadron Lifetimes:** The lifetimes of the different bottom hadrons are taken from [2] to be

$$\begin{aligned} \tau_{\mathrm{B}^+} &= (1.65 \pm 0.04)\ \mathrm{ps}, \\ \tau_{\mathrm{B}^0} &= (1.56 \pm 0.04)\ \mathrm{ps}, \\ \tau_{\mathrm{B}_{\mathrm{s}}^0} &= (1.54 \pm 0.07)\ \mathrm{ps}, \text{ and} \\ \tau_{\Lambda_{\mathrm{b}}^0} &= (1.24 \pm 0.08)\ \mathrm{ps}, \end{aligned}$$

  and are varied in the Monte Carlo simulation within their experimental errors.
- **c Fragmentation:** $\mathrm{c\bar{c}}$ Monte Carlo events are reweighted by varying the Peterson fragmentation parameter ϵ_P^{c} in the range of $0.025 < \epsilon_P^{\mathrm{c}} < 0.031$. This corresponds to a variation of the mean scaled energy $2\langle E_{\mathrm{c}}\rangle/\sqrt{s}$ of weakly decaying c hadrons in Z decays in the range of $2\langle E_{\mathrm{c}}\rangle/\sqrt{s} = 0.484 \pm 0.008$ [45].
- **c Decay Multiplicity:** The average charged track multiplicities $\langle n_c\rangle$ of D^+, D^0 and $\mathrm{D}_{\mathrm{s}}^+$ decays are varied in the Monte Carlo simulation within the ranges [56] of

$$\begin{aligned} \langle n_c\rangle(\mathrm{D}^0) &= 2.56 \pm 0.04 \pm 0.03, \\ \langle n_c\rangle(\mathrm{D}^+) &= 2.38 \pm 0.04 \pm 0.05, \text{ and} \\ \langle n_c\rangle(\mathrm{D}_{\mathrm{s}}^+) &= 2.69 \pm 0.31 \pm 0.11. \end{aligned}$$

- **c Hadron Composition:** With the constraint $f(\mathrm{c}\to\mathrm{D}^0)+f(\mathrm{c}\to\mathrm{D}^+)+f(\mathrm{c}\to\mathrm{D}_\mathrm{s}^+)+f(\mathrm{c}\to\mathrm{c_{baryon}})=1$, the following hadronisation fractions have been determined in [3]:

$$\begin{aligned} f(\mathrm{c}\to\mathrm{D}^+) &= 0.234\pm0.016, \\ f(\mathrm{c}\to\mathrm{D}_\mathrm{s}^+) &= 0.119\pm0.025, \text{ and} \\ f(\mathrm{c}\to\mathrm{c_{baryon}}) &= 0.085\pm0.022. \end{aligned}$$

  These fractions are varied independently by their errors and compensated by the D^0 fraction to evaluate the uncertainty on the charm efficiency.
- **c Hadron Lifetimes:** Charmed hadron lifetimes are taken from [2] to be

$$\begin{aligned} \tau_{\mathrm{D}^+} &= (1.057\pm0.015)\text{ ps}, \\ \tau_{\mathrm{D}^0} &= (0.415\pm0.004)\text{ ps}, \\ \tau_{\mathrm{D}_\mathrm{s}^+} &= (0.467\pm0.017)\text{ ps, and} \\ \tau_{\Lambda_\mathrm{c}^+} &= (0.206\pm0.012)\text{ ps}, \end{aligned}$$

  and are varied within their experimental errors.

3.5.1.3 Four-Fermion Background

Above the WW production threshold, the four-fermion background is largely dominated by W pairs. The uncertainty in the W pair production cross-section is taken into account and is found to have a negligible systematic effect. The background from W pairs has the highest probability to be accepted in the tagged sample when one or both W bosons decay into a final state containing a charm quark. The systematic error on the W pair tagging efficiency is estimated by varying the charm physics modelling parameters as described above. The effect of the detector resolution is also taken into account, as described in section 3.5.1.5.

3.5.1.4 Monte Carlo Statistics

Tagging efficiencies and charge identification probabilities are varied by the statistical error arising from the finite number of Monte Carlo simulated events.

3.5.1.5 Track Reconstruction

The effect of the detector resolution on the track parameters is estimated by degrading or improving the resolution of all tracks in the Monte Carlo simulation. This is done by applying a single multiplicative scale factor to the difference between the reconstructed and true track parameters. A $\pm10\%$ variation is applied independently to the $r\phi$ and rz track parameters. In addition, the matching efficiency for assigning measurement points in the silicon microvertex detector to the tracks is varied by 1% in $r\phi$ and 3% in rz. The systematic errors resulting from the individual variations are summed in quadrature.

3.5.2 Systematic Errors on $A_{\mathrm{FB}}^{\mathrm{b}}$ and $A_{\mathrm{FB}}^{\mathrm{c}}$ with the Lepton and Slow Pion Tag

Three different groups of systematic errors are considered: those from detector effects, those related to physics models and external inputs used in the analysis, and effects introduced by

the limited Monte Carlo statistics and the fitting procedure. A list of all systematic errors is given in table 3.12.

error source	$\Delta A_{\mathrm{FB}}^{\mathrm{b}}$	$\Delta A_{\mathrm{FB}}^{\mathrm{c}}$
track reconstruction	0.088	0.070
electron identification	0.007	0.006
muon identification	0.005	0.010
slow pion identification	0.004	0.007
input modelling	0.045	0.022
lifetimes	0.002	0.001
fragmentation modelling	0.024	0.033
semileptonic decay models	0.007	0.005
D^{*+} spin alignment	0.000	0.001
branching ratios and hadronisation fractions	0.008	0.006
$\mathrm{B}-\overline{\mathrm{B}}$ mixing	0.003	0.001
background asymmetries (4f, radiative events)	0.008	0.004
background asymmetries (lepton, slow pion backgrounds)	0.022	0.066
final state QCD corrections	0.008	0.011
Monte Carlo statistics	0.061	0.032
fitting procedure	0.009	0.003
total systematic error	0.122	0.111

Table 3.12: A breakdown of the systematic errors is given for the asymmetry measurement with leptons and slow pions at 189 GeV. Similar systematic errors have been obtained for the measurements at the other centre-of-mass energies above the Z resonance.

3.5.2.1 Detector Systematics

The lepton and slow pion identification relies on the proper modelling of the detector response in the Monte Carlo simulation.

- **Track Reconstruction:** The influence of the simulated detector resolution and matching efficiency for hits in the microvertex detector is estimated as described in section 3.5.1.5.
- **Lepton Identification:** The fractions of misidentified electrons and muons are taken from Monte Carlo simulation. The modelling of the input variables to the artificial neural network for electron identification is studied on Z calibration data in a manner similar to that described in [30]. Differences between the data and the modelling in the Monte Carlo simulation are determined using a pure sample of electrons from photon conversions and an inclusive sample of tracks depleted in conversion electrons. The dependence of the efficiency and background contamination of the selected electron sample on these differences is studied, and the resulting uncertainties for each input are added in quadrature. In addition, it is shown that there is no large dependence of the resulting systematic error on the position of the $\mathcal{N}_{\mathrm{el}}$ cut. The systematic error is evaluated separately for each year of data taking at energies above the Z resonance; the uncertainty on the efficiency is around 10%, and that on the background contamination around 20%.

The performance of the muon tagging network is studied on $\gamma\gamma \to \mu^+\mu^-$ events recorded at LEP energies above the Z resonance and on an inclusive sample of tracks from the Z calibration data that fail the "best match" preselection criterion. The muon and background rates are compared between data and Monte Carlo simulation in bins of $\mathcal{N}_\mu$, and the simulation is reweighted to match the data distribution. Details concerning the determination of the reweighting factors can be found in appendix A. The reweighting factors in each bin are varied independently by their statistical errors, and the resulting variations of the measured asymmetries are added in quadrature. For the inclusive muon sample selected with a cut at $\mathcal{N}_\mu > 0.65$, the reweighting factors for muon signal and background are 0.95 ± 0.05 and 0.97 ± 0.04, respectively.

Conversion candidates are explicitly removed from the sample of events used in the fit. The conversion finding efficiency is tested in the data using an algorithm which does not need the $\mathcal{N}_{\rm el}$ outputs for the two tracks as input. The accuracy of this test is 18%, and the conversion rate is varied by this amount to calculate the systematic error. The rate of non-prompt muons from pion and kaon decays in flight has been studied previously in [51], and has been found to be modelled to within 9%.

- **Slow Pion Efficiency:** Because of the large backgrounds in the slow pion sample, it is crucial to check that the slow pion reconstruction is modelled correctly in the Monte Carlo simulation. The efficiency is studied by reconstructing slow pions in the Z calibration data using the same cuts as described in section 3.4.2.3, except for the upper momentum cut which is lowered to $p_{\pi_s}^{\rm max}(\sqrt{s} = m_{\rm Z}) = 4.17$ GeV. The slow pion content in this sample is measured using a fit to the p_t^2 spectrum. Functions which are found to describe the shape of the background distribution well in the simulation are fitted to the p_t^2 sideband from 0.03 to 0.10 GeV^2. The number of signal slow pion events is then determined by extrapolating the background estimate to $p_t^2 = 0$. In the Z calibration data, this fit has a relative statistical precision of 6%, but an additional systematic error of 23% is assigned to cover biases resulting from the extrapolation procedure and the particular choice of fit function. Additional details concerning these fits are given in appendix B.

  Combining this result with the OPAL measured yield of $\rm D^{*+}$ mesons in hadronic Z decays of $\bar{n}_{\rm Z\to D^{*+}X} = 0.1854 \pm 0.0041 \pm 0.0059 \pm 0.0069$ [53], the efficiency of the slow pion reconstruction in Z decays is measured to be (37.3 ± 9.0)%, where the relative errors of 6% and 23% have been added in quadrature. This is consistent with the value in the simulation of $(31.9 \pm 1.5(stat.))$%. The relative error on the slow pion efficiency of 24% is then assigned to the slow pion efficiencies at energies above the Z resonance, which are taken from the simulation. In order to determine the systematic error on the asymmetry measurements, the expected number of slow pions in each of the different subsamples is varied according to the error on the efficiency, and balanced by the expected number of background events so that the total number of tagged events is kept constant.

  No additional systematic error is assigned for the modelling of the shape of the slow pion signal p_t^2 distribution since the signal shape in Z decays is found to be well described in the simulation.

- **Modelling of Artificial Neural Network Inputs:** Each of the input distributions used in the flavour separation networks has been compared between data and Monte Carlo simulation. The simulated distributions are reweighted for each input variable in turn to agree with the corresponding data distributions, and the analysis is repeated with

the weighted events. The observed differences from the original fit result are added in quadrature to yield the systematic uncertainty due to the modelling of the input variables.

3.5.2.2 Physics Systematics

The fragmentation of charm and bottom quarks and the momentum spectra of leptons emitted in their semileptonic decay are described using phenomenological models tuned to experimental data. The momentum spectrum of slow pions depends on the spin alignment of D^{*+} mesons. Systematic errors introduced by models of heavy hadron semileptonic decays, by the use of externally measured inputs, and from the assumed asymmetries of background candidates are assessed as follows:

- **Lifetimes:** The lifetimes of weakly decaying bottom and charm hadrons are varied as described in section 3.5.1.2. The resulting changes in measured asymmetries are negligible.
- **Fragmentation:** Bottom and charm fragmentation uncertainties are estimated as described in section 3.5.1.2.
- **Semileptonic Decay Models:** Systematic effects due to the modelling of heavy hadron semileptonic decays are studied following the recommendations in [45]. In the simulation, these decays are modelled according to the model of Altarelli et al. (ACCMM) [57] which has two free parameters: the Fermi momentum p_{f} and the mass of the charm (or strange) quark produced in the semileptonic decay of the bottom (or charm) quark. For bottom hadron decays, values of $p_{\mathrm{f}} = 298$ MeV and $m_{\mathrm{c}} = 1.673$ GeV are used, which have been obtained from a fit to CLEO data [58]. For charm hadron decays, the combined measurements of DELCO [59] and MARK III [60] have been used to derive values of $p_{\mathrm{f}} = 467$ MeV and $m_{\mathrm{s}} = 1$ MeV.

  The systematic uncertainties are determined according to the procedure from [45]. The lepton momentum spectra in the Monte Carlo simulation are reweighted as follows:

  – For $\mathrm{b} \to \ell$ decays, the model of Isgur et al. [61] (ISGW) provides an alternative parametrization of the lepton momentum in the rest frame of the decaying bottom hadron. However, this model has been found to describe CLEO data better when the fraction of bottom hadron decays to D^{**} mesons is set to 32% instead of 11% as calculated in [61], which yields a modified model (ISGW**). To determine the systematic error, the lepton momentum spectrum in the simulation is reweighted in turn to agree with either of these two alternative models.

  – Uncertainties affecting the modelling of $\mathrm{c} \to \ell$ decays are estimated by using alternative versions of the ACCMM model based on different sets of values for the parameters m_{s} and p_{f}. The results with the lepton spectrum reweighted according to the parameter sets

  $$\begin{aligned} m_{\mathrm{s}} = &\quad 1\,\mathrm{MeV} \quad \text{and} \quad p_{\mathrm{f}} = 353\,\mathrm{MeV} \quad \text{as well as} \\ m_{\mathrm{s}} = &\ 153\,\mathrm{MeV} \quad \text{and} \quad p_{\mathrm{f}} = 467\,\mathrm{MeV} \end{aligned}$$

  are compared with the default result to determine the systematic error.

  – For cascade decays $\mathrm{b} \to \mathrm{c} \to \ell$, the D momentum spectrum measured by CLEO [62] is combined with the $\mathrm{c} \to \ell$ model to generate the lepton momentum distribution. The uncertainty in the CLEO $\mathrm{b} \to \mathrm{D}$ momentum spectrum is negligible compared to the effect of varying m_{s} and p_{f}.

The systematic errors from the variations of the $b \to \ell$ and $c \to \ell$ spectra are added in quadrature to yield the uncertainty given in table 3.12.

- **D^{*+} Spin Alignment:** For $D^{*+} \to D^0\pi^+$ decays, the angular distribution of the decay products in the D^{*+} rest frame is proportional to $\sin^2\theta^*$ for helicity ± 1 D^{*+} states and to $\cos^2\theta^*$ for helicity 0 states. Here, θ^* is the emission angle of one of the decay products in the D^{*+} rest frame with respect to the D^{*+} momentum in the laboratory frame. The slow pion reconstruction efficiency depends on the slow pion momentum and transverse momentum, which in turn depend on the emission angle θ^*. Thus, the efficiency may be sensitive to the fraction of D^{*+} mesons that are produced in the helicity 0 state, which is given by the helicity density matrix element ρ_{00}.

  The Monte Carlo simulation is reweighted to the measured values of ρ_{00} for D^{*+} mesons produced in $b\overline{b}$ and $c\overline{c}$ events [25] of

$$\begin{aligned} \rho_{00}(b \to [c,\overline{c}] \to D^{*\pm}) &= 0.34\,^{+\,0.02}_{-\,0.03} \text{ and} \\ \rho_{00}(c \to D^{*+}) &= 0.40 \pm 0.02\,. \end{aligned}$$

  The uncertainty from a variation of the reweighting within the above errors is negligible.

- **Branching Ratios and Hadronisation Fractions:** In the simulation, the central values from the following measurements of semileptonic branching ratios [45] and hadronisation fractions [53] are used:

$$\begin{aligned} Br(b \to \ell) &= 0.1087 \pm 0.0024 \\ Br(b \to c \to \ell) &= 0.0791 \pm 0.0039 \\ Br(b \to \overline{c} \to \ell) &= 0.0162^{+0.0044}_{-0.0036} \\ Br(c \to \ell) &= 0.098 \pm 0.005 \\ f(b \to [c,\overline{c}] \to D^{*\pm}) &= 0.173 \pm 0.020 \\ f(c \to D^{*+}) &= 0.222 \pm 0.020 \end{aligned}$$

  To determine the associated systematic error on the asymmetry measurement, the simulation is reweighted according to a variation by the measurement error for each of these inputs, and the uncertainties are added in quadrature.

  In the absence of any measurements, the fraction $f(b \to \overline{c} \to D^{*-})/f(b \to [c,\overline{c}] \to D^{*\pm})$ is taken from the simulation and varied by 100% in order to assess the systematic error.

- **$B-\overline{B}$ Mixing:** The $B-\overline{B}$ mixing parameter is taken as an external input. The value of $\overline{\chi} = 0.118 \pm 0.006$ [2] is used, and the variation within its error yields the systematic uncertainty listed in table 3.12.

- **Background Asymmetries:** Prompt leptons and slow pions from four-fermion background in the selected event sample can affect the measured asymmetries. They may lead to a rather large observed forward-backward asymmetry, but their contribution to the overall sample is small. The asymmetry from these events is varied within ± 0.5 to determine the systematic error. The error due to the uncertainties on the bottom and charm asymmetries in radiative events is negligible.

  The asymmetry in the y distribution of mis-identified lepton and slow pion candidates is assumed to be zero for any event type. For lepton candidates, this assumption is verified within an accuracy of 2% on an inclusive sample of tracks that pass the lepton momentum

cuts and do not pass the cut on $\mathcal{P}_{\rm sig}$. For slow pions, a sample of tracks that pass the cuts on the slow pion momentum and transverse momentum, but do not pass the cut on $\mathcal{P}_{\rm sig}$, is used. The asymmetry of slow pion background is found to be zero with an error of 4%. The asymmetries from lepton and slow pion backgrounds are then varied within these limits to assess the associated systematic errors.

- **Final State QCD Corrections:** As described in Section 3.5.1.1, half the QCD correction to $A_{\rm FB}^{\rm b}$ and $A_{\rm FB}^{\rm c}$ as computed using ZFITTER is assigned as systematic error.

3.5.2.3 Monte Carlo Statistics

An error arises from the limited statistics in the Monte Carlo simulation that is used to predict the fractions f_i for each subsample (see section 3.4.4). This uncertainty is evaluated by varying for each subsample in turn the contribution from each source by its statistical error, redoing the fit, and adding all observed differences in quadrature.

3.5.2.4 Checks of the Fitting Method

Consistent results are observed when the fit is repeated with the numbers of bins in $\mathcal{N}_{\rm b}$, $\mathcal{N}_{\rm bc}$, $\mathcal{N}_{\rm c}$, and $|y|$ varied independently between 2 and 4. In addition, all selection cuts are varied, with no significant deviations in the results. Consistent results are found when the slow pion tagged events are not used in the fit. In the 189 GeV data sample, the statistical error of the charm asymmetry increases from 0.18 to 0.21 without the information from slow pion tagged events, while the error on the bottom asymmetry stays the same.

In principle, likelihood fits can be biased if low statistics data samples are fitted [63]. In order to test the fitting procedure and to determine the extent of such biases, if existent, a Monte Carlo technique is used. Given the integrated luminosity and the expected efficiencies and sample compositions as determined from the Monte Carlo simulation of the OPAL detector, a large number of toy-Monte Carlo experiments is generated. In each of these toy-experiments, the numbers of candidates and their distributions are varied by the appropriate statistical errors. Thus, a large set of possible toy-data samples is generated, which are then subjected to the same fitting procedure as the real data. The errors determined in the fit are then compared with the deviations from the generated asymmetry values on a statistical basis.

Toy-Monte Carlo simulations are performed for data sample sizes corresponding to each of the datasets given in table 3.2 in order to account for the different data sample sizes. First, a reference study is performed in which the bottom and charm asymmetries are set to their Standard Model values. For these studies, the distributions of the normalized deviations $\delta_{A_{\rm FB}} = (A_{\rm FB}^{\rm rec} - A_{\rm FB}^{\rm gen})/\sigma_{A_{\rm FB}^{\rm rec}}$ are shown in figure 3.15 for the simulations for the data sample sizes recorded at 172 GeV, 183 GeV, and 189 GeV (corresponding to a small, medium size, and large data sample). A Gaussian distribution of width one centered at zero corresponds to an unbiased fit. In order to identify and quantify biases, the distributions are fitted with a single Gaussian, which provides an adequate description for the purposes of this study. It is found that for the low statistics samples, the statistical errors are underestimated by a factor $\mathcal{S}$ of up to 1.2, and there is a bias of the fitted asymmetries towards zero at the 0.1σ level, where σ denotes the corrected statistical error according to the factor $\mathcal{S}$. The bottom asymmetry is more prone to biases than the charm asymmetry. These biases disappear for larger data samples, as expected [63].

The fit biases are given for each data sample in table 3.13 and are also plotted in figure 3.16. The results of the asymmetry measurements are corrected and the statistical errors adjusted according to the values given in table 3.13.

E_{CM}	$\int \mathcal{L}\mathrm{d}t$	$A_{\mathrm{FB}}^{\mathrm{b}}$		$A_{\mathrm{FB}}^{\mathrm{c}}$	
		$\mathcal{S}$	$\langle\delta_{A_{\mathrm{FB}}}\rangle$	$\mathcal{S}$	$\langle\delta_{A_{\mathrm{FB}}}\rangle$
133 GeV	10 pb^{-1}	1.065 ± 0.017	-0.057 ± 0.022	1.029 ± 0.016	-0.029 ± 0.022
161 GeV	10 pb^{-1}	1.133 ± 0.018	-0.104 ± 0.022	1.035 ± 0.016	-0.062 ± 0.022
172 GeV	10 pb^{-1}	1.158 ± 0.018	-0.119 ± 0.022	1.047 ± 0.017	-0.011 ± 0.022
183 GeV	56 pb^{-1}	1.048 ± 0.017	-0.022 ± 0.022	0.993 ± 0.016	$+0.001 \pm 0.022$
189 GeV	177 pb^{-1}	1.007 ± 0.016	-0.040 ± 0.022	0.992 ± 0.016	-0.014 ± 0.022

Table 3.13: The fit biases as determined for different sample sizes corresponding to the integrated luminosities at the different centre-of-mass energies. The Gaussian width yields the scale factor $\mathcal{S}$ for the statistical error as determined in the asymmetry fit, while the position of the mean $\langle\delta_{A_{\mathrm{FB}}}\rangle$ is indicative of the fit bias. The errors given in the table are the statistical errors from the toy-Monte Carlo simulation.

In additional toy-Monte Carlo studies, the bottom and charm asymmetries are then set to values above and below the corresponding Standard Model expectation to test the dependence of the bias on the assumed value. These studies are performed for the different data sample sizes. In all cases, the dependence is found to be small enough to be neglected in comparison to the statistical error of the asymmetry measurement itself. As an example, the results of these studies for the 189 GeV data sample are shown in figure 3.17.

3.6 Results

Using data collected at centre-of-mass energies between 130 GeV and 189 GeV with the OPAL detector at LEP, the relative $\mathrm{e^+e^-} \to \mathrm{b\overline{b}}$ production rate and the forward-backward asymmetries in $\mathrm{e^+e^-} \to \mathrm{b\overline{b}}$ and $\mathrm{e^+e^-} \to \mathrm{c\overline{c}}$ production have been measured to be

energy	R_{b}	$A_{\mathrm{FB}}^{\mathrm{b}}$	$A_{\mathrm{FB}}^{\mathrm{c}}$
133 GeV	$0.190 \pm 0.023 \pm 0.007$	$0.19 \pm 0.30 \pm 0.12$	$0.50\ ^{+0.31}_{-0.32} \pm 0.13$
161 GeV	$0.195 \pm 0.035 \pm 0.007$	$-0.03\ ^{+0.45}_{-0.42} \pm 0.11$	$0.87\ ^{+0.58}_{-0.60} \pm 0.12$
172 GeV	$0.091 \pm 0.034 \pm 0.005$	$0.82\ ^{+0.67}_{-0.72} \pm 0.14$	$0.69\ ^{+0.49}_{-0.53} \pm 0.12$
183 GeV	$0.213 \pm 0.020 \pm 0.009$	$0.77\ ^{+0.23}_{-0.24} \pm 0.10$	$0.55\ ^{+0.27}_{-0.28} \pm 0.11$
189 GeV	$0.158 \pm 0.012 \pm 0.007$	$0.63\ ^{+0.15}_{-0.16} \pm 0.10$	$0.50\ ^{+0.18}_{-0.19} \pm 0.11$

where in each case, the first error is statistical and the second systematic. These values are illustrated in figure 5.1 together with the dependences on the centre-of-mass energy as predicted in the Standard Model. For all measurements, good agreement is observed with the Standard Model expectation.

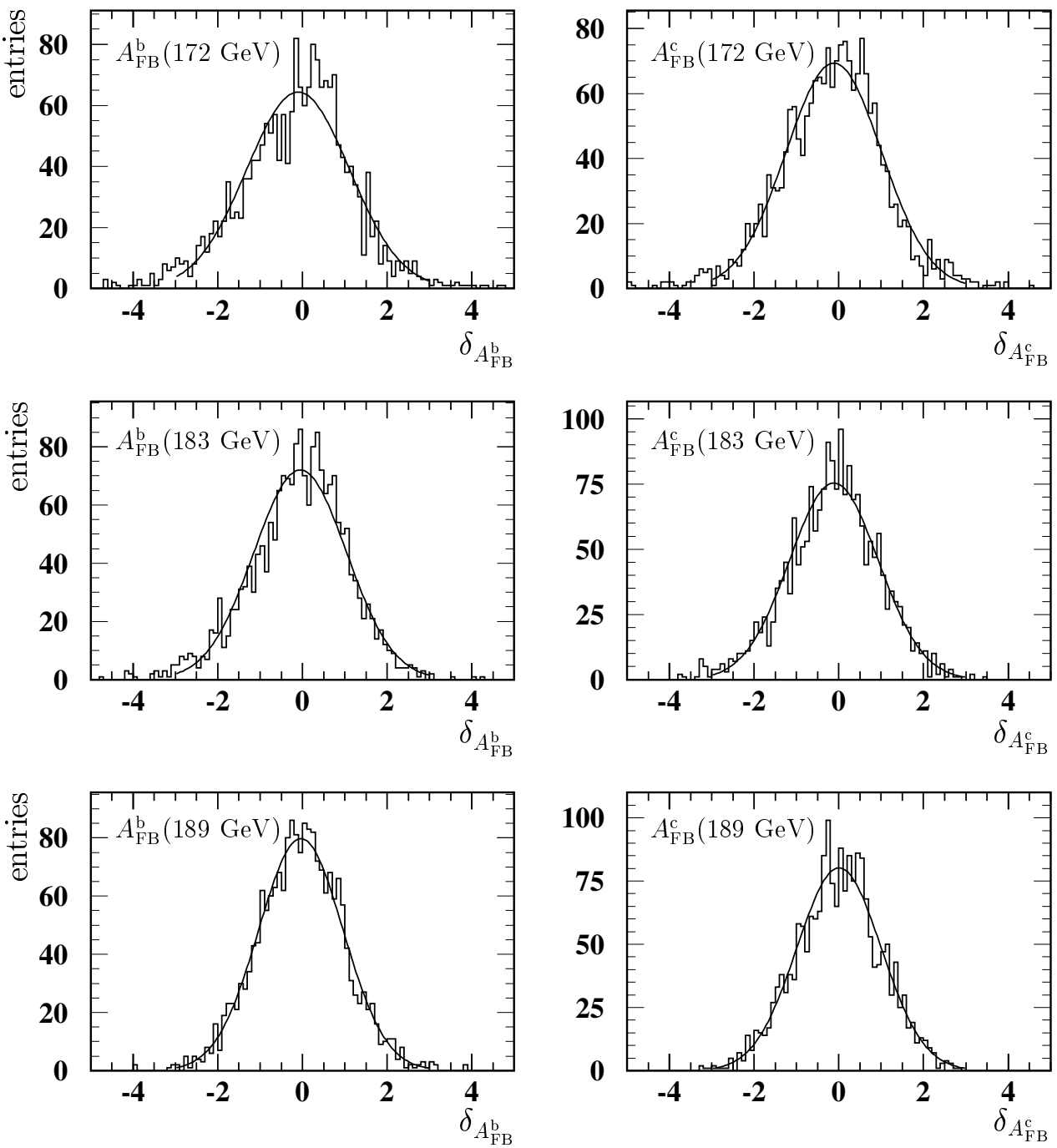

Figure 3.15: The distributions of the normalized differences δ as found in the toy-Monte Carlo simulation for the data samples recorded at 172 GeV, 183 GeV, and 189 GeV.

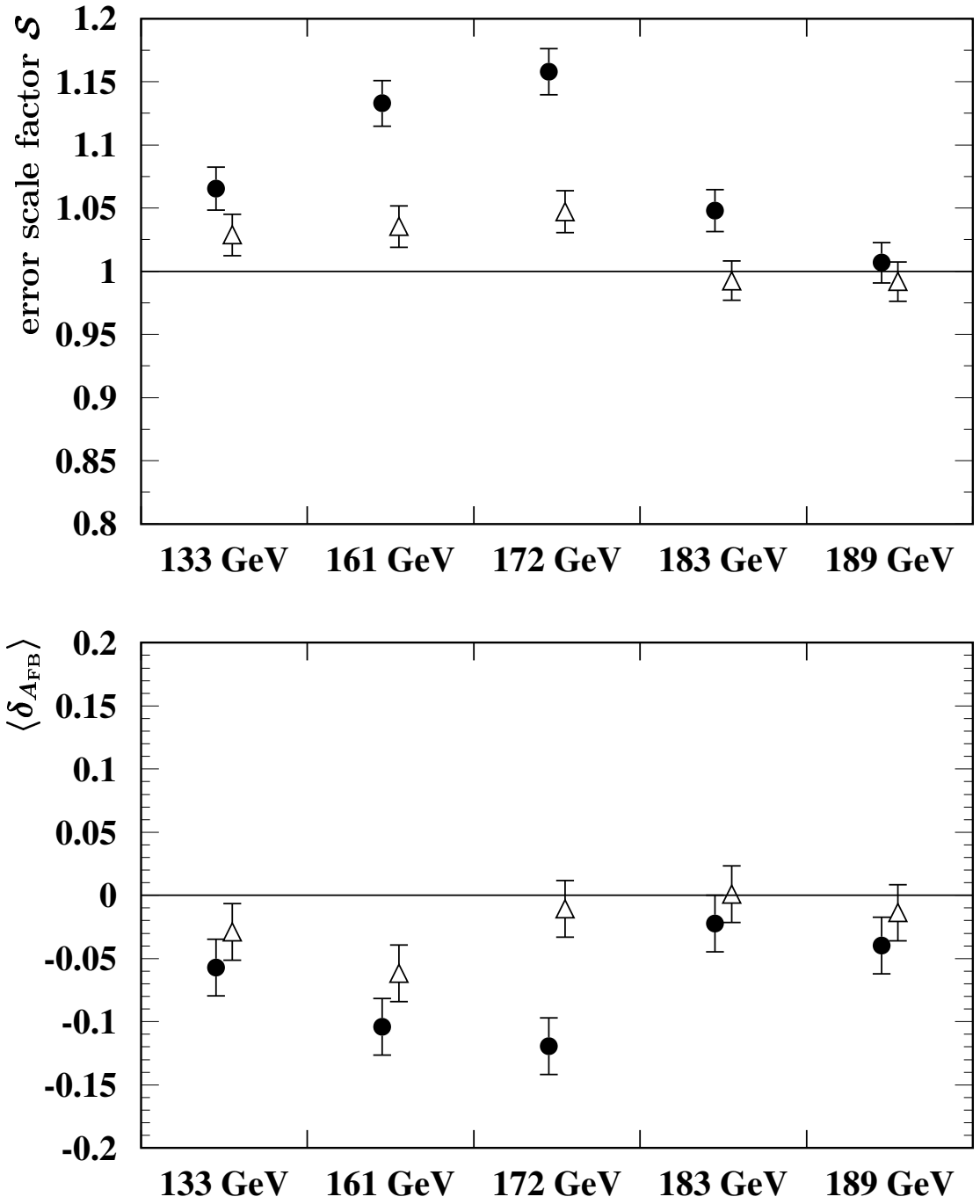

Figure 3.16: In the top plot, the scale factors $\mathcal{S}$ for the statistical error on the asymmetries are shown as determined in the toy-Monte Carlo simulation for the different data samples. The scale factors for the error on the bottom asymmetry are denoted by the black dots, while the open triangles correspond to those for the error on the charm asymmetry. The error bars indicate the statistical error from the toy-Monte Carlo simulation. The fit biases $\langle \delta_{A_{\mathrm{FB}}} \rangle = \langle (A_{\mathrm{FB}}^{\mathrm{rec}} - A_{\mathrm{FB}}^{\mathrm{gen}}) / \sigma_{A_{\mathrm{FB}}^{\mathrm{rec}}} \rangle$, normalized to the corrected statistical error, are shown in the bottom plot.

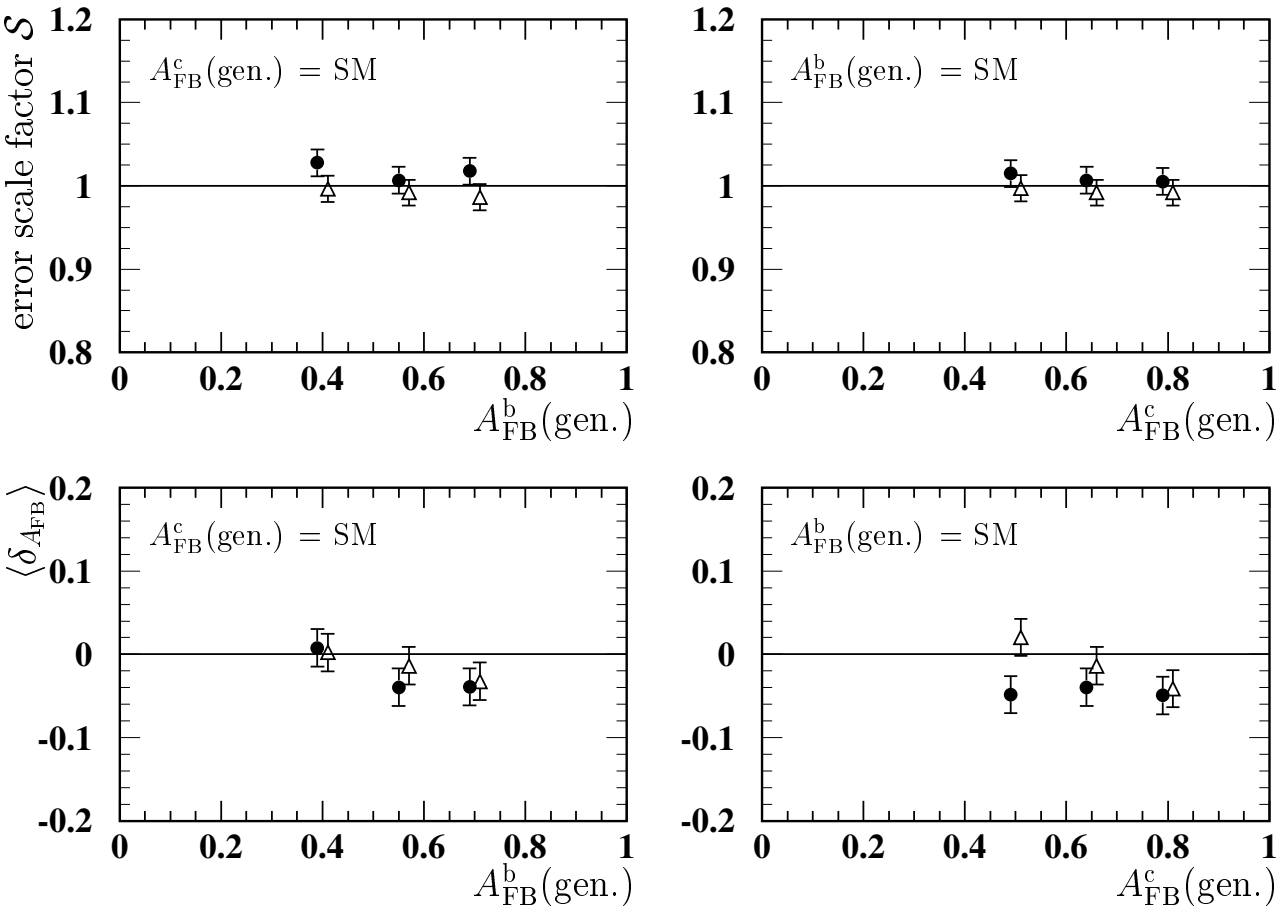

Figure 3.17: The error scale factors $\mathcal{S}$ (upper plots) and fit biases $\langle\delta_{A_{FB}}\rangle$ (lower plots) as determined for the 189 GeV data sample for different generated asymmetry values. For the left plots, the bottom asymmetry has been varied while fixing the charm asymmetry at its Standard Model value, and vice versa for the right plots. As before, the black dots indicate the results for the bottom asymmetry, while the open triangles denote the values for the charm asymmetry. A slight displacement has been introduced in the plots so that both dots and triangles are visible. Similar studies were performed for the other datasets, and no significant dependence on the generated asymmetries has been found.

Chapter 4

Heavy Quark Production below the Z Resonance

In this section, a measurement of the bottom and charm asymmetries at effective centre-of-mass energies between the TRISTAN ($\sim$ 60 GeV) and LEP1 ($\sim$ 91 GeV) energies is presented. A particular feature of this analysis is the identification of radiative events among non-radiative Z decays. In contrast to the situation at LEP2, no clear separation between radiative and non-radiative events exists, and care must be taken to minimise the non-radiative background. The event selection is described in section 4.3. The asymmetry measurement is similar to that presented in the previous sections, although it is performed in the effective $q\bar{q}$ centre-of-mass frame after initial state radiation. It is described in section 4.4. The measurement technique has been tested with radiative events recorded at centre-of-mass energies above the Z resonance. This check is presented in section 4.5. Section 4.6 summarizes the systematic uncertainties.

4.1 Region of Interest

The effective centre-of-mass energy $\sqrt{s'}$ after initial state photon radiation can have values between 0 and $\sqrt{s}$; the predicted spectrum for $\sqrt{s} = m_Z$ is shown in figure 4.1. The following two considerations limit the $\sqrt{s'}$ range of interest for the measurement presented here:

1. At TRISTAN, the bottom and charm asymmetries have already been measured at e^+e^- centre-of-mass energies of around 60 GeV. The precision of the combined TRISTAN measurements is approximately 0.07 for both A_{FB}^b and A_{FB}^c, see table 5.1. On the other hand, the cross-section for radiative events at LEP falls rapidly with $\sqrt{s'}$, as can be seen from figure 4.1. With the given statistics, OPAL could reach an accuracy of $\sigma(A_{FB}^b) \sim 0.8$ and $\sigma(A_{FB}^c) \sim 0.4$ in a window of $50\,\text{GeV} < \sqrt{s'} < 70\,\text{GeV}$. Thus, even for all four LEP experiments taken together, it is not worthwhile to compete with the existing TRISTAN measurements at $\sqrt{s'} \sim 60\,\text{GeV}$. Similarly, the existing measurements at PEP and PETRA are more accurate than the expected precision at LEP for the corresponding effective centre-of-mass energies.
2. For the selection of radiative events with $\sqrt{s'} \geq 60\,\text{GeV}$, non-radiative events with mismeasured effective centre-of-mass energy are the main background, since two-photon events are found predominantly at much lower effective centre-of-mass energies. The

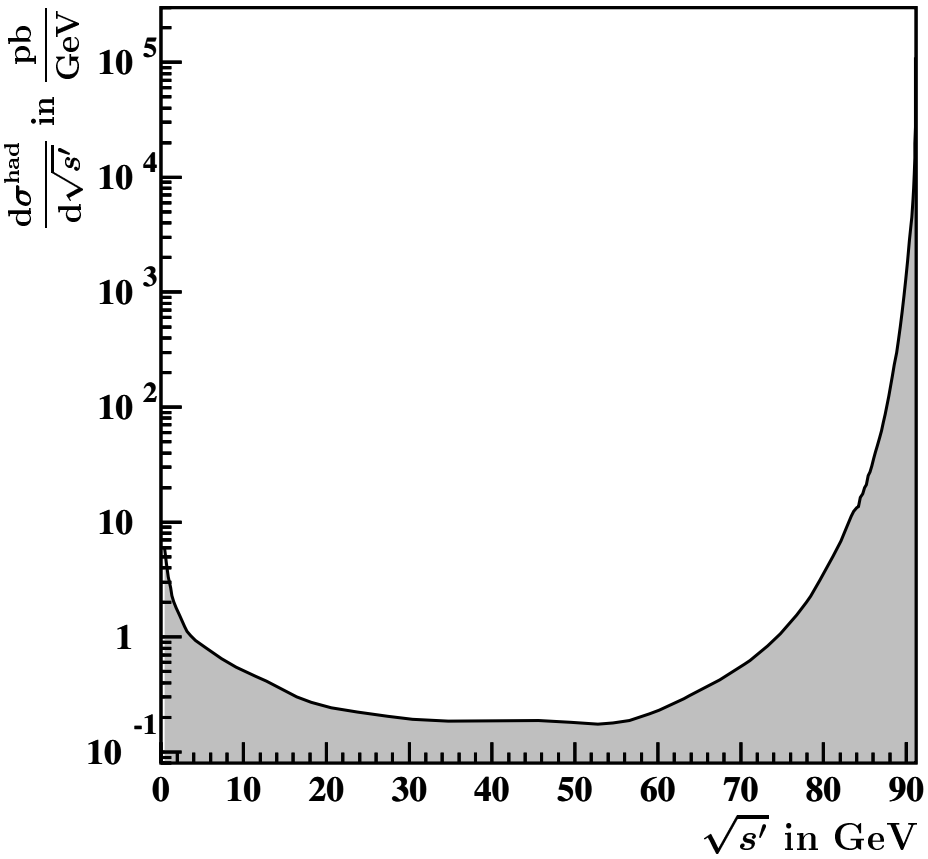

Figure 4.1: The ZFITTER prediction for the differential hadronic cross-section in e^+e^- collisions at $\sqrt{s} = m_Z$ as a function of the effective centre-of-mass energy. Because of numerical instabilities, the curve is only approximate in the region 20 GeV $< \sqrt{s'} <$ 50 GeV. The production of $q\bar{q}$ resonances at $\sqrt{s'}$ around 10 GeV and below is not taken into account.

non-radiative background puts an upper experimental limit on the effective centre-of-mass energies that can be used. Qualitatively, this can be understood as follows: In the vicinity of the Z resonance, the cross-section follows a Breit-Wigner curve. On the other hand, the momentum of a hard initial state photon (which is linearly related to the effective centre-of-mass energy close to the full energy $\sqrt{s}$) is measured with a Gaussian resolution. The Gaussian tail from mis-measured non-radiative events falls faster than the cross-section for $\sqrt{s'} < \sqrt{s}$. Thus, the background contamination is smaller for events at moderately low $\sqrt{s'}$ (where two-photon background is still small); or, conversely, it is impossible to select a pure sample of radiative events at effective centre-of-mass energies close to the full centre-of-mass energy.

Even though the cross-section for radiative hadronic events in the region 80 GeV $< \sqrt{s'} <$ 85 GeV is ~ 2.5 times larger than for 60 GeV $< \sqrt{s'} <$ 80 GeV, the expected accuracy of an asymmetry measurement is comparable because of the larger backgrounds for events that are closer to the Z resonance. However, a large "lever arm" with respect to the accurate LEP1 and SLD measurements at $\sqrt{s'} = \sqrt{s} \approx m_Z$ is necessary to place additional constraints on the effective quark couplings or S-Matrix parameters.

Given these considerations, events with effective centre-of-mass energies within 60 GeV $< \sqrt{s'} <$ 80 GeV are selected in the following measurement.

4.2 Simulation of Events

For the simulation of events with true effective centre-of-mass energy above 85 GeV, the standard LEP1 Monte Carlo samples are used. They have been generated using the JETSET 7.4 Monte Carlo model [43] with parameters tuned to reproduce the OPAL data [64]. The fragmentation of heavy quarks is parametrised by the fragmentation function of Peterson et al. [65] with the same fragmentation parameters ϵ_P as used for the LEP2 measurements. Events with true effective centre-of-mass energy below 85 GeV are excluded from these samples. For these events, the YFS3ff [66] Monte Carlo generator has been used to generate the $\mathrm{q\bar{q}}\gamma^{\mathrm{isr}}$ system. The fragmentation and hadronisation are simulated via JETSET as above. The YFS exponentiation scheme allows for an arbitrary number of photons to be radiated from both the incoming and the outgoing fermion lines (and thus corresponds to a sum up to an infinite order in α_{QED}). However, difficulties arise for the description of final state photon radiation, since the competition between photon and gluon radiation cannot be treated in the above setup. Thus, final state radiation is disabled in YFS3ff, and the JETSET implementation of both final state photon and gluon radiation is used.

The relative normalisation of the two Monte Carlo samples has been determined from the ZFITTER predictions for the cross-sections. In the asymmetry measurement described below, no distinction is made between events taken at $\sqrt{s} = m_{\mathrm{Z}}$ (denoted "peak" events in the following) and those taken during the LEP1 energy scans at centre-of- mass energies above and below the Z mass (called "peak+2" and "peak-2"). However, the relative probability for events within the selected $\sqrt{s'}$ range differs significantly for these samples, as shown in table 4.1. Radiative events are identified with a cut on the absolute value of the reconstructed effective

$\langle\sqrt{s}\rangle$	$\int \mathcal{L}\mathrm{d}t$	$\sigma(\mathrm{e^+e^-} \to \mathrm{q\bar{q}})$, 60 GeV $< \sqrt{s'} <$ 80 GeV	$\sigma(\mathrm{e^+e^-} \to \mathrm{q\bar{q}})$, $0 < \sqrt{s'} < \sqrt{s}$	signal isr fraction
89.44 GeV	19.3 pb^{-1}	20.3 pb	9990 pb	0.204%
91.21 GeV	109.5 pb^{-1}	17.0 pb	30500 pb	0.056%
92.91 GeV	20.2 pb^{-1}	15.1 pb	14800 pb	0.102%

Table 4.1: The data taken during LEP1 running is grouped in three sets according to the centre-of-mass energy. For each of these samples, the mean centre-of-mass energy and the integrated luminosity are given, and the radiative hadronic cross-section for events within the selected $\sqrt{s'}$ range is compared to the total hadronic cross-section. The values have been computed using ZFITTER. A number of 2560 hadronic events with 60 GeV $< \sqrt{s'} <$ 80 GeV is expected in the data.

centre-of-mass energy $\sqrt{s'}$. Thus, the probability for mis-identification of non-radiative events is expected to vary with $\sqrt{s}$, and individual Monte Carlo simulated samples of events are used for $\sqrt{s} \approx$ 89 GeV, 91 GeV, and 93 GeV. Their relative weights are determined according to

the corresponding integrated luminosities of the data. In contrast to the non-radiative events, radiative events are only simulated for $\sqrt{s} = m_{\mathrm{Z}}$ since the efficiency is not expected to change much for the different centre-of-mass energies; however, the relative abundance of radiative events as given in table 4.1 is taken into account. For both radiative and non-radiative events, separate samples of Monte Carlo simulated events are used for all relevant years of LEP1 data taking. These samples are weighted according to the corresponding integrated luminosities.

Two-photon events with low Q^2 have been generated with the PHOJET [67] generator, and passed through the JETSET simulation for fragmentation and hadronisation. The F2GEN program [68] is used for events with $Q^2 > 1\,\mathrm{GeV}^2$. Since the background from two-photon events is small and no large variations with $\sqrt{s}$ are expected, no distinction between different years of data-taking or centre-of-mass energies are made.

4.3 Identification of Events with Hard Initial State Radiation

Qualitatively, radiative events in the interesting region with effective centre-of-mass energies between around 60 GeV and 80 GeV have properties that lie between those of hadronic two-photon events and hadronic events from non-radiative $\mathrm{e^+e^-}$ collisions with the full centre-of-mass energy. This section gives details of the event selection as well as the calibration of the efficiency from LEP2 data.

4.3.1 Event Selection

The information from the silicon microvertex detector plays an important role for the flavour separation of the lepton or slow pion tagged events, where secondary vertex information is used (see section 3.4.3). Therefore, only events for which the microvertex detector was operational are used. In the following, the selection of radiative hadronic events is described. The distributions of the selection variables are shown in figure 4.2 for an inclusive sample of hadronic events.

- **Preselection of hadronic events:**
  Hadronic events are selected with the same criteria as described in section 3.2. However, since the momentum imbalance $R_{\mathrm{bal}} \equiv |\sum (E \cdot \cos\theta)_{\mathrm{clus}}| \,/\, \sum E_{\mathrm{clus}}$ is strongly correlated with the effective centre-of-mass energy, the cut $|R_{\mathrm{bal}}| < 0.75$ is not applied here. The reconstruction of the effective centre-of-mass energy is poor for events with large activity close to the beam pipe, and therefore, only events with a thrust axis satisfying $|\cos\theta_{\mathrm{thrust}}| < 0.98$ are retained.
- **Reconstruction of the effective centre-of-mass energy:**
  A kinematic fit is applied to these hadronic events, similar to that described in section 3.2. However, only one radiated photon in the initial state is allowed here[1]. Clusters in the electromagnetic calorimeter are not considered in the fit, because for the relevant effective centre-of-mass energies, the photon energy from initial state radiation is smaller than for "radiative return" events at LEP2, and the background from other photon sources is expected to be too large. Events with a fit probability P_{fit} of less than 5% are rejected.

[1] Events where two energetic photons in the initial state are required by the kinematic fit are rare [50]; events without initial state radiation yield an energy of the radiated photon close to 0.

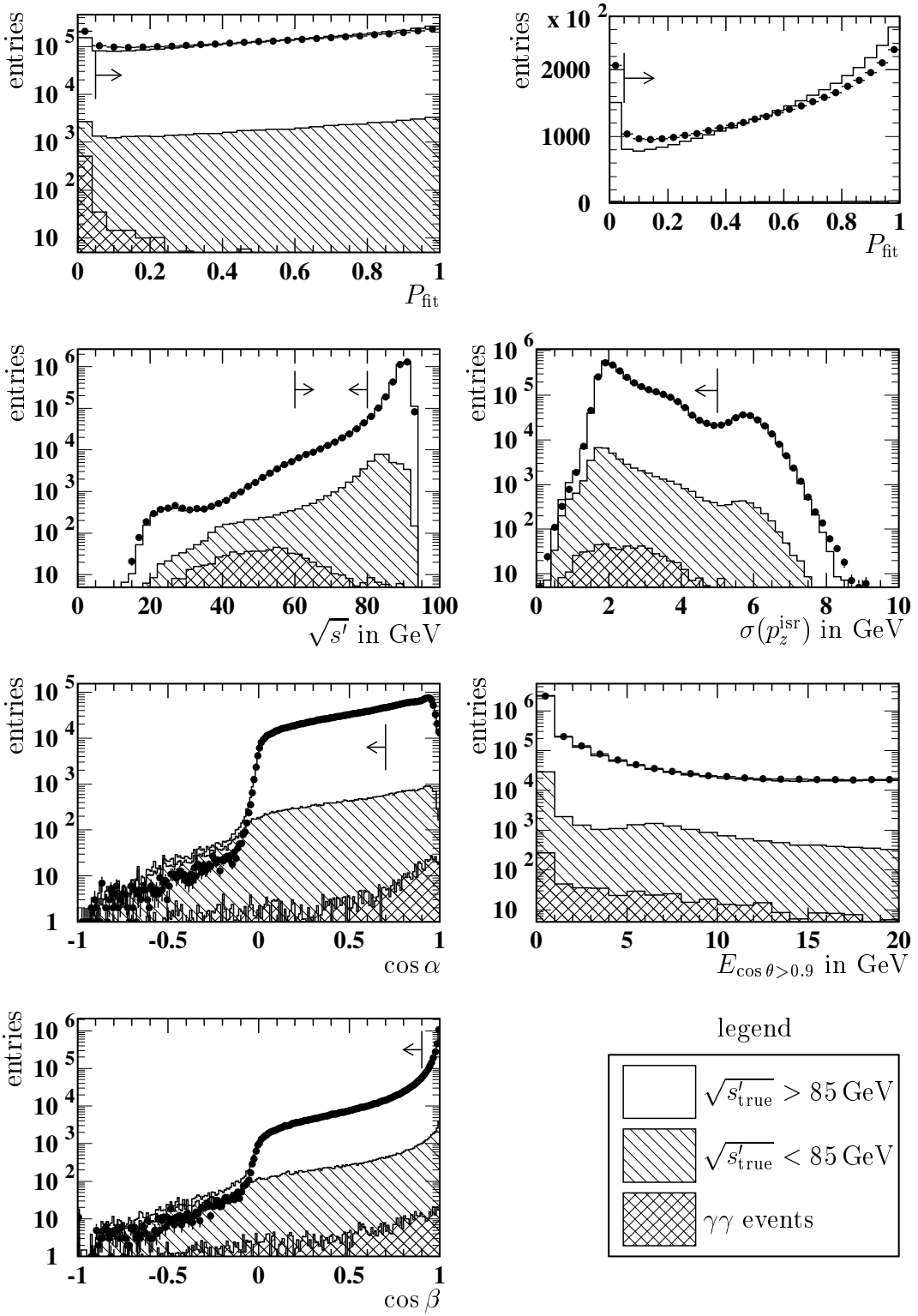

Figure 4.2: The variables used for the selection of radiative events at LEP1 are shown for an inclusive hadronic event sample. Points with error bars represent the data and the solid and hatched histograms the Monte Carlo expectation as explained in the legend. The arrows point into the accepted regions. The $P_{\rm fit}$ distribution is also shown on a linear scale to make the discrepancies between data and simulation visible. The symbol $E_{\cos\theta>0.9}$ denotes the energy measured within $\cos\theta > 0.9$, where θ is measured with respect to the fitted direction of the isr photon. The entries in the first bin correspond dominantly to $E_{\cos\theta>0.9} = 0$.

Events are selected if the fitted effective centre-of-mass energy lies in the range $60\,\mathrm{GeV} < \sqrt{s'} < 80\,\mathrm{GeV}$. For events at $\sqrt{s} = m_\mathrm{Z}$, this corresponds to a z component of the isr photon momentum of $10.5\ \mathrm{GeV} < |p_z^{\mathrm{isr}}| < 25.9\ \mathrm{GeV}$. In addition, the uncertainty on p_z^{isr} as determined in the fit is required to be less than 5 GeV.

- **Suppression of non-radiative background:**
  Non-radiative events may have a reconstructed missing momentum in z direction when particles escape in the beam pipe. These escaping particles tend to be misidentified as isr photons by the kinematic fit. However, a hadronic jet close to the fitted isr photon momentum is indicative of such cases. Thus, the cosine of the smallest angle between the fitted isr photon momentum and any jet in the event, $\cos\alpha$, is required to be smaller than 0.7. In addition, it is required that no energy deposits be found in the detector within a cone with half angle $\theta = 25.8^\circ$ (corresponding to $\cos\theta = 0.9$) around p_z^{isr}.

  Semileptonic decays of bottom and charm hadrons lead to missing energy due to the undetected neutrino. Since the neutrino is often emitted close to the jet axis, the angle β between the missing momentum and the closest jet is used to discriminate against non-radiative events with neutrinos. A value of $\cos\beta < 0.9$ is required.

The composition of the selected event sample as determined from the simulation is given in table 4.2 and is also shown in figure 4.3.

reconstructed $\sqrt{s'}$ in GeV	number of events	sample composition, $\sqrt{s'_{\mathrm{true}}}$ in GeV			
		$\gamma\gamma$	< 60	$60 - 80$	$80 - \sqrt{s}$
$60 - 80$	1284	1.5%	3.4%	62.9%	32.2%

Table 4.2: The composition of the selected radiative hadronic events as determined from the simulation. Events without a tagged lepton or slow pion are included in this table. The sample composition is slightly different for tagged events because of the variations of R_b and R_c with the centre-of-mass energy and missing transverse momentum from neutrinos in bottom and charm events. The resulting small effects are accounted for in the asymmetry measurement.

The selection of radiative events relies on the very forward regions of the detector, for which the modelling is in general less accurate than for the barrel region. Discrepancies between the data and the simulation affect mainly the distribution of probabilities P_{fit} for the kinematic fit and the variables $\cos\alpha$ and $\cos\beta$ for events with a very large momentum imbalance. Since the cross-section for initial state radiation is well known (for instance, the radiative cross-section at LEP2 is reproduced in the simulation) and the properties of $\mathrm{e^+e^-} \to \mathrm{q\bar{q}}$ events at centre-of-mass energies of $\sim 60\,\mathrm{GeV}$ and $\sim 91\,\mathrm{GeV}$ are well measured, the discrepancies in the modelling of the selection variables can be attributed to problems in the modelling of the detector response for events in the forward region of the detector.

4.3.2 Calibration of the Event Selection Efficiency

In order to be independent of uncertainties in the detector modelling, radiative events at LEP2 are used to calibrate the efficiency of the event selection. It is not assumed that the efficiencies

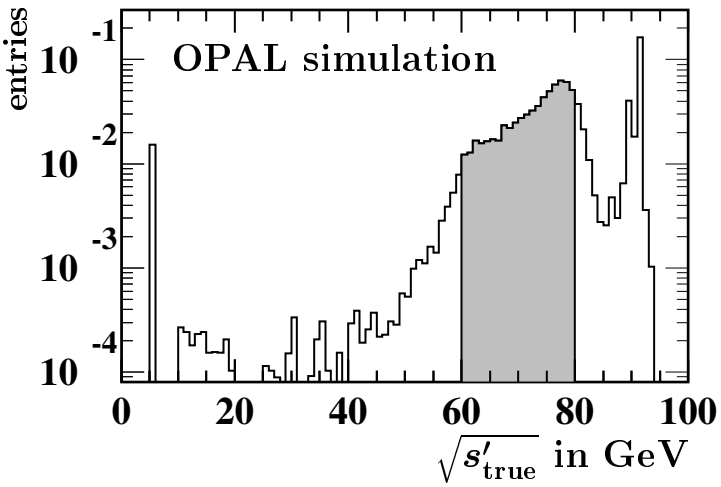

Figure 4.3: The distribution of true effective centre-of-mass energies is shown for the selected event sample in the simulation, normalized to one. The signal region for the fit is shown in grey. The contribution from two-photon events is shown as the first non-zero bin; the energy of 5 GeV is arbitrary. The structure at $\sqrt{s'} \approx m_{\mathrm{Z}}$ is due to the contributions from non-radiative background from the different LEP1 centre-of-mass energies.

for reconstructing radiative events are equal at LEP1 and LEP2; rather, correction factors $\mathcal{C}_\varepsilon$ for the efficiency are determined from LEP2 data as a function of $\sqrt{s'/s}$. The appropriate corrections are then applied to the event selection efficiency as determined from the LEP1 simulation.

For each of the five centre-of-mass energies above the Z resonance, the inclusive sample of hadronic events that satisfy $\sqrt{s'/s} < 80\,\mathrm{GeV}/m_{\mathrm{Z}}$ is considered. It has been checked that the angular distribution of initial state photons is similar at a given value of $\sqrt{s'/s}$ for simulated events at LEP1 and LEP2. For consistency, the effective centre-of-mass energy $\sqrt{s'}$ is reconstructed with the same technique as used for the selection of radiative events at LEP1, which differs slightly from that described in section 3.2. Events with $\sqrt{s'/s} < 80$ GeV$/m_{\mathrm{Z}}$ are selected. The selection of radiative events described in section 4.3.1 is then applied to this inclusive sample of radiative hadronic events. The fraction $f_{\mathrm{sel}}^{\mathrm{data}}$ of events that pass the additional event selection is computed and compared to the corresponding number $f_{\mathrm{sel}}^{\mathrm{MC}}$ in the simulation. Under the assumption that the inclusive sample is 100% pure in radiative hadronic events, the ratio $f_{\mathrm{sel}}^{\mathrm{data}}/f_{\mathrm{sel}}^{\mathrm{MC}}$ yields the desired correction factor $\mathcal{C}_\varepsilon$ for the event selection efficiency. The correction factor $\mathcal{C}_\varepsilon$ is shown in figure 4.4 as a function of $\sqrt{m_{\mathrm{Z}}^2/s}$.

A small uncertainty enters due to the fact that the selection of radiative events at LEP2 is not 100% pure. The contamination from non-radiative events with $\sqrt{s'_{\mathrm{true}}/s} > 80\,\mathrm{GeV}/m_{\mathrm{Z}}$ is typically around $1-2$% after the cut on the reconstructed $\sqrt{s'}$. A 100% systematic error is assigned to this component. After the additional event selection cuts, this contamination is reduced to $\mathcal{O}(10^{-3})$, which can be neglected for the purpose of this study.

This study does not cover exactly the range in $\sqrt{s'/s}$ that is used in the asymmetry analysis. Therefore, a linear function is fitted to the correction factor $\mathcal{C}_\varepsilon$ as a function of $\sqrt{s'/s}$, as shown in figure 4.4. The results from this fit are used to correct the efficiency of the radiative event

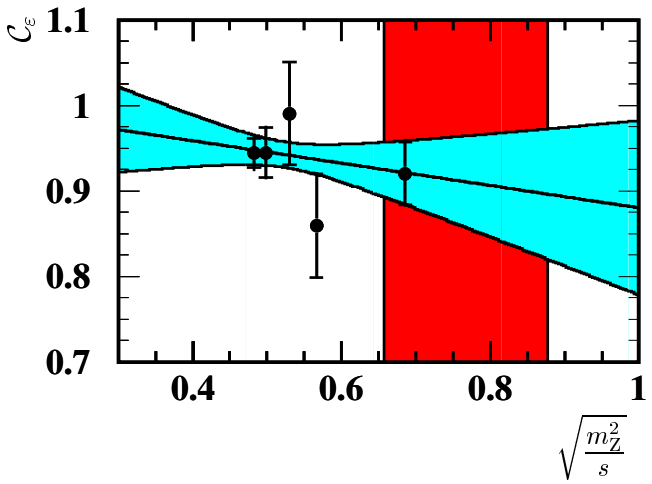

Figure 4.4: The points with error bars give the values for the efficiency correction factor $\mathcal{C}_\varepsilon$ as determined from the five radiative hadronic event samples at LEP2. The light grey band shows the allowed region within one standard deviation as a function of $\sqrt{m_Z^2/s}$, which was determined from a straight line fit to the data points. The dark grey band indicates the signal region for the measurement with isr events at LEP1.

selection at LEP1. The expected number of selected radiative events is then

$$N_{\rm sel}^{\rm rad} = \mathcal{C}_\varepsilon^{\rm rad}\, \varepsilon\, N^{\rm rad} \quad \text{with} \quad \mathcal{C}_\varepsilon^{\rm rad} = 0.905 \pm 0.062\,, \tag{4.1}$$

where the total number $N^{\rm rad}$ of true radiative events in the data is taken from the ZFITTER prediction. The correction factor has been determined for an energy of 73.5 GeV, which corresponds to the mean effective centre-of-mass energy of selected events within $60\,{\rm GeV} < \sqrt{s'} < 80\,{\rm GeV}$. Similarly, the expected number of selected events from two-photon processes, $N_{\rm sel}^{\gamma\gamma}$, is adjusted according to the mean reconstructed effective centre-of-mass energy of these events. The background from non-radiative events is then

$$N_{\rm sel}^{\rm non-rad} = N_{\rm sel}^{\rm total} - N_{\rm sel}^{\rm rad} - N_{\rm sel}^{\gamma\gamma}\,. \tag{4.2}$$

The correction factors are varied simultaneously within the errors from the fit as shown in figure 4.4 to assess the associated systematic error on the measured asymmetries.

4.4 Asymmetry Analysis

In each selected event, tracks and clusters are boosted into the effective centre-of-mass frame, assuming one radiated photon in the initial state with momentum $\vec{p}^{\,\rm isr} = (0, 0, p_z^{\rm isr})$. The thrust axis $\vec{T}^*$ is then computed from the boosted tracks and clusters. This axis is a good approximation to the flight axis of the initial quark-antiquark pair in the boosted frame, as can be seen from figure 4.5. The asymmetry measurement uses the quantity $y^* = -q\cos\theta_T^*$ in a manner analogous to $y = -q\cos\theta_T$ in section 3.4.4.

The lepton and slow pion selection proceeds as described in section 3.4.2. The selection criteria are the same, with the following two exceptions:

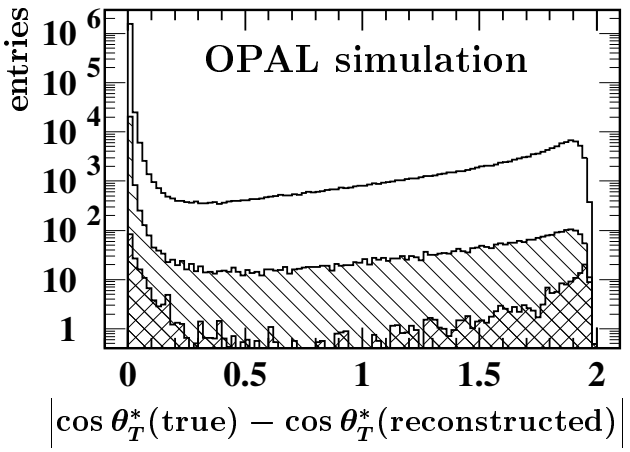

Figure 4.5: The resolution in $\cos\theta_T^*$ is shown for simulated events at OPAL. For the quantity $\cos\theta_T^*$(true), the correct $\mathrm{q\bar{q}}$ rest frame has been taken to compute the thrust axis. The open histogram indicates non-radiative events, the hatched area corresponds to the contribution from those events with $\sqrt{s'} < 85$ GeV, and the cross-hatched histogram shows the distribution for two-photon events. The rise of the distributions towards values of 2 is due to events where the thrust axis flips when the reconstructed $\mathrm{q\bar{q}}$ rest frame is used instead of the true one.

- Electron candidates are only accepted within $|\cos\theta| < 0.8$ because of modelling problems in the endcaps of the detector for the LEP1 simulation.
- The upper momentum cut in the slow pion selection is adjusted according to the expected energy of the heavy quark in the laboratory frame before hadronisation: The $\mathrm{q\bar{q}}\gamma^{\mathrm{isr}}$ system after initial state radiation is treated as a three-body system of massless particles. The momentum $(0, 0, p_z^{\mathrm{isr}})$ of the photon is taken from the kinematic fit, and the angles θ_{q}^* and $\theta_{\overline{\mathrm{q}}}^*$ of the two quarks in their rest frame are approximated by the boosted thrust axis. Given the total energy of the $\mathrm{e^+e^-}$ collision, one can then compute the energy $E_{\mathrm{q}}^{\mathrm{LAB}}$ of the parent quark of a given slow pion candidate in the laboratory frame as

$$E_{\mathrm{q}}^{\mathrm{LAB}} = \frac{1}{2}\left(\sqrt{s} - \left|p_\gamma^{\mathrm{isr},\ z}\right| - p_\gamma^{\mathrm{isr},\ z}\cos\theta_{\mathrm{q}}^*\right) \tag{4.3}$$

  with $|\cos\theta_{\mathrm{q}}^*| = |\cos\theta_T^*|$. The corresponding equation holds for the antiquark $\overline{\mathrm{q}}$ with the substitution $\cos\theta_{\overline{\mathrm{q}}}^* = -\cos\theta_{\mathrm{q}}^*$. The upper momentum cut for slow pions is then set for each event to the maximum momentum expected in the laboratory frame according to equation 3.11, where $2 \cdot E_{\mathrm{q}}^{\mathrm{LAB}}$ is substituted for $\sqrt{s}$.

For the flavour separation of the selected electron, muon, and slow pion tagged events, the same neural nets as for the LEP2 analysis are used, with input quantities scaled by the factor $2E_{\mathrm{q}}^{\mathrm{LAB}}/\sqrt{s_{\mathrm{train}}}$ where appropriate, as described in section 3.4.3. No significant gain in performance was observed when the flavour separation nets were retrained using simulated events at the Z resonance instead of $\sqrt{s_{\mathrm{train}}} = 183$ GeV.

In table 4.3, the efficiencies of the lepton and slow pion selection and the sample composition are given. The output distributions of the flavour separation nets are shown in figure 4.6.

The asymmetry fit uses the signed cosine of the polar thrust angle in the effective centre-of-mass frame, y^*, instead of the corresponding unboosted quantity y, but is otherwise identical

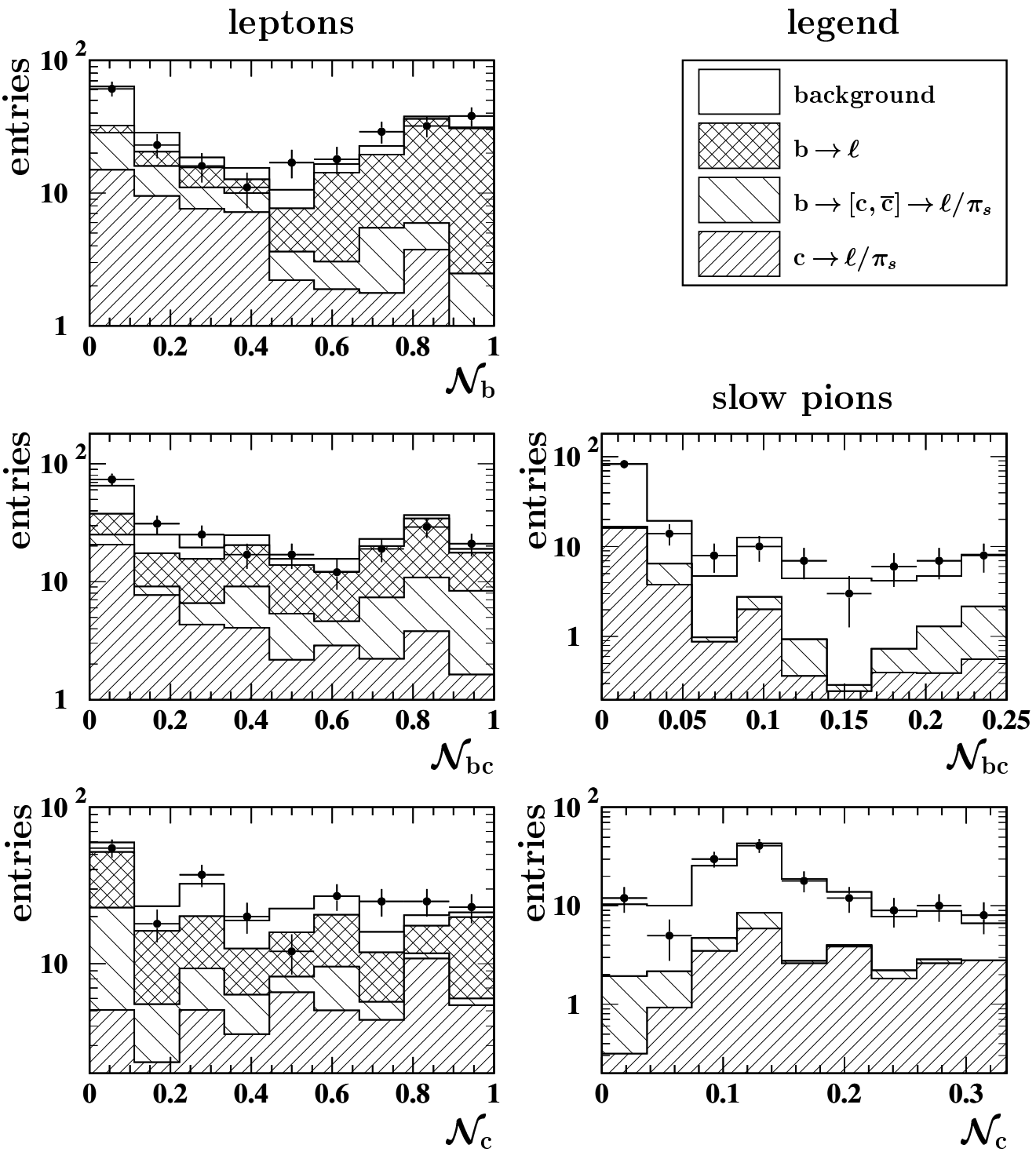

Figure 4.6: The $\mathcal{N}_{\rm b}$, $\mathcal{N}_{\rm c}$, and $\mathcal{N}_{\rm bc}$ distributions for lepton and slow pion tagged radiative events. The points with error bars correspond to the data. The open histogram represents the Monte Carlo expectation, where the contributions from signal events are shown hatched as explained in the legend. The fraction of true radiative events does not change significantly with the network outputs and is not indicated.

source	sample composition			efficiencies		
	electrons	muons	slow pions	electrons	muons	slow pions
$b \to \ell$	58 %	53 %		33 %	54 %	
$b \to [c, \overline{c}] \to \ell/\pi_s$	16 %	13 %	7 %	16 %	27 %	9 %
$c \to \ell/\pi_s$	17 %	15 %	14 %	25 %	43 %	27 %
non-prompt leptons	5 %	10 %				
other background	4 %	9 %	79 %			

Table 4.3: The estimated composition of the lepton and slow pion tagged event samples after the selection. The efficiencies of the prompt lepton and slow pion selection are given with respect to all prompt leptons and slow pions in the final event sample that are reconstructed as tracks in the detector, irrespective of the effective centre-of-mass energy of the selected event. The lower lepton background rates compared to the LEP2 case (see table 3.7) are due to the lower particle momenta and multiplicities.

to the LEP2 case. The inclusive y^* distributions are shown in figure 4.7. As before, the events are divided into subsamples of different bottom and charm purity. The likelihood $\mathcal{L}_{\rm sub}$ for one subsample is given by

$$\ln \mathcal{L}_{\rm sub} = \sum_{\rm candidates} \ln \left(1 + (y^*)^2 + \frac{8}{3} A_{\rm FB}^{obs}(y^*) \right) \ , \tag{4.4}$$

where the sum is taken over all candidates in the subsample, and the total likelihood is given by the product of the likelihoods of all subsamples. The expected observed asymmetry $A_{\rm FB}^{obs}$ in each subsample is computed as

$$A_{\rm FB}^{obs}(\mathcal{N}_{\rm b}, \mathcal{N}_{\rm bc}, \mathcal{N}_{\rm c}, |\cos\theta_{\rm jet}|) = \sum_{i=1}^{5} f_i(\mathcal{N}_{\rm b}, \mathcal{N}_{\rm bc}, \mathcal{N}_{\rm c}, |\cos\theta_{\rm jet}|)\, A_{\rm FB}^{i} \ . \tag{4.5}$$

As before, f_i denotes the predicted fraction of leptons or slow pions from source i, and $A_{\rm FB}^{i}$ is the corresponding asymmetry:

$$\left\{ \begin{array}{rrll} A_{\rm FB}^{1} = & (1 - 2\overline{\chi_1}^{\rm eff})\, A_{\rm FB}^{\rm b} & \text{for } b \to \ell \, , \\ A_{\rm FB}^{2} = & -(1 - 2\overline{\chi_2}^{\rm eff})\, A_{\rm FB}^{\rm b} & \text{for } b \to c \to \ell/\pi_s \, , \\ A_{\rm FB}^{3} = & (1 - 2\overline{\chi_3}^{\rm eff})\, A_{\rm FB}^{\rm b} & \text{for } b \to \overline{c} \to \ell/\pi_s \, , \\ A_{\rm FB}^{4} = & -\, A_{\rm FB}^{\rm c} & \text{for } c \to \ell/\pi_s \, , \text{ and} \\ A_{\rm FB}^{5} = & 0 & \text{for background,} \end{array} \right. \tag{4.6}$$

where $\overline{\chi_i}^{\rm eff}$ is the effective $B - \overline{B}$ mixing parameter. The fractions f_i are calculated from the Monte Carlo simulation. The sample composition is evaluated in bins of $|\cos\theta_{\rm jet}|$, determined in the laboratory frame for the jet that contains the tagged lepton or slow pion. This is justified because the tagging efficiency and purity vary with $|\cos\theta|$ due to detector effects in the identification of the lepton or slow pion and the flavour separation. Properties of the most energetic jet in the opposite hemisphere of the $q\bar{q}$ rest frame (for radiative events, this jet is found at a different $|\cos\theta_{\rm jet}|$ in the laboratory frame) are less important for the flavour separation. A binning according to the thrust direction is only adequate for non-radiative events

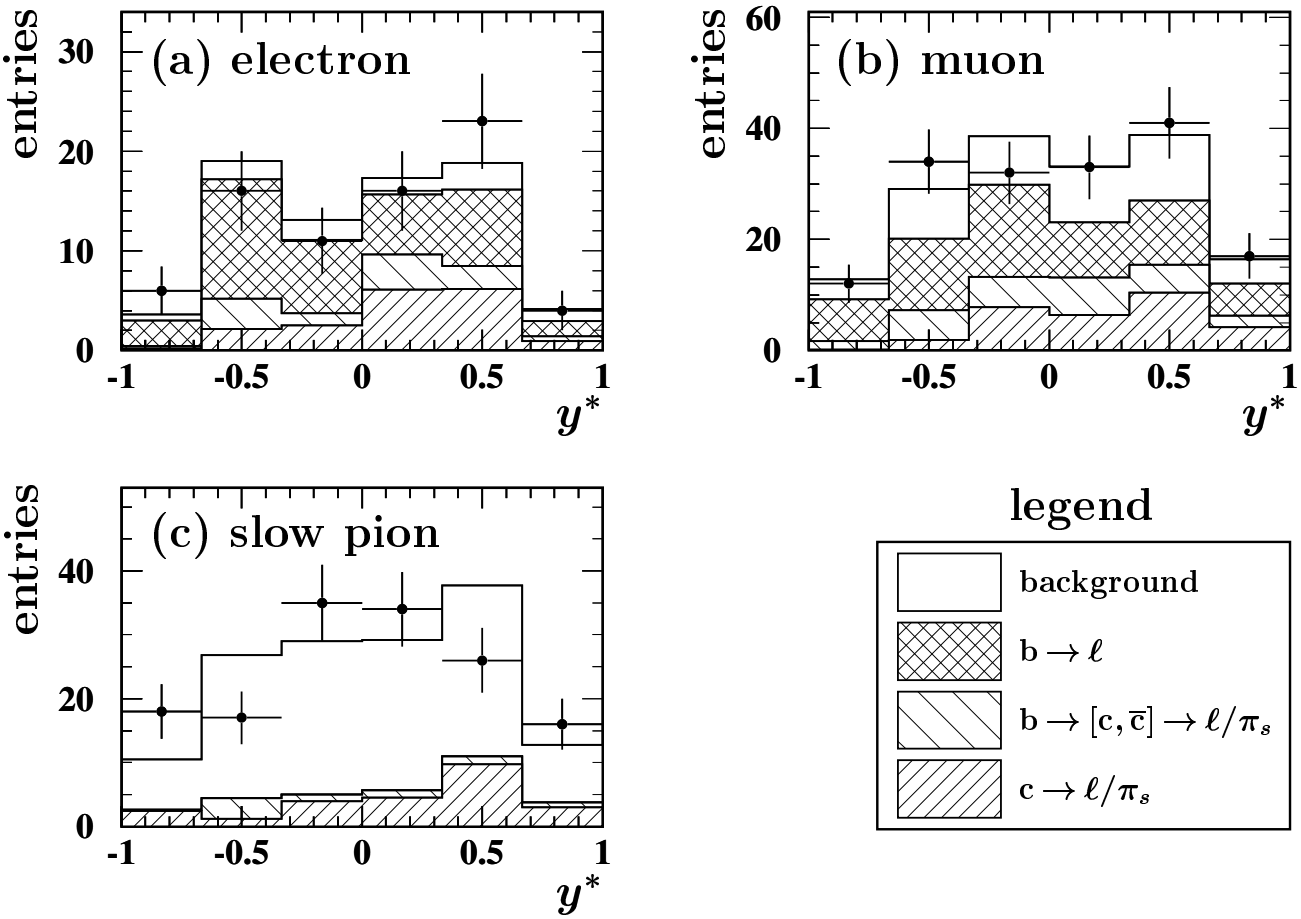

Figure 4.7: The y^* distributions of (a) electron, (b) muon, and (c) slow pion tagged radiative events are given by the points with error bars. Also plotted is the expectation from the simulation together with the contributions from $b \to \ell$ (cross-hatch), $b \to [c, \bar{c}] \to \ell/\pi_s$ (wide diagonal hatch), and $c \to \ell/\pi_s$ decays (narrow diagonal hatch). The components from true radiative events and non-radiative background are not distinguished in the plot to avoid confusion.

like in the LEP2 measurement. For radiative events, the two hemispheres are not back-to-back, and the thrust direction may equally likely be aligned with the flight direction in the laboratory frame of the primary quark or antiquark.

The contributions to the observed asymmetry from mis-identified non-radiative events are determined according to the LEP1 averages of the heavy flavour asymmetries [3] and are fixed in the fit. This is justified because even after the selection of radiative events, the remaining non-radiative background is very strongly peaked at $\sqrt{s'} \approx \sqrt{s}$, see figure 4.3. The different LEP1 centre-of-mass energies are accounted for according to table 4.1. The asymmetries around the Z resonance are varied by their errors to determine the associated systematic uncertainty. Similarly, the small contributions to the observed asymmetry from two-photon events are accounted for, but left out of the list in equation 4.6 for simplicity.

In table 4.4, the numbers of radiative lepton and slow pion tagged events are given, and the results of the fit for the bottom and charm asymmetries are summarised together with

the errors and correlation. The measurements are also shown in figure 5.1 together with the results of the LEP2 analysis and previous measurements at other centre-of-mass energies. The systematic errors have been evaluated as described in section 4.6.

energy $\langle\sqrt{s'}\rangle$	electrons	muons	slow pions	measured asymmetries	correlation	predicted asymmetries
74 GeV	76	169	145	$A_{\mathrm{FB}}^{\mathrm{b}} = -0.01\,^{+0.27}_{-0.28} \pm 0.12$ $A_{\mathrm{FB}}^{\mathrm{c}} = -0.38\,^{+0.37}_{-0.35} \pm 0.18$	+22%	$A_{\mathrm{FB}}^{\mathrm{b,SM}} = -0.37$ $A_{\mathrm{FB}}^{\mathrm{c,SM}} = -0.64$

Table 4.4: The numbers of lepton and slow pion tagged events, the results for the bottom and charm asymmetries as measured with the lepton and slow pion tag, and their correlation are listed. In the last column, the Standard Model predictions for the asymmetries are given.

The values of R_{b} and R_{c} are fixed to the Standard Model expectations. The dependence of the measured asymmetries on the assumed values is parametrised according to equation 3.18. In table 4.5, the the Standard Model values of R_{b} and R_{c} are given, and the coefficients that parametrise the dependence are listed.

energy	${R_{\mathrm{b}}}^{\mathrm{SM}}$	${R_{\mathrm{c}}}^{\mathrm{SM}}$	$a^{\mathrm{b}}(R_{\mathrm{b}})$	$a^{\mathrm{b}}(R_{\mathrm{c}})$	$a^{\mathrm{c}}(R_{\mathrm{b}})$	$a^{\mathrm{c}}(R_{\mathrm{c}})$
74 GeV	0.175	0.235	+0.08	−0.02	−0.07	+0.09

Table 4.5: The Standard Model predictions for the partial hadronic decay widths R_{b} and R_{c} and the dependence of the results on their values are given. The symbols are defined in equation 3.18. The values of the coefficients have opposite signs with respect to those listed in table 3.10, because the measured asymmetries have the opposite sign.

4.5 Cross-Check of the Analysis

As mentioned in section 1.1.3, radiative events at LEP2 provide an important cross-check: The same measurement technique can be applied, but these events can easily be identified experimentally, and the heavy quark asymmetries in $\mathrm{e^+e^-}$ collisions at the Z mass are well known.

For each of the five energy bins at LEP2, radiative events are selected with the same cuts as described in section 3.2, with the exception that here, events with reconstructed $\sqrt{s'/s} < 0.85$ are accepted. For these event samples, the background from non-radiative hadronic events is of the order of $1 - 2\%$. These events are subjected to the same asymmetry measurement as described in section 4.4, i.e. the bottom and charm asymmetries are measured in the $\mathrm{q\bar{q}}$ centre-of-mass frame. The results are shown in figure 4.8. Good agreement with the LEP1 averages is found. As another check, the full selection of LEP1 radiative events is also applied in addition to the $\sqrt{s'/s} < 0.85$ cut. The resulting values are consistent with the previous measurements and with the LEP1 averages, although with larger statistical errors.

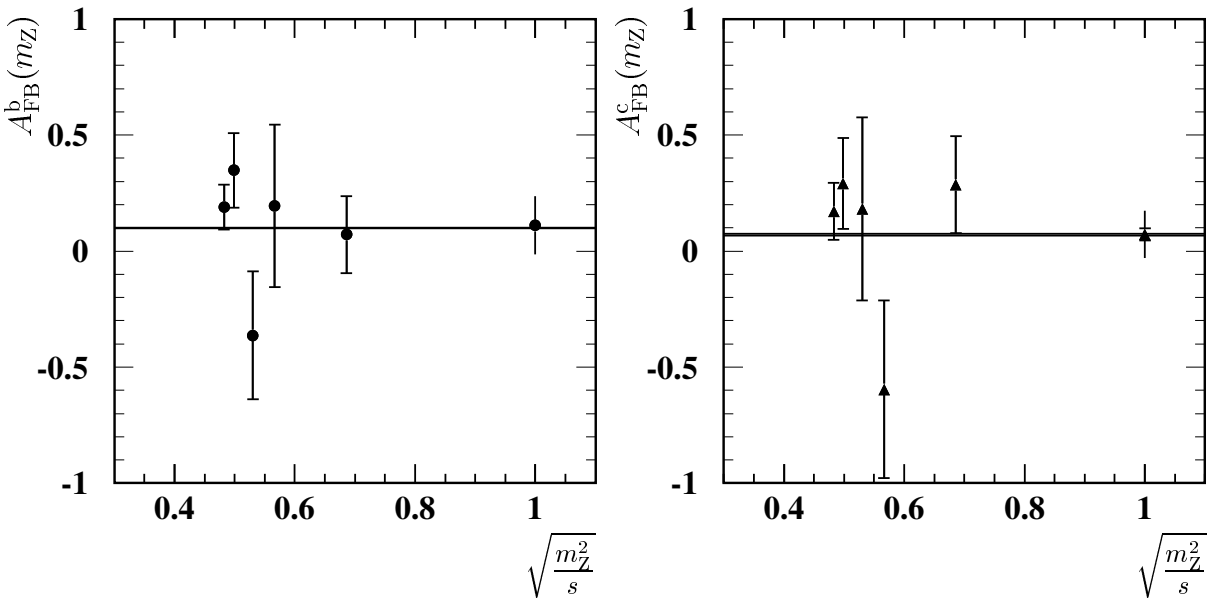

Figure 4.8: The values of $A_{\rm FB}^{\rm b}$ (left plot) and $A_{\rm FB}^{\rm c}$ (right plot) as measured using radiative events at LEP2 are shown as a function of $\sqrt{m_{\rm Z}^2/s}$. Only statistical errors have been evaluated. Also indicated at $\sqrt{m_{\rm Z}^2/s} = 1$ is the measurement using the calibration data taken on the Z resonance during LEP2 running, which is mentioned in section 3.4.4. For this latter measurement, no selection of radiative events and no boost are performed, and the error is dominated by the limited Monte Carlo statistics.
The horizontal lines show the LEP1 averages for the asymmetries on the Z peak. All measurements are consistent with these values, and no dependence on $\sqrt{m_{\rm Z}^2/s}$ is observed.

4.6 Systematic Errors

The systematic errors for this analysis can be divided into two categories: Those that are related to the identification of events with hard initial state radiation and the boost into the effective centre-of-mass frame, and uncertainties that arise from the asymmetry analysis within this $\rm q\overline{q}$ rest frame. The modelling of the event selection and boost is tested with events recorded at energies above the Z resonance, where radiative return events to the Z can be relatively easily separated from non-radiative events. The procedure and the resulting errors are discussed in section 4.6.1. The uncertainties from the asymmetry analysis are identical in nature to those discussed in section 3.5.2 and will be only briefly mentioned in section 4.6.3. An exception is the reconstruction efficiency for slow pions, where the systematic errors have been determined in a previous OPAL publication. An overview of all systematic errors is given in table 4.6.

error source	$\Delta A_{\mathrm{FB}}^{\mathrm{b}}$	$\Delta A_{\mathrm{FB}}^{\mathrm{c}}$
event selection	0.005	0.003
isr/fsr interference	0.011	0.021
track reconstruction	0.069	0.153
electron identification	0.004	0.004
muon identification	0.002	0.002
slow pion identification	0.000	0.003
input modelling	0.010	0.011
lifetimes	0.004	0.002
fragmentation modelling	0.019	0.023
semileptonic decay models	0.008	0.006
D^{*+} spin alignment	0.001	0.000
branching ratios and hadronisation fractions	0.008	0.006
$B-\overline{B}$ mixing	0.001	0.001
background asymmetries (4f, radiative events)	0.002	0.003
background asymmetries (lepton, slow pion backgrounds)	0.010	0.035
final state QCD corrections	0.008	0.011
Monte Carlo statistics	0.089	0.091
fitting procedure	0.020	0.009
total systematic error	0.119	0.184

Table 4.6: A breakdown of the systematic errors is given for the asymmetry measurement in radiative events at LEP1.

4.6.1 Event Selection and Determination of the Effective Centre-of-Mass Frame

As described in section 4.5 above, radiative events at centre-of-mass energies above the Z resonance are used to calibrate the event selection efficiency. In order to determine the corresponding systematic error, the efficiencies for selecting radiative and two-photon events are simultaneously varied within their uncertainties determined in section 4.5. The background from non-radiative events is adjusted according to the total number of selected events, as given by equation 4.2. The observed variations in the measured asymmetry are assigned as systematic error.

The above calibration assumes that the resolution and absolute scale of the reconstructed effective centre-of-mass energy is correctly modelled in the simulation, since a cut on the reconstructed $\sqrt{s'}$ is applied to select the sample of radiative hadronic LEP2 events. This resolution and scale have been determined by comparing the position and width of the radiative Z peak in hadronic events at LEP2 with the corresponding quantities in the simulation. The position of the reconstructed Z peak has been found to be modelled to within $\pm 0.2\%$, while the resolution is modelled to within $\pm 7.6\%$. Similar to the variation of the tracking resolution (see section 3.5.1.5), the difference between reconstructed and true $\sqrt{s'}$ in the simulation has been scaled on an event-by-event basis according to these uncertainties. The observed differences in the measured asymmetries have been added in quadrature and are treated as an additional

systematic error.

4.6.2 Interference between Initial and Final State Radiation

The measurement values are interpreted as forward-backward asymmetries at effective centre-of-mass energies below the Z resonance, which is possible only if interference effects between initial and final state photon radiation are negligibly small. To assess the corresponding uncertainty, the asymmetries in the $q\bar{q}$ rest frame for simulated events with and without this interference taken into account are compared. The observed difference is taken as the systematic uncertainty on the interpretation of the A_{FB}^{b} and A_{FB}^{c} measurements.

Interference effects between isr and fsr are only implemented in the Monte Carlo generator according to an $\mathcal{O}(\alpha)$ QED calculation; the YFS exponentiation scheme can only be used without accounting for this interference. For consistency, the comparison is made between samples of simulated events using the $\mathcal{O}(\alpha)$ calculation. An additional complication arises since gluon radiation, which competes with final state photon radiation, is not simulated in the YFS3ff generator. The comparison is therefore made on the level of primary quarks. Differences of 0.011 (for bottom quarks) and 0.021 (for charm quarks) are determined between the generated asymmetries with and without interference, which are assigned as systematic errors.

4.6.3 Asymmetry Analysis

The systematic errors that arise from the uncertainties in the modelling of the detector resolution and the lepton identification have been evaluated as described in section 3.5.2. Only those uncertainties where the treatment is not identical are mentioned in the following:

- **Lepton Identification:**
  The modelling of the electron and conversion identification algorithms has been studied previously [69, 70] for the LEP1 detector configuration. A 4.0% relative variation of the electron efficiency and a 21% variation of the electron fake rate have been applied to cover the uncertainties found in this study. Similarly, the conversion rate has been varied by 3.5%.

  The modelling of efficiency and fake rate for the muon identification algorithm have been tested as described in appendix A. For an inclusive sample selected with a cut $\mathcal{N}_{\mu} > 0.65$, the relative errors on muon efficiency and fake rate are 1.1% and 2.5%, respectively. The rate of non-prompt muon reconstruction is varied by 9% [51].

- **Slow Pion Efficiency:**
  In a previous OPAL measurement of $f(c \to D^{*+})$, $f(b \to [c,\overline{c}] \to D^{*\pm})$, and R_c [53] on the Z resonance, the systematic uncertainties on the slow pion preselection efficiency have been determined to be 5.1% for slow pions from charm events and 5.6% for slow pions from $b \to [c,\overline{c}] \to \pi_s$ decays, respectively[2].

  Similar to the procedure used in section 3.5.2.1, the efficiency for reconstructing slow pions in radiative events is taken from the simulation. It is then varied by these relative

[2]The upper slow pion momentum cut is set at 3 GeV instead of 4.17 GeV. However, the number of reconstructed true slow pions in this momentum range is small, and the analysis from [53] can safely be taken to test the slow pion efficiency.

uncertainties to assess the associated systematic error on the heavy flavour asymmetry measurements. It is not assumed that the absolute efficiencies be identical for radiative and non-radiative events.

- **Neural Net Input Modelling:**
  As for the LEP2 analysis, each of the net input distributions for the flavour separation networks $\mathcal{N}_{\mathrm{b}}$, $\mathcal{N}_{\mathrm{bc}}$, and $\mathcal{N}_{\mathrm{c}}$ has been considered separately, and the simulation reweighted such that the distribution matches the measured one. Any systematic deviations in the modelling of the inputs to the flavour separation networks are expected to be independent of the effective centre-of-mass energy to a good approximation. Therefore, to be more independent from statistical fluctuations, the inputs to the flavour separation networks have been studied on an inclusive sample of hadronic events at LEP1, before the selection of radiative events is applied.

- **Background Asymmetries:**
  The observed asymmetry of muons and slow pions from two-photon events are expected to be zero and set to this value in the fit; the corresponding value for electrons is expected to be zero for untagged two-photon events and close to 1 for tagged events. These values are varied by ± 0.5 to assess the systematic error. Since the two-photon contribution to the event sample is small, the resulting error is negligible.

  Compared to the LEP2 case, the background from events at $\sqrt{s'} \approx m_{\mathrm{Z}}$ is large; however, the asymmetries for non-radiative events close to the Z peak are well known. They are varied by their experimental errors to assess the associated systematic uncertainties.

  As in the LEP2 measurement, the asymmetries from mis-identified leptons and slow pions are determined from inclusive track samples. They are found to be zero within 1.2% (leptons) and 1.6% (slow pions), and varied within this range to determine the systematic error.

4.7 Summary

The first measurement of heavy quark forward-backward asymmetries at effective centre-of-mass energies between $\sim 60\,\mathrm{GeV}$ (TRISTAN) and $\sim m_{\mathrm{Z}}$ (LEP1 and SLD) has been presented, using radiative events recorded with the OPAL detector at LEP. The bottom and charm asymmetries have been measured to be

$$\begin{aligned} A_{\mathrm{FB}}^{\mathrm{b}}(74\,\mathrm{GeV}) &= -0.01\,^{+0.27}_{-0.28}\,(stat.) \pm 0.12\,(syst.) \text{ and} \\ A_{\mathrm{FB}}^{\mathrm{c}}(74\,\mathrm{GeV}) &= -0.38\,^{+0.37}_{-0.35}\,(stat.) \pm 0.18\,(syst.), \end{aligned} \tag{4.7}$$

consistent with the Standard Model predictions. Radiative events at centre-of-mass energies above the Z resonance have been used to calibrate and cross-check the analysis.

Chapter 5

Interpretation of the Measurements of Heavy Quark Production

In the heavy quark measurements presented in the previous chapters, no significant deviations from the Standard Model predictions have been found. Therefore, the measured values can be interpreted within the framework of the Standard Model to obtain values for the effective bottom and charm vector and axial vector couplings to the Z boson. As discussed in section 1.1, measurements at energies above and below the Z resonance can resolve the ambiguities that arise in the determination of effective couplings from Z peak data alone. The interpretation of the measurements within this context is presented in section 5.2.

Additional information on the $\gamma - \mathrm{Z}$ interference can be obtained in the S-Matrix parametrisation of cross-sections and asymmetries. For the determination of the interference terms, measurements at centre-of-mass energies off the Z resonance are mandatory. In this thesis, an analysis of the $\mathrm{e^+e^-} \to \mathrm{b\bar{b}}$ and $\mathrm{e^+e^-} \to \mathrm{c\bar{c}}$ processes within the S-Matrix framework is performed for the first time. This analysis is described in section 5.3. The precision that can be achieved in S-Matrix fits using measurements from the expected final LEP2 dataset and one year of data-taking at a future $\mathrm{e^+e^-}$ linear collider experiment is assessed. A summary is given in section 5.4.

5.1 Heavy Flavour Measurements used in the Fits

In this section, the existing and expected future heavy flavour electroweak measurements used in the fits are summarised. The measurements of heavy flavour production and forward-backward asymmetries are shown in figure 5.1, and all values are listed in table 5.1. For the determination of the effective couplings and the bottom and charm S-Matrix parameters, information from other electroweak measurements is also needed. These additional inputs are described in sections 5.2 and 5.3 together with the individual fits, since different quantities are used in the two cases.

Below the Z Resonance: The experiments at PEP [8], PETRA [9], and TRISTAN [10] have performed heavy quark measurements at $\mathrm{e^+e^-}$ centre-of-mass energies between around 30 GeV and 60 GeV. The measurements of $A_{\mathrm{FB}}^{\mathrm{b}}$ are corrected using the effective mixing parameter $\overline{\chi} = 0.118$ [2]. The measured $\mathrm{b\bar{b}}$ and $\mathrm{c\bar{c}}$ production cross-sections have been transformed

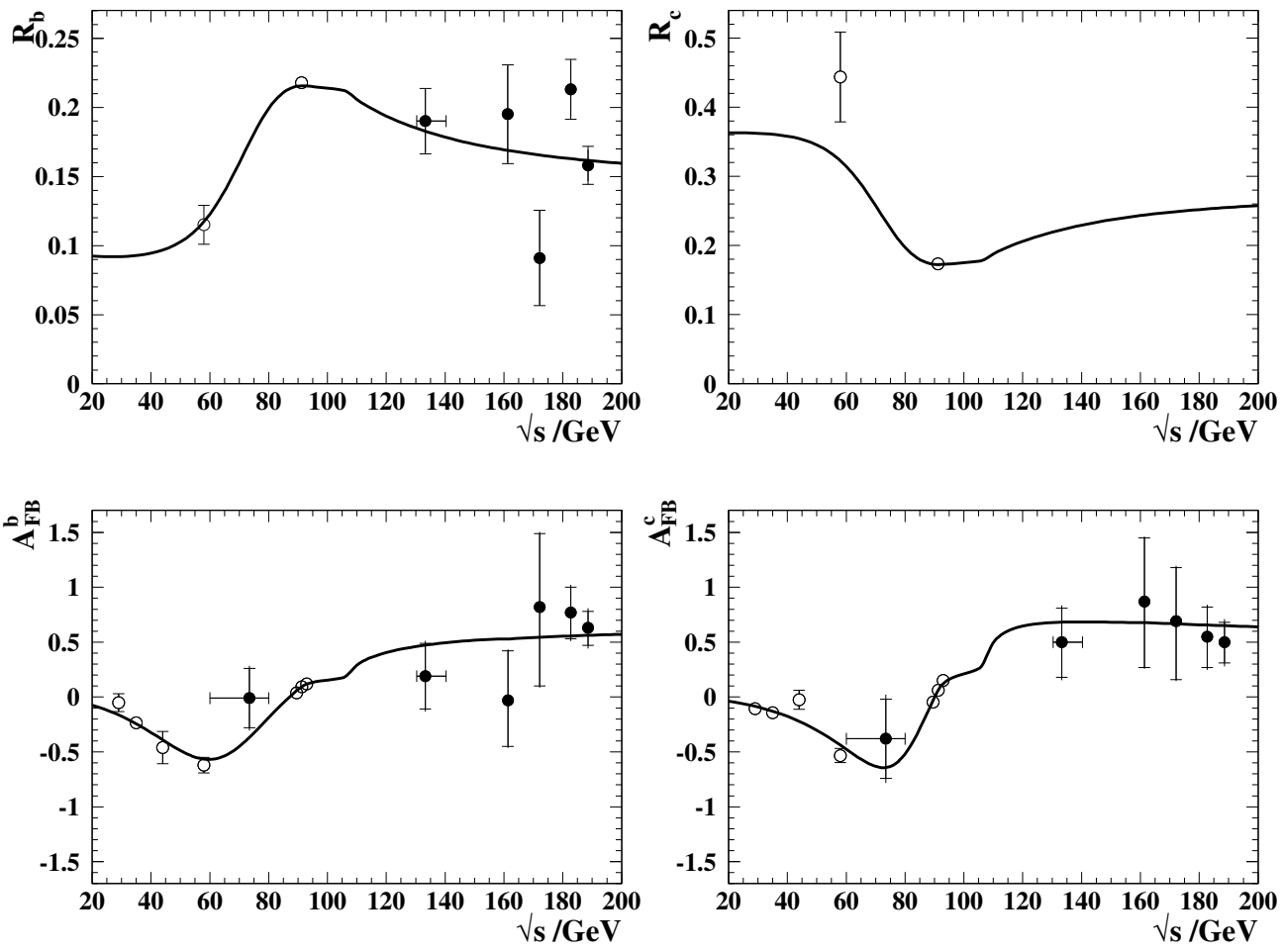

Figure 5.1: The measurements of R_{b}, R_{c}, $A_{\mathrm{FB}}^{\mathrm{b}}$, and $A_{\mathrm{FB}}^{\mathrm{c}}$ that are used in the fits are shown. Those measurements that are indicated by full circles have been presented in this thesis in chapter 4 (at 74 GeV) and chapter 3 (above the Z resonance); here, the statistical and total measurement errors are shown separately, and the horizontal error bars show the range of centre-of-mass energies used in each measurement. For the measurements around the Z resonance, the error bars are smaller than the points. The Standard Model predictions as computed by ZFITTER are shown by the lines. The behaviour of the curves at $\sqrt{s} \approx 110$ GeV is due to the cut $\sqrt{s'/s} > 0.85$ that is applied in the measurements at energies above the Z resonance.

energy	R_b	R_c	A_{FB}^b	A_{FB}^c
29 GeV	–	–	-0.052 ± 0.081	-0.106 ± 0.026
35 GeV	–	–	-0.236 ± 0.043	-0.142 ± 0.024
44 GeV	–	–	-0.460 ± 0.147	-0.025 ± 0.087
58 GeV	0.115 ± 0.014	0.444 ± 0.065	-0.620 ± 0.071	-0.533 ± 0.065
74 GeV	–	–	-0.01 ± 0.30	-0.38 ± 0.40
89.55 GeV	–	–	0.0553 ± 0.0088	-0.030 ± 0.018
91.26 GeV	0.21656 ± 0.00074	0.1736 ± 0.0044	0.0972 ± 0.0022	0.0643 ± 0.0046
92.94 GeV	–	–	0.1081 ± 0.0077	0.134 ± 0.015
133 GeV	0.190 ± 0.024	–	0.19 ± 0.32	0.50 ± 0.35
161 GeV	0.195 ± 0.036	–	-0.03 ± 0.44	0.87 ± 0.60
172 GeV	0.091 ± 0.034	–	0.82 ± 0.71	0.69 ± 0.52
183 GeV	0.213 ± 0.022	–	0.77 ± 0.26	0.55 ± 0.30
189 GeV	0.158 ± 0.014	–	0.63 ± 0.19	0.50 ± 0.21
189 GeV	0.1550 ± 0.0086	$0.267\ ^{+0.018}_{-0.028}$	*0.58 ± 0.10*	*0.66 ± 0.11*
∼ 200 GeV	*0.1621 ± 0.0069*	*0.258* $\ ^{+0.015}_{-0.026}$	*0.583 ± 0.074*	*0.649 ± 0.087*
∼ 350 GeV	*0.1492 ± 0.0011*	*0.2733 ± 0.0086*	*0.6041 ± 0.0012*	*0.5932 ± 0.0026*

Table 5.1: The heavy flavour measurements used in the fit are summarized. In the upper part of the table, the measurements at PEP [8], PETRA [9], TRISTAN [10], LEP1 and SLD [3], and those presented in this thesis are listed. The SLD $A_{LR,FB}$ measurements yield values of $\mathcal{A}_b = 0.911 \pm 0.025$ and $\mathcal{A}_c = 0.630 \pm 0.026$, which have been included in the fit for the effective heavy quark couplings. The values of R_b and R_c at the Z peak are quoted for pure Z exchange (R_b^0 and R_c^0).
For the determination of the expected final LEP2 reach, the existing measurements by ALEPH [14], DELPHI [15], and OPAL (see chapter 3) have been combined to obtain the expected precision at 189 GeV and extrapolated to the expected statistics at around 200 GeV. The resulting values are listed in the bottom part of the table, together with estimates of the expected precision of measurements at a linear collider. The Standard Model predictions have been taken as central values. Expected future measurements are denoted by italic numbers.

into values for the cross-section ratios R_b and R_c. An average of most of the asymmetry measurements can also be found in [71].

The asymmetry values at 74 GeV have been taken from the measurement described in chapter 4 of this thesis.

Around the Z Resonance: The values for R_b, R_c, A_{FB}^b, and A_{FB}^c close to the Z resonance have been taken from a combined fit to all measurements performed by the LEP and SLD experiments [3]. For the asymmetries, also values at centre-of-mass energies above and below the Z peak are provided, corresponding to the LEP energies shown in table 4.1. These values and the full correlation matrix are used in the fit. At the SLD experiment, more information

on the heavy quark couplings is available due to the non-zero electron beam polarisation. The measured left-right forward-backward asymmetries, which provide information on the quark couplings only (see equation 1.10), are used in the fit for the effective couplings. In the S-Matrix framework, however, their description is independent from that of total cross-sections and forward-backward asymmetries.

Above the Z Resonance: For energies between 133 and 189 GeV, the measurements from chapter 3 have been taken. The correlation between the bottom and charm asymmetry as well as their dependence on R_{b} and R_{c} are accounted for in the fits.

Future Improvements: Significant improvements of measurements of the effective heavy quark couplings will be possible if a future linear $\mathrm{e^+e^-}$ collider can also be operated at the Z resonance with high luminosity ("Z factory"). These prospects are discussed in [72]. The constraints on the effective heavy quark couplings from expected future measurements at energies above the Z resonance are expected to be weak in comparison and will consequently not be discussed here.

In the S-Matrix approach, however, future improvements in the determination of $\gamma - \mathrm{Z}$ interference parameters will rely mostly on the availability of precision measurements above the Z resonance. In order to assess the possible improvements of the S-Matrix fit results from measurements at LEP2 and an experiment at a future linear $\mathrm{e^+e^-}$ collider, additional fits have been performed with fictitious measurement points at 189 GeV, 200 GeV, and 350 GeV included. The final LEP2 accuracy has been obtained by extrapolating existing measurements to the expected integrated luminosity. Measurements at energies between 130 GeV and 183 GeV are not considered in this fit since they are based on relatively small data samples.

The precision of measurements at a linear collider has been assessed from the expected integrated luminosity after one year of operation and from the estimated bottom and charm tagging performance. At a linear collider with a polarized electron beam, a measurement of the left-right forward-backward asymmetry will be possible similar to the SLD case. In the framework of effective heavy quark couplings to the Z, such a measurement yields more information than one of the forward-backward asymmetry alone. However, in the S-Matrix framework, the description of left-right forward-backward asymmetries is independent from that of forward-backward asymmetries, and additional S-Matrix parameters would be needed to describe these measurements. Therefore, only partial hadronic cross-section and forward-backward asymmetry measurements are considered here, where it is assumed that equal integrated luminosities are taken with positive and negative electron beam polarisation of equal magnitude. In such a case, a measurement of A_{FB} is obtained when using all data without accounting for the electron polarisation.

The ALEPH collaboration has measured [14]

$$\begin{aligned} R_{\mathrm{b}}(189\ \mathrm{GeV}) &= 0.151 \pm 0.011\ ^{+0.002}_{-0.004}\,, \\ R_{\mathrm{c}}(189\ \mathrm{GeV}) &= 0.266 \pm 0.018\ ^{+0.004}_{-0.022}\,, \\ A^{\mathrm{b}}_{\mathrm{FB}}(189\ \mathrm{GeV}) &= 0.34 \pm 0.19 \pm 0.02\,, \text{ and} \\ A^{\mathrm{c}}_{\mathrm{FB}}(183\ \mathrm{GeV}) &= 0.95 \pm 0.27\ ^{+0.11}_{-0.09} \end{aligned} \tag{5.1}$$

for integrated luminosities of 174 pb^{-1} at 189 GeV and 56.1 pb^{-1} at 183 GeV, respectively. When the $A^{\mathrm{c}}_{\mathrm{FB}}$ measurement is extrapolated to the number of events taken at 189 GeV, one expects a measurement with a statistical precision of 0.15. This is taken for the calculation of the assumed total precision at 189 GeV.

The DELPHI collaboration has measured [15]

$$\begin{aligned} R_{\rm b}(189\ {\rm GeV}) &= 0.167 \pm 0.012\,(stat.+syst.) - 0.21(R_{\rm c} - 0.252) - 0.03(R_{\rm uds} - 0.581)\,, \\ R_{\rm uds}(189\ {\rm GeV}) &= 0.571 \pm 0.022\,(stat.+syst.) - 0.07(R_{\rm b} - 0.167) - 0.63(R_{\rm c} - 0.252)\,, \\ A^{\rm b}_{\rm FB}(161-172\ {\rm GeV}) &= 1.05 \pm 0.35(stat.+syst.)\,, \text{ and} \\ A^{\rm c}_{\rm FB}(161-172\ {\rm GeV}) &= 1.14 \pm 0.81(stat.+syst.) \end{aligned} \tag{5.2}$$

for 158 pb^{-1} recorded at 189 GeV. No integrated luminosity is given for 161 and 172 GeV, so the OPAL value of (9.6 + 9.9) pb^{-1} is assumed. With the constraint $R_{\rm b} + R_{\rm c} + R_{\rm uds} = 1$, the $R_{\rm b}$ and $R_{\rm uds}$ measurements given together with the dependences can be transformed into measurements of $R_{\rm b}$ and $R_{\rm c}$. One finds

$$\begin{aligned} R_{\rm b}(189\ {\rm GeV}) &= 0.158 \pm 0.023\,(\Delta R_{\rm b}) \pm 0.021\,(\Delta R_{\rm uds}) \text{ and} \\ R_{\rm c}(189\ {\rm GeV}) &= 0.303 \mp 0.058\,(\Delta R_{\rm b}) \mp 0.111\,(\Delta R_{\rm uds})\,. \end{aligned} \tag{5.3}$$

From the hadronic cross-section ratio of 0.687 and the ratio 8.92 of the integrated luminosities at 189 and 161 + 172 GeV, the expected precision of the asymmetry measurements at 189 GeV is calculated to be 0.14 for $A^{\rm b}_{\rm FB}$ and 0.32 for $A^{\rm c}_{\rm FB}$.

The assumed precision of the combined LEP2 measurements by ALEPH, DELPHI, and OPAL at 189 GeV and ∼200 GeV is given in table 5.1. For the expected measurements at ∼200 GeV, an integrated luminosity of 300 pb^{-1} has been assumed.

In order to assess the precision that can be obtained from measurements at a future e^+e^- linear collider, values at 350 GeV corresponding to an integrated luminosity of 500 fb^{-1} have been included. For simplicity, the centre-of-mass energy has been assumed to be below the threshold of on-shell $t\bar{t}$ production, so that the ZFITTER and SMATASY programs can be used in the fit without complications. The tagging efficiencies and purities are based on the conceptual design report for a linear collider experiment [73] and on studies presented in [74]. It has been assumed that only events within $|\cos\theta_T| < 0.8$ are used in the measurements to reject WW pair background. The selection of non-radiative hadronic events is then assumed to be 91% efficient and 97% pure. For the tagging of bottom and charm event hemispheres, the following efficiencies ε, purities π, and charge identification probabilities P have been taken:

	ε	π	P
$b\bar{b}$ events	74%	98.5%	68%
$c\bar{c}$ events	50%	75%	–

For the measurements of $R_{\rm b}$ and $R_{\rm c}$, it is assumed that a double tag technique is used, similar to [30]: From the numbers

$$\begin{aligned} N_t &\sim 2R_{\rm b}\varepsilon_{\rm b} + 2R_{\rm c}\varepsilon_{\rm c} + 2(1-R_{\rm b}-R_{\rm c})\varepsilon_{\rm uds} \quad \text{and} \\ N_{tt} &\sim R_{\rm b}\varepsilon_{\rm b}^2 + R_{\rm c}\varepsilon_{\rm c}^2 + (1-R_{\rm b}-R_{\rm c})\varepsilon_{\rm uds}^2 \end{aligned} \tag{5.4}$$

of single and double tagged events, one determines $R_{\rm b}$ as

$$R_{\rm b} = \frac{1}{4}\,\frac{(N_t - N_{t,\,\rm bkg})^2}{N_{tt} - N_{tt,\,\rm bkg}}\,, \tag{5.5}$$

where correlations have been neglected. The corresponding formula holds for R_c. The background tagging rates have been assumed to be known to within $\pm 2\%$, and the resulting systematic errors dominate the uncertainties quoted in table 5.1.

The uncertainty of a measurement of A_{FB}^b with a hemisphere charge method is estimated from the above tagging performance, assuming a single-tag measurement and taking into account charge identification probability and angular acceptance. In addition, the OPAL measurement of bottom and charm asymmetries at the Z resonance with prompt leptons [31] has been extrapolated to the above scenario. The statistical error is assumed to be identical (better flavour separation performance compensating for somewhat fewer events), and the relative systematic error is assumed to decrease by a factor of two due to smaller modelling errors. The two A_{FB}^b measurements have comparable errors and have been combined.

5.2 Determination of the Effective Heavy Quark Couplings

It is evident from equation 1.2 that the electron and heavy quark couplings cannot be viewed separately: Heavy quark measurements in unpolarized e^+e^- collisions are always sensitive to a product of electron and heavy quark couplings. Therefore, the heavy quark measurements from this thesis are fitted simultaneously with previous electroweak measurements performed at LEP1 and SLD. In this combined fit, the effective lepton (assuming lepton universality) and heavy quark couplings are left free.

The LEP Electroweak Working Group and the SLD Heavy Flavour and Electroweak Group perform a combined fit to the Z lineshape, using data from all five experiments. This fit yields the following results [3]:

m_Z	=	(91.1867 $\pm$0.0021) GeV	(mass of the Z)
Γ_Z	=	(2.4939 $\pm$0.0024) GeV	(total width of the Z)
σ_h^0	=	(41.491 $\pm$0.058) nb	(hadronic Z pole cross-section)
R_ℓ	=	20.765 $\pm$0.026	(ratio of hadronic and leptonic Z decay widths)
$A_{FB}^{0,\ell}$	=	0.01683$\pm$0.00096	(leptonic pole asymmetry)

These parameters are used in the fit together with the full correlation matrix. Information on the effective lepton couplings to the Z can also be obtained from measurements of the polarisation of τ pairs in Z decays, which yield a value of $\mathcal{A}_\ell = 0.1452 \pm 0.0034$ [3], and from the left-right asymmetry A_{LR} at SLD, where one finds $\mathcal{A}_\ell = 0.1504 \pm 0.0023$ [3]. For the calculation of radiative corrections, the value of the strong coupling constant at the Z mass is also needed.

The fit is based on a program provided by Klaus Mönig [71], which has been extended to cover the energy points above the Z resonance. In addition to the effective electron, charm, and bottom couplings to the Z boson, also the Z mass, the total and hadronic Z widths, and the value of the strong coupling constant α_s at the Z mass are left free. In each step of the minimization, the cross-sections and asymmetries are computed from the current values of the effective couplings using the ZFITTER program. These are compared with the measurements to calculate the χ^2 to be minimized. In the application of the ZFITTER program, care has been

data	coupling	fitted values	correlations					
LEP1, SLD	c_V^e	-0.03750 ± 0.00039	1.00	−0.04	−0.48	0.42	0.10	0.01
	c_A^e	-0.50000 ± 0.00026	−0.04	1.00	0.07	−0.03	−0.01	0.01
	c_V^b	-0.31819 ± 0.00887	−0.44	0.07	1.00	−0.97	−0.22	0.05
	c_A^b	-0.51677 ± 0.00574	0.42	−0.03	−0.97	1.00	0.20	−0.01
	c_V^c	0.17562 ± 0.00652	0.10	−0.01	−0.22	0.20	1.00	−0.03
	c_A^c	0.49937 ± 0.00555	0.01	0.01	0.05	−0.01	−0.03	1.00
PEP, PETRA, TRISTAN, LEP1, SLD, this thesis	c_V^e	-0.03749 ± 0.00039	1.00	−0.06	−0.39	0.38	0.11	0.01
	c_A^e	-0.50000 ± 0.00026	−0.06	1.00	0.08	−0.03	−0.04	0.02
	c_V^b	-0.31857 ± 0.00881	−0.39	0.08	1.00	−0.98	−0.15	0.00
	c_A^b	-0.51657 ± 0.00574	0.38	−0.03	−0.98	1.00	0.15	0.02
	c_V^c	0.17572 ± 0.00668	0.11	−0.04	−0.15	0.15	1.00	−0.08
	c_A^c	0.49908 ± 0.00566	0.01	0.02	0.00	0.02	−0.08	1.00

Table 5.2: The fitted effective vector and axial vector couplings to the Z boson for electrons, charm quarks, and bottom quarks are listed together with their correlations. For the results in the upper half of the table, only LEP1 and SLD measurements have been used, while for those in the lower half, also results from e^+e^- collisions below the Z resonance and from this thesis have been taken.

taken to account for the different conventions and cuts: The PEP, PETRA, and TRISTAN values are quoted at Born level, the LEP1/SLD values of R_b and R_c are given for pure Z exchange, and the LEP2 measurements are based on a $\sqrt{s'/s} > 0.85$ cut. The Standard Model predictions are used[1] for the hadronic cross-sections in order to compare the measured R_b values at TRISTAN and LEP2 with the ZFITTER prediction of $\sigma(e^+e^- \to b\bar{b})$.

From the fits, the effective coupling parameters of bottom and charm quarks to the Z boson can be extracted. The results are given in table 5.2 and are illustrated in the contour plots shown in figure 5.2. The results from the measurements above and below the Z resonance are consistent with the values determined from Z resonance data; however, for the determination of the size of the couplings, the measurements below and above the Z resonance add almost no additional information.

From measurements directly on the Z peak alone, there remain ambiguities in the determination of the effective vector and axial vector heavy quark couplings: These measurements are insensitive to an interchange of vector and axial vector couplings, or to a simultaneous sign change of both. According to equation 1.2, these ambiguities can be resolved with measurements at centre-of-mass energies away from the Z peak. To determine whether the alternative solutions are excluded by the data, the effective vector coupling is fixed, and the fit is performed with all other parameters left free. From the ambiguities, one expects secondary minima in the

[1]No significant deviations between the measured and predicted hadronic cross-sections have been observed; see for instance [38].

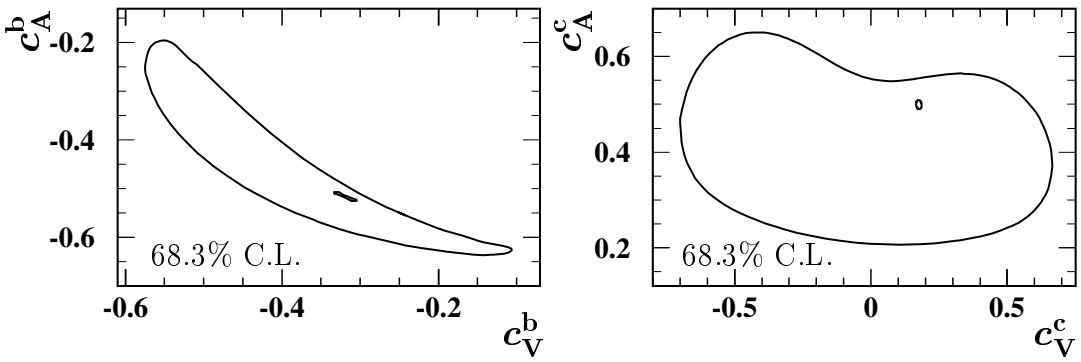

Figure 5.2: The fitted error contours at 68.3% confidence level (corresponding to $\Delta\chi^2 = 2.295$ with respect to the best fit result) are shown in the $c_V^q - c_A^q$ plane for bottom (left plot) and charm quarks (right plot). In both cases, the large area shows the constraints obtained from the measurements of this thesis alone. Additional constraints on the effective charm couplings would be possible with measurements of R_c at LEP2. As a comparison, the small contour corresponding to the allowed region from the combined LEP1 and SLD data is also indicated.

$\Delta\chi^2$ curves at values

$$c_V^q(\text{fixed}) \approx \begin{cases} c_A^q(\text{best fit}) & \text{(corresponding to an exchange } c_V^q \leftrightarrow c_A^q\text{),} \\ -c_V^q(\text{best fit}) & \text{(corresponding to sign changes } c_V^q \leftrightarrow -c_V^q, c_A^q \leftrightarrow -c_A^q\text{), and} \\ -c_A^q(\text{best fit}) & \text{(corresponding to both } c_V^q \leftrightarrow c_A^q \text{ exchange and sign changes).} \end{cases}$$

For both bottom and charm quarks, the dependence of the $\Delta\chi^2$ with respect to the best fit result is shown in figure 5.3 as a function of the fixed effective vector coupling. The ambiguities involving a sign change of both couplings are already fully resolved by the LEP1 and SLD measurements, and the sign of the third component I_3 of the weak isospin is unambiguous for both bottom and charm quarks (cf. equation 1.5). The solution with vector and axial vector couplings interchanged is also already excluded for charm quarks, while for bottom quarks, the data from LEP1 and SLD only exclude this alternative solution at $\Delta\chi^2 = 3.25$, corresponding to a 92.9% confidence limit. This is expected since the values of the effective bottom vector and axial vector couplings lie closer than those for charm quarks. The additional information from the measurements above and below the Z resonance can fully resolve this ambiguity, as shown in table 5.3.

5.3 An S-Matrix Parametrisation of the $e^+e^- \to b\bar{b}$ and $e^+e^- \to c\bar{c}$ Processes

In the framework of effective heavy quark vector and axial vector couplings to the Z, the measurements of heavy quark production and forward-backward asymmetries above and below the Z resonance are consistent with the Z resonance results. However, within this picture, the interference between s-channel γ and Z exchange is fixed once the effective couplings are known. As discussed in section 1.1.1, this is not the case in the S-Matrix approach, where the interference term is parametrised independently of pure γ and Z exchange.

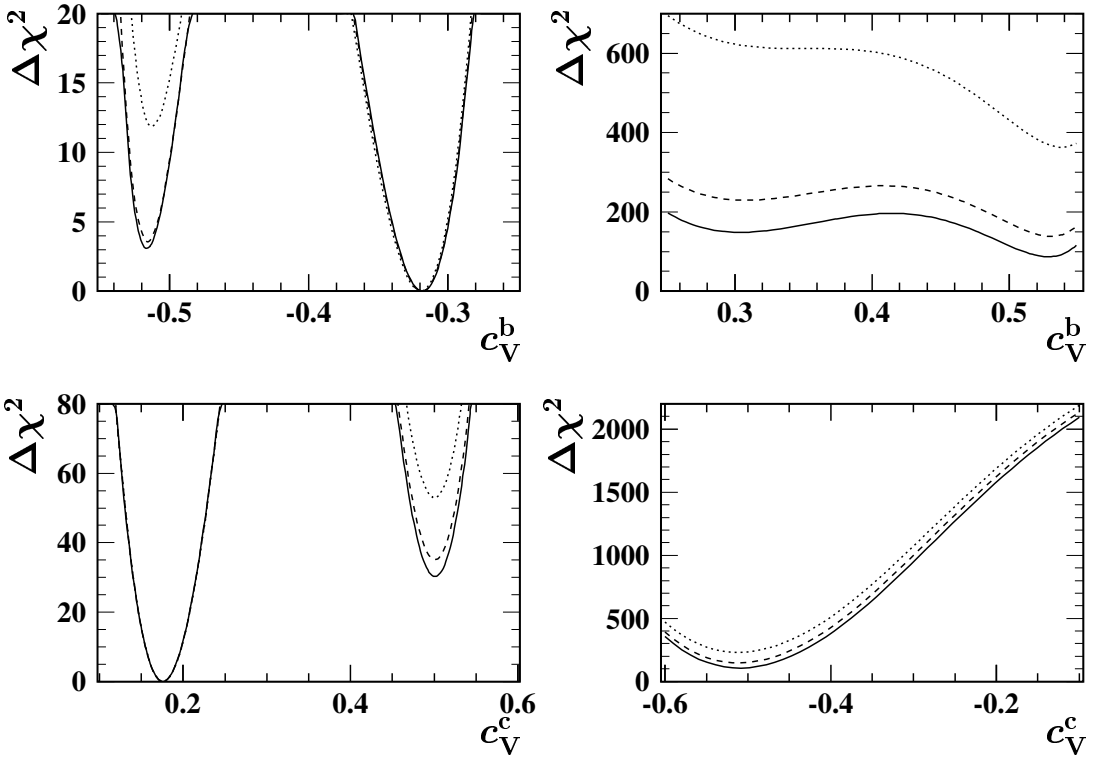

Figure 5.3: The $\Delta\chi^2$ with respect to the best fit result as determined from the fits with fixed effective heavy quark vector coupling are shown. The upper two plots show the results for bottom quarks, the lower plots those for charm quarks. The c_V^q ranges in the right plots cover the ambiguities that include a sign change in both couplings. In each plot, the solid line corresponds to the results obtained when only measurements from LEP1 and SLD are used; for the dashed line, also the results from this thesis are included, and the dotted line indicates the $\Delta\chi^2$ with PEP, PETRA, and TRISTAN measurements also taken into account.

measurements	$\Delta\chi^2$	confidence level
LEP1 and SLD	3.25	92.9%
LEP1, SLD, and this thesis	3.76	94.8%
LEP1, SLD, this thesis, PEP, PETRA, and TRISTAN	12.48	99.9%

Table 5.3: The confidence level at which the solution with c_V^b and c_A^b interchanged is excluded by different sets of data. While the measurements from this thesis contribute, the input from earlier measurements in e^+e^- collisions far below the Z resonance is still essential.

In this section, the S-Matrix parameters describing the $e^+e^- \to b\bar{b}$ and $e^+e^- \to c\bar{c}$ processes are determined for the first time. In previous S-Matrix fits, the hadronic two-fermion final states have only been treated inclusively, such that no information on $b\bar{b}$ and $c\bar{c}$ production, nor on

forward-backward asymmetries for processes with quarks in the final state could be obtained. It should be noted that a measurement of the S-Matrix parameters in the context of the Standard Model would in principle be possible with measurements at energies around and below the Z mass alone; however, this interpretation is only valid since no deviation from the Standard Model predictions is seen also for higher energies, as measured for instance in this thesis.

The measurements listed in table 5.1 are used in a fit to determine the S-Matrix parameters. For a given set of parameters, the $b\bar{b}$ or $c\bar{c}$ cross-section is determined, so the hadronic cross-section is needed as an input for a comparison with the measured values of R_b and R_c. For consistency, the hadronic cross-section is calculated in each step of the minimisation using the hadronic S-Matrix parameters determined by the LEP Electroweak Working Group in a fit to LEP1 and LEP2 data [3]. These parameters in turn are correlated with the leptonic[2] S-Matrix parameters and the Z mass and width. The inputs from the LEP1/LEP2 S-Matrix fit together with the correlation matrix are given in table 5.4.

parameter	average value	correlation matrix							
m_Z [GeV]	91.1882±0.0031	1.00	-0.13	-0.09	-0.08	-0.75	-0.43	0.14	-0.02
Γ_Z [GeV]	2.4945±0.0024	-0.13	1.00	0.80	0.61	0.16	0.09	0.00	0.07
r_{had}^{tot}	2.9637±0.0062	-0.09	0.80	1.00	0.77	0.13	0.06	0.02	0.09
r_ℓ^{tot}	0.14245±0.00032	-0.08	0.61	0.77	1.00	0.12	0.12	0.03	0.12
j_{had}^{tot}	0.14±0.14	-0.75	0.16	0.13	0.12	1.00	0.47	-0.14	0.03
j_ℓ^{tot}	0.004±0.012	-0.43	0.09	0.06	0.12	0.47	1.00	-0.05	0.02
r_ℓ^{fb}	0.00292±0.00019	0.14	0.00	0.02	0.03	-0.14	-0.05	1.00	0.15
j_ℓ^{fb}	0.780±0.013	-0.02	0.07	0.09	0.12	0.03	0.02	0.15	1.00

Table 5.4: The S-Matrix parameters and their correlations as determined by the LEP Electroweak Working Group in the fit to leptonic and hadronic events at LEP1 and LEP2 [3]. The mass and width of the Z boson have been corrected according to equation 1.12 to correspond to the usual definition.

In the fit, the S-Matrix parameters that describe pure photon exchange are fixed to the QED prediction. The following 16 parameters are fitted:

- the mass and width of the Z boson;
- the S-Matrix parameters r^{tot} for the total cross-section in pure Z exchange of leptonic, hadronic, $b\bar{b}$, and $c\bar{c}$ events;
- the $\gamma - Z$ interference terms j^{tot} for the total cross-section of leptonic, hadronic, $b\bar{b}$, and $c\bar{c}$ events;
- the parameters r^{fb} for the forward-backward asymmetric cross-section in pure Z exchange of leptonic, $b\bar{b}$, and $c\bar{c}$ events; and
- the $\gamma - Z$ interference terms j^{fb} for the forward-backward asymmetric cross-section of leptonic, $b\bar{b}$, and $c\bar{c}$ events.

[2]Lepton universality is assumed.

The full result of the fit to the measurements from PEP, PETRA, TRISTAN, LEP1, SLD, and from this thesis (which are listed in the upper part of table 3.1) is given in table 5.5. The correlation matrix is shown in table 5.6. The χ^2 per degrees of freedom for the central fit result is $41.2/(45-16)$, corresponding to a 6.6% fit probability (for a result with equal or higher χ^2). The most interesting parameters are those describing $\gamma-\mathrm{Z}$ interference for $\mathrm{b\bar{b}}$ and $\mathrm{c\bar{c}}$ final states. The error contours at 68.3% confidence level in the $j_{\mathrm{b}}^{\mathrm{tot}}-j_{\mathrm{b}}^{\mathrm{fb}}$ and $j_{\mathrm{c}}^{\mathrm{tot}}-j_{\mathrm{c}}^{\mathrm{fb}}$ planes are shown in figure 5.4. Within the errors, the measurements are consistent with the Standard Model expectations. The deviation of the $j_{\mathrm{b}}^{\mathrm{tot}}$ measurement from the predicted value does not represent a significant discrepancy at the current level of precision.

parameter	average value	Standard Model expectation
m_{Z} [GeV]	91.1881 ±0.0031	—
Γ_{Z} [GeV]	2.4945 ±0.0025	2.4944
$r_{\mathrm{had}}^{\mathrm{tot}}$	2.9638 ±0.0062	2.9656
r_{ℓ}^{tot}	0.14245±0.00032	0.14271
$r_{\mathrm{b}}^{\mathrm{tot}}$	0.6448 ±0.0026	0.6402
$r_{\mathrm{c}}^{\mathrm{tot}}$	0.494 ±0.011	0.511
$j_{\mathrm{had}}^{\mathrm{tot}}$	0.14 ±0.14	0.22
j_{ℓ}^{tot}	0.004 ±0.012	0.004
$j_{\mathrm{b}}^{\mathrm{tot}}$	0.234 ±0.056	0.042
$j_{\mathrm{c}}^{\mathrm{tot}}$	-0.33 ±0.16	0.05
r_{ℓ}^{fb}	0.00292±0.00019	0.00273
$r_{\mathrm{b}}^{\mathrm{fb}}$	0.0838 ±0.0017	0.0849
$r_{\mathrm{c}}^{\mathrm{fb}}$	0.0455 ±0.0025	0.0472
j_{ℓ}^{fb}	0.780 ±0.013	0.799
$j_{\mathrm{b}}^{\mathrm{fb}}$	0.670 ±0.058	0.799
$j_{\mathrm{c}}^{\mathrm{fb}}$	1.76 ±0.12	1.60

Table 5.5: The measured S-Matrix parameters. The Z mass and width, as well as the leptonic and hadronic S-Matrix parameters as determined by the LEP Electroweak Working Group have been fitted together with the heavy flavour measurements from PEP, PETRA, TRISTAN, LEP1, SLD, and this thesis.

When only the LEP1 and SLD heavy flavour measurements are used in the fit, the parameters describing $\gamma-\mathrm{Z}$ interference are essentially unconstrained, as expected. Conversely, an improvement will already be possible with the use of the full LEP2 data, as shown in figure 5.4. When data corresponding to the integrated luminosity of one year of operation of a future linear collider are also included, either precision measurements of the $\gamma-\mathrm{Z}$ interference for flavour tagged hadronic final states will be possible within the context of the Standard Model, or a clear failure of the approach used here should be found, indicating the presence of effects beyond the description in the Standard Model.

	m_Z	Γ_Z	r^{tot}_{had}	r^{tot}_{ℓ}	r^{tot}_{b}	r^{tot}_{c}	j^{tot}_{had}	j^{tot}_{ℓ}	j^{tot}_{b}	j^{tot}_{c}	r^{fb}_{ℓ}	r^{fb}_{b}	r^{fb}_{c}	j^{fb}_{ℓ}	j^{fb}_{b}	j^{fb}_{c}
m_Z	1.00	−.12	−.08	−.07	−.05	−.03	−.74	−.40	−.22	−.05	.14	.04	.04	−.02	.10	.02
Γ_Z	−.12	1.00	.80	.61	.43	.06	.15	.11	.05	.00	.01	.10	.03	.08	−.02	.01
r^{tot}_{had}	−.08	.80	1.00	.77	.54	.09	.12	.06	.04	.00	.02	.10	.03	.08	.00	.02
r^{tot}_{ℓ}	−.07	.61	.77	1.00	.41	.07	.11	.11	.04	.00	.04	.07	.02	.11	.00	.02
r^{tot}_{b}	−.05	.43	.54	.41	1.00	−.03	.06	.01	.05	.00	−.03	.11	−.02	.04	−.02	−.02
r^{tot}_{c}	−.03	.06	.09	.07	−.03	1.00	.02	.00	−.03	−.01	−.02	.04	.30	.01	.05	.12
j^{tot}_{had}	−.74	.15	.12	.11	.06	.02	1.00	.45	.30	.05	−.13	−.03	−.03	.02	−.14	−.01
j^{tot}_{ℓ}	−.40	.11	.06	.11	.01	.00	.45	1.00	.13	.04	−.06	−.01	−.01	.05	−.08	−.02
j^{tot}_{b}	−.22	.05	.04	.04	.05	−.03	.30	.13	1.00	−.42	−.03	−.06	.00	.01	−.44	.10
j^{tot}_{c}	−.05	.00	.00	.00	.00	−.01	.05	.04	−.42	1.00	.00	.04	−.05	−.02	.24	−.27
r^{fb}_{ℓ}	.14	.01	.02	.04	−.03	−.02	−.13	−.06	−.03	.00	1.00	−.01	.00	.07	.01	.00
r^{fb}_{b}	.04	.10	.10	.07	.11	.04	−.03	−.01	−.06	.04	−.01	1.00	.09	−.03	.09	−.01
r^{fb}_{c}	.04	.03	.03	.02	−.02	.30	−.03	−.01	.00	−.05	.00	.09	1.00	.00	−.01	.20
j^{fb}_{ℓ}	−.02	.08	.08	.11	.04	.01	.02	.05	.01	−.02	.07	−.03	.00	1.00	−.03	.01
j^{fb}_{b}	.10	−.02	.00	.00	−.02	.05	−.14	−.08	−.44	.24	.01	.09	−.01	−.03	1.00	−.03
j^{fb}_{c}	.02	.01	.02	.02	−.02	.12	−.01	−.02	.10	−.27	.00	−.01	.20	.01	−.03	1.00

Table 5.6: The correlation matrix of the measured S-Matrix parameters corresponding to the results in table 5.5.

5.4 Conclusion

From the heavy flavour measurements at 74 GeV and between 130 GeV and 189 GeV presented in chapters 4 and 3, the effective vector and axial vector couplings of bottom and charm quarks to the Z boson have been determined. The results are consistent with the effective coupling parameters obtained from the combined LEP1 and SLD data. The ambiguities in the effective heavy quark couplings that arise from measurements in Z decays alone have been studied. It has been found that all ambiguities are resolved at least at 99.9% confidence level. To exclude a solution with effective vector and axial vector bottom couplings interchanged, it is necessary to take into account measurements at e^+e^- centre-of-mass energies between $\sim$ 30 GeV and $\sim$ 60 GeV.

For the first time, an S-Matrix fit to the $e^+e^- \to b\bar{b}$ and $e^+e^- \to c\bar{c}$ processes has been performed. Heavy flavour measurements performed at the PEP, PETRA, and TRISTAN accelerators are combined with results obtained around the Z resonance by the LEP1 and SLD collaborations and with the heavy quark measurements above and below the Z resonance presented in this thesis. An S-Matrix fit to these data is performed, and the $\gamma - Z$ interference parameters j^{tot} and j^{fb} for $b\bar{b}$ and $c\bar{c}$ production are determined for the first time. They are

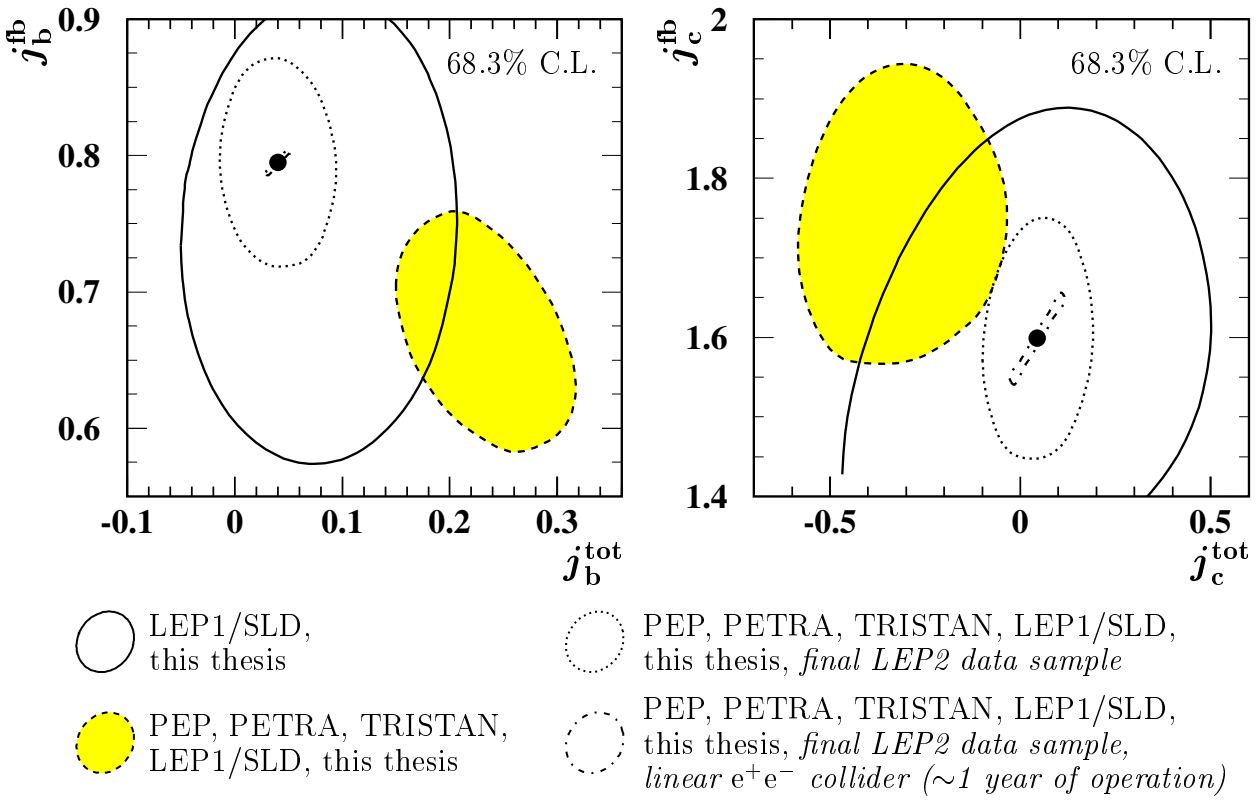

Figure 5.4: The S-Matrix fit results on the $\gamma - \mathrm{Z}$ interference parameters for heavy quarks are visualised. The fitted error contours at 68.3% confidence level (corresponding to $\Delta\chi^2 = 2.295$ with respect to the best fit result) are shown in the $j^{\mathrm{tot}} - j^{\mathrm{fb}}$ plane for both bottom (left plot) and charm quarks (right plot). Several fits have been performed with different sets of heavy flavour measurements used as input. The corresponding results are distinguished by the straight, dashed, dotted, and dash-dotted lines as explained in the figure. When the OPAL heavy flavour measurements from this thesis are used together with PEP, PETRA, TRISTAN, and LEP1/SLD results, the shaded area is allowed at 68.3% confidence level. For the fits with the expected final LEP2 precision and the measurements at a linear collider, only the size of the error ellipse is meaningful. The Standard Model expectation for the S-Matrix parameters is indicated by the black dots.

found to be

$$\begin{aligned} j_{\mathrm{b}}^{\mathrm{tot}} &= 0.234 \pm 0.056\,, \\ j_{\mathrm{c}}^{\mathrm{tot}} &= -0.33 \pm 0.16\,, \\ j_{\mathrm{b}}^{\mathrm{fb}} &= 0.670 \pm 0.058\,, \text{ and} \\ j_{\mathrm{c}}^{\mathrm{fb}} &= 1.76 \pm 0.12\,, \end{aligned} \tag{5.6}$$

consistent within the errors with the Standard Model expectations. The deviation of $j_{\mathrm{b}}^{\mathrm{tot}}$ from the Standard Model expectation of 0.042 is not significant.

The existing measurements at LEP2 are extrapolated to the full expected data sample, and the precision of heavy quark measurements at a future linear $\mathrm{e^+e^-}$ collider is estimated. The results with this expected data included are encouraging and will enable precision model-independent measurements of the interference of s-channel γ and Z exchange in flavour tagged hadronic final states.

Chapter 6

Measurements of D^{*0} and D_s^{*+} Production in Z Decays

In this chapter, measurements of D^{*0} and D_s^{*+} production in Z decays are presented. The hadronisation fraction $f(c \to D^{*0})$ is needed to obtain a complete picture of charm meson production in $Z \to c\bar{c}$ decays. This measurement is then used in the determination of the relative production of vector and pseudoscalar charmed mesons, which is described in chapter 7. This chapter is organized as follows: Section 6.1 describes the reconstruction of D^{*0} decays, the selection of signal candidates, and the background determination. In section 6.2, the measurement of the hadronisation fraction $f(c \to D^{*0})$ and its systematic uncertainties are discussed, while section 6.3 describes the measurement of D_s^{*+} production. The results are summarized in section 6.4.

6.1 Reconstruction and Selection of D^{*0} Candidates

In Z decays, D^{*0} mesons are dominantly produced in $Z \to c\bar{c}$ events and in the decay of bottom hadrons. The criteria for selecting hadronic Z decays are identical to those applied in the previous sections, with the momentum imbalance requirement set to $R_{\mathrm{bal}} \equiv |\sum (E \cdot \cos\theta)_{\mathrm{clus}}| \,/\, \sum E_{\mathrm{clus}} < 0.65$. Of the events recorded with the OPAL detector between 1990 and 1995, 4.32 million satisfy the event selection criteria.

Samples of simulated hadronic events are used for the determination of selection criteria and for the calculation of selection efficiencies. The same samples as used in chapter 4 for the simulation of non-radiative events are taken. They have been generated using the JETSET 7.4 Monte Carlo model [43] with parameters tuned to reproduce the OPAL data [64]. The fragmentation of heavy quarks is parametrised by the fragmentation function of Peterson et al. [65]. The simulated events are then processed by the detector simulation program [47] and by the same reconstruction algorithm which is also applied to the data.

In the selected hadronic events, D^{*0} mesons are reconstructed in the decay modes $D^{*0} \to D^0\gamma$ and $D^{*0} \to D^0\pi^0$. The transition photon or π^0 meson is expected to be dominantly produced in the core of the jet that contains the D^{*0}. Thus, for the reconstruction of $D^{*0} \to D^0\gamma$ decays, a considerable background level is expected from photons originating in decays of π^0 mesons from other sources, while the reconstruction of $D^{*0} \to D^0\pi^0$ decays suffers from combinatorial

background in the $\pi^0 \to \gamma\gamma$ reconstruction. The reconstruction proceeds by first finding D^0 candidates, which are then combined with a photon or a π^0. After a loose preselection, a likelihood method is used for the final selection of candidates. In this section, the selection and the background determination are described.

6.1.1 Reconstruction of D^0 Mesons, Photons, and π^0 Mesons

Both the preselection for the D^0, photon, and π^0 reconstruction and the likelihood for the D^{*0} selection are based on the variables which are explained below.

The decay mode $D^0 \to K^-\pi^+$ is used to reconstruct D^0 mesons. Initially, all possible pairs of oppositely charged tracks are formed, assigning kaon and pion masses to the tracks. Variables for the selection of D^0 candidates are:

- the invariant mass m_{D^0} and the scaled energy $x_{D^0} = E_{D^0}/E_{\text{beam}}$ of the D^0 candidate;
- the cosine of the helicity angle θ^* measured between the direction of the charged pion in the D^0 rest frame and the D^0 direction in the laboratory frame;
- the signed probability W_X as defined in section 2.1 that a given track is compatible with the particle hypothesis X, based on its specific energy loss and its measured momentum;
- the signed decay length d_{xy} in the xy plane defined as the distance between the primary vertex and the secondary vertex formed by the D^0 decay products; and
- the largest longitudinal momentum p^l_{frag} relative to the D^0 flight direction of any track which is not used in the D^0 reconstruction and whose charge is inconsistent with that of an accompanying hadron of the D^0 candidate. This variable helps to separate signal candidates in $Z \to c\bar{c}$ events from background, since in the formation of D^0 mesons in $Z \to c\bar{c}$ events, there is a correlation between the charge of the primary quark and that of the fragmentation particle with the highest longitudinal momentum [75]. The track with the largest longitudinal momentum whose charge is inconsistent with being the accompanying hadron is expected to be softer for signal than for background.

Contributions from D^{*+} decays are suppressed by searching for a track that could have been the pion in a $D^{*+} \to D^0\pi^+$ decay. The corresponding D^0 candidate is rejected if a track is found with the correct charge and a mass difference within $141\text{MeV} < m_{D^0\pi^+} - m_{D^0} < 152\text{MeV}$.

A loose preselection of D^0 candidates is done using the invariant mass m_{D^0}, the scaled energy x_{D^0}, the helicity angle $\cos\theta^*$, and the particle identification probabilities. The exact cuts are listed in table 6.1.

Photons are reconstructed either as showers in the electromagnetic calorimeter, or through conversions $\gamma \to e^+e^-$. For the latter, pairs of oppositely charged tracks are identified as conversions with the algorithm described in [76]. The z components of the track momenta are determined in a fit to the conversion point to improve the momentum resolution. The total photon momentum is taken as the sum of both track momenta.

In the barrel region of the electromagnetic calorimeter, photons are identified as described in [76] by fitting electromagnetic showers to energy deposits which are not associated with any charged particle track. The lateral shower profile is fixed to the Monte Carlo expectation, and the normalisation gives the shower energy. The fitted shower energy is then corrected for losses in the material in front of the calorimeter using information from the presampler and time-of-flight system. Each of the fitted showers is treated as a photon candidate. The photon

D^0 reconstruction
$1.81\,\mathrm{GeV} < m_{D^0} < 1.93\,\mathrm{GeV}$
$0.3 < x_{D^0}$
$-0.85 < \cos\theta^* < 0.85$
$W_K(K) < -1\%$ or $+3\% < W_K(K)$
$-35\% < W_\pi(K) < 0\%$
$W_\pi(\pi) < -1\%$ or $+1\% < W_\pi(\pi)$
photon and π^0 reconstruction
$800\mathrm{MeV} < E_\gamma$ or $800\mathrm{MeV} < E_{\pi^0}$
$60\mathrm{MeV} < m_{\gamma\gamma} < 280\mathrm{MeV}$

Table 6.1: The preselection cuts for the reconstruction of D^{*0} candidates. The selection variables are defined in the text.

momenta are calculated assuming that the photons originated at the primary vertex of the event.

Any pair of photons (showers or conversions) with an invariant mass between 60MeV and 280MeV is considered as a π^0 candidate. The resolution of the π^0 energy is improved by a constraint to the nominal π^0 mass [77] using a kinematic fit [76].

A number of variables similar to those in reference [76] are calculated for each photon and π^0 candidate:

- the energy of the photon or π^0 candidate, denoted E_γ or E_{π^0}, respectively;
- for photon conversions, the signed electron identification probabilities W_e calculated from the energy loss of the two conversion tracks;
- for showers in the calorimeter, a variable which parametrises how well the fitted shower describes the measured energy distribution in the 9 calorimeter blocks around the fitted shower maximum; and three variables that describe their effective separation from the closest neighbouring shower and the closest charged track entering the calorimeter.

The following variables are only used in the selection of π^0 mesons:

- the invariant mass of the $\gamma\gamma$ system and the opening angle between the two photons; as well as
- the number of additional photon candidates in a cone around each of the two photon candidates under consideration. In each case, the opening angle of the cone is twice the angle between the two photons.

A loose preselection of photons and π^0 candidates is done using the photon or π^0 energy and the invariant $\gamma\gamma$ mass before the constraint to the π^0 mass, as listed in table 6.1.

To form D^{*0} candidates, each of the preselected D^0 candidates is in turn combined with every preselected shower photon or π^0 candidate in the event. Figure 6.1 shows the distribution of these D^{*0} candidates in four of the most powerful selection variables. Tighter requirements are then applied to further reduce the background level in the D^{*0} sample. They are based on the variables listed above and on the total number of D^{*0} candidates in the hemisphere. For each variable x_i, a purity function $\lambda_i(x_i)$ is calculated based on the simulation as the ratio of $c \to D^{*0}$

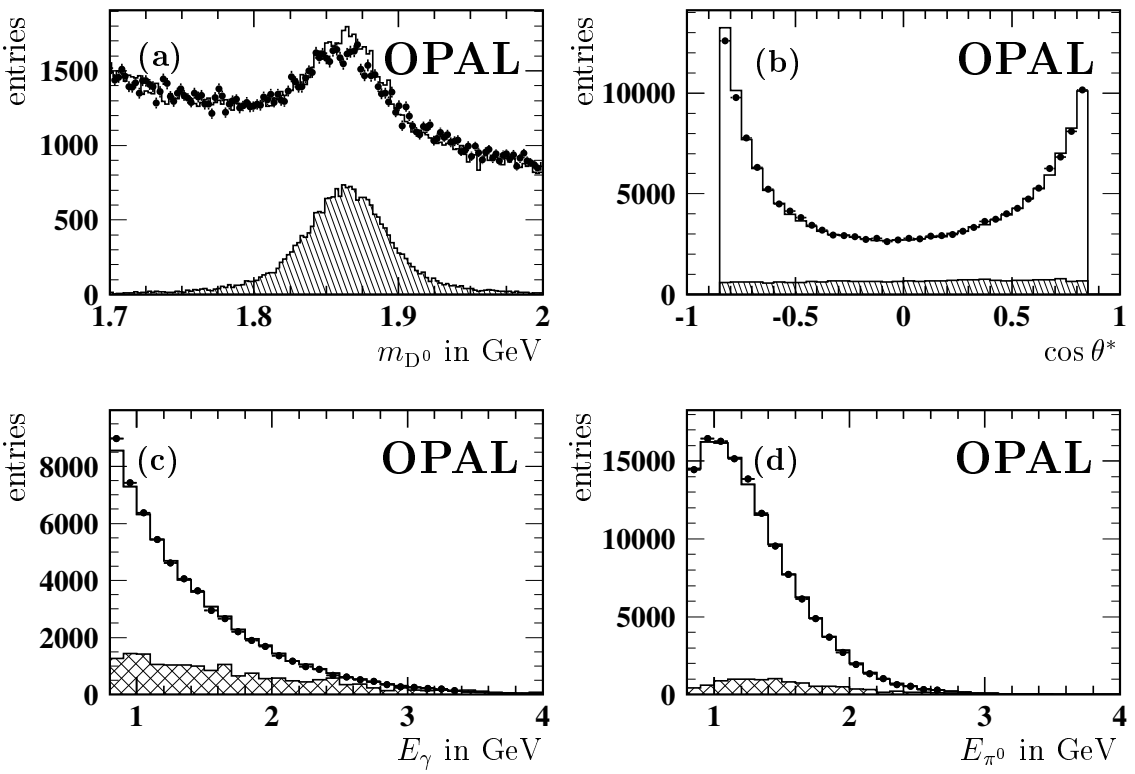

Figure 6.1: The distributions of the four D^{*0} selection variables m_{D^0}, $\cos\theta^*$, E_γ and E_{π^0} are shown for all preselected candidates. In each case, points with error bars correspond to the data and the open histogram to the simulation, scaled to the same number of entries. In figures (a) and (b), the contribution from D^{*0} candidates with a correctly reconstructed $\mathrm{D}^0 \to \mathrm{K}^-\pi^+$ decay is shown as the hatched area. The cross-hatched areas in figures (c) and (d) correspond to 10 times the contribution of correctly reconstructed photons or π^0 mesons from a D^{*0} decay.

signal candidates to all candidates:

$$\lambda_i(x_i) = \frac{\text{signal}}{(\text{signal} + \text{background})}(x_i)\,, \tag{6.1}$$

and a likelihood is constructed as

$$\mathcal{L}(x_1, ..., x_n) = \left(\prod_{i=1}^{n} \lambda_i(x_i) \right)^{1/n} . \tag{6.2}$$

Finally, D^{*0} candidates are selected using a cut on the likelihood value. This cut has been chosen such that the statistical error on the result for the hadronisation fraction $f(\mathrm{c} \to \mathrm{D}^{*0})$ is minimised according to an independent sample of simulated events. The distributions of the likelihood functions $\mathcal{L}$ are shown in figure 6.2 together with the cut values.

In figure 6.3, the $\Delta m = m_{\mathrm{D}^{*0}} - m_{\mathrm{D}^0}$ mass difference distributions of the selected candidates are shown. The peaks at low mass differences are due to the signal from D^{*0} decays. The background shape is determined from the data as described below in section 6.1.2. Using this shape, the D^{*0} yield is extracted from a fit to the mass difference distributions, which is discussed in section 6.2.2.

If correlations are present between different input variables x_i for either signal or background, the likelihood in equation 6.2 is non-optimal, and a better separation of signal and background could in principle be achieved with a selection based on an artificial neural network. However, the most powerful selection variables are essentially uncorrelated in the simulation, leaving little room for improvement. On the other hand, the procedure for background determination discussed in section 6.1.2 relies on the likelihood selection described above and would not be possible for a neural network based selection.

6.1.2 Background Determination

Even after applying the likelihood selection, the background level in the samples of D^{*0} candidates is still high. To minimise the dependence on Monte Carlo modelling, a method has been developed to determine the shape of the background in the Δm distributions from the data.

A sample of candidates enriched in background rather than signal is prepared with a method similar to the one for the signal selection (see section 6.1.1). The likelihood is modified to select background candidates from the m_{D^0} sideband regions $1.70\ \mathrm{GeV} < m_{\mathrm{D}^0} < 1.84\ \mathrm{GeV}$ and $1.91\ \mathrm{GeV} < m_{\mathrm{D}^0} < 2.00\ \mathrm{GeV}$. The sidebands are chosen to lie close to the signal region so that the kinematical properties of candidates in the sidebands do not differ significantly from those of candidates in the signal region. The modified likelihood function is of the form

$$\mathcal{L}'(x_1, ..., x_n) = \left(\lambda'_{m_{\mathrm{D}^0}}(m_{\mathrm{D}^0})\, \lambda'_{\cos\theta^*}(\cos\theta^*) \prod_{x_i \neq m_{\mathrm{D}^0}, \cos\theta^*} \lambda_i(x_i) \right)^{1/n} , \tag{6.3}$$

with the λ functions left unchanged for all selection variables except m_{D^0} and $\cos\theta^*$. Because the original likelihood function $\mathcal{L}$ depends on m_{D^0} and $\cos\theta^*$, new functions $\lambda'_{m_{\mathrm{D}^0}}(m_{\mathrm{D}^0})$ and $\lambda'_{\cos\theta^*}(\cos\theta^*)$ have to be introduced such that the shapes of the distributions of the likelihoods $\mathcal{L}$ and $\mathcal{L}'$ agree for background. In practise, this is done by constructing the λ' functions for

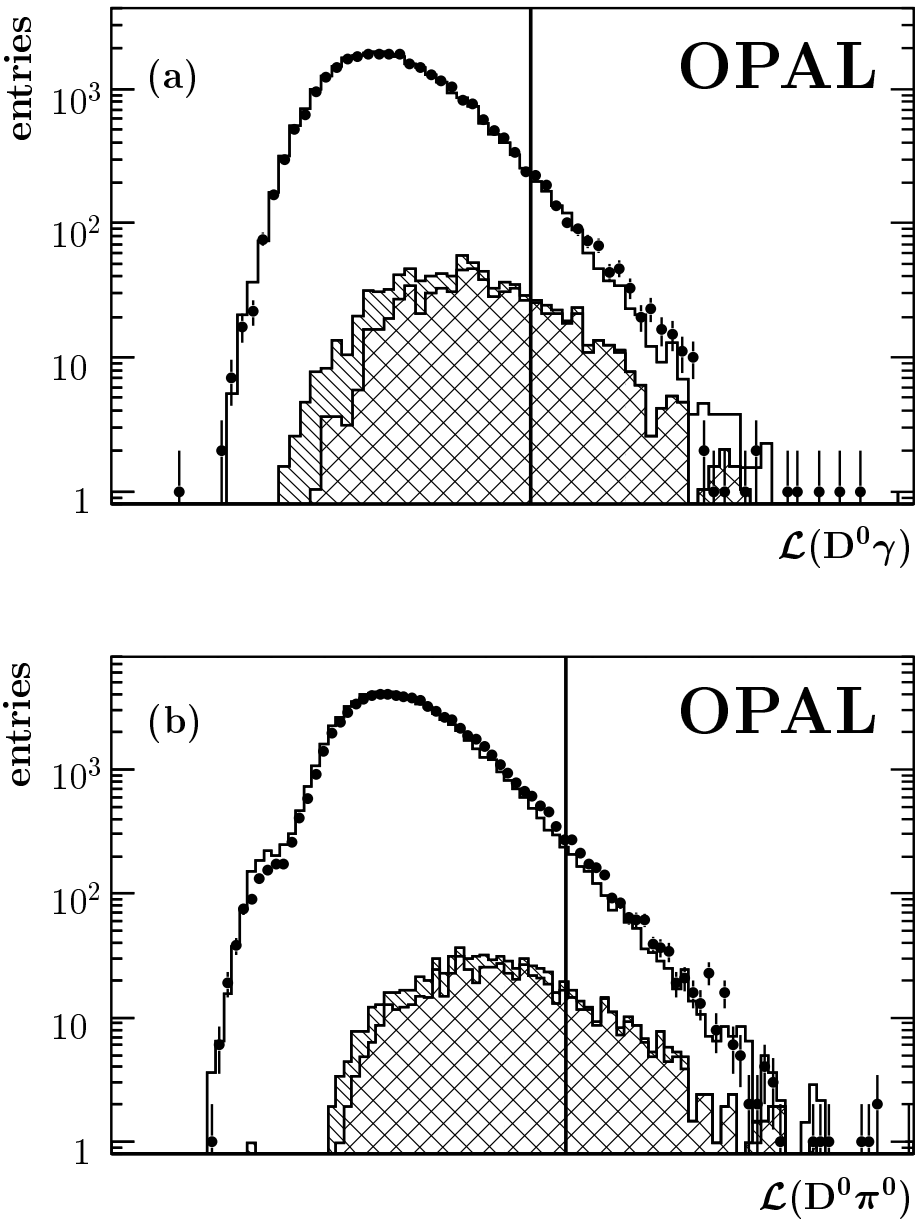

Figure 6.2: The distributions of the likelihood functions $\mathcal{L}$ for the two D^{*0} decay channels. Points with error bars represent the data and open histograms the simulation, scaled to the same number of entries. The hatched histograms show candidates in the simulation with a correctly identified photon or π^0 from a D^{*0} decay; for candidates entering the cross-hatched histogram, the $D^0 \to K^-\pi^+$ decay is also correctly reconstructed. The vertical lines represent the cuts on the likelihood functions. No scale is given for the likelihood values since only the relative position of the cut is relevant.

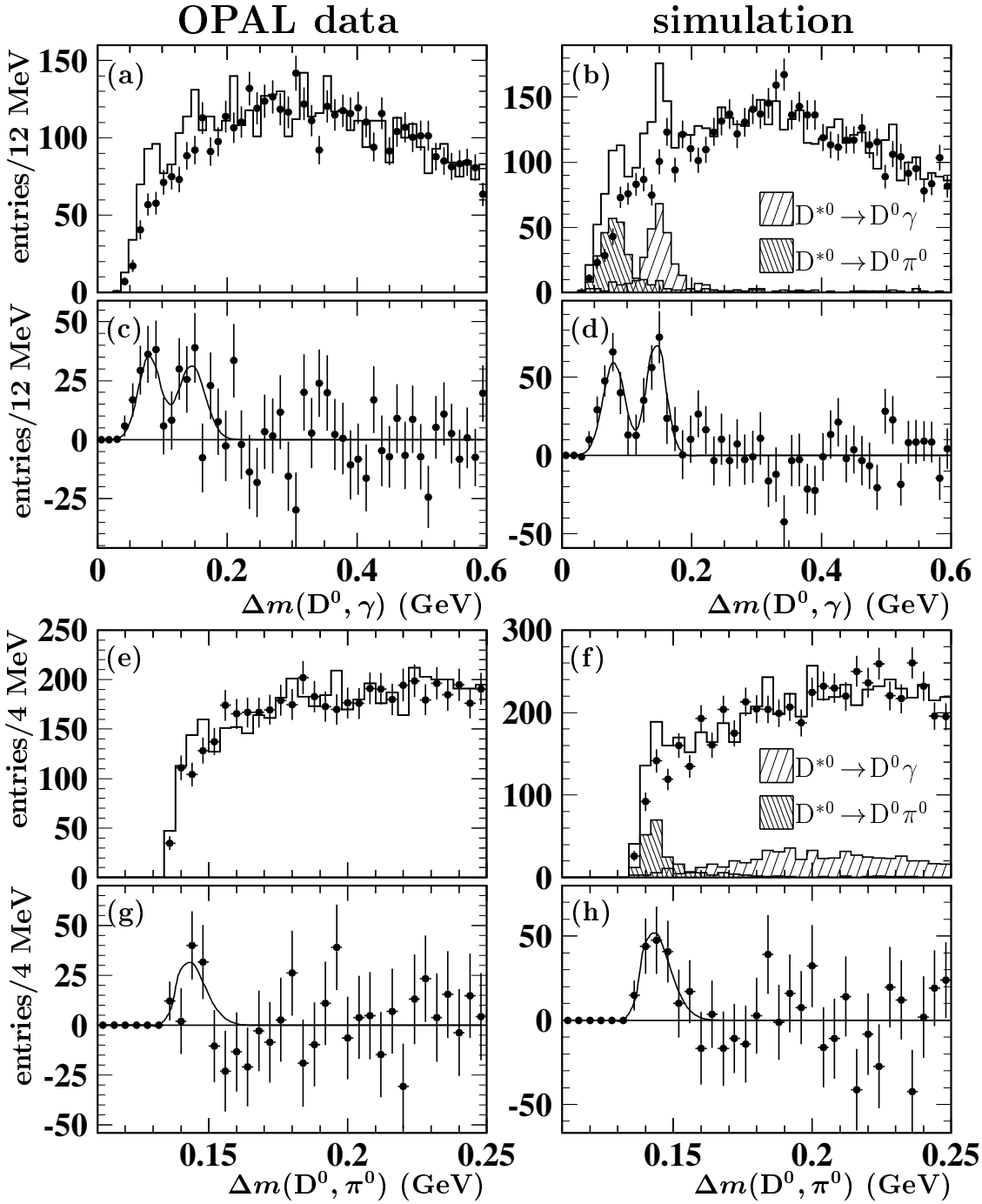

Figure 6.3: The $\Delta m(\mathrm{D}^0, \gamma)$ and $\Delta m(\mathrm{D}^0, \pi^0)$ mass difference distributions in the data and the simulation.
In (a), (b), (e), and (f), the distributions obtained in the signal selection procedure are shown as solid histograms, and those obtained in the background selection procedure as points with error bars, where the relative normalisation of the latter distribution has been determined in the fit. In addition, the hatched histograms show the distributions of signal candidates reconstructed in the simulation with the signal selection procedure.
In (c), (d), (g), and (h), the corresponding background subtracted distributions are shown together with the fit results; the error bars show the statistical errors only.

m_{D^0} and $\cos\theta^*$ separately, with the same set of values as for the corresponding λ function. For the selection of background candidates, the same cut is placed on $\mathcal{L}'$ as is on $\mathcal{L}$ for signal candidates.

One of the main requirements for the background selection is that it correctly reproduces the Δm shape of true background. If the selection variables m_{D^0} and $\cos\theta^*$ are assumed to be uncorrelated with the other selection variables and the mass difference Δm, the Δm shapes of background candidates from the same source in the signal and background samples agree by construction. For true background, the correlations between m_{D^0} ($\cos\theta^*$) and any other selection variable have been found in the simulation to be $\leq 1\%$ ($< 10\%$), where the largest correlations are between $\cos\theta^*$ and p^l_{frag} (-9%) or $W_\pi(\pi)$ (-7%). It has been tested in the simulation that even with this level of correlations, the background shape is correctly reproduced for background candidates from the same source.

Background can be classified into candidates where a correctly reconstructed D^0 is combined with a photon or π^0 that does not come from a D^{*0} decay and other background, in which the charged pion and kaon candidates do not come from the same D^0 decay. For these two contributions, the shapes of the Δm distributions are found to be slightly different in the simulation. As outlined above, it is expected that the background determination procedure yields the correct background shapes individually for both contributions. However, the background sample contains fewer candidates with a correctly reconstructed D^0 than the signal sample. This leads to a small bias in the overall background shape derived from the background selection, which is taken into account by reweighting this shape according to the sample composition in the signal and background samples as found in the simulation.

Candidates that pass the cuts on $\mathcal{L}$ and also on $\mathcal{L}'$ are rejected from both the signal and the background samples. In the simulation, it has been found that this requirement rejects 8% of the true signal from the signal sample, and 27% of the true signal in the background sample. It has also been verified that the fraction of candidates removed by this requirement is the same within errors for the data and the simulation.

Although the background sample is depleted in signal candidates relative to the signal sample, there is a remaining D^{*0} signal contamination in the background sample. Typically, the signal fraction is a factor of 5 smaller (cf. table 6.2) in the background samples. These candidates have the effect of reducing the number of signal candidates after background subtraction and are taken into account by calculating an effective efficiency, which is described in the next section.

6.1.3 Reconstruction Efficiency

The efficiencies of the D^{*0} reconstruction are determined from a Monte Carlo sample which is statistically independent from the one that has been used for the determination of the likelihood. In this sample of 6.5 million simulated hadronic events, the numbers of true D^{*0} mesons that pass the cuts on $\mathcal{L}$ are computed. The resulting efficiencies in the different decay modes are listed in table 6.2, separately for $\mathrm{Z}\to\mathrm{c\bar{c}}$ and $\mathrm{Z}\to\mathrm{b\bar{b}}$ events.

As discussed in section 6.1.2, some D^{*0} mesons are also contained in the background-enriched samples. This number is determined from the same set of simulated events, and an effective efficiency is computed from the values given in table 6.2 that takes into account the relative signal to background ratio of the background sample that is given in the last column of the

table. In the fit to the mass difference distributions described in section 6.2.2, these effective efficiencies are used.

decay chain	distribution	efficiency, $c \to D^*$	efficiency, $b \to [c, \bar{c}] \to D^*$	$(\frac{s}{b})^{bkg}/(\frac{s}{b})^{sig}$
$D^{*0} \to D^0\gamma$ $\hookrightarrow K^-\pi^+$	$\Delta m(D^0, \gamma)$	$(2.88 \pm 0.16)\%$	$(2.15 \pm 0.19)\%$	0.20 ± 0.03
$D^{*0} \to D^0\pi^0$ $\hookrightarrow K^-\pi^+$	$\Delta m(D^0, \gamma)$ $\Delta m(D^0, \pi^0)$	$(1.80 \pm 0.10)\%$ $(1.18 \pm 0.08)\%$	$(1.01 \pm 0.10)\%$ $(1.05 \pm 0.10)\%$	0.20 ± 0.03 0.16 ± 0.01

Table 6.2: The reconstruction efficiencies for a given decay chain in a given mass difference distribution as determined from the simulation. Note that $D^{*0} \to D^0\pi^0$ decays are measured in both the $\Delta m(D^0, \gamma)$ and $\Delta m(D^0, \pi^0)$ distributions. The efficiencies are based on candidates with scaled energies $x_{D^0} > 0.3$. Only statistical errors are listed. The signal to background ratios $(\frac{s}{b})^{bkg}$ in the background samples relative to the ratio $(\frac{s}{b})^{sig}$ in the corresponding signal sample are given in the last column.

6.2 Measurement of $f(c \to D^{*0})$

The dominant sources of D^{*0} mesons in Z decays are the production in $Z \to c\bar{c}$ events and in bottom hadron decays. For scaled energies $x_{D^0} > 0.3$, the production of D^{*0} mesons in gluon splitting processes $g \to c\bar{c}$ is highly suppressed and will be neglected in the following.

The hadronisation fraction $f(c \to D^{*0})$ is determined in a fit to the $\Delta m = m_{D^{*0}} - m_{D^0}$ distributions of the selected signal and background samples. A simultaneous fit is performed to the Δm distributions of both $D^0\gamma$ and $D^0\pi^0$ candidates. In the fit, the contributions from b hadron decays are subtracted, and the fitted signals are corrected for the efficiency in $Z \to c\bar{c}$ events. In this section, the determination of the signal contributions from b hadron decays, the fit to the mass difference distributions, and systematic uncertainties of the measurement are discussed.

6.2.1 Subtraction of the Component from b Hadron Decays

The determination of the contribution from b hadron decays is based on a previous measurement of D^{*+} production in $Z \to b\bar{b}$ events [53]. For decays of non-strange B mesons, this is justified from the CLEO measurement [78] of

$$\frac{Br(B \to D^{*0}X)}{Br(B \to D^{*+}X)} = 1.03 \pm 0.14\,, \tag{6.4}$$

where the error is taken into account as described in section 6.2.4.4. Decays of $\overline{B}^0$ and B^- mesons account for most D^{*0} mesons from b hadron decays at LEP, since $\overline{B_s^0}$ mesons preferentially decay to final states with a D_s^+ [77], and b baryons are expected to decay dominantly to final states with a c baryon. The production of D^{*0} mesons in $\overline{B_s^0}$ and b baryon decays is assessed as described in section 6.2.4.4. The subtraction of the component from $Z \to b\bar{b}$ events is done for scaled energies $x_{D^0} > 0.3$, and the remaining $c \to D^{*0}$ signal is then extrapolated to the full x_{D^0} range.

Previously, OPAL has measured the production of D^{*+} mesons in $Z \to b\bar{b}$ events to be $R_b\, f(b \to [c,\bar{c}] \to D^{*\pm})\, Br(D^{*+} \to D^0\pi^+)\, Br(D^0 \to K^-\pi^+) = (1.334 \pm 0.049 \pm 0.078) \times 10^{-3}$ [53]. Using this number and the branching ratio $Br(D^{*+} \to D^0\pi^+) = 0.683 \pm 0.014$ [77], the D^{*+} production rate in $Z \to b\bar{b}$ events for $x_{D^0} > 0.3$ is calculated to be

$$\beta \equiv R_b\, f(b \to [c,\bar{c}] \to D^{*\pm})\, Br(D^0 \to K^-\pi^+)\big|_{x_{D^0}>0.3} = (0.980 \pm 0.068) \times 10^{-3}\ . \qquad (6.5)$$

The error includes both the statistical and systematic errors. The restriction to $x_{D^0} > 0.3$ is based on Monte Carlo simulation and the measured parameters of the b fragmentation function.

This information is used to obtain the number of reconstructed D^{*0} signal candidates from b hadron decays, which is then subtracted from the fitted signal. Thus, the hadronisation fraction $f(c \to D^{*0})\big|_{x_{D^0}>0.3}$ is determined in the fit from

$$R_c\, f(c \to D^{*0})\, Br(D^0 \to K^-\pi^+)\big|_{x_{D^0}>0.3} = \sum_{X=\gamma,\pi^0} \frac{\frac{N_{sig}(D^{*0} \to D^0 X)}{2N_{had}} - \beta\, Br(D^{*0} \to D^0 X)\ \varepsilon_b^{D^{*0} \to D^0 X}}{\varepsilon_c^{D^{*0} \to D^0 X}}, \qquad (6.6)$$

where N_{sig} denotes the signal as obtained from the mass difference distribution, N_{had} is the number of hadronic Z decays analysed, ε_c and ε_b are the effective efficiencies for reconstructing D^{*0} decays with $x_{D^0} > 0.3$ from $Z \to c\bar{c}$ and $Z \to b\bar{b}$ decays, respectively, and the sum runs over the two decay modes of the D^{*0}.

6.2.2 The Fit to the Mass Difference Distributions

The number of reconstructed D^{*0} decays is determined in a simultaneous fit to the mass difference distributions of the selected signal and background samples in the two decay modes $D^{*0} \to D^0\gamma$ and $D^{*0} \to D^0\pi^0$.

Two signal peaks are visible in the mass difference distribution of $D^0\gamma$ candidates, which is shown in figure 6.3a. The peak at the nominal D^{*0}–D^0 mass difference of 142 MeV [77] is due to $D^{*0} \to D^0\gamma$ decays, whereas the one at lower Δm values is from $D^{*0} \to D^0\pi^0$ decays, where only one photon from the π^0 decay is combined with the D^0 candidate.

In the mass difference distribution of $D^0\pi^0$ candidates, the signal from $D^{*0} \to D^0\pi^0$ decays is expected around the nominal mass difference. Additional contributions are expected from $D^{*0} \to D^0\gamma$ and $D^{*0} \to D^0\pi^0$ decays, where only one of the two photons from the π^0 decay is used. In both cases, an unrelated photon candidate is added to form a π^0 candidate. In the simulation, both contributions have been found to be broad and very similar in shape to the overall background. Therefore, they are not explicitly accounted for.

In both mass distributions, the signal is parametrised with a functional form, while the background shape is determined from the background sample as decribed in section 6.1.2, with its normalisation determined in the fit. A sum of two Gaussians is used as signal parametrisation for the Δm distribution of $D^0\gamma$ candidates (see figure 6.3c and d) in order to accomodate the contributions from both $D^{*0} \to D^0\gamma$ and $D^{*0} \to D^0\pi^0$ decays. The mean values of the Gaussians are fixed to 145 MeV ($D^{*0} \to D^0\gamma$) and 80 MeV ($D^{*0} \to D^0\pi^0$) as determined from the simulation,

and the widths are allowed to vary. For $\mathrm{D}^0\pi^0$ candidates, a modified Gaussian of the form

$$\frac{\mathrm{d}n}{\mathrm{d}(\Delta m)} \sim \left(\Delta m - m_{\pi^0}\right) \exp\left(-\frac{1}{2}\left(\frac{\Delta m - m_{\pi^0}}{\sigma}\right)^2\right) ; \quad \Delta m > m_{\pi^0} \tag{6.7}$$

is taken as the signal parametrisation (see figure 6.3g and h) to account for threshold effects. Here, m_{π^0} denotes the nominal π^0 mass [77], and the parameter σ and the normalisation are determined in the fit. In the simulation, such a function has been found to parametrise the distribution of $\mathrm{D}^0\pi^0$ signal candidates well.

The hadronisation fraction $f(\mathrm{c} \to \mathrm{D}^{*0})$ is determined from a simultaneous fit to both Δm distributions, with the constraint that the efficiency corrected number of $\mathrm{D}^{*0} \to \mathrm{D}^0\pi^0$ decays be the same whether determined from the peak at lower Δm values in the $\Delta m(\mathrm{D}^0, \gamma)$ distribution or from the $\Delta m(\mathrm{D}^0, \pi^0)$ distribution. Also, the efficiency corrected numbers for the two D^{*0} decay channels are fixed to the world average value of the branching ratio $Br(\mathrm{D}^{*0} \to \mathrm{D}^0\gamma)/Br(\mathrm{D}^{*0} \to \mathrm{D}^0\pi^0) = 0.616 \pm 0.076$ [77], and it is assumed that these two decay modes saturate the D^{*0} width. The contribution from bottom hadron decays, which is derived from an earlier OPAL measurement as described in section 6.2.1, is subtracted in the fit.

The fit results are illustrated in figure 6.3, where the obtained signal parametrisations are shown together with the background subtracted mass difference distributions. The combined fit for the D^{*0} measurement has a χ^2 of 61.6 for 69 degrees of freedom. The hadronisation fraction $f(\mathrm{c} \to \mathrm{D}^{*0})\big|_{x_{\mathrm{D}^0} > 0.3}$ is extrapolated to the full range of scaled energies x_{D^0} using the simulation; it is found to be

$$R_\mathrm{c}\, f(\mathrm{c} \to \mathrm{D}^{*0})\, Br(\mathrm{D}^0 \to \mathrm{K}^-\pi^+) \;\; = \;\; (1.44 \pm 0.36) \times 10^{-3}\,, \tag{6.8}$$

where the error is statistical.

6.2.3 Consistency Checks

A number of consistency checks has been performed, in particular to test the sensitivity of the result to the background subtraction procedure. Monte Carlo simulation has been used to check that the procedure as outlined in section 6.1.2 accurately describes the shape of the background in the signal sample. Also, it has been verified that the shape is not sensitive to the specific choice of λ' functions. The background determination is sensitive to correlations between m_{D^0} or $\cos\theta^*$ and any other selection variable. Any correlation seen in the data is well reproduced in the simulation. Finally, the analysis has been repeated on the simulation, and the generated rates are reproduced within the statistical errors.

For all selections, the likelihood cut has been varied and the analysis repeated. The ranges of cut values correspond to relative changes in efficiency of about $\pm 50\%$. The variations have been found to be consistent with statistical fluctuations.

In the fit, the ratio $Br(\mathrm{D}^{*0} \to \mathrm{D}^0\gamma)/Br(\mathrm{D}^{*0} \to \mathrm{D}^0\pi^0)$ is fixed to its world average value of 0.616 ± 0.076 [77]. If instead, it is allowed to vary, a value of $Br(\mathrm{D}^{*0} \to \mathrm{D}^0\gamma)/Br(\mathrm{D}^{*0} \to \mathrm{D}^0\pi^0) = 0.39 \pm 0.17\,(\mathit{stat.})$ is found, which is consistent with the world average. The resulting hadronisation fraction $f(\mathrm{c} \to \mathrm{D}^{*0})$ changes by -7.5%.

6.2.4 Systematic Uncertainties

Systematic uncertainties are related to the modelling of the selection variables, the detector resolution, the procedure used to subtract the background, the determination of the $b \to [c, \overline{c}] \to D^{*0}/\overline{D}^{*0}$ contribution to the measured signal, and to the extrapolation to the full range of scaled energies x_{D^0}. In the following sections, each of these categories is discussed in turn. The relative values of all errors are listed in table 6.3.

relative statistical error	24.9%
relative systematic errors:	
modelling of selection variables:	
D^0 mass resolution	1.3%
$\langle x(D^*) \rangle_{Z \to c\bar{c} \to D^{*0}}$	3.9%
$\langle x(X_b) \rangle_{Z \to b\bar{b} \to X_b}$	3.0%
D^0 lifetime	0.8%
D^{*0} spin alignment	0.3%
effective shower isolation	9.7%
photon pair opening angle	2.8%
number of π^0 candidates	0.2%
number of D^{*0} candidates	1.3%
dE/dx	3.6%
dE/dx preselection cuts	3.1%
fragmentation tracks	2.7%
shower fit	5.9%
detector resolution:	
tracking resolution	6.4%
calorimeter energy scale and resolution	1.7%
fit procedure:	
background normalisation	3.4%
$Br(D^{*0} \to D^0\gamma)/Br(D^{*0} \to D^0\pi^0)$	2.0%
background shape	5.5%
contributions from other D^0 decays	0.4%
contributions from D^{*+} and D_s^{*+} decays	1.4%
b subtraction and extrapolation:	
contribution from b hadron decays	12.2%
extrapolation to $x_{D^0} = 0$	1.2%
total relative systematic error	20.8%

Table 6.3: A breakdown of the relative statistical and systematic errors on the hadronisation fraction $f(c \to D^{*0})$.

6.2.4.1 Uncertainties from the Modelling of Selection Variables

Possible differences between distributions in data and simulation could influence the efficiencies and the background determination. These effects are studied separately for each selection

variable. The resulting systematic errors are assumed to be uncorrelated and are therefore added in quadrature.

Two principal methods are used to determine systematic uncertainties in the modelling of a selection variable:
(A) Variables for which the distributions of signal candidates are measured are treated by reweighting the events in the Monte Carlo simulation such that for the weighted events, the simulated signal distribution agrees with the measured one. Using the likelihood given in equation 6.2, the background determination and the fit are then repeated and the original result is corrected according to the observed difference; the uncertainty in the difference is interpreted as a systematic error. This method takes correlations between the selection variables into account to the extent that in the case of non-zero correlations, the reweighting of events alters also the distribution of any variable that is correlated with the one variable in question. This procedure is applied

- to the invariant mass distribution of D^0 candidates,
- to the Peterson et al. fragmentation parameters which have been varied in the ranges corresponding to mean scaled energies of D^{*0} mesons in $\mathrm{Z} \to \mathrm{c\bar{c}}$ decays of $0.506 < \langle x(\mathrm{D}^{*0})\rangle_{\mathrm{Z}\to\mathrm{c\bar{c}}\to\mathrm{D}^*} < 0.531$ and of weakly decaying b hadrons in $\mathrm{Z} \to \mathrm{b\bar{b}}$ decays of $0.702 < \langle x(\mathrm{X_b})\rangle_{\mathrm{Z}\to\mathrm{b\bar{b}}\to\mathrm{X_b}} < 0.730$ [79], respectively[1],
- to the lifetime of D^0 mesons, which has been varied within $\tau_{\mathrm{D}^0} = (0.415 \pm 0.004)\,\mathrm{ps}$ [77],
- to the distributions of energies E_γ and E_{π^0}, where the simulated events are reweighted such that the helicity angle distributions in $\mathrm{D}^{*0} \to \mathrm{D}^0\gamma$ and $\mathrm{D}^{*0} \to \mathrm{D}^0\pi^0$ decays agree with the measured D^{*+} spin alignment in $\mathrm{Z} \to \mathrm{c\bar{c}}$ events (the spin density matrix element is $\rho_{00} = 0.40 \pm 0.02$ [25]),
- to the effective separation of a shower from the closest other shower in the electromagnetic calorimeter,
- to the opening angle of a pair of photons, and
- to the numbers of reconstructed π^0 and D^{*0} candidates.

The last three of the above variables depend on the event topology. For these variables, possible deviations between data and simulation affect the signal and the background in the same way. The simulated events are therefore reweighted such that the distributions of all candidates in data and simulation agree. The analysis is then repeated, and the observed difference in the fit result is treated as a systematic error.

(B) The second method is used for the remaining selection variables, which are

- the track probabilities calculated from $\mathrm{d}E/\mathrm{d}x$ information,
- the largest longitudinal momentum of fragmentation tracks inconsistent with being an accompanying hadron, and
- the goodness of the shower fit.

The corresponding function $\lambda_i(x_i)$ is set to its maximum value for one variable x_i at a time. The resulting modified likelihood functions $\mathcal{L}_i$ and $\mathcal{L}'_i$ are independent of that particular variable x_i, so using these functions instead of the original likelihoods removes any possible bias due to the simulation of x_i. The selection of the signal and background D^{*0} candidate samples is repeated with these modified likelihoods. By construction, these samples also contain those candidates selected with the original likelihoods $\mathcal{L}$ and $\mathcal{L}'$. The ratio of the fit results obtained with the original $(\mathcal{L}, \mathcal{L}')$ and the modified $(\mathcal{L}_i, \mathcal{L}'_i)$ likelihoods is calculated for the data and

[1] These variations in the mean energies are larger than the current errors and account also for errors related to the modelling of the shapes of the fragmentation functions.

the simulation, where the statistical correlation between the samples is taken into account. The relative difference of these ratios is interpreted as the systematic error associated with the variable x_i. In the case of the signed particle identification probabilities, the cuts for the preselection of charged kaons and pions (see section 6.1.1) are retained in order to obtain a clear signal. In reference [80], an error of 3.1% has been determined for these cuts in the D^0 selection. This error is included as an additional systematic uncertainty.

6.2.4.2 Uncertainties in the Detector Resolution

Tracking resolution:
Uncertainties in the modelling of the central detector are assessed by repeating the analysis with the tracking resolutions varied by $\pm 10\%$ around the values that describe the data best. The redetermined efficiencies are compared with the original ones, and the relative difference is interpreted as a systematic error.

Calorimeter energy scale and resolution:
The energy scale and resolution of the electromagnetic calorimeter and the multiplicity and resolution in the time-of-flight scintillators are treated analogously. The reconstructed π^0 mass distribution has been used to determine the corresponding resolution and scaling parameters. Thus, the width and position of the π^0 mass peak are well reproduced in the simulation [76], and any possible bias is accomodated by the variation of the detector resolution.

6.2.4.3 Uncertainties in the Fit Procedure

Background normalisation:
To check the determination of the background normalisation, the fit to the mass difference distributions has been repeated with the range restricted to values of $\Delta m(D^0, \gamma)$<0.4 GeV and $\Delta m(D^0, \pi^0)$<0.2 GeV. Deviations from the previous results are interpreted as systematic errors.

D^{*0} branching ratio:
The fit to the $\Delta m(D^0, \gamma)$ and $\Delta m(D^0, \pi^0)$ distributions is constrained to the world average of the branching ratio $Br(D^{*0} \to D^0\gamma)/Br(D^{*0} \to D^0\pi^0) = 0.616 \pm 0.076$ [77]. The fit is repeated with this ratio varied within its errors, and the observed difference is taken as a systematic error.

Background shape:
Background candidates with a correctly reconstructed D^0 lead to a bias in the Δm distribution, which is taken into account in the background subtraction as outlined in section 6.1.2. The analysis has been repeated without correcting for this bias, and half the difference from the original result is assigned as a systematic error.

The origin of background candidates has been studied in the simulation, and no other source for a bias of the background shape has been identified. In particular, it has been checked that the contributions from photons or π^0 mesons from D^{**}, B^*, and B^{**} decays are small and do not exhibit a pronounced structure.

Contributions from other D^0 decays:
In the simulation, the contribution to the signal sample of D^{*0} candidates from D^0 mesons not decaying to $K^-\pi^+$ is found to be 5.9%. This contribution is accounted for in the efficiency

determination. However, mismodelling of the branching ratios for these other decay modes can introduce a potential bias in the D^{*0} measurement. The corresponding systematic error is evaluated assuming relative contributions of other decay modes as in [53] and assigning errors according to the errors on the branching ratios as given in [77].

Contributions from D^{*+} and D_s^{*+} decays:
In the reconstruction of D^{*0} decays, there are contributions from D^{*+} and D_s^{*+} mesons, which can also decay via γ or π^0 emission. In principle, these decays can lead to a signal in the Δm distributions similar to that being measured. However, it has been found in the simulation that the relative contribution from D^{*+} and D_s^{*+} decays to the selected signal and background samples is approximately equal. A small correction is applied to account for residual effects, and half this correction is assigned as a systematic error.

It has been checked that the statistical correlation between the $D^{*0} \to D^0\pi^0$ signals in the $\Delta m(D^0, \pi^0)$ and $\Delta m(D^0, \gamma)$ distributions is negligible. Also, there is only a negligible fraction of cases where both photons from a $D^{*0} \to D^0\pi^0$ decay lead to an entry in the $\Delta m(D^0, \gamma)$ distribution.

6.2.4.4 Uncertainties from the b Subtraction and the Extrapolation

Contribution from b hadron decays:
As mentioned in section 6.2.1, it is assumed that the production of D^{*0} and D^{*+} mesons in b hadron decays is equal for scaled energies $x_{D^0}>0.3$. The error on the production of D^{*+} mesons in $Z \to b\bar{b}$ decays as given in equation 6.5 is taken into account. In addition, the production of D^{*0} mesons in $\overline{B}^0$ and B^- meson decays is varied within the range of the CLEO measurement given in equation 6.4 to assess the systematic error due to this assumption. At LEP, $\overline{B}^0$ and B^- mesons account for $(75.6 \pm 4.4)\%$ of all weakly decaying b hadrons [77]. To evaluate the production of D^{*0} mesons in decays of other bottom hadrons, the world average of $Br(\overline{B}^0$ or $B^- \to D^{*+}X) = (23.1 \pm 3.3)\%$ [77] is compared with the OPAL measurement of $R_b f(b \to [c, \overline{c}] \to D^{*\pm})\, Br(D^{*+} \to D^0\pi^+)\, Br(D^0 \to K^-\pi^+) = (1.334 \pm 0.049 \pm 0.078) \times 10^{-3}$ [53]. From the branching ratios as given in [77], the production of D^{*+} mesons in $\overline{B}_s^0$ and Λ_b decays is then found to be $Br(\overline{B}_s^0$ or $\Lambda_b \to D^{*+}X) = 0.25 \pm 0.13$. Assuming equal D^{*0} and D^{*+} production in $\overline{B}_s^0$ and Λ_b decays, this leads to $R_b f(b \to \overline{B}_s^0$ or $\Lambda_b \to D^{*0}X) = 0.013$. A 100% error is assigned to this quantity.

Extrapolation to $x_{D^0} = 0$:
The extrapolation of the measured quantity $R_c\, f(c \to D^{*0})\, Br(D^0 \to K^-\pi^+)\big|_{x_{D^0}>0.3}$ from $x_{D^0}>0.3$ to the full range of scaled energies is based on the fragmentation function of Peterson et al. [65]. To assess the uncertainty associated with this extrapolation, it is repeated with mean scaled energies of D^{*0} mesons from $Z \to c\bar{c}$ decays varied in the range given in section 6.2.4.1. The difference from the previous result is interpreted as a systematic error.

6.3 Measurement of D_s^{*+} Production

The decays of D_s^{*+} mesons are very simliar to those of D^{*0} mesons. The techniques developed for the D^{*0} analysis can therefore be used for the reconstruction of D_s^{*+} mesons.

The D_s^{*+} meson decays dominantly to the $D_s^+\gamma$ final state, since the $D_s^+\pi^0$ channel is suppressed by isospin invariance: $Br(D_s^{*+} \to D_s^+\pi^0)/Br(D_s^{*+} \to D_s^+\gamma) = 0.062^{+0.020}_{-0.018} \pm 0.022$ [81]. Thus, for the measurement of the production rate, only the $D_s^{*+} \to D_s^+\gamma$ decay is used. The D_s^+ mesons are reconstructed in their decay chain $D_s^+ \to \phi\pi^+$, $\phi \to K^+K^-$. Candidates with invariant masses m_ϕ<1.05 GeV and 1.90 GeV<$m_{D_s^+}$<2.04 GeV, a scaled energy of $x_{D_s^+}$>0.35, and a helicity angle of the pion in the D_s^+ rest frame satisfying $-0.90<\cos\theta^*<0.95$ are retained if the dE/dx requirements stated in section 6.1.1 are fulfilled for the kaon and pion candidate tracks. The preselection of photons is identical to that described in section 6.1.1.

The D_s^{*+} candidates are selected with a cut on a likelihood using the variables described in section 6.1.1 accordingly, and taking the reconstructed mass of the ϕ and the cosine of the angle between the D_s^+ and one of the kaons in the ϕ rest frame as additional inputs. The background shape is determined from candidates in sidebands of m_ϕ and $m_{D_s^+}$ using the technique described in section 6.1.2. The resulting mass difference distribution is shown in figure 6.4.

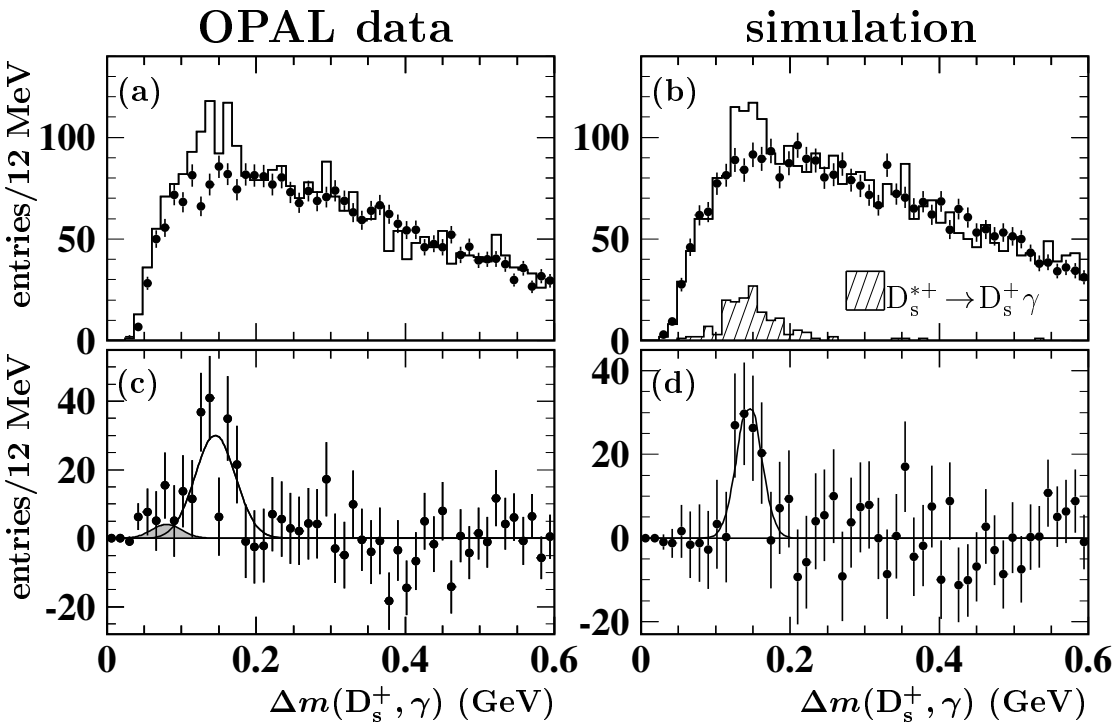

Figure 6.4: The mass difference distribution for the decay $D_s^{*+} \to D_s^+\gamma$. As before, in (a) and (b), the solid histogram corresponds to the signal sample, and points with error bars to the background sample. The signal contribution in the simulation is indicated by the hatched histogram.
The corresponding background subtracted distributions are shown in (c) and (d) together with the fitted signal parametrisation. The shaded Gaussian in figure (c) shows the expected contribution from $D_s^{*+} \to D_s^+\pi^0$ decays which is fixed in the fit.

No attempt is made to separate the contributions from the processes $c \to D_s^{*+}$ and $b \to [c, \bar{c}] \to D_s^{*\pm}$. However, the efficiencies for D_s^{*+} reconstruction in $Z \to c\bar{c}$ and $Z \to b\bar{b}$ events

have been found to be equal within errors. Thus, it is still reasonable to extract the overall D_s^{*+} production in Z decays from a fit to the $\Delta m(D_s^+, \gamma)$ distribution. No isospin violating decays $D_s^{*+} \to D_s^+ \pi^0$ have been generated in the simulation; in the data, a small contribution from such decays is expected at Δm values below the nominal D_s^{*+}–D_s^+ mass difference as shown in figure 6.4c. A double Gaussian is used to parametrise the signal, where the Gaussian at lower Δm is fixed to the expectation and varied by ±100% in case of the data. The number of D_s^{*+} mesons with $x_{D_s^+}$>0.35 per hadronic Z decay is found to be

$$\bar{n}(Z \to D_s^{*+})\, Br(D_s^{*+} \to D_s^+ \gamma)\, Br(D_s^+ \to \phi\pi^+)\, Br(\phi \to K^+K^-)\big|_{x_{D_s^+}>0.35} = (6.6 \pm 1.8 \pm 1.6) \times 10^{-4}\,, \tag{6.9}$$

where the first error is statistical and the second systematic. The fit to the data has a χ^2 of 37.1 for 43 degrees of freedom.

The contributions to the systematic error have been evaluated in a similar way as described earlier. Table 6.4 lists the most important errors. The largest systematic error on the value in equation 6.9 is introduced from the uncertainty in the background shape. The background sample is taken from a sideband in m_ϕ, and a correction has to be applied to account for the fact that fewer correctly reconstructed $\phi \to K^+K^-$ decays enter the background than the signal sample. When the fit is repeated with the same signal parametrisation plus an exponential to account for potential problems in the modelling of this bias, a consistent result is found. The deviation from the previous result is interpreted as systematic error. No other sources have been identified that could lead to a significant bias in the background shape.

relative statistical error	27.4%
relative systematic errors:	
extrapolation to $x_{D_s^+}$=0	(19.6%)
background shape	11.8%
tracking resolution	8.5%
D_s^+ lifetime	8.5%
effective shower isolation	8.1%
shower fit	6.9%
dE/dx preselection cuts	6.4%
$\langle x(X_b)\rangle_{Z\to b\bar{b}\to X_b}$	6.2%
others (evaluation similar to the D^{*0})	9.5%
total relative systematic error	23.8% (30.8%)

Table 6.4: A breakdown of the relative statistical and dominant systematic errors on the D_s^{*+} measurement. The errors in brackets apply only when considering the value which has been extrapolated to all scaled energies $x_{D_s^+}$.

The above D_s^{*+} measurement is extrapolated to the full range of scaled energies $x_{D_s^+}$. Here, a large systematic uncertainty is introduced from the unknown relative contribution from $c \to D_s^{*+}$ and $b \to [c, \bar{c}] \to D_s^{*\pm}$ components. When varying the ratio $f(b \to D_s^{*+})/f(b \to D_s^+)$ within[2]

[2]Recently, the ALEPH collaboration has published measurements of D_s^{*+} production in both $Z \to b\bar{b}$

0.53 ± 0.19, one finds the total rate

$$\begin{aligned}\bar{n}(\mathrm{Z}\to\mathrm{D_s^{*+}})\, Br(\mathrm{D_s^{*+}}\to\mathrm{D_s^{+}}\gamma)\, Br(\mathrm{D_s^{+}}\to\phi\pi^{+})\, Br(\phi\to\mathrm{K^{+}K^{-}}) \\ = (1.57 \pm 0.43 \pm 0.37 \pm 0.31) \times 10^{-3}\,,\end{aligned} \tag{6.10}$$

where the third error is introduced from the extrapolation to the full range of scaled energies. This rate is consistent with expectations and can be regarded as a further cross-check of the $\mathrm{D^{*0}}$ analysis, which uses very similar techniques.

6.4 Results of the $\mathrm{D^{*0}}$ and $\mathrm{D_s^{*+}}$ Measurements

The production of $\mathrm{D^{*0}}$ mesons in $\mathrm{Z}\to\mathrm{c\bar{c}}$ events is measured to be

$$R_{\mathrm{c}}\, f(\mathrm{c}\to\mathrm{D^{*0}})\, Br(\mathrm{D^0}\to\mathrm{K^{-}}\pi^{+}) \;=\; (1.44 \pm 0.36\,(\mathit{stat.}) \pm 0.30\,(\mathit{syst.}))\times 10^{-3}\,. \tag{6.11}$$

From this value, from the branching ratio $Br(\mathrm{D^0}\to\mathrm{K^{-}}\pi^{+}) = (3.85 \pm 0.09)\%$ [77], and from the standard model prediction of $R_{\mathrm{c}} = 0.172$ [3], the hadronisation fraction $f(\mathrm{c}\to\mathrm{D^{*0}})$ is computed to be

$$f(\mathrm{c}\to\mathrm{D^{*0}}) \;=\; 0.217 \pm 0.054\,(\mathit{stat.}) \pm 0.045\,(\mathit{syst.}) \pm 0.005\,(\mathit{ext.}). \tag{6.12}$$

Here, the last error corresponds to the error on the $\mathrm{D^0}$ branching ratio.

For the production of $\mathrm{D_s^{*+}}$ mesons in hadronic Z decays, the product branching ratio

$$\begin{aligned}\bar{n}(\mathrm{Z}\to\mathrm{D_s^{*+}})\, Br(\mathrm{D_s^{*+}}\to\mathrm{D_s^{+}}\gamma)\, Br(\mathrm{D_s^{+}}\to\phi\pi^{+})\, Br(\phi\to\mathrm{K^{+}K^{-}}) \\ = (1.57 \pm 0.43\,(\mathit{stat.}) \pm 0.48\,(\mathit{syst.})) \times 10^{-3}\,,\end{aligned} \tag{6.13}$$

is measured. This corresponds to

$$\bar{n}(\mathrm{Z}\to\mathrm{D_s^{*+}}) \;=\; 0.095 \pm 0.026\,(\mathit{stat.}) \pm 0.029\,(\mathit{syst.}) \pm 0.024\,(\mathit{ext.}) \tag{6.14}$$

$\mathrm{D_s^{*+}}$ mesons per hadronic Z decay, where the last error corresponds to the uncertainties on the branching ratios [77, 81] $Br(\mathrm{D_s^{*+}}\to\mathrm{D_s^{+}}\gamma) = (94.2 \pm 2.5)\%$, $Br(\mathrm{D_s^{+}}\to\phi\pi^{+}) = (3.6 \pm 0.9)\%$, and $Br(\phi\to\mathrm{K^{+}K^{-}}) = (49.1 \pm 0.6)\%$.

and $\mathrm{Z}\to\mathrm{c\bar{c}}$ decays [27]. From the ALEPH measurement of $f(\mathrm{b}\to[\mathrm{c},\overline{\mathrm{c}}]\to\mathrm{D_s^{*\pm}})$ and the OPAL value for $f(\mathrm{b}\to[\mathrm{c},\overline{\mathrm{c}}]\to\mathrm{D_s^{\pm}})$ [80], the ratio of $\mathrm{D_s^{*+}}$ and $\mathrm{D_s^{+}}$ production in $\mathrm{Z}\to\mathrm{b\bar{b}}$ events is found to be 0.53 ± 0.19. However, when the ALEPH measurement is subtracted from the total rate of $\mathrm{D_s^{*+}}$ production in Z decays as determined in this section (similar to the procedure in section 6.2.1), the hadronisation fraction $f(\mathrm{c}\to\mathrm{D_s^{*+}})$ is essentially unconstrained due to the large measurement errors.

Chapter 7

Analysis of Charmed Vector Meson Production

In this chapter, the relative production rate $P_V{=}V/(V{+}P)$ of charmed vector and pseudoscalar mesons is analysed. In section 7.1, the measurement of the hadronisation fraction $f(\mathrm{c}\to\mathrm{D}^{*0})$ presented in the previous chapter is used to test the assumption of isospin invariance in charm hadronisation. The analysis of the parameter P_V in section 7.2 is based on this assumption. The effective value P_V^{eff} is determined, where no distinction is made between direct and indirect meson production. The primary value P_V^{prim}, corrected for effects from $L = 1$ meson decays, is studied for the first time. In the absence of measurements of all $L = 1$ charmed mesons, a model independent formula is presented for P_V^{prim}. In addition, the analysis of direct vector meson production allows a check of hadronisation models to be performed. In section 7.3, the hadronisation properties of charm and bottom quarks are compared, and a conclusion is drawn.

The following discussions are based on the $f(\mathrm{c}\to\mathrm{D}^{*0})$ measurement described in chapter 6 and on previous OPAL measurements of charmed meson hadronisation fractions. Table 7.1 contains an overview of the values entering the computations.

7.1 Tests of Isospin Invariance

Isospin invariance suggests equal primary production rates for corresponding $\mathrm{c\bar{u}}$ and $\mathrm{c\bar{d}}$ mesons. Thus, the hadronisation fractions $f(\mathrm{c}\to\mathrm{D}^{*0})$ and $f(\mathrm{c}\to\mathrm{D}^{*+})$ are expected to be the same, as long as decays of higher resonances contribute equally to both D^{*0} and D^{*+} production. For the vector mesons D^{*0} and D^{*+}, isospin invariance can therefore be tested directly from the D^{*0} and D^{*+} production rate measurements and the branching ratio $Br(\mathrm{D}^{*+}\to\mathrm{D}^0\pi^+)$ as listed in table 7.1, resulting in a ratio of

$$\frac{f(\mathrm{c}\to\mathrm{D}^{*0})}{f(\mathrm{c}\to\mathrm{D}^{*+})} = 0.94 \pm 0.31\,, \tag{7.1}$$

consistent with 1. As mentioned in section 6.2.1, the $\mathrm{c}\to\mathrm{D}^{*0}$ measurement assumes equal production of D^{*0} and D^{*+} mesons in b hadron decays as justified by the CLEO result given in equation 6.4. The error on the CLEO measurement is treated as a systematic uncertainty on $f(\mathrm{c}\to\mathrm{D}^{*0})$ as discussed in section 6.2.4.4, and it can be seen from table 6.3 that this systematic error is substantially smaller than the statistical error on $f(\mathrm{c}\to\mathrm{D}^{*0})$.

charmed meson production, OPAL measurements	value and reference
$R_c\ f(c \to D^{*0})\ Br(D^0 \to K^-\pi^+)$	$(1.44 \pm 0.36 \pm 0.30) \times 10^{-3}$ (section 6.4)
$R_c\ f(c \to D^{*+})\ Br(D^{*+} \to D^0\pi^+)\, Br(D^0 \to K^-\pi^+)$	$(1.041 \pm 0.020 \pm 0.040) \times 10^{-3}$ [53]
$R_c\ f(c \to D^0)\ Br(D^0 \to K^-\pi^+)$	$(0.389 \pm 0.027^{+0.026}_{-0.024}) \times 10^{-2}$ [80]
$R_c\ f(c \to D^+)\ Br(D^+ \to K^-\pi^+\pi^+)$	$(0.358 \pm 0.046^{+0.025}_{-0.031}) \times 10^{-2}$ [80]
$R_c\ f(c \to D_1^0 \text{ or } D_2^{*0})\ Br(D_1^0 \text{ or } D_2^{*0} \to D^{*+}\pi^-)$	$(4.2 \pm 1.1^{+0.5+0.2}_{-0.7-0.3}) \times 10^{-3}$ [82]
$\frac{f(c \to D_1^0 \to D^{*+}\pi^-)}{f(c \to D_1^0 \to D^{*+}\pi^-) + f(c \to D_2^{*0} \to D^{*+}\pi^-)}$	$0.56 \pm 0.15^{+0.03}_{-0.04}$ [82]
$R_c\ f(c \to D_{s1}^+)$	$(2.8^{+0.8}_{-0.7} \pm 0.3 \pm 0.4) \times 10^{-3}$ [82]

branching ratios	value and reference
$Br(D^0 \to K^-\pi^+)$	0.0385 ± 0.0009 [77]
$Br(D^+ \to K^-\pi^+\pi^+)/Br(D^0 \to K^-\pi^+)$	$2.35 \pm 0.16 \pm 0.16$ [83]
$Br(D^{*+} \to D^0\pi^+)$	0.683 ± 0.014 [77]
$\frac{Br(D_2^* \to D^*\pi)}{Br(D_2^* \to D^*\pi) + Br(D_2^* \to D\pi)} \approx Br(D_2^* \to D^*\pi)$	0.311 ± 0.051 [77]
$\frac{Br(D_{s2}^{*+} \to D^*K)}{Br(D_{s2}^{*+} \to D^*K) + Br(D_{s2}^{*+} \to DK)} \approx Br(D_{s2}^{*+} \to D^*K)$	0.107 ± 0.016 [82, 84, 85]

assumption on relative D** meson production in a spin counting model	
$f(c \to D_0^{*0}) : f(c \to D_1'^0) : f(c \to D_1^0) : f(c \to D_2^{*0})$ $f(c \to D_{s0}^{*+}) : f(c \to D_{s1}'^+) : f(c \to D_{s1}^+) : f(c \to D_{s2}^{*+})$	$\Big\}$ 1 : 3 : 3 : 5

Table 7.1: The measurements and assumptions entering the computations in this chapter. The broad D^{**} state with $J^P = 1^+$ is denoted by the symbol D_1' to distinguish it from the narrow state which is conventionally called D_1.

Since $D^{*0} \to D^+\pi^-$ decays are kinematically forbidden while $D^{*+} \to D^0\pi^+$ decays are not, the observed hadronisation fractions of D^0 and D^+ mesons are expected to differ even if the primary production rates are equal. When assuming isospin invariance between D^0 and D^+ mesons, any difference between their hadronisation fractions should be due to these D^{*+} decays, and the ratio of observed and expected differences between the D^0 and D^+ hadronisation fractions

$$R \equiv \frac{f(c \to D^0) - f(c \to D^+)}{f(c \to D^{*0}) + \Big(2Br(D^{*+} \to D^0\pi^+) - 1\Big)\, f(c \to D^{*+})} \tag{7.2}$$

should be equal to one. From the values given in table 7.1, one obtains $R = 1.18 \pm 0.36$, consistent with 1. Under the assumption of equal hadronisation fractions $f(c \to D^{*0}) = f(c \to D^{*+})$, other experiments [23] have obtained values consistent with this result.

With isospin invariance thus confirmed within experimental errors, the hadronisation fractions of D^{*0} and D^{*+} mesons are assumed to be equal in the following. The mean $D^{*0/+}$ hadronisation fraction is then defined as the weighted average of the values of $f(c \to D^{*0/+})$ determined from equation 7.2 and from the direct measurements of $f(c \to D^{*0})$ and $f(c \to D^{*+})$. The resulting value of

$$R_c\, f(c \to D^{*0/+})\, Br(D^{*+} \to D^0\pi^+)\, Br(D^0 \to K^-\pi^+) = (1.045 \pm 0.043) \times 10^{-3} \tag{7.3}$$

is used in the computation of P_V in the following sections. Similarly, the hadronisation fractions of corresponding $L = 1$ $c\bar{u}$ and $c\bar{d}$ mesons are assumed to be equal.

7.2 The Relative Production Rate of Charmed Vector Mesons in $Z \to c\bar{c}$ Decays

For the relative production rate of vector mesons containing the primary quark, there are two possible definitions: the quantity P_V^{eff}, where inclusive production (including contributions from decays of higher resonances) is considered, and P_V^{prim}, which is defined when considering direct production only. These two values may differ due to the effects from resonance decays, where some decays are forbidden by spin and parity conservation, as discussed in section 1.2.3.

In the first part of this section, the existing OPAL measurements of the production of charmed mesons with no orbital angular momentum are used to derive a value of P_V^{eff}. This parameter is interpreted in conjunction with a measurement of the D^{*+} spin alignment, which provides information on the relative production of different vector meson spin states. Thus, the combination of these two measurements provides further insight into the inclusive production of charmed mesons in the fragmentation process [22].

In the second part, additional input from orbitally excited D mesons is used to study P_V^{prim}. This quantity can be compared more directly to model calculations, since such models generally make predictions for primary hadron production. However, a determination of P_V^{prim} is experimentally challenging because of the difficulties in assessing the fraction of hadrons produced in decays of higher resonances. In this thesis, the production of L=1 mesons is taken into account, while production and decay of higher states are considered a part of the fragmentation process. Using the OPAL measurements of the hadronisation fractions $f(c \to D_1^0)$, $f(c \to D_2^{*0})$, and $f(c \to D_{s1}^+)$ [82], decays of D^{**} mesons are taken into account to study the P_V^{prim} ratio. First, the dependence of P_V^{prim} on the production of the unmeasured L=1 resonances is discussed, and a model independent formula for the calculation of P_V^{prim} is derived. Second, it is shown that the analysis of direct vector meson production provides a test with which the self-consistency of a hadronisation model can be checked when the production of the unmeasured L=1 resonances is fixed to the model prediction. This method is illustrated with a simple spin counting picture as an example.

7.2.1 Effective Charmed Meson Production

The effective value P_V^{eff} is calculated from the mean $D^{*0/+}$ hadronisation fraction given in equation 7.3 and the measurements listed in table 7.1 to be

$$P_V^{\text{eff}} = \frac{2 f(c \to D^{*0/+})}{f(c \to D^0) + f(c \to D^+)} = 0.57 \pm 0.05\,. \tag{7.4}$$

Here, the assumption has been made that isospin invariance is valid, as tested in the previous section. If, instead, the measured hadronisation fractions are directly combined without the assumption of isospin invariance for D^{*0} and D^{*+} production, a value of $P_V^{\text{eff}} = \frac{f(c \to D^{*0}) + f(c \to D^{*+})}{f(c \to D^0) + f(c \to D^+)} = 0.55 \pm 0.10$ is obtained. In principle, the measurements are expected to be correlated. The largest correlation is expected between $f(c \to D^0)$ and $f(c \to D^{*+})$ and has been estimated to be smaller than 30%. A shift on P_V^{eff} of less than 0.01 is introduced by this correlation.

The result from equation 7.4 can be interpreted in connection with the D^* spin alignment. In the fragmentation process, four different spin states of charmed mesons without orbital

excitation can be formed: The vector mesons D^{*0}, D^{*+}, and D_s^{*+} with states $J = 1$ and $m = -1, 0, +1$, as well as the pseudoscalar mesons D^0, D^+, and D_s^+ with $J = m = 0$. The relative inclusive production probabilities $\mathcal{P}$ for these states are related to $P_V^{\rm eff}$ and to the spin density matrix element ρ_{00} of D^* mesons from $Z \to c\bar{c}$ events via [22, 19]

$$\begin{aligned} P_V^{\rm eff} &= \mathcal{P}_{J=1}^{m=0} + \mathcal{P}_{J=1}^{m=\pm1} \quad \text{and} \\ \rho_{00} &= \mathcal{P}_{J=1}^{m=0} / (\mathcal{P}_{J=1}^{m=0} + \mathcal{P}_{J=1}^{m=\pm1}) \, . \end{aligned} \tag{7.5}$$

Here, $\mathcal{P}_{J=1}^{m=\pm1}$ denotes the sum of the production probabilities for the $m = +1$ and $m = -1$ states, which cannot be distinguished experimentally. The spin density matrix element ρ_{00} gives the probability to find a vector meson in the $m = 0$ state. A simple spin counting model suggests values of $\mathcal{P}_{J=1}^{m=\pm1} = \frac{1}{2}$ and $\mathcal{P}_{J=1}^{m=0} = \mathcal{P}_{J=0}^{m=0} = \frac{1}{4}$ (see for instance [19]).

For D^{*+} mesons from $Z \to c\bar{c}$ decays with scaled energies $x_{D^{*+}} > 0.2$, ρ_{00} has been measured at OPAL to be $\rho_{00} = 0.40 \pm 0.02$ [25]. From this result and the above value of $P_V^{\rm eff}$, the production probabilities

$$\begin{aligned} \mathcal{P}_{J=1}^{m=0} = \rho_{00} P_V^{\rm eff} &= 0.23 \pm 0.02 \, , \\ \mathcal{P}_{J=1}^{m=\pm1} = (1 - \rho_{00}) P_V^{\rm eff} &= 0.34 \pm 0.03 \, , \quad \text{and} \\ \mathcal{P}_{J=0}^{m=0} = 1 - P_V^{\rm eff} &= 0.43 \pm 0.05 \end{aligned} \tag{7.6}$$

can be derived, where it has been assumed that the measured spin density matrix element ρ_{00} applies to both D^{*0} and D^{*+} mesons in $Z \to c\bar{c}$ events.

These probabilities show a clear deviation from the simple spin counting picture. The production of vector mesons is suppressed in favour of pseudoscalar mesons. This is mostly due to a suppression of the $m{=}\pm1$ vector states, while the production of the $J{=}1$, $m{=}0$ state agrees within errors with a spin counting picture.

An overall suppression of vector meson production is, for instance, expected in thermodynamic models, where the constituents of hadrons are pictured as a gas with a temperature T, such that a relative suppression of the heavier states by a factor of $\exp(-\Delta m/T)$ is predicted. From the above value of $P_V^{\rm eff}$, the temperature is calculated to be $T = \left(174^{+63}_{-36}\right)$ MeV, consistent with the value determined in [86]. It should be noted, however, that thermodynamic models fail to explain the observed non-zero spin alignment.

7.2.2 Primary Charmed Meson Production

For the determination of $P_V^{\rm prim}$, the effects of the decays of $L{=}1$ charmed mesons have to be taken into account. The hadronisation fractions $f(c \to D_1^0)$, $f(c \to D_2^{*0})$, and $f(c \to D_{s1}^+)$ have been measured at LEP, whereas the production of the broad resonances D_0^* and D_1' has not yet been measured. Since the charged D^{**+} mesons have not yet been observed in Z decays, isospin invariance is assumed to be valid in charm fragmentation to assess the production of these resonances, which implies equal hadronisation fractions for corresponding D^{**+} and D^{**0} states. Furthermore, it is assumed in the following that for D^{**} mesons, the relative production of the different spin states does not depend on the light quark flavour.

The ratio $P_V^{\rm prim}$ can be expressed as a function of two unmeasured hadronisation fractions, $f(c \to D_0^{*0})$ and $f(c \to D_1'^0)$, and two known parameters A and B which depend on the measure-

ments listed in table 7.1:

$$P_V^{\rm prim} = \frac{A - R_{\rm c} f({\rm c} \to {\rm D}_1^{\prime 0})}{B - R_{\rm c} \left[f({\rm c} \to {\rm D}_0^{*0}) + f({\rm c} \to {\rm D}_1^{\prime 0}) \right]} \,. \tag{7.7}$$

The complete derivation and the exact formulae for A and B are given in appendix C. The parameters A and B are found to be

$$\begin{aligned} A &= (2.29 \pm 0.34) \times 10^{-2} \text{ and} \\ B &= (3.82 \pm 0.88) \times 10^{-2} \,, \end{aligned} \tag{7.8}$$

with a positive correlation between A and B of 77%.

In figure 7.1, the results for $P_V^{\rm prim}$ are shown as a function of the two unknown hadronisation fractions. In general, low values of $P_V^{\rm prim}$ are obtained for small ${\rm D}_0^*$ and large ${\rm D}_1'$ production and vice versa. This analysis shows that the value of $P_V^{\rm prim}$ is not very sensitive to the production of the unmeasured broad ${\rm D}^{**}$ resonances. Generally, the range of $P_V^{\rm prim}$ values is consistent with predictions. However, to test a given model, a clearer statement can be made when following the procedure outlined below.

In contrast to the above discussion, a test of any specific fragmentation model can be performed when using its prediction for the relative primary production of the different L=0 and L=1 states. While the prediction for the L=0 states is directly equivalent to a prediction of $P_V^{\rm prim}$, the model prediction in the L=1 sector provides information on the production of the unmeasured L=1 resonances, which can in turn be used in conjunction with the measured hadronisation fractions to obtain an experimental value of $P_V^{\rm prim}$. Such a test is described in the following for the simplest case, a spin counting model.

A spin counting model predicts the relative primary production of D and ${\rm D}^*$ mesons to be 1 : 3. At the same time, for ${\rm D}^{**}$ mesons, the relative production of the ${\rm D}_0^* : {\rm D}_1' : {\rm D}_1 : {\rm D}_2^*$ resonances is predicted to be 1 : 3 : 3 : 5. When using the latter prediction, $P_V^{\rm prim}$ is found to be

$$P_V^{\rm prim}(\text{spin counting for } {\rm D}^{**}) = 0.55 \pm 0.08 \,. \tag{7.9}$$

However, since the validity of spin counting was assumed in the calculation, the value of $P_V^{\rm prim}$ is fixed and should be 0.75. Thus, from the discrepancy between the above value and 0.75, the simultanous description of both L=0 and L=1 charmed meson production in a spin counting picture is disfavoured by 2.7 standard deviations. Within the framework of this model test, the relative production of the four ${\rm D}^{**}$ spin states need not be taken from experiment, since it is predicted by the model. Thus, the experimental error on the model test is reduced as compared to the model independent values shown in figure 7.1. As mentioned above, the value in equation 7.9 is part of a consistency check of a specific model and should not be interpreted as a stand-alone measurement.

In principle, a comparison of the hadronisation fractions $f({\rm c} \to {\rm D}_{\rm s}^{*+})$ and $f({\rm c} \to {\rm D}_{\rm s}^{+})$ yields a model independent measurement of $P_V^{\rm prim}$. However, the result from section 6.3 cannot be interpreted in terms of vector and pseudoscalar meson production in charm hadronisation, since the ${\rm c} \to {\rm D}_{\rm s}^{*+}$ and ${\rm b} \to {\rm D}_{\rm s}^{*+}$ components are not separated.

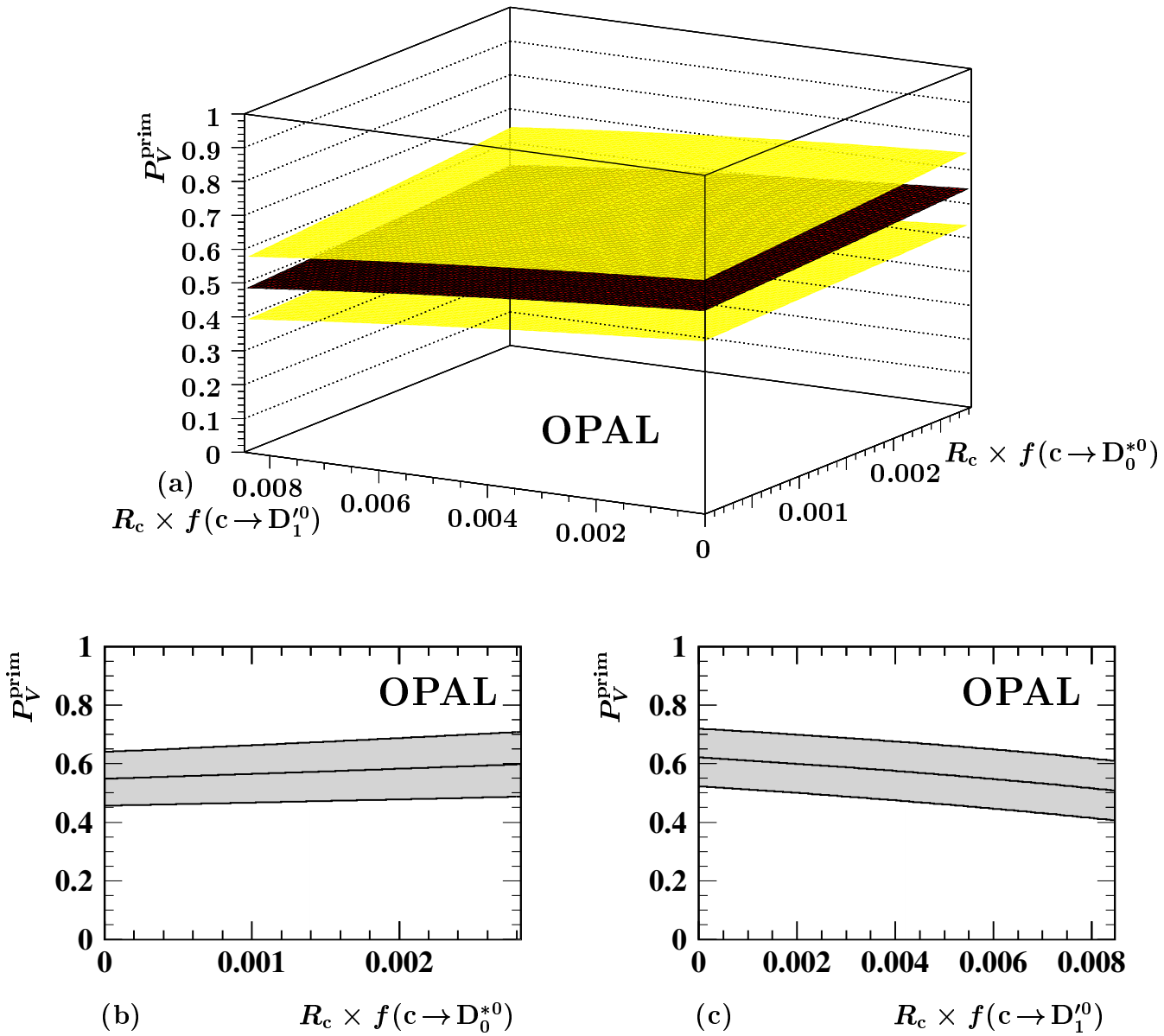

Figure 7.1: The dependence of $P_V^{\rm prim}$ on the two unmeasured multiplicities $R_c \times f(c \to D_0^{*0})$ and $R_c \times f(c \to D_1'^0)$ is shown in figure (a). Each of these quantities is varied between 0 and twice the value as expected from a spin counting picture. Plots (b) and (c) show the dependence on each one of these multiplicities when the other is fixed at the spin counting expectation. The error contours correspond to one standard deviation. They include the experimental error on the relative production of D_1^0 and D_2^{*0} mesons as measured in [82].

7.3 Comparison of Charm and Bottom Meson Production

Several measurements of the production of B^* [20] and B^{**} [87] mesons exist at LEP. In the following, these measurements are interpreted in terms of the P_V ratio, and the results are compared with those for charmed meson production.

The measurements of B^* production do not distinguish between the light quark flavours u,

d, and s since they rely on inclusive reconstruction techniques for B mesons. The parameter $P_V^{\rm eff}$ is directly extracted from the number of $\rm B^*$ mesons in the data and the reconstruction efficiency for the photons from $\rm B^* \to B\gamma$ decay; its LEP average is

$$P_V^{\rm eff}(\rm b) = 0.749 \pm 0.049\,. \tag{7.10}$$

In contrast to $\rm D^{*+}$ production in $\rm Z \to c\bar{c}$ decays, the spin alignment of $\rm B^*$ mesons has been measured to be $\rho_{00}(\rm B^*) = 0.33 \pm 0.04$ [26], consistent with the expectation from HQET in the $m_{\rm b} \to \infty$ limit. The production probabilities

$$\begin{aligned} \mathcal{P}_{J=1}^{m=0} = \rho_{00} P_V^{\rm eff} &= 0.25 \pm 0.03\,, \\ \mathcal{P}_{J=1}^{m=\pm1} = (1-\rho_{00}) P_V^{\rm eff} &= 0.50 \pm 0.04\,, \quad \text{and} \\ \mathcal{P}_{J=0}^{m=0} = 1 - P_V^{\rm eff} &= 0.25 \pm 0.05 \end{aligned} \tag{7.11}$$

are computed from the spin alignment and the above $P_V^{\rm eff}$ value, consistent with the spin counting expectation.

The LEP experiments have measured the inclusive production of $\rm B^{**}$ mesons; however, no information exists on the relative contributions from the different spin states. The branching ratios to $\rm B^*$ mesons are varied within

$$\begin{aligned} Br(\rm B^{**0/+} \to B^{*0/+}\pi) &= \left(63^{+19}_{-31}\right)\,\% \text{ and} \\ Br(\rm B_s^{**0} \to B^{*0/+}K) &= \left(55^{+22}_{-28}\right)\,\%\,, \end{aligned} \tag{7.12}$$

where the central values have been computed using the HQET prediction according to [19] and the variations correspond to half the possible spread. When accounting for $\rm B^{**}$ decays, one then finds

$$P_V^{\rm prim}(\rm b) = 0.812 \pm 0.073^{-0.092}_{+0.148} \tag{7.13}$$

where the last error comes from a simultaneous variation of the branchings $Br(\rm B^{**}_{(s)} \to B^*X)$ within the above limits. When a spin counting model is assumed to be valid for $L = 1$ bottom meson production, this last error does not appear. The value of 0.812 ± 0.073 is consistent with the spin counting expectation of $P_V^{\rm prim} = 0.75$. Since no spin alignment of $\rm B^*$ mesons has been observed, bottom meson production is consistent with the expectations from a spin counting picture.

The mass difference between vector and pseudoscalar bottom mesons is not large enough to measure the hadronic temperature. However, one can instead determine it from the total $\rm B^{**}$ production. A value of

$$T = (167 \pm 11)\,\rm MeV \tag{7.14}$$

is found, consistent with the value for charm hadronisation. Uncertainties from the $\rm B^{**}$ production rate, the mass difference between $\rm B^{**}$ and B mesons, and the branching ratio $Br(\rm B^{**0/+} \to B^{*0/+}\pi)$ (which has an effect since the $\rm B^{**} - B^*$ mass difference is smaller than that between $\rm B^{**}$ and B mesons) have been taken into account. The uncertainty on the $\rm B^{**}$ production rate dominates the error.

Table 7.2 gives an overview of the comparison between charm and bottom meson production. While significant deviations from the predictions of a simple spin counting picture are observed for charm hadronisation, the agreement is good in the bottom case.

quantity	charm hadronisation	bottom hadronisation	spin counting prediction
P_V^{eff}	0.57 ± 0.05	0.75 ± 0.05	0.73 (charm) 0.71 (bottom)
$\mathcal{P}_{J=1}^{m=0}$ $\mathcal{P}_{J=1}^{m=\pm1}$ $\mathcal{P}_{J=0}^{m=0}$	0.23 ± 0.02 0.34 ± 0.03 0.43 ± 0.05	0.25 ± 0.03 0.50 ± 0.04 0.25 ± 0.05	0.24 0.47 0.29
T	$\left(174^{+63}_{-36}\right)$ MeV	(167 ± 11) MeV	
P_V^{prim}	$(0.48 \pm 0.09) - (0.65 \pm 0.11)$	$0.81 \pm 0.07^{-0.09}_{+0.15}$	0.75
χ^2 with respect to spin counting	2.7 (P_V^{prim}) +3.3 (spin alignment)	0.85 (P_V^{prim}) +0 (spin alignment)	

Table 7.2: This table gives an overview of the results for charm and bottom meson production from the analysis of this chapter. The upper part lists effective quantities, computed without the distinction between direct and indirect meson production; for the quantities in the lower part of the table, contributions from $L = 1$ meson decays are explicitly accounted for. For the range of P_V^{prim} values in charm hadronisation, the production of the unmeasured D^{**} mesons has been varied within 0 and twice the spin counting expectation, as shown in figure 7.1. For comparison, the predictions from HQET in the $m_{\mathrm{Q}} \to \infty$ limit (spin counting model) with a suppression of $L = 1$ meson production according to a hadronic temperature of 170 MeV are listed in the rightmost column.

7.4 Summary

The relative production of charmed vector and pseudoscalar mesons in $\mathrm{Z} \to \mathrm{c\bar{c}}$ decays, P_V, is evaluated both considering inclusive production (P_V^{eff}) and taking into account the effects of secondary production in D^{**} decays (P_V^{prim}). A value of

$$P_V^{\text{eff}} = 0.57 \pm 0.05 \tag{7.15}$$

is derived from OPAL measurements, consistent with previous results. In a model independent calculation, the parameter P_V^{prim} is determined as a function of the unmeasured D^{**} hadronisation fractions, where a weak dependence is found. From the study of P_V^{prim}, it is found that for the description of charmed meson production in $\mathrm{Z} \to \mathrm{c\bar{c}}$ decays, a simple spin counting picture (corresponding to the HQET prediction in the limit $m_{\mathrm{Q}} \to \infty$) is disfavoured by 2.7 standard deviations. In contrast to the charm case, the corresponding measurements for bottom hadronisation show no evidence for a deviation from these predictions.

Chapter 8

Summary

The bottom and charm forward-backward asymmetries $A_{\rm FB}^{\rm b}$ and $A_{\rm FB}^{\rm c}$ have been measured with the OPAL detector at LEP in e^+e^- collisions at effective centre-of-mass energies of 74 GeV and between 130 GeV and 189 GeV. For the measurement at 74 GeV, events with significant initial state radiation recorded at e^+e^- centre-of-mass energies close to the Z mass have been boosted into the effective rest frame of the hadronic system. This technique has been calibrated and cross-checked with radiative hadronic events at centre-of-mass energies above the Z resonance, where events with hard initial state radiation can be easily identified. The measurements at centre-of-mass energies between 130 GeV and 189 GeV use hadronic events without significant initial state radiation and are cross-checked with data taken on the Z resonance.

The forward-backward asymmetries have been measured using prompt leptons from semileptonic decays of bottom and charm hadrons as well as inclusively reconstructed slow pions from $D^{*+} \to D^0\pi^+$ decays. The measurement techniques have been optimised for the available data samples. A neural network for muon identification at OPAL has been developed and tested, and the determination of the origin of prompt leptons has been improved with respect to previous techniques.

The bottom asymmetry measurements at energies above the Z resonance have been combined with OPAL measurements obtained with a hemisphere charge technique in secondary vertex tagged events. Events which are tagged by both analyses are assigned on an event-by-event basis to that analysis which optimally uses the given information, so that statistical overlaps can be avoided.

The following values have been obtained:

energy	$A_{\rm FB}^{\rm b}$	$A_{\rm FB}^{\rm c}$
74 GeV	$-0.01\ ^{+0.27}_{-0.28} \pm 0.12$	$-0.38\ ^{+0.37}_{-0.35} \pm 0.18$
133 GeV	$0.19 \pm 0.30 \pm 0.12$	$0.50\ ^{+0.31}_{-0.32} \pm 0.13$
161 GeV	$-0.03\ ^{+0.45}_{-0.42} \pm 0.11$	$0.87\ ^{+0.58}_{-0.60} \pm 0.12$
172 GeV	$0.82\ ^{+0.67}_{-0.72} \pm 0.14$	$0.69\ ^{+0.49}_{-0.53} \pm 0.12$
183 GeV	$0.77\ ^{+0.23}_{-0.24} \pm 0.10$	$0.55\ ^{+0.27}_{-0.28} \pm 0.11$
189 GeV	$0.63\ ^{+0.15}_{-0.16} \pm 0.10$	$0.50\ ^{+0.18}_{-0.19} \pm 0.11$

where in each case, the first error is statistical and the second systematic. All results are in agreement with the Standard Model predictions.

The measured asymmetries have been interpreted together with OPAL measurements of the cross-section ratio $R_{\mathrm{b}} = \sigma(\mathrm{e^+e^-} \to \mathrm{b\bar{b}})/\sigma(\mathrm{e^+e^-} \to \mathrm{q\bar{q}})$ at energies between 130 GeV and 189 GeV and with previous measurements in $\mathrm{e^+e^-}$ collisions around and below the Z resonance. The effective bottom and charm quark couplings to the Z boson have been studied. Together with the measurements above and below the Z resonance, all ambiguities that arise from measurements in Z decays alone are excluded at least at 99.9% confidence level.

For the first time, the measurements have also been interpreted using the S-Matrix parametrisation of the $\mathrm{e^+e^-} \to \mathrm{b\bar{b}}$ and $\mathrm{e^+e^-} \to \mathrm{c\bar{c}}$ processes. The contributions of interference between s-channel photon and Z exchange to the cross-sections and asymmetries have thus been determined in a model independent way. The S-Matrix parameters describing the interference contributions to the $\mathrm{e^+e^-} \to \mathrm{b\bar{b}}$ and $\mathrm{e^+e^-} \to \mathrm{c\bar{c}}$ total (tot) and forward-backward asymmetric (fb) cross-sections have been measured to be

$$\begin{aligned} j_{\mathrm{b}}^{\mathrm{tot}} &= 0.234 \pm 0.056\,, & j_{\mathrm{c}}^{\mathrm{tot}} &= -0.33 \pm 0.16\,, \\ j_{\mathrm{b}}^{\mathrm{fb}} &= 0.670 \pm 0.058\,, \text{ and } & j_{\mathrm{c}}^{\mathrm{fb}} &= 1.76 \pm 0.12\,. \end{aligned}$$

The improvements that can be obtained with the final LEP2 data sample and the expected precision after one year of data-taking at a future $\mathrm{e^+e^-}$ linear collider experiment are assessed. The results are promising, and precision measurements of the $\gamma - \mathrm{Z}$ interference parameters will be possible for flavour tagged hadronic final states.

In a second analysis, D^{*0} mesons have been reconstructed in Z decays for the first time, using data collected with the OPAL detector. The D^{*0} mesons have been identified in their decays $\mathrm{D}^{*0} \to \mathrm{D}^0\gamma$ and $\mathrm{D}^{*0} \to \mathrm{D}^0\pi^0$. To reconstruct D^0 mesons, $\mathrm{D}^0 \to \mathrm{K}^-\pi^+$ decays have been used. Photons and $\pi^0 \to \gamma\gamma$ decays have been identified in the electromagnetic calorimeter and via photon conversions. The hadronisation fraction of D^{*0} mesons in $\mathrm{Z} \to \mathrm{c\bar{c}}$ decays has been determined as

$$f(\mathrm{c} \to \mathrm{D}^{*0}) = 0.218 \pm 0.054 \pm 0.045 \pm 0.007\,,$$

where the errors correspond to the statistical and systematic errors specific to this analysis, and to systematic uncertainties from externally measured branching ratios, respectively. This value is consistent with the hadronisation fraction for D^{*+} mesons and allows a complete test of isospin symmetry in charm fragmentation, including the vector meson hadronisation fractions, to be made for the first time. The first measurement of the inclusive $\mathrm{D}_{\mathrm{s}}^{*+}$ production rate in hadronic Z decays has been presented, where $\mathrm{D}_{\mathrm{s}}^{+}\gamma$ final states have been identified with similar reconstruction techniques as used in the D^{*0} analysis.

Together with previous OPAL measurements of the hadronisation fractions of other charmed mesons, the measurement of $f(\mathrm{c} \to \mathrm{D}^{*0})$ has been used to investigate the relative production of vector and pseudoscalar charmed mesons in $\mathrm{Z} \to \mathrm{c\bar{c}}$ decays. The effective production ratio has been determined to be

$$P_V^{\mathrm{eff}} = V/(V+P) = 0.57 \pm 0.05\ .$$

The relative primary production of vector and pseudoscalar mesons, P_V^{prim}, has been studied in the context of the production and decay of orbitally excited charmed resonances. A model independent formula for the P_V^{prim} ratio in charm hadronisation has been derived. It suggests similar values for P_V^{eff} and P_V^{prim} and yields a weak dependence of the primary production ratio on the assumed production rates of the unmeasured D^{**} states.

A self-consistency test has been developed for hadronisation models, where the P_V^{prim} ratio is calculated from the predictions for the relative production of the different orbitally excited

mesons. As an example, this test has been applied for a simple spin counting picture, which corresponds to the HQET prediction in the heavy quark limit. While the results for charm hadronisation show a clear deviation from these predictions, measurements of bottom hadronisation are described well.

Appendix A

An Artificial Neural Network For Muon Identification

The measurement of heavy quark asymmetries in low statistics event samples makes demands on the analysis that differ from those in the corresponding LEP1 measurement [31]: For the measurements presented in this thesis, the statistical error dominates. It has therefore been tried to reduce the statistical error as much as possible, even if at the expense of (moderately) large systematic uncertainties. With respect to the LEP1 analysis, the following aspects have been studied:

- The default OPAL algorithms for the identification of electrons and muons in hadronic jets have been developed for LEP1 measurements. Not all available information is exploited in order to keep the systematic uncertainties related to these algorithms small. In principle, this leaves room for improvement for statistics limited analyses.
- There are relatively large modelling uncertainties in the decay chain $\mathrm{b} \to \overline{\mathrm{c}} \to \ell$, and in addition to $\mathrm{B}-\overline{\mathrm{B}}$ mixing, this process further dilutes the charge information from $\mathrm{b} \to [\mathrm{c}, \overline{\mathrm{c}}] \to \ell$ cascade decays. Therefore, the LEP1 measurement does not attempt to use the information from cascade decays: In the flavour separation, only the $\mathrm{b} \to \ell$ and $\mathrm{c} \to \ell$ processes are identified, and cascade decays are dominantly classified as background [31]. For the analyses presented in this thesis, an additional neural network has been trained to identify cascade decays, so the corresponding information can be used in the asymmetry measurement. Also, the existing flavour separation networks have been retrained to optimise the statistical separation.
- Due to the large backgrounds, there are large systematic uncertainties associated with the number of inclusively reconstructed slow pions from D^{*+} decays (see for example section 3.5.2.1), and this information is not useful for the LEP1 analysis. However, for the statistical precision of the measurements presented here, inclusively reconstructed slow pions can still reduce the statistical error without an intolerable rise of the systematic uncertainty.

For the identification of electrons at OPAL, an artificial neural network trained for the LEP1 environment is already used by default. It provides an optimal way to combine the tagging of low-momentum electrons (which mainly relies on $\mathrm{d}E/\mathrm{d}x$ information) with that of high-momentum electrons (where the information from the electromagnetic calorimeter is crucial). Because of modelling problems, not all available information is used in this neural network. In

addition, the differences between LEP1 and LEP2 in momentum spectra and particle densities within jets suggest that this algorithm could be improved for the measurements in this thesis. However, it has been found that only a marginal enhancement of the statistical separation can be achieved at the expense of larger systematic uncertainties.

In contrast, the default muon identification algorithm at OPAL is based on cuts, and a significant improvement has been possible. An artificial neural network has been trained which is used in the heavy flavour asymmetry measurements described in chapters 3 and 4. The neural network approach yields a significantly better purity at a given efficiency than the default method, and it is an algorithm that is of interest also for other OPAL analyses. A description of the muon tagging variables used in the neural network is given in section A.2, and section A.3 compares its performance with that of the default algorithm. Studies of systematic errors of both efficiency and background rates have been performed and are described in section A.4. A summary is given in section A.5.

A.1 Muon Identification at OPAL

The default algorithm for the identification of muons at OPAL [88] relies almost entirely on the position match between track segments in the muon chambers and tracks from the central tracking chambers which have been extrapolated to the muon chambers. Optionally, a loose $\mathrm{d}E/\mathrm{d}x$ cut can also be applied. The main advantage of this algorithm is that it is very well understood and has reasonable systematic errors on both efficiency and misidentification rate [89]. On the other hand, the following shortcomings should be noted:

1. It does not provide any coverage in the acceptance holes of the muon chambers;
2. muons below ≈ 2 GeV cannot be tagged, since they are not expected to reach the muon chambers;
3. the default algorithm is cut based, so no optimal information exists indicating how good a muon candidate a selected track is; and
4. for muons within hadronic jets, the purity is limited.

There exists an alternative algorithm to tag muons using information from the hadronic calorimeter instead of the muon chambers [90], which thus in principle provides a way around shortcomings 1 and 2. However, the efficiency gain is not large, and the purity of this selection is not as good as that of the default algorithm, particularly for muons within hadronic jets.

The new algorithm described here uses a different approach with a focus on improving the tagging of muons in hadronic events: After applying the preselection of the default algorithm, information from the hadronic calorimeter and the specific energy loss in the tracking chamber is used in a neural network in addition to the matching information to purify the sample in muons and to provide a continuous output which can be used in later stages of an analysis. Thus, an improvement is expected for points 3 and 4 listed above, while the first two points are not addressed.

A.2 The Selection Variables

Muons have several distinct signatures which allow an identification even for non-isolated muons in a hadronic environment:

- In contrast to any other known charged particles, muons with a momentum of around 2 GeV or more are expected to penetrate the hadronic calorimeter and leave a track segment in the muon chambers.
- In contrast to hadrons, muons are expected to deposit only a relatively small fraction of their energy in the hadronic calorimeter. On the other hand, hits in the outer calorimeter layers are expected on the path of a muon to the muon chambers.
- Muons can be distinguished from heavier charged particles (kaons, protons) via the $\mathrm{d}E/\mathrm{d}x$ measurement in the central detector. There is hardly any separation from charged pions, however.

The tagging of isolated muons is in principle not difficult and is not considered here.

In the default algorithm, the muon selection proceeds as follows. Muon track segments are formed from the hits in the muon chambers. Tracks from the central tracking chambers with a momentum greater than 2 GeV are extrapolated to the muon chambers. For each track segment in the muon chambers, only the "best matching" central track is considered further, which is defined as the extrapolated track that has the smallest angular separation α to the muon track segment in question. A χ_{pos} for the position match in θ and ϕ between every track segment in the muon chambers and the "best matching" track from the central detector is formed, and tracks are selected as muon candidates if they pass a cut on χ_{pos}, typically set to 3.0. Additional optional cuts are usually applied on the muon $\mathrm{d}E/\mathrm{d}x$ weight W_μ for tracks with a minimum number of $\mathrm{d}E/\mathrm{d}x$ samplings and on the number of track segments in the muon chambers in the vicinity of the extrapolated track position.

It has been found that in hadronic events, any sample of candidates that are not selected as "best matching" tracks according to the above algorithm is very impure. For the neural network approach, this "best match" requirement is therefore kept as a preselection. In addition, the track momentum is required to be larger than 2 GeV. However, no cuts on χ_{pos} or $\mathrm{d}E/\mathrm{d}x$ information are applied, and no requirement on the number of muon chamber track segments in the vicinity of the extrapolated track is made. Eleven quantities are used as inputs to the neural network for the selection of muons among these preselected candidates. The inputs are shown in figure A.1 for hadronic events at 183 GeV. They are:

- Information from the matching:
  - χ_{pos}, the square root of the χ^2 for the position match in θ and ϕ between the extrapolated track and the associated muon track segment in the muon chambers, as described in [51];
  - the ratio of distances $R_{\mu mis} = \alpha^{(1)}/\alpha^{(2)}$ of the best and second best matching track to the muon segment; this is a measure of how ambiguous the choice of the best matching track was in the preselection; and
  - $\mathcal{P}_\mu$, the χ^2 probability for the matching which is computed using both position and direction information for the track in the central detector and the associated muon track segment as described in [52]. This quantity is not expected to be uncorrelated with χ_{pos}, but this is not a problem in the neural network approach.

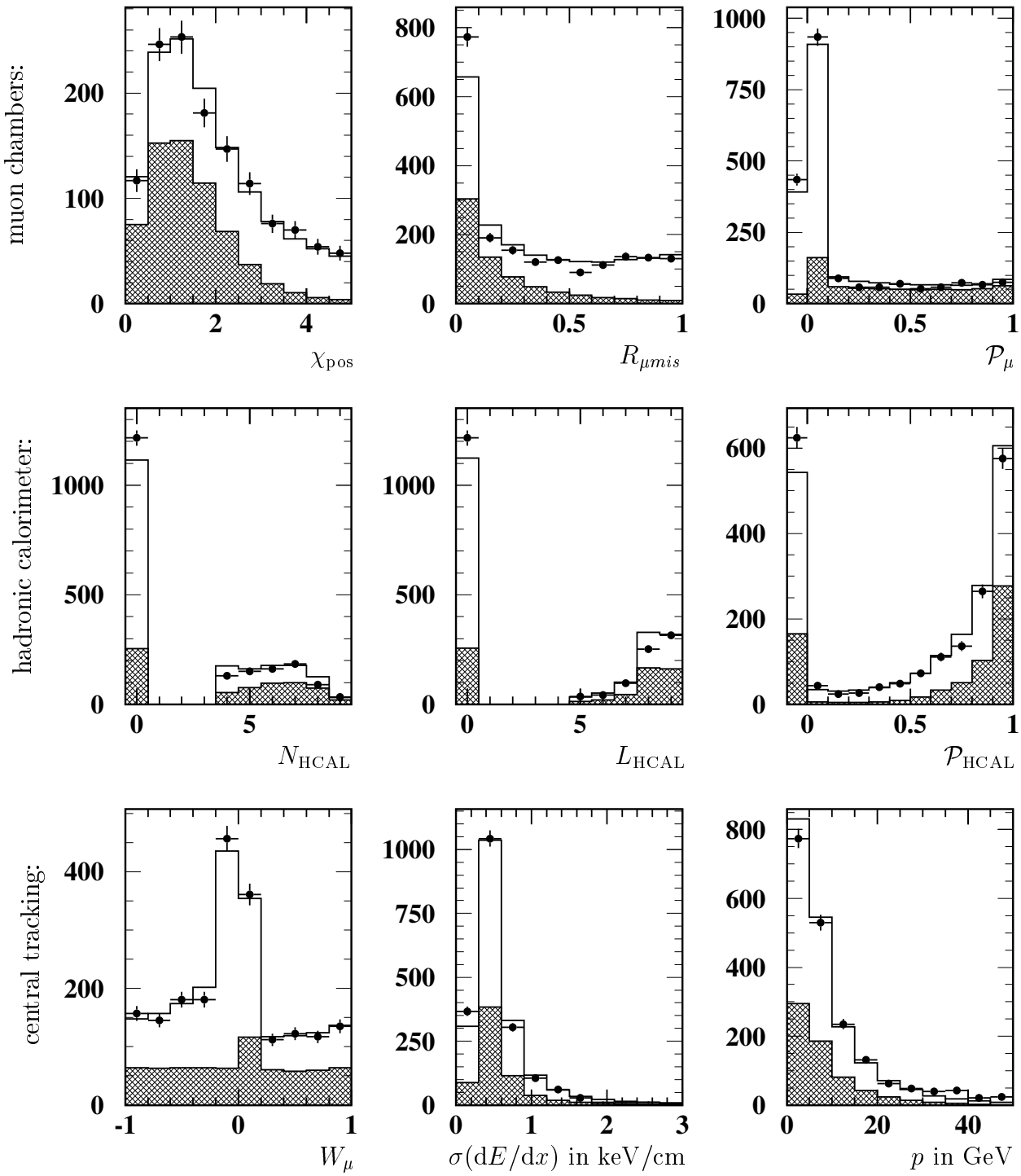

Figure A.1: The input quantities to the neural network for muon identification, except for the extrapolated position in $|\cos\theta|$ and ϕ of the track at the entrance of the muon chambers. The inputs are described in the text. In each plot, the vertical axis shows the number of entries, where the points with error bars denote preselected muon candidates in selected hadronic two-fermion events at 183 GeV. The solid histogram corresponds to the expectation from the simulation, and the hatched histogram to the muon contribution.

- Information from the hadronic calorimeter:
  - The number N_{HCAL} of calorimeter layers in the cluster associated with the central track;
  - the number L_{HCAL} of the outermost such layer; and
  - the χ^2 probability $\mathcal{P}_{\mathrm{HCAL}}$ for the match in θ and ϕ between the track (extrapolated to the hadron calorimeter) and the associated cluster.
  - (It has been tried to include the cluster energy divided by the track momentum as an additional input; however, this does not improve the overall performance of the network.)
- Specific energy loss:
  - The muon $\mathrm{d}E/\mathrm{d}x$ weight W_μ for the track, which is a measure of the probability that the track is compatible with a muon hypothesis, signed negative if the observed energy loss is smaller than that expected for a muon of the observed momentum;
  - $\sigma_{\mathrm{d}E/\mathrm{d}x}$, the error on the $\mathrm{d}E/\mathrm{d}x$ measurement; and
  - the momentum p of the track.
- Geometrical information:
  - In addition, the position in $|\cos\theta|$ and ϕ where the extrapolated track enters the muon chambers is used, since the hadronic calorimeter and muon chambers are not uniform over the whole acceptance.

A.3 Implementation and Performance of the Neural Net

The neural network has been trained using JETNET [91] with muon candidates in simulated hadronic two-fermion events at 183 GeV. A topology with 18 nodes in one hidden layer has been found to perform best on a statistically independent sample. The network performance is largely independent of the signal and background momentum distributions; therefore it is not necessary to retrain the neural network for events at LEP1. An exception are isolated, high-momentum muons, where the default cuts perform better. This is not unexpected since these muons and the associated backgrounds have rather different properties from those in hadronic jets, which have been used in the neural network training.

Figure A.2 shows the distribution of the network output $\mathcal{N}_\mu$ as well as the efficiency vs. purity curve when varying the cut on $\mathcal{N}_\mu$. The corresponding curve for a cut on χ_{pos} is also shown. High purity muon samples can be obtained, which is impossible with a simple cut on χ_{pos}. The improvement is lower for loose cuts, as expected (see section A.1).

The largest statistical improvement is expected when the muon network output is used as a continuous input to a subsequent analysis (e.g. another neural net) with only a loose preselection on the muon network output itself, as is the case in the heavy flavour asymmetry measurements presented in this thesis.

A.4 Systematic Errors

Systematic errors on the efficiency and misidentification rate have been studied both for the LEP1 and LEP2 detector configurations. For systematic error evaluation in physics analyses

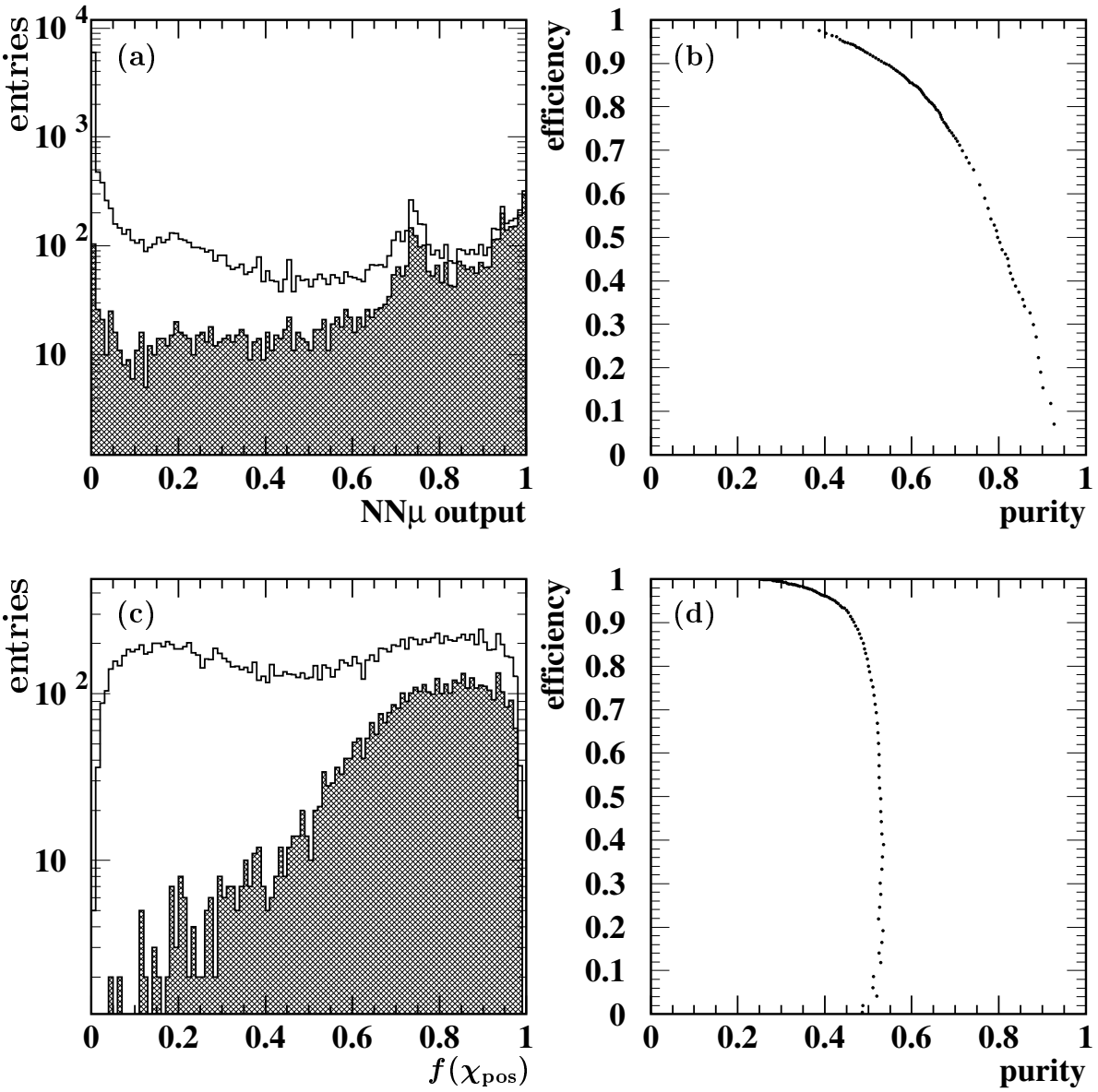

Figure A.2: In figure (a), the muon network output is shown as points with error bars for tracks in simulated hadronic two-fermion events at 183 GeV. The expectation from the simulation is given by the solid histogram, where the muon component is shown as the hatched histogram. The efficiency vs. purity curve obtained from this distribution is shown in (b). Each dot corresponds to a cut on the network output; the efficiency drops and the purity rises as the cut is moved to higher network output values.
In figures (c) and (d), the corresponding plots are shown for cuts on $\chi_{\rm pos}$. No $\mathrm{d}E/\mathrm{d}x$ cut has been applied, and the muon preselection (best matching tracks with $p > 2\,\mathrm{GeV}$) is identical to that in the top plots. In figure (c), the value of $\chi_{\rm pos}$ has been transformed to lie within the range $[0, 1]$; a cut at $\chi_{\rm pos} = 3$ corresponds to a transformed value $f(\chi_{\rm pos}) = 0.555$.

that use the neural network muon identification, tables of weights for Monte Carlo simulated events are provided in bins of the network output $\mathcal{N}_\mu$ [92]. As an example, the reweighting table for simulated events at LEP2 is given in table A.1. Tables with similar reweighting factors have been determined for the LEP1 simulation, separately for each year of data taking. For analyses like the asymmetry measurements in chapters 3 and 4 which use the muon network output as a continuous input variable, it is recommended to reweight the Monte Carlo simulation for each muon with the factors given in the appropriate table according to the $\mathcal{N}_\mu$ value. To compute the systematic error, the reweighting factors for each bin are then to be varied independently by their uncertainty from the comparison between data and simulation (which is also listed in table A.1) and the resulting systematic deviations in all bins added in quadrature. Analyses which simply cut on the muon network output (a cut at $\mathcal{N}_\mu > 0.65$ is recommended) may instead use the averaged reweighting factors accordingly. It should be noted that the systematic studies presented here are not as extensive as those for the default selection [89], so for systematics limited analyses, it may be safer (and not a large compromise as far as the total measurement error is concerned) to use the default selection instead of the neural network.

In the following, the determination of reweighting factors using event samples that are enhanced and depleted in muons is described. These studies have been performed together with Dave Charlton, who has determined the reweighting factors for muon signal, while I have worked out the method to obtain the corresponding factors for the background.

A.4.1 Systematic Errors at LEP1

To check the description of the muon signal in the simulation, the neural network output has been studied with samples of muons from $\mathrm{Z} \to \mu^+\mu^-$ and $\gamma\gamma \to \mu^+\mu^-$ events as in [89]. The tracks in the muon test samples are isolated, and a systematic error arises from potential differences between isolated tracks and tracks in a jet environment. This effect has been studied in [89] and yields an additional error of 0.4%. Another error of $1.1 - 1.6\%$ on the efficiency is due to the uncertainty in the tracking resolution itself [89] as described in section 3.5.1.5, but is usually evaluated separately and thus not listed explicitly here.

For a check of the inclusive background, tracks from the central detector that are *not* best matching candidates are used. This sample is highly depleted in muons; the fraction of true muons is typically between 5% and 10% at high neural network outputs and is treated as a systematic error.

The relative content of pions, kaons, and protons in the inclusive background test sample is similar, but not identical to that of the background in the sample of best matching tracks. This is taken into account as follows:

1. Let the fraction of particles of type i ($i = \pi, \mathrm{K}, \mathrm{p}$) in the "best match" and "not best match" samples be denoted $f_{\mathrm{bm}}(i)$ and $f_{\mathrm{nbm}}(i)$.
2. Assume that the total systematic error σ_{nbm} as tested in the "not best match" test sample were due to particle species i only ($i = \pi, \mathrm{K}, \mathrm{p}$).
3. The error on background of species i itself is then the total systematic error determined so far divided by the fraction $f_{\mathrm{nbm}}(i)$:

$$\sigma(i) = \frac{\sigma_{\mathrm{nbm}}}{f_{\mathrm{nbm}}(i)} \ .$$

4. Since it is not known in point 2. above which particle species is responsible for which portion of the systematic error, all contributions from 3. are summed in quadrature. This leads to an error of

$$\begin{aligned} \sigma_{\mathrm{bm}} &= \sqrt{\sum_i \left(f_{\mathrm{bm}}(i)\sigma(i)\right)^2} \\ &= \sigma_{\mathrm{nbm}} \sqrt{\sum_i \left(\frac{f_{\mathrm{bm}}(i)}{f_{\mathrm{nbm}}(i)}\right)^2} \quad . \end{aligned}$$

The factors $\sqrt{\sum_i \left(\frac{f_{\mathrm{bm}}(i)}{f_{\mathrm{nbm}}(i)}\right)^2}$ are evaluated in bins of $\mathcal{N}_\mu$, and are typically between 2 and 3.

The statistical errors of the reweighting factors have been scaled according to these factors.

A.4.2 Systematic Errors at LEP2

At LEP2, $\gamma\gamma \to \mu^+\mu^-$ events can be used to study the network output for muons, similar to the LEP1 case, as shown in figure A.3 and table A.1. The quoted systematic error is larger than for LEP1, so that differences between the modelling of isolated tracks and tracks within jets can be neglected even though the track density in jets is higher at LEP2 than at LEP1.

The inclusive background check with muon candidates that are *not* best candidates is performed as for LEP1, and the results are shown in figure A.4. Again, the fraction of true muons in this sample is typically between 5% and 10% at high neural network outputs and is treated as a systematic error in the comparison of data and the simulation. The statistical errors are scaled according to the pion, kaon, and proton contents of the samples as described in section A.4.1.

A.5 Conclusion

A neural network routine for muon identification at OPAL has been developed. Its statistical performance is significantly better than that of the default algorithm. Systematic errors for signal and background modelling have been studied both for LEP1 and LEP2 configurations of the detector. For a cut on the neural network output at $\mathcal{N}_\mu > 0.65$, weighting factors for Monte Carlo signal and background have been determined as follows:

	signal	background
LEP1	0.994 ± 0.011	1.025 ± 0.025
LEP2	0.953 ± 0.047	0.971 ± 0.041

For physics analyses that use the muon network output as a continuous value, tables with corresponding weighting factors in bins of the muon network output are provided.

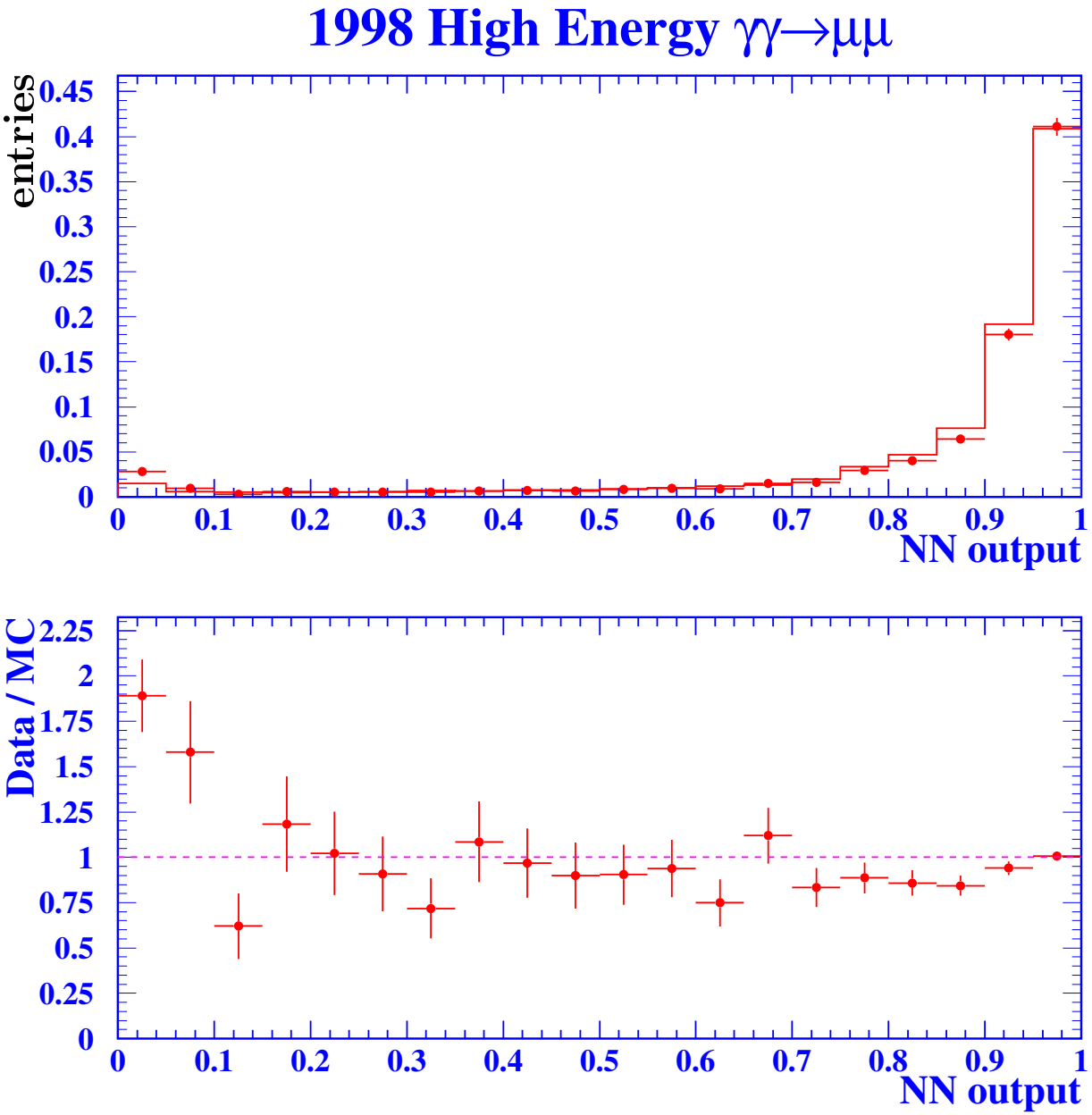

Figure A.3: In the top plot, the muon network output for tracks from $\gamma\gamma \to \mu\mu$ events is shown for LEP2 data taken in 1998 (points with error bars) and the simulation (solid histogram), normalized to one muon candidate. The bottom plot shows the ratio of the two distributions, which is also listed in table A.1.

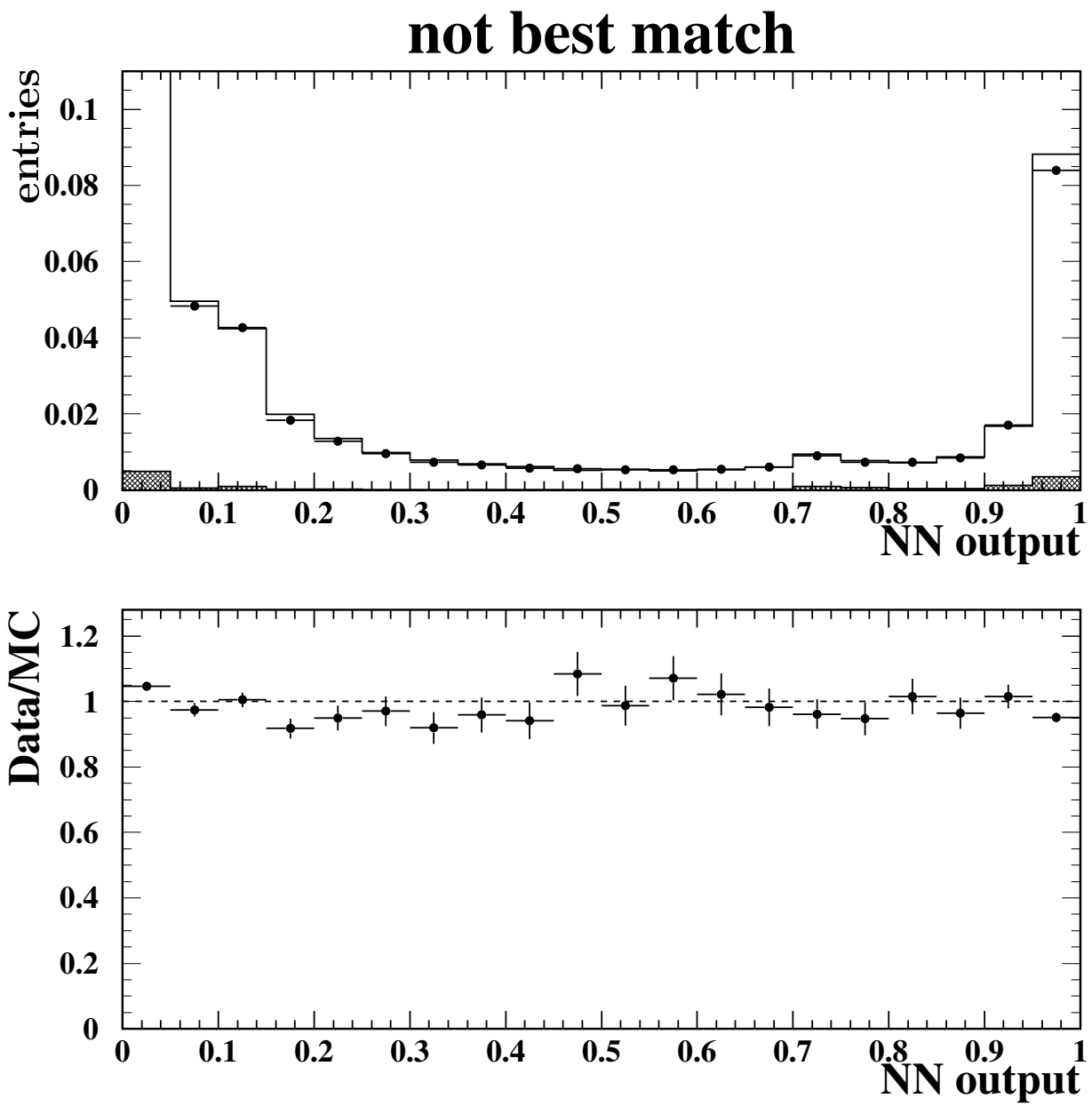

Figure A.4: In the top plot, the muon network output distribution is shown for tracks in hadronic events that are *not best matching tracks*. The points with error bars show the LEP2 calibration data and the solid histogram the Monte Carlo simulation. The residual muon component is indicated by the hatched histogram. The bottom plot shows the ratio of data and simulation, which is also listed in table A.1.

$\mathcal{N}_\mu$ bin	weighting factor	
	signal	background
	$\gamma\gamma \to \mu\mu$	*not best match*
$0.0 - 0.05$	1.891 ± 0.200	$1.046 \pm 0.017 \pm 0.008$
$0.05 - 0.1$	1.579 ± 0.283	$0.975 \pm 0.062 \pm 0.012$
$0.1 - 0.15$	0.621 ± 0.181	$1.005 \pm 0.066 \pm 0.023$
$0.15 - 0.2$	1.183 ± 0.263	$0.917 \pm 0.110 \pm 0.014$
$0.2 - 0.25$	1.022 ± 0.230	$0.950 \pm 0.095 \pm 0.018$
$0.25 - 0.3$	0.908 ± 0.207	$0.971 \pm 0.188 \pm 0.011$
$0.3 - 0.35$	0.718 ± 0.165	$0.919 \pm 0.504 \pm 0.016$
$0.35 - 0.4$	1.085 ± 0.222	$0.959 \pm 0.147 \pm 0.023$
$0.4 - 0.45$	0.968 ± 0.190	$0.941 \pm 0.227 \pm 0.020$
$0.45 - 0.5$	0.899 ± 0.181	$1.085 \pm 0.198 \pm 0.022$
$0.5 - 0.55$	0.904 ± 0.166	$0.987 \pm 0.305 \pm 0.044$
$0.55 - 0.6$	0.938 ± 0.159	$1.071 \pm 0.242 \pm 0.039$
$0.6 - 0.65$	0.749 ± 0.130	$1.022 \pm 0.211 \pm 0.046$
$0.65 - 0.7$	1.120 ± 0.154	$0.983 \pm 0.185 \pm 0.043$
$0.7 - 0.75$	0.833 ± 0.108	$0.962 \pm 0.154 \pm 0.100$
$0.75 - 0.8$	0.886 ± 0.086	$0.948 \pm 0.142 \pm 0.088$
$0.8 - 0.85$	0.859 ± 0.071	$1.015 \pm 0.158 \pm 0.059$
$0.85 - 0.9$	0.844 ± 0.055	$0.964 \pm 0.149 \pm 0.046$
$0.9 - 0.95$	0.940 ± 0.037	$1.015 \pm 0.105 \pm 0.072$
$0.95 - 1.0$	1.006 ± 0.026	$0.951 \pm 0.042 \pm 0.039$
$0.65 - 1.0$	0.953 ± 0.018	$0.971 \pm 0.034 \pm 0.023$
$0.65 - 1.0$	0.953 ± 0.047	0.971 ± 0.041

Table A.1: The reweighting factors for the LEP2 Monte Carlo simulation in bins of the network output $\mathcal{N}_\mu$. For the inclusive background test, the first error is due to data and Monte Carlo statistics, scaled in the way described in the text, and the second error is the systematic error from the muon contamination in the muon depleted sample. The last line contains the integrated reweighting factors with the recommended variations for analyses where a value $\mathcal{N}_\mu > 0.65$ is required without using the $\mathcal{N}_\mu$ value as continuous input. Similar reweighting factors have been determined for LEP1 and are listed in full detail in [92].

Appendix B

Systematic Errors Related to the Slow Pion Reconstruction

In this appendix, the determination of the systematic uncertainty on the efficiency for slow pion reconstruction is described. This method is used for the asymmetry measurements at LEP2 (see section 3.5.2.1). A similar technique has been applied in [53], where the corresponding error for the LEP1 data sample has been evaluated.

In contrast to the electron and muon selection, there is no control sample with which the slow pion content in the LEP2 data could be measured easily. Therefore, the calibration data is taken to check the modelling of slow pions in the Monte Carlo simulation. A fit is applied to the p_t^2 spectrum of slow pion candidates in the Z calibration data to extract the efficiency of slow pion reconstruction in Z decays during the years of LEP2 data taking. This efficiency is compared with that in the LEP2 simulation to obtain a systematic error on the efficiency for slow pion reconstruction at centre-of-mass energies above the Z resonance.

B.1 The Technique

Since the number of D^{*+} mesons in Z decays is known ($\bar{n}_{\mathrm{D}^{*+}} = 0.1854 \pm 0.0041 \pm 0.0059 \pm 0.0069$ per hadronic Z decay [53]), the slow pion reconstruction efficiency in Z decays can be determined in the LEP2 calibration data when measuring the slow pion content in the data. Any difference between the efficiencies in data and the simulation would then imply modelling problems in the simulation. In case no significant deviation is observed, the uncertainty on the difference can be used to determine the systematic error for the slow pion reconstruction at LEP2 energies.

This procedure is consistent with the asymmetry analysis, where the Standard Model predictions are assumed for the relative hadronic production cross-sections R_{b} and R_{c}, and the dependence of the asymmetries on the assumed values is given (see sections 3.4.5 and 4.4). In addition, the values of $f(\mathrm{c} \to \mathrm{D}^{*+})$ and $f(\mathrm{b} \to [\mathrm{c}, \overline{\mathrm{c}}] \to \mathrm{D}^{*\pm})$ are taken from [53] and varied within their errors. The branching ratio $Br(\mathrm{D}^{*+} \to \mathrm{D}^0 \pi^+)$ is taken as another external input from reference [2]. Thus, for this given set of parameters, the number of slow pions in the data is assumed to be known in the asymmetry measurement (as is, for similar reasons, the number of prompt leptons), and only the reconstruction efficiency remains to be tested. For a given slow pion reconstruction efficiency, the number of slow pions in the selected sample is known,

and the rest of the candidates can be treated as background. Variations of bottom and charm production, hadronisation fractions, and branching ratios are independent of the systematic error on the slow pion efficiency determined in this appendix.

It is not assumed that the efficiencies for slow pion reconstruction in Z decays and at LEP2 be equal. The efficiency at LEP2 is taken from the Monte Carlo simulation (as for the prompt leptons). The relative difference of efficiencies for slow pion reconstruction in the calibration data and Monte Carlo simulation is used in order to correct the efficiency at LEP2 (if necessary), and the error on the relative difference is assigned as an error to the knowledge of the slow pion efficiency in the LEP2 data.

B.2 Determination of the Slow Pion Reconstruction Efficiency

Slow pions are reconstructed in the Z calibration data with the same selection as used at LEP2. Only the upper momentum cut is adjusted according to the kinematic limit given in equation 3.11 (8.65 GeV at 189 GeV, 4.17 GeV at $\sqrt{s} = m_{\mathrm{Z}}$). Then, the background content in the sample is determined in a fit to the p_t^2 spectrum[1] and subtracted from the total number of candidates in order to obtain the number of reconstructed slow pions in the data.

The p_t^2 spectra of background candidates in the data and simulation do not match. Thus, it is not possible to use the background p_t^2 distribution from the Monte Carlo simulation in order to determine the slow pion content in the data. Instead, a function is fitted to the sideband of the p_t^2 spectrum and extrapolated to $p_t^2 = 0$. The fit is generally stable if two parameters are fitted. Two different functions have been found that describe the background in the p_t^2 distribution well:

$$\begin{aligned} f_1(p_t^2) &= p_1 \cdot e^{p_2 \cdot p_t^2} \quad \text{and} \\ f_2(p_t^2) &= \frac{p_1 \cdot p_2}{\left[1 + \left(p_t^2 - 0.03\,\mathrm{GeV}^2\right)\right]^{\,p_2}} \,, \end{aligned} \tag{B.1}$$

where p_1 and p_2 are the fitted parameters.

The procedure for the determination of the systematic uncertainty on the slow pion efficiency is outlined below and is also summarized in table B.1.

- The total numbers of slow pions in the data and Monte Carlo simulated samples are computed as given in table B.1.
- The background distributions in the Monte Carlo simulation are fitted to show that these functions can reproduce the background distributions. The results of these fits are shown in figure B.1. The fitted functions describe the background p_t^2 distribution well.
- The total distributions (including signal) are then fitted in the sideband range of $0.03\,\mathrm{GeV}^2 < p_t^2 < 0.1\,\mathrm{GeV}^2$ (which explains the parameter of $0.03\,\mathrm{GeV}^2$ in the second function, see equation B.1). In each step of the minimisation, the fitted signal is determined as the number of candidates at $p_t^2 < 0.01\,\mathrm{GeV}^2$ minus the integral of the fitted function in that region. Assuming the shape of the signal p_t^2 spectrum to be correctly

[1] The transverse momentum squared is defined with respect to the recalculated momentum of the parent D^{*+} jet as outlined in section 3.4.2.3.

	Z calibration data	**simulation**
total sample:		
events	169102	255782
$\bar{n}_{\mathrm{D}^{*+}}$	$0.1854 \pm 0.0041 \pm 0.0059 \pm 0.0069$	0.2363
$\rightarrow \mathrm{D}^{*+}$	31350 ± 1690	60448
$\rightarrow$ slow pions	21410 ± 1230 (*syst.*)	41286
reconstructed:		
true slow pions	?	13173
raw fit result	6520 ± 320 (*stat.*)	10760 ± 320 (*stat.*)
fit bias	$-18.3\% \pm 23.0\%$ (*bias*)	-18.3%
fit result	7980 ± 390 (*stat.*) ± 450 (*syst.*) ± 1840 (*bias*)	
$\Rightarrow$ efficiency	$\mathbf{0.373 \pm 0.090}$	**0.319**

Table B.1: The procedure for the determination of the error on the slow pion reconstruction efficiency is summarized. In the upper part of the table, the data and Monte Carlo simulated samples and their slow pion contents are given. The determination of the fit bias from the simulation and the corrected fit result in the data are shown in the second part. The slow pion efficiencies in the Z calibration data and Monte Carlo simulation are given in the last line of the table.

modelled, this number is then used to account for the small contamination of true slow pions that extends into the sideband region $p_t^2 > 0.03\,\mathrm{GeV}^2$.

In figure B.2, the results of this fit to the Monte Carlo simulation are shown. For both fit functions, the signal is underestimated. A cross-check of the fitting program has been performed, using the true background shape in the fit, and it has been found that the background is exactly reproduced. The weighted mean of the fit results is a number of 10760 ± 320 slow pions (taking the larger statistical error of one fit as the error), which corresponds to a fit bias with respect to the true number of -18.3% relative.

- The same fit is then applied to the data distribution. The results are shown in figure B.3. In addition, it has been tried to use the Monte Carlo background distribution in a fit to the data, as shown in figure B.4. The signal p_t^2 spectrum obtained with this fit does not agree with that in the simulation; however, it has been found in the OPAL D^{*+} measurement [53] that this distribution is well modelled. It is concluded that the background p_t^2 distribution is not well modelled in the simulation, so that the result of this latter fit cannot be used.
- The raw results of the fits to the data distribution are then corrected for the fit bias of $-18.3\% \pm 23.0\%$ determined from the Monte Carlo simulation, where the larger one of the differences between one of the two fit results in the simulation and the true number of slow pions is assigned as a systematic error. The fitted number of slow pions in the data is then $n_{\mathrm{data}} = 7980 \pm 1930$, where again, the weighted mean of the two fit results has been taken together with the larger statistical error of one fit. The error from the bias is the dominant contribution to the total error.

The efficiencies in the data and Monte Carlo simulation are consistent within the error,

which is dominated by the systematic uncertainty. The error of 9.0% on the efficiency of 37.3% corresponds to a relative error of 24.2%, by which the slow pion efficiency at LEP2 is varied in order to determine the systematic error on the asymmetry measurement.

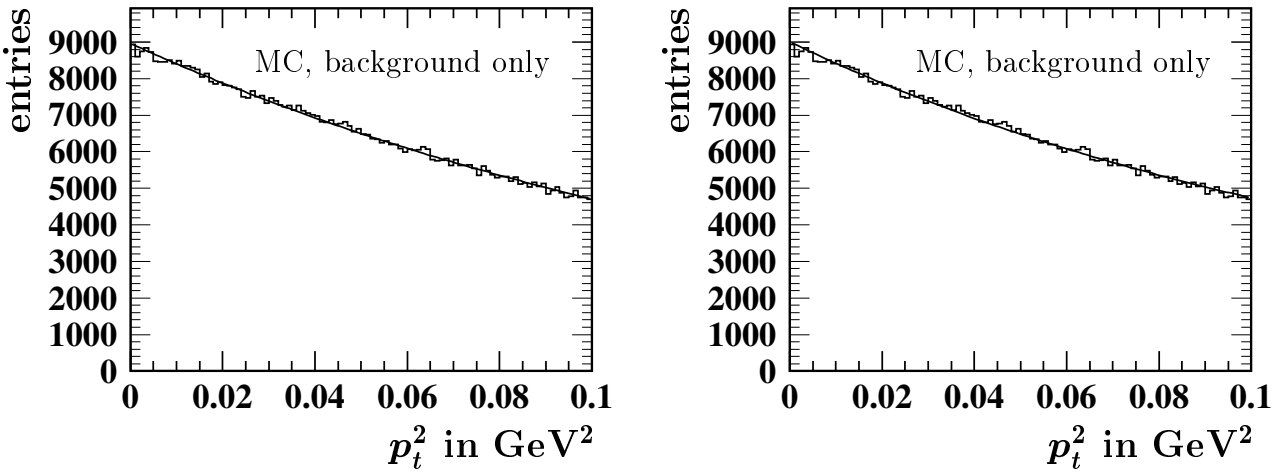

Figure B.1: The fit test on the slow pion background distribution in the Monte Carlo simulation. The left plot shows the fit using function f_1, the right plot the one with f_2 as given in equation B.1. In each case, the slow pion candidates in the simulation are indicated by the solid histogram, and the fitted function is given by the line.

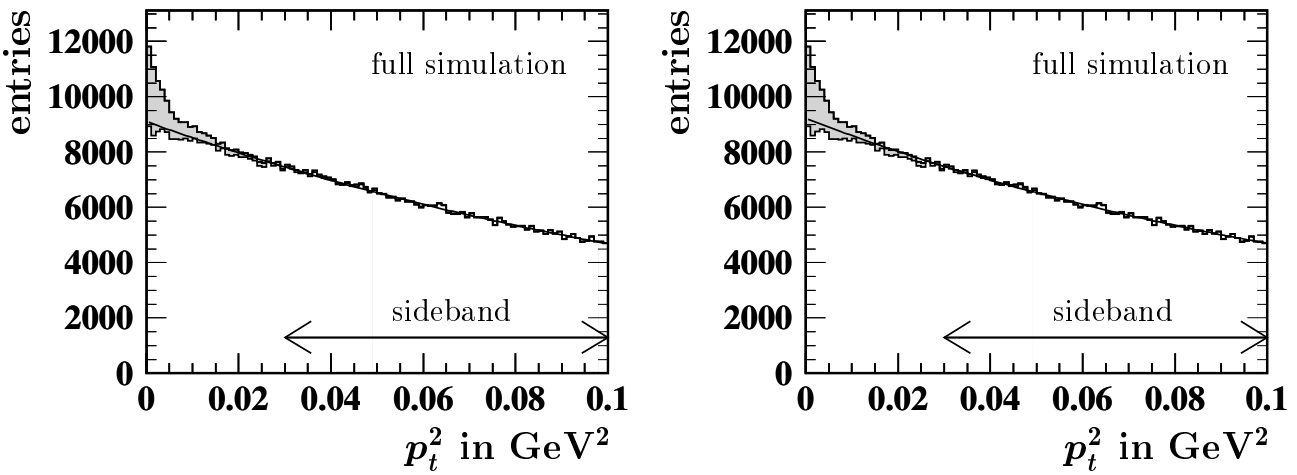

Figure B.2: The fit of the total p_t^2 distribution in Monte Carlo simulation. The left plot shows the fit using function f_1, the right plot the one with f_2. The contribution from true slow pions is shown as the shaded area. The line indicates the fit result, where the fitted p_t^2 sideband is given by the arrow.

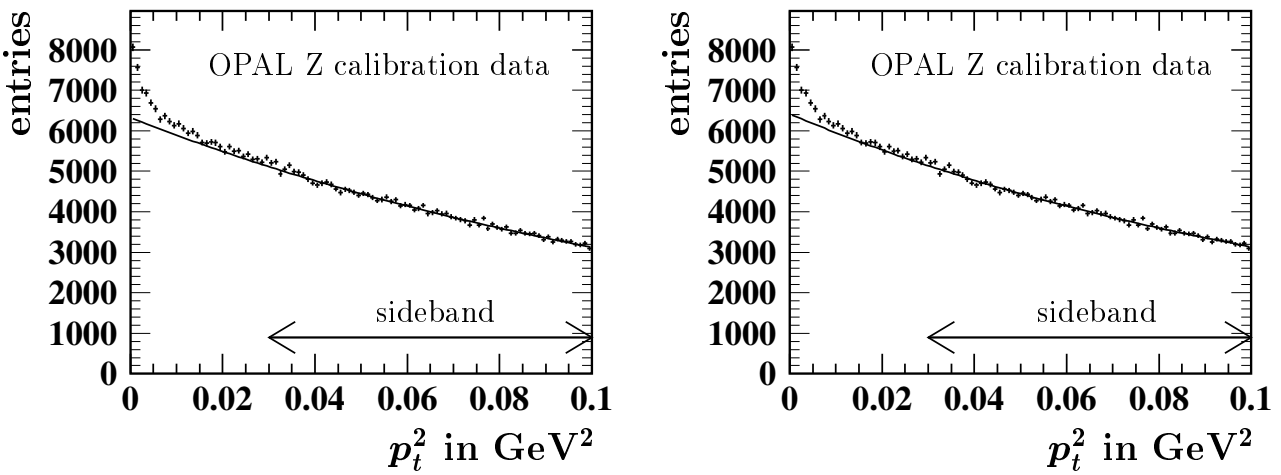

Figure B.3: The fit of the p_t^2 distribution in the Z calibration data. The left plot shows the fit using function f_1, the right plot the one with f_2. In both cases, the data is shown by the points with error bars, and the fitted function is given by the line.

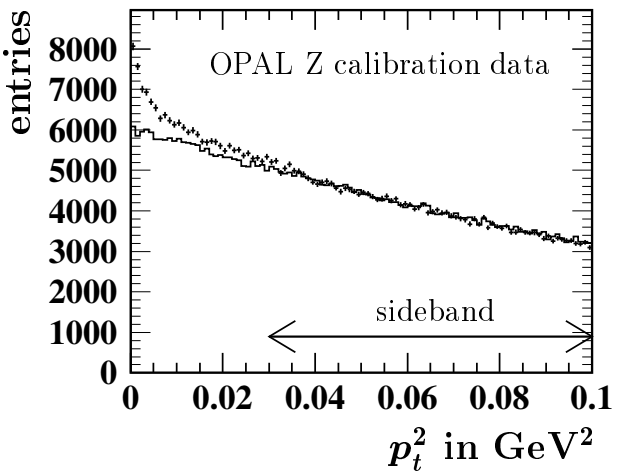

Figure B.4: The fit to the data distribution, using the background distribution from the Monte Carlo simulation to determine the background content. The data is indicated by the points with error bars. The background p_t^2 distribution is shown by the solid histogram, where the normalisation has been determined in the fit to the p_t^2 sideband.

Appendix C

Model Independent Calculation of $P_V^{\rm prim}$

In this appendix, details of the calculations that lead to the dependence of the model independent value of $P_V^{\rm prim}$ on the production of the broad L=1 charmed mesons (equation 7.7) are provided.

As discussed in the text, the contributions from decays of D^{**} mesons have to be taken into account when calculating $P_V^{\rm prim}$. Two assumptions are made on D^{**} production:

- Since D^{**+} mesons have not yet been observed in $\mathrm{Z} \to \mathrm{c\bar{c}}$ decays, isospin invariance is assumed to be valid which yields equal production rates for corresponding D^{**0} and D^{**+} spin states.
- For each light quark flavour q=u,d,s, two broad and two narrow L=1 $\mathrm{c\bar{q}}$ mesons are predicted. For the $\mathrm{c\bar{u}}$ system, both narrow resonances (D_1^0 and D_2^{*0}) have been measured at OPAL, whereas only one narrow $\mathrm{c\bar{s}}$ resonance ($\mathrm{D}_{\mathrm{s}1}^+$) has been measured because $\mathrm{D}_{\mathrm{s}2}^{*+} \to \mathrm{D}^*\mathrm{K}$ decays occur too far from threshold to give rise to a clear signal. Thus, the additional assumption is made that the relative production of the different L=1 spin states does not depend on the flavour of the light quark.

Under these two assumptions, the production of any L=1 charmed meson can be expressed in terms of measured rates and two unknown parameters, $f(\mathrm{c} \to \mathrm{D}_0^{*0})$ and $f(\mathrm{c} \to \mathrm{D}_1^{\prime 0})$.

The OPAL $\mathrm{D}_{\mathrm{s}1}^+$ production measurement [82] assumes a 100% branching ratio for $\mathrm{D}_{\mathrm{s}1}^+ \to \mathrm{D}^{(*)}\mathrm{K}$ decays (i.e. to non-strange, charmed non-orbitally excited mesons). Therefore, any contribution from $\mathrm{D}_{\mathrm{s}}^{**+} \to \mathrm{D}_{\mathrm{s}}^{(*)+}\mathrm{X}$ decays is implicitly taken into account when using the measured $\mathrm{D}_{\mathrm{s}1}^+$ hadronisation fraction for an evaluation of $P_V^{\rm prim}$.

The quantity $P_V^{\rm prim}$ is calculated as follows:

$$P_V^{\rm prim} = \frac{V^{\rm prim}}{V^{\rm prim} + P^{\rm prim}} \tag{C.1}$$

$$= \frac{V^{\rm eff} - \left(T_{(\mathrm{s})} \to V\right)}{(V+P)^{\rm eff} - \left(T_{(\mathrm{s})} \to V \text{ or } P\right)} , \tag{C.2}$$

where in the above formula, V and P stand for non-strange charmed vector and pseudoscalar mesons, respectively, whereas $T_{(\mathrm{s})}$ denotes the sum of non-strange and strange charmed tensor

mesons (D^{**} and $\mathrm{D}_\mathrm{s}^{**}$). Thus,

$$P_V^{\mathrm{prim}} = \frac{2f(\mathrm{c}\to\mathrm{D}^{*0/+}) - 2f(\mathrm{c}\to\mathrm{D}^{**0}\to\mathrm{D}^{*0/+}) - f(\mathrm{c}\to\mathrm{D}_\mathrm{s}^{**+}\to\mathrm{D}^{*0/+})}{f(\mathrm{c}\to\mathrm{D}^0) + f(\mathrm{c}\to\mathrm{D}^+) - 2f(\mathrm{c}\to\mathrm{D}^{**0}) - f(\mathrm{c}\to\mathrm{D}_\mathrm{s}^{**+})}\,, \qquad \text{(C.3)}$$

where the factors of 2 are introduced from the assumptions $f(\mathrm{c}\to\mathrm{D}^{*0}) = f(\mathrm{c}\to\mathrm{D}^{*+})$ and $f(\mathrm{c}\to\mathrm{D}^{**0}) = f(\mathrm{c}\to\mathrm{D}^{**+})$.

The symbol $f(\mathrm{c}\to\mathrm{D}^{**}\to\mathrm{D}^{*0/+})$ is a shorthand notation for the hadronisation fraction of a charmed quark to a D^{**} meson times the fraction of D^{**} mesons decaying to a $\mathrm{D}^{*0/+}$. Spin and parity conservation restrict the possible decays of the different D^{**} spin states, as is illustrated in table 1.2 and figure 1.2. The fraction of D^{**} mesons decaying to a $\mathrm{D}^{*0/+}$ depends both on the relative production of the different D^{**} spin states and on the branching ratio $Br(\mathrm{D}_2^*\to\mathrm{D}^{*0/+})$, since for the D_2^* resonance, decays to both D^* and D are allowed. Due to phase-space effects, the branching ratio $Br_\mathrm{s}^{**} \equiv Br(\mathrm{D}_{\mathrm{s}2}^{*+}\to\mathrm{D}^{*0/+})$ of $\mathrm{D}_{\mathrm{s}2}^{*+}$ mesons to a D^{*0} or D^{*+} is expected to differ from the corresponding quantity $Br^{**} \equiv Br(\mathrm{D}_2^{*0}\to\mathrm{D}^{*0/+})$ for non-strange D^{**} mesons, see table 7.1.

Using the shorthand notation $f_{\mathrm{D_X}} \equiv f(\mathrm{c}\to\mathrm{D_X})$, equation 7.7 can then be derived as follows:

$$\begin{aligned} P_V^{\mathrm{prim}} &= \frac{2f_{\mathrm{D}^*} - 2\left(f_{\mathrm{D}_1'^0} + f_{\mathrm{D}_1^0} + Br^{**}f_{\mathrm{D}_2^{*0}}\right) - \frac{f_{\mathrm{D}_{\mathrm{s}1}^+}}{f_{\mathrm{D}_1^0}}\left(f_{\mathrm{D}_1'^0} + f_{\mathrm{D}_1^0} + Br_\mathrm{s}^{**}f_{\mathrm{D}_2^{*0}}\right)}{f_{\mathrm{D}^0} + f_{\mathrm{D}^+} - 2\left(f_{\mathrm{D}_0^{*0}} + f_{\mathrm{D}_1'^0} + f_{\mathrm{D}_1^0} + f_{\mathrm{D}_2^{*0}}\right) - \frac{f_{\mathrm{D}_{\mathrm{s}1}^+}}{f_{\mathrm{D}_1^0}}\left(f_{\mathrm{D}_0^{*0}} + f_{\mathrm{D}_1'^0} + f_{\mathrm{D}_1^0} + f_{\mathrm{D}_2^{*0}}\right)} \qquad \text{(C.4)} \\ &=: \frac{A - R_\mathrm{c} f_{\mathrm{D}_1'^0}}{B - R_\mathrm{c}\left(f_{\mathrm{D}_1'^0} + f_{\mathrm{D}_0^{*0}}\right)}\,, \end{aligned}$$

where in the transition to the second line, both numerator and denominator are multiplied by a factor of $R_\mathrm{c}/\left(2 + \frac{f(\mathrm{c}\to\mathrm{D}_\mathrm{s}^{**+})}{f(\mathrm{c}\to\mathrm{D}^{**0})}\right)$. The parameters A and B are then given by

$$\begin{aligned} A &= R_\mathrm{c}\left[2\,f(\mathrm{c}\to\mathrm{D}^{*0/+}) - 2\left(f(\mathrm{c}\to\mathrm{D}_1^0) + f(\mathrm{c}\to\mathrm{D}_2^{*0}\to\mathrm{D}^{*0/+})\right)\right. \\ &\qquad \left. - \left(f(\mathrm{c}\to\mathrm{D}_{\mathrm{s}1}^+) + f(\mathrm{c}\to\mathrm{D}_{\mathrm{s}2}^{*+}\to\mathrm{D}^{*0/+})\right)\right] \Big/ \left[2 + \frac{f(\mathrm{c}\to\mathrm{D}_\mathrm{s}^{**+})}{f(\mathrm{c}\to\mathrm{D}^{**0})}\right] \quad \text{and} \qquad \text{(C.5)} \\ B &\equiv R_\mathrm{c}\left[f(\mathrm{c}\to\mathrm{D}^0) + f(\mathrm{c}\to\mathrm{D}^+) - 2\left(f(\mathrm{c}\to\mathrm{D}_1^0) + f(\mathrm{c}\to\mathrm{D}_2^{*0})\right)\right. \\ &\qquad \left. - \frac{f(\mathrm{c}\to\mathrm{D}_\mathrm{s}^{**+})}{f(\mathrm{c}\to\mathrm{D}^{**0})}\left(f(\mathrm{c}\to\mathrm{D}_{\mathrm{s}1}^+) + f(\mathrm{c}\to\mathrm{D}_{\mathrm{s}2}^{*+})\right)\right] \Big/ \left[2 + \frac{f(\mathrm{c}\to\mathrm{D}_\mathrm{s}^{**+})}{f(\mathrm{c}\to\mathrm{D}^{**0})}\right]\,, \qquad \text{(C.6)} \end{aligned}$$

respectively.

Bibliography

[1] M. Consoli, W. Hollik, and F. Jegerlehner, *Electroweak radiative corrections for* Z *physics,* in *Proceedings of the Workshop on* Z *Physics at LEP1,* CERN 89-08, Vol. 1, 7.

[2] Particle Data Group, C. Caso et al., Eur. Phys. J. **C3** (1998) 1.

[3] The 4 LEP experiments: ALEPH, DELPHI, L3 and OPAL, the LEP Electroweak Working Group, and the SLD Heavy Flavour and Electroweak Groups, *A Combination of Preliminary Electroweak Measurements and Constraints on the Standard Model,* CERN-EP/99-015, 8th February 1999.

[4] A. Leike, T. Riemann, and J. Rose, Phys. Lett. **B273** (1991) 513;
T. Riemann, Phys. Lett. **B293** (1992) 451;
S. Kirsch and T. Riemann, Comp. Phys. Comm. **88** (1995) 89.

[5] D. Bardin et al., CERN-TH 6443/92 (May 1992); Phys. Lett. **B255** (1991) 290; Nucl. Phys. **B351** (1991) 1; Z. Phys. **C44** (1989) 493; ZFITTER version 6.11 is used.

[6] S. Kirsch and T. Riemann, Comp. Phys. Commun. **88** (1995) 89; SMATASY version 6.11 is used.

[7] For experimental studies of $\gamma - \mathrm{Z}$ interference, see:
ALEPH Collaboration, Phys. Lett. **B399** (1997) 329;
DELPHI Collaboration, Z. Phys. **C72** (1996) 31.

[8] Measurements at $\sqrt{s} = 29$ GeV from the following publications are used in the computations in this thesis:
HRS Collaboration, ANL-HEP-PR-88-11 (1988);
MAC Collaboration, Phys. Lett. **B218** (1989) 369;
TPC Collaboration, Phys. Rev. **D31** (1985) 2719;
TPC Collaboration, Z. Phys. **C27** (1985) 39;
HRS Collaboration, Phys. Lett. **B206** (1988) 551;
TPC Collaboration, Phys. Rev. **D34** (1986) 1945.

[9] Measurements at $\sqrt{s} = 35$ GeV and $\sqrt{s} = 44$ GeV from the following publications are used in the computations in this thesis:
JADE Collaboration, Phys. Lett. **B146** (1984) 437;
MARK J Collaboration, Phys. Rep. **C109** (1984) 131;
JADE Collaboration, Z. Phys. **C44** (1989) 567;
TASSO Collaboration, Z. Phys. **C44** (1989) 365;
JADE Collaboration, Z. Phys. **C46** (1990) 349;

CELLO Collaboration, Z. Phys. **C47** (1990) 333;
TASSO Collaboration, Z. Phys. **C48** (1990) 433.

[10] Measurements at $\sqrt{s} = 58$ GeV from the following publications are used in the computations in this thesis:
TOPAZ Collaboration, Phys. Lett. **B268** (1991) 457;
VENUS Collaboration, Phys. Lett. **B278** (1992) 393;
VENUS Collaboration, Phys. Lett. **B278** (1992) 499;
TOPAZ Collaboration, Phys. Lett. **B340** (1994) 135;
VENUS Collaboration, Phys. Lett. **B313** (1993) 245;
VENUS Collaboration, Phys. Lett. **B313** (1993) 288;
TOPAZ Collaboration, Phys. Lett. **B314** (1993) 471;
AMY Collaboration, Phys. Rev. **D49** (1994) 4339;
AMY Collaboration, Phys. Lett. **B381** (1996) 365.

[11] OPAL Collaboration, *Measurements of* R_{b}, $A_{\mathrm{FB}}^{\mathrm{b}}$, *and* $A_{\mathrm{FB}}^{\mathrm{c}}$ *in* $\mathrm{e^+e^-}$ *Collisions at 130–183 GeV with the OPAL Detector at LEP,* OPAL Physics Note PN348, 3rd July 1998, submitted to ICHEP 1998 (Vancouver).

[12] OPAL Collaboration, *Measurements of* R_{b}, $A_{\mathrm{FB}}^{\mathrm{b}}$, *and* $A_{\mathrm{FB}}^{\mathrm{c}}$ *in* $\mathrm{e^+e^-}$ *Collisions at 189 GeV with the OPAL Detector at LEP,* OPAL Physics Note PN380, 12th March 1999, submitted to Moriond EW, March 13-20, 1999.

[13] OPAL Collaboration, *Measurements of* R_{b}, $A_{\mathrm{FB}}^{\mathrm{b}}$, *and* $A_{\mathrm{FB}}^{\mathrm{c}}$ *in* $\mathrm{e^+e^-}$ *Collisions at 130–189 GeV with the OPAL Detector at LEP,* to be submitted to Eur. Phys. J. **C**.

[14] ALEPH Collaboration, *Fermion Pair Production in* $\mathrm{e^+e^-}$ *Collisions at 189 GeV and Limits on Physics beyond the Standard Model,* ALEPH note 99-018, presented at the EPS-HEP Conference in Tampere, 1999, as EPS-HEP99 #6-694;
ALEPH Collaboration, *Study of Fermion Pair Production in* $\mathrm{e^+e^-}$ *Collisions at 130–183 GeV,* CERN-EP/99-042, 3rd March 1999, submitted to Eur. Phys. J. **C**.

[15] DELPHI Collaboration, *A measurement of the cross-section ratios for flavour tagged events at energies of 183 and 189 GeV,* DELPHI note 99-99, presented at the EPS-HEP Conference in Tampere, 1999, as EPS-HEP99 #6-219;
DELPHI Collaboration, *Measurement and Interpretation of Fermion-Pair Production at LEP energies from 130 to 172 GeV,* CERN-EP/99-005, (January 1999), submitted to Eur. Phys. J. **C**.

[16] ALEPH Collaboration, *A Measurement of the Gluon Splitting Rate into b anti-b Pairs in Hadronic* Z *Decays,* Phys. Lett. **B434** (1998) 437.

[17] DELPHI Collaboration, *Measurement of the Multiplicity of Gluons Splitting to Bottom Quark Pairs in Hadronic* Z *Decays,* Phys. Lett. **B405** (1997) 202.

[18] OPAL Collaboration, *Measurement of the Production Rate of Charm Quark Pairs from Gluons in Hadronic* Z *Decays,* CERN-EP/99-089, 31. July 1999, submitted to Eur. Phys. J.. **C**.

[19] A. F. Falk and M. E. Peskin, Phys. Rev. **D49** (1994) 3320.

[20] OPAL Collaboration, Z. Phys. **C74** (1997) 413;
ALEPH Collaboration, Z. Phys. **C69** (1996) 393;
L3 Collaboration, Phys. Lett. **B345** (1995) 589;
DELPHI Collaboration, Z. Phys. **C68** (1995) 353.

[21] K. Cheung, *Recent Progress on Perturbative QCD Fragmentation Functions,* Proceedings of the 1995 PASCOS/Hopkins Workshop, Baltimore, or hep-ph/**9505365**;
E. Braaten, K. Cheung, S. Fleming, and T.C. Yuan, Phys. Rev. **D51** (1995) 4819;
Y.-Q. Chen, Phys. Rev. **D48** (1993) 5181;
M. Suzuki, Phys. Rev. **D33** (1986) 676;
R. Suaya, J. S. Townsend, Phys. Rev. **D19** (1979) 1414.

[22] M. Anselmino et al., Phys. Lett. **B427** (1998) 356.

[23] ALEPH Collaboration, *Study of charm production in* Z *decays,* CERN-EP/99-094, submitted to Eur. Phys. J. **C**;
DELPHI Collaboration, P. Abreu et al., Z. Phys. **C59** (1993) 533, erratum-ibid. **C65** (1995) 709.

[24] Yi-Jin Pei, Z. Phys. **C72** (1996) 39.

[25] OPAL Collaboration, Z. Phys. **C74** (1997) 437.

[26] OPAL Collaboration, Z. Phys. **C74** (1997) 413;
ALEPH Collaboration, Z. Phys. **C69** (1996) 393;
DELPHI Collaboration, Z. Phys. **C68** (1995) 353.

[27] ALEPH Collaboration, *Study of charm production in* Z *decays,* CERN-EP/99-094, submitted to Eur. Phys. J. **C**.

[28] S. Anderson et al., Nucl. Instr. and Meth. **A403** (1998) 326;
OPAL Collaboration, Nucl. Instr. and Meth. **A346** (1994) 476;
B. E. Anderson et al., IEEE Transactions on Nuclear Science **41** (1994) 845;
OPAL Collaboration, Nucl. Instr. and Meth. **A324** (1993) 34;
O. Biebel et al., Nucl. Instr. and Meth. **A323** (1992) 169;
M. Hauschild et al., Nucl. Instr. and Meth. **A314** (1992) 74;
OPAL Collaboration, Nucl. Instr. and Meth. **A305** (1991) 275.

[29] See for example: D. H. Perkins, *Introduction to High Energy Physics,* 3$^{\rm rd}$ edition, Addison-Wesley Publishing Co. (1987).

[30] OPAL Collaboration, CERN-EP/98-137, accepted by Eur. Phys. J.

[31] OPAL Collaboration, Z. Phys. **C70** (1996) 357.

[32] OPAL Collaboration, Z. Phys. **C75** (1997) 385.

[33] OPAL Collaboration, Z. Phys. **C73** (1997) 379.

[34] OPAL Collaboration, Eur. Phys. J. **C6** (1999) 1.

[35] N. Brown and W. J. Stirling, Phys. Lett. **B252** (1990) 657;
S. Bethke, Z. Kunszt, D. Soper and W.J. Stirling, Nucl. Phys. **B370** (1992) 310;
S. Catani et al., Phys. Lett. **B269** (1991) 432;
N. Brown and W. J. Stirling, Z. Phys. **C53** (1992) 629.

[36] OPAL Collaboration, Phys. Lett. **B253** (1990) 511.

[37] OPAL Collaboration, Phys. Lett. **B376** (1996) 232.

[38] OPAL Collaboration, *Tests of the Standard Model and Constraints on New Physics from Measurements of Fermion-pair Production at 189 GeV at LEP,* CERN-EP/99-097, 8th July 1999, Submitted to Eur. Phys. J. **C**.

[39] F. Boudjema and B. Mele (conveners), E. Accomando et al., *Standard Model Processes,* in *Proceedings of the Workshop on Physics at LEP2,* CERN 96-01, Vol. 1, 207.

[40] JADE Collaboration, Z. Phys. **C33** (1986) 23;
JADE Collaboration, Phys. Lett. **B213** (1988) 235.

[41] OPAL Collaboration, Z. Phys. **C49** (1991) 341.

[42] S. Arcelli, A. Fanfani, S. Marcellini, and A. Montanari, *A Measurement of $R_{\rm b}$ and $A_{\rm FB}^{\rm b}$ at LEP2 Using a 3-D Vertex Tagging Algorithm,* OPAL Technical Note TN544, 15th May 1998.

[43] PYTHIA 5.721 and JETSET 7.408 generators: T. Sjöstrand, Comp Phys Comm. **82**, (1994), 74; T. Sjöstrand, LUTP 95-20.

[44] C. Peterson et al., Phys. Rev. **D27** (1983) 105.

[45] The LEP Collaborations, ALEPH, DELPHI, L3 and OPAL, Nucl. Instrum. Methods **A378** (1996) 101.

Updated averages are described in "Input Parameters for the LEP Electroweak Heavy Flavour Results for Summer 1998 Conferences", LEPHF 98-01 (see http://www.cern.ch/LEPEWWG/heavy/).

[46] J. Fujimoto et al., Comput. Phys. Commun. **100** (1997) 128.

[47] J. Allison et al., Nucl. Instr. and Meth. **A317** (1992) 47.

[48] OPAL Collaboration, Z. Phys. **C74** (1997) 1.

[49] OPAL Collaboration, Z. Phys. **C66** (1995) 19.

[50] OPAL Collaboration, Eur. Phys. J. **C2** (1998) 441.

[51] OPAL Collaboration, Z. Phys. **C65** (1995) 17.

[52] V. K. Jirsa and G. D. Lafferty, *The Routine ODMMWT for Muon Identification in OPAL,* OPAL TN066, September 1991.

[53] OPAL Collaboration, Eur. Phys. J. **C1** (1998) 439.

[54] OPAL Collaboration, Z. Phys. **C66** (1995) 555.

[55] LEP Heavy Flavor Working Group, D. Abbaneo et al., Eur. Phys. J. **C4** (1998) 185.

[56] MARK III Collaboration, Phys. Lett. **B263** (1991) 135.

[57] G. Altarelli et al., Nucl. Phys. **B208** (1982) 365.

[58] CLEO Collaboration, Phys. Rev. **D 45** (1992) 2212.

[59] DELCO Collaboration, Phys. Rev. Lett. **43** (1979) 1073.

[60] MARK III Collaboration, Phys. Rev. Lett. **54** (1985) 1976.

[61] N. Isgur, D. Scora, B. Grinstein and M. Wise, Phys. Rev. **D39** (1989) 799.

[62] CLEO Collaboration, Phys. Rev. **D45** (1992) 21.

[63] R. J. Barlow, *Statistics. A guide to the Use of Statistical Methods in the Physical Sciences,* The Manchester Physics Series, John Wiley & Sons, West Sussex, England, 1989.

[64] OPAL Collaboration, Z. Phys. **C69** (1996) 543.

[65] C. Peterson, D. Schlatter, I. Schmitt and P. M. Zerwas, Phys. Rev. **D27** (1983) 105.

[66] YFS3ff is a Monte Carlo program by S. Jadach, B. F. L. Ward, and Z. Was for fermion pair production with initial and final state photon exponentiation. No specific writeup or documentation exists. The program has now been superseded by the KK2f generator. Related information can be found in http://home.cern.ch/~jadach .

[67] R. Engel and J. Ranft, Phys. Rev. **D54** (1996) 4244;
R. Engel, Z. Phys. **C66** (1995) 203.

[68] A. Buijs, W. G. J. Langeveld, M. H. Lehto, and D. J. Miller, Comp. Phys. Commun. **79** (1994) 523.
The special purpose Monte Carlo program TWOGEN was developed within the OPAL collaboration. The version used for structure function analysis is called F2GEN.

[69] OPAL Collaboration, Eur. Phys. J. **C8** (1999) 217.

[70] O. Cooke and C. Jones, *Neural Network Electron and Photon Conversion Identification,* OPAL Technical Note TN556, 2nd July 1998.

[71] K. Mönig, *Status of Electroweak Tests with Heavy Quarks,* CERN-EP/98-78, 7 May 1998.

[72] R. Hawkings and K. Mönig, *Electroweak and CP violation physics at a linear collider Z-factory,* DESY-99-157, hep-ex/9910022, October 1999. Accepted by Eur. Phys. J. Direct **C**.

[73] *Conceptual Design of a* 500 GeV e^+e^- *Linear Collider with Integrated X-ray Laser Facility,* ed. R. Brinkmann, G. Materlik, J. Rossbach, and A. Wagner, DESY 1997-048, ECFA 1997-182.

[74] R. Hawkings, transparencies presented at the Fifth ECFA/DESY Linear Collider Workshop, Obernai, 16-19 October 1999. The charm tagging efficiencies and purities presented here differ from those of reference [73].

[75] OPAL Collaboration, Z. Phys. **C66** (1995) 19.

[76] OPAL Collaboration, Z. Phys. **C73** (1997) 587.

[77] Particle Data Group, R. M. Barnett et al., Phys. Rev. **D54** (1996) 1.

[78] CLEO Collaboration, Phys. Rev. **D56** (1997) 3783.

[79] The LEP Collaborations ALEPH, DELPHI, L3, and OPAL, and the LEP Electroweak working group, *Combining Heavy Flavour Electroweak Measurements at LEP,* CERN-PPE/96-017 (1996).

[80] OPAL Collaboration, Z. Phys. **C72** (1996) 1.

[81] CLEO Collaboration, Phys. Rev. Lett. **75** (1995) 3232.

[82] OPAL Collaboration, Z. Phys. **C76** (1997) 425.

[83] CLEO Collaboration, Phys. Rev. Lett. **72** (1994) 2328.

[84] S. Godfrey and R. Kokoski, Phys. Rev. **D43** (1991) 1679.

[85] CLEO Collaboration, Phys. Rev. Lett. **72** (1994) 1972.

[86] F. Becattini, *Universality of thermal hadron production in* pp, $\mathrm{p\bar{p}}$ *and* $\mathrm{e^+e^-}$ *collisions,* hep-ph/9701275, v2, proceedings of the XXXIII Eloisatron Workshop on Universality features in multihadron production and the leading effect, October 19-25 1996, Erice, Italy.

[87] ALEPH Collaboration, Phys. Lett. **B425** (1998) 215;
ALEPH Collaboration, Z. Phys. **C69** (1996) 393;
OPAL Collaboration, Z. Phys. **C66** (1995) 19;
DELPHI Collaboration, Phys. Lett. **B345** (1995) 598;
DELPHI Collaboration, *A direct measurement of the branching fractions of the* b*-quark into strange, neutral and charged* B*-mesons,* 1999 EPS Conf., Tampere.

[88] OPAL Muon Identification Working Group, *Identification of Muons in Hadronic* Z *Decays*, OPAL Technical Note TN107, July 1992.

[89] D. Charlton and P. Gagnon, *Muon Identification Efficiency and Background for PASS7 LEP1 Data,* OPAL Technical Note TN572, October 1998;
D. Charlton, *Muon Identification Efficiency and Background for Pass-5 Data*, OPAL Technical Note TN211, February 1994.

[90] S. Marcellini and A. Montanari, *Identification of Inclusive Muons in Multihadronic Events with the Hadron Calorimeter,* OPAL Technical Note TN083, February 1992.

[91] C. Peterson, T. Rögnvaldsson, and L. Lönnblad, Comput. Phys. Commun. **81** (1994) 185.

[92] F. Fiedler, *A Neural Net For Muon Identification,* OPAL Technical Note TN591, 22nd January 1999.

Acknowledgements

I am aware that this thesis would not have been possible without the help, advice, and friendship of many people, to whom I feel greatly indebted. Moreover, it is because of these people that the time during which I worked on this thesis was in general a very happy one. Special thanks (in alphabetical order) to Albrecht Wagner, Alessandra Fanfani, Alex Oh, Andreas Sittler, Carsten Hensel, Christian Carl, Dave Charlton, Götz Gaycken, Jakob Hauschildt, Jens Meyer, Johannes Steuerer, Jules Gascon, Klaus Desch, Klaus Mönig, Kristian Harder, Niels Meyer, Norbert Tesch, Oliver Cooke, Petra Hüntemeyer, Ramona Matthes, Richard Hawkings, Rick Van Kooten, Rolf Heuer, Silke Petzold, Silvia Arcelli, Stefano Marcellini, Ties Behnke, Vasiliy Morgunov, Wolfgang Menges, Wolfram Zeuner, to the many others who contributed, and in particular to you. And above all, what would I do if it were not for Grit and Lukas?